CRANFIELD INSTITUTE OF TECHNOLOGY
SCHOOL OF MECHANICAL ENGINEERING

Ph.D Thesis.

Eli Jidere Bala

DEVELOPMENT OF A SOLAR-ENERGY ACTIVATED ORGANIC RANKINE-CYCLE PILOT POWER PLANT.

SUPERVISOR: Dr. P. W. O'Callaghan.

August 1984.

DEDICATED

TO

LINDA AND UBA.

ACKNOWLEDGEMENT

I would like to express my profound gratitude to my supervisor Dr. P.W.O'Callaghan, for the guidance he gave me over the past three years.

My sincere thanks to Prof. S. D. Probert, for the immense constructive criticisms and the help he rendered to me even on none academic problems.

I am grateful to Dr. Mohey Hussein, who paved the way to the current work for me.

I am also most grateful to Dr. Mike Shilston and Dr. Brian Norton for the encouragement and help I received from them.

To Mr. John Dawe and Mr. Charlie Knight, thank you for the immense help rendered to me during the course of my experiments.

To my wife Linda, your patience and understanding was invaluable. Thank you.

SUMMARY

With the development of a low-grade energy engine in the School of Mechanical Engineering at Cranfield, there began a venture towards utilizing the Sun's power to operate the engine via a thermodynamic cycle, in an Egyptian desert area, i.e latitude 30° N. The derived mechanical power is to drive an irrigation pump at the site.

The solar thermal system is to operate in a Rankine-cycle using an organic working fluid. The engine is in the form of a multi-vane expander. The solar-energy collector comprises of an array of gravity-assisted heat- pipes each enclosed within a cylindrical high-vacuum glass tube. The irrigation water which is to be sucked from below ground level, is also to cool the shell-and-tube condenser.

The first section(i.e.PART A) of this thesis is a presentation of some design optimization concepts in the development of the thermodynamically operated solar-energy system.

As in any desert area dust will constitute a problem, reducing the harnessing capability of the collector array. Regular cleaning would therefore be essential. However, cleaning a large array (≃1000) of such fragile tubes in situ is unlikely to be accomplished without cracks and breakages occurring. This perhaps means that the high-vacuum which is essential for each collectors continued adequate thermal performance could be easily lost. The collectors are also considered expensive. For example, one tube with an effective aperture area of about 0.102m² costs about twenty pounds Sterling. These and the fact that the maximum anticipated working temperature in the organic Rankine-cycle would be about 120°C, led to the study into a means other than evacuation of reducing thermal losses from the receiver of a flat-plate solar-energy collector in the second section (i.e. PART B).

A flat-plate collector employing a simple slatted convection suppression device was studied. It was shown that a flat-plate collector employing an effective convection suppression device and an initial cost of about £100/m² would be more cost effective than the evacuated-tube collector, when employed to activate the pilot power plant for operating temperaures of (80→120)° C.

The cost per peak watt could be reduced by an average value of about 15% depending upon the operating temperture. Whereas the break-even time against electricity could be reduced by about 43%. However, the overall efficiency of the power plant could fall by an average value of about 23%, depending upon the operating temperature.

PART A

CONTENTS

NOMENCLATURE

A	Area (m^2)
B	Constant ($=E\sigma T_a^4$) (W/m^2)
$\vec{C}$	Critical incident solar ray on the reflector.
d	Solar declination (Degrees).
D	Diameter of the receiver or the glass tube (m)
E	Effective emissivity $\left(= \left[\frac{1}{\varepsilon_r} + \frac{(1-\varepsilon_g)}{\varepsilon_g}\frac{D_r}{D_g}\right]^{-1}\right)$.
h	Heat transfer coefficient ($W/m^2 K$).
H	The long term monthly mean of daily solar radiation on a horizontal plane (MJ/m^2).
i	Incidence angle (Degrees).
I	solar energy intensity (W/m^2).
K	Thermal conductivity (W/m K)
k	Clearness index ($=H_t/H_e$).
L	Latitude (Degrees).
m	Mass of the working fluid (Kg).
$\dot{m}$	Mass flow rate (Kg/s).
M	Aperture width of the reflector-see fig.5 (m).
$\vec{n}$	Tangent to the reflector.
N	Day of the year, e.g. on January 1^{st}, N=1.
Nu	Nusselt number ($=hD/K_a$).
p	Absolute pressure (N/m^2).
P	Power (W).
$\dot{q}$	Energy rate per unit receiver area (W/m^2).
r	Reflectance of the reflector.
R	Thermal resistance (K/W).
Re_D	Reynolds number ($=vD\rho/\mu$).
$\vec{S}$	A vector from a point on the compound parabolic reflector and tangential to the cylindrical receiver surface.
t	Sun time, with mornings positive and t=Ø at solar-noon (hrs.)
T	Absolute temperature (K).
U	Overall steady-state heat transfer coefficient ($W/m^2 K$)
V	Volume of the working fluid (m^3).
$\dot{V}$	Volume flow rate of the working fluid (m^3/s).
v	Velocity (m/s).
x	Heat exergy (W).
$\dot{x}$	Rate of heat exergy gain per unit receiver area (W/m^2).
w	Cost of a solar-energy collector tube (£).

Greek alphabet

α Solar-energy absorptance of the receiver selective coating.

β Angle between a solar ray and a reference axis—see figs.11 and B1 (Degrees).

γ The surface azimuth angle,i.e. the deviation of the normal to a surface from the local meridian, with east positive and south zero (Degrees).

δ Ratio of ΔT to the ambient temperature.

Δp Pressure difference (N/m^2).

ΔT Difference in temperature between the heat pipe condenser and the fluid bulk inside the manifold-see fig.7. ($^{\circ}C$).

ε Emissivity of the glass tube or receiver coating.

ξ A factor that accounts for reflector imperfections and contructional deficiencies.

η Efficiency of the collector, engine, pump or the overall system.

θ An angle from the axis of symmetry of the compound parabolic reflector, measured anti-clockwise from the negative Y-axis--see fig.A2. (Degrees).

θ_a Half acceptance angle of the compound parabolic reflector (Degrees).

λ Concentration ratio of the truncated compound parabolic reflector.

μ Dynamic viscosity of air (Ns/m^2).

ξ Inclination of the heat pipe to the horizontal—see fig.4. (Degrees).

ρ Density of the working fluid (Kg/m^3).

σ Stefan-Boltzman constant (W/m^2K^4).

τ Solar-energy transmittance of the glass tube.

ϕ Ratio of the mean surface temperature of the receiver to the ambient temperature ($=T_r/T_a$).

Φ Collector tilt-angle from the horizontal (Degrees).

ψ Ratio of the temperature of the condenser to that of the surroundings ($=T_c/T_a$).

Ψ The angle between the east-west vertical plane and the projection of the Sun vector on the X-Z plane—see fig.B2. (Degrees).

ω Solar hour angle, i.e. the angular displacement of the Sun, east or west of the local meridian due to rotation of the Earth on its axis at 15 per hour (Degrees).

Ω Constant ($= I\tau\alpha r\lambda\xi$) ($W/m^2$).

Subscripts

a	Ambient environment
A	Solar altitude angle.
b	Beam solar insolation.
c	Condenser.
col	Solar-energy collector.
d	Diffuse solar insolation.
e	Extra-terrestrial.
E	Rankine-cycle engine.
f	Rankine-cycle working fluid.
g	Glass tube.
G	Overall system.
L	Lubricant
o	Collector thermal losses.
max.	Maximum value
min.	Minimum value
mix.	Mixture of freon and lubricant.
p	Pump
r	Solar-energy receiver.
s	Sunset
t	Total radiation, i.e. beam and diffuse.
u	Collector useful gains
z	Zenith angle
1	Radiation between the receiver and its surrounding glass tube-see fig.6.
2	Radiation between the glass tube and its surroundings - see fig.6.
3	Convection from the glass tube - see fig.6 At an angle .

Superscripts

*	Optimal value for the solar-energy collector.
**	Optimal value for the overall collector and engine system.
/	For the truncated reflector.
-	Average value.

CHAPTER ONE

INTRODUCTION

With the development of a low-grade energy engine in the School of Mechanical Engineering at Cranfield Institute of Technology, a venture towards utilizing the Sun's power to drive the engine in an Egyptian desert area (i.e. latitude 30° N) was initiated-called the 'King Tut' project. The venture involved the Institute, the Egyptian Government and two British companies, i.e. Denco Ltd and the General Electric Company.

The solar-energy thermal system, which is to drive a water pump for an irrigation scheme is to operate in a Rankine-cycle using trichlorotrifluoroethane (i.e. R-113) as the working fluid. The engine is in the form of a multi-vane expander (Ref.1). The solar-energy collectors (see fig.1) comprise of gravity-assisted heat-pipes each enclosed within a cylindrical high-vacuum glass tube. A truncated compound parabolic reflector is incorporated within each glass tube so as to concentrate the Sun's rays on to the heat-pipe. The Rankine-cycle feed pump is of the positive displacement sliding-vanes type to be directly coupled to the prime mover. The irrigation water which is to be sucked from below ground level is also to cool the shell-and-tube condenser. The arrangement of the expander, feed pump and the irrigation pump is shown in fig.2, whereas the schematic diagram of the solar-thermal system is depicted in fig.3.

In such a thermodynamically operated solar-energy power plant, conflicting requirements are encountered with respect to high thermal performance of the solar-energy collector and that for the heat engine. The efficiency of a solar-energy collector decreases with increase in the difference between its output temperature and that of the surroundings, whereas a heat engine performs better at higher temperature differences. However, the overall thermal efficiency of the system may be defined as the product of the solar-energy collector and heat engine efficiencies. As a result of these conflicting requirements, it was expected that an optimal collector output temperature that maximizes the thermal efficiency of such a system might occur. The steady-state thermal performance of the high-vacuum tube solar-energy collector was therefore simulated and the overall efficiency of the heat engine and collector optimized with respect to the

heat-pipe's surface temperature, which is related to the output temperature.

In order to maximize the amount of solar-radiation reaching the absorber of the solar-energy collector, it would be desirable that the Sun's relative motion be tracked. However, in a large array of tubes such as in the power generation unit envisaged in this study, practical problems could arise even when seasonal tracking is involved. Tracking mechanisms could also be expensive. Thus the collector is to be employed stationary. However, to maximize solar radiation incident on to the aperture of the stationary collector over a required period, its tilt-angle above the horizontal must be optimized. A systematic method that seeks to determine the optimal angle was thus outlined. In addition, the method gives a criterion for choosing the average design insolation value, considering the variable nature of solar-energy intensity.

The choice of a working fluid in a Rankine-cycle is usually based paramountly on its thermal stability at the boiler temperature and its performance with the heat engine. It is also, however, important to choose a fluid which has acceptable efficiency characteristics with the feed pump. This is considered desirable in a system where the feed pump is to be directly driven by the prime mover, because the fraction of the total power developed that is used up by the feed pump, plays a role in determining the overall efficiency of the system. So tests were conducted with the then available organic working fluids (i.e. R-113 and R-11), to investigate that which gives the better performance with the positive displacement sliding-vanes pump. The chemical name of R-11 is trichlorofluoromethane.

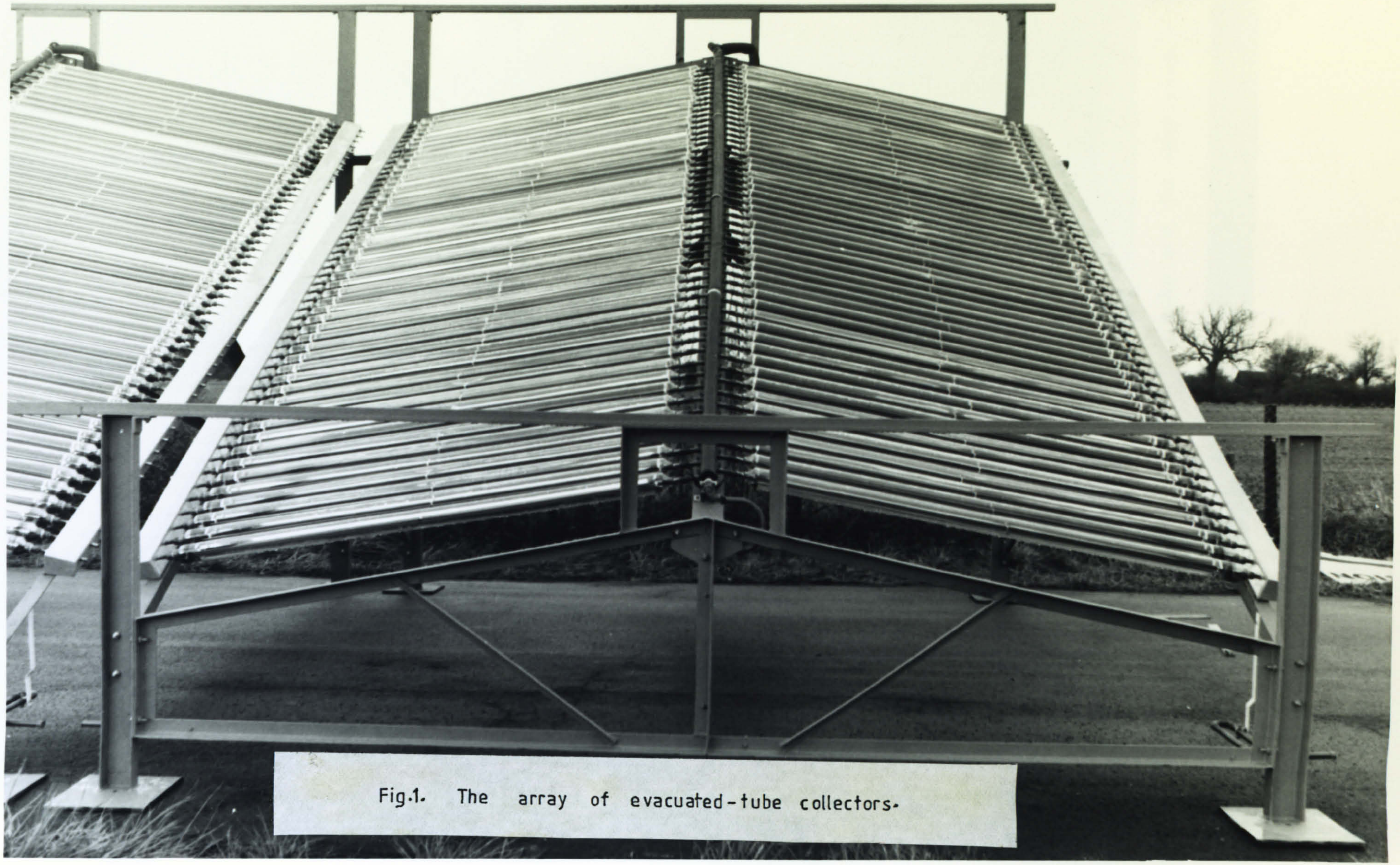

Fig.1. The array of evacuated-tube collectors.

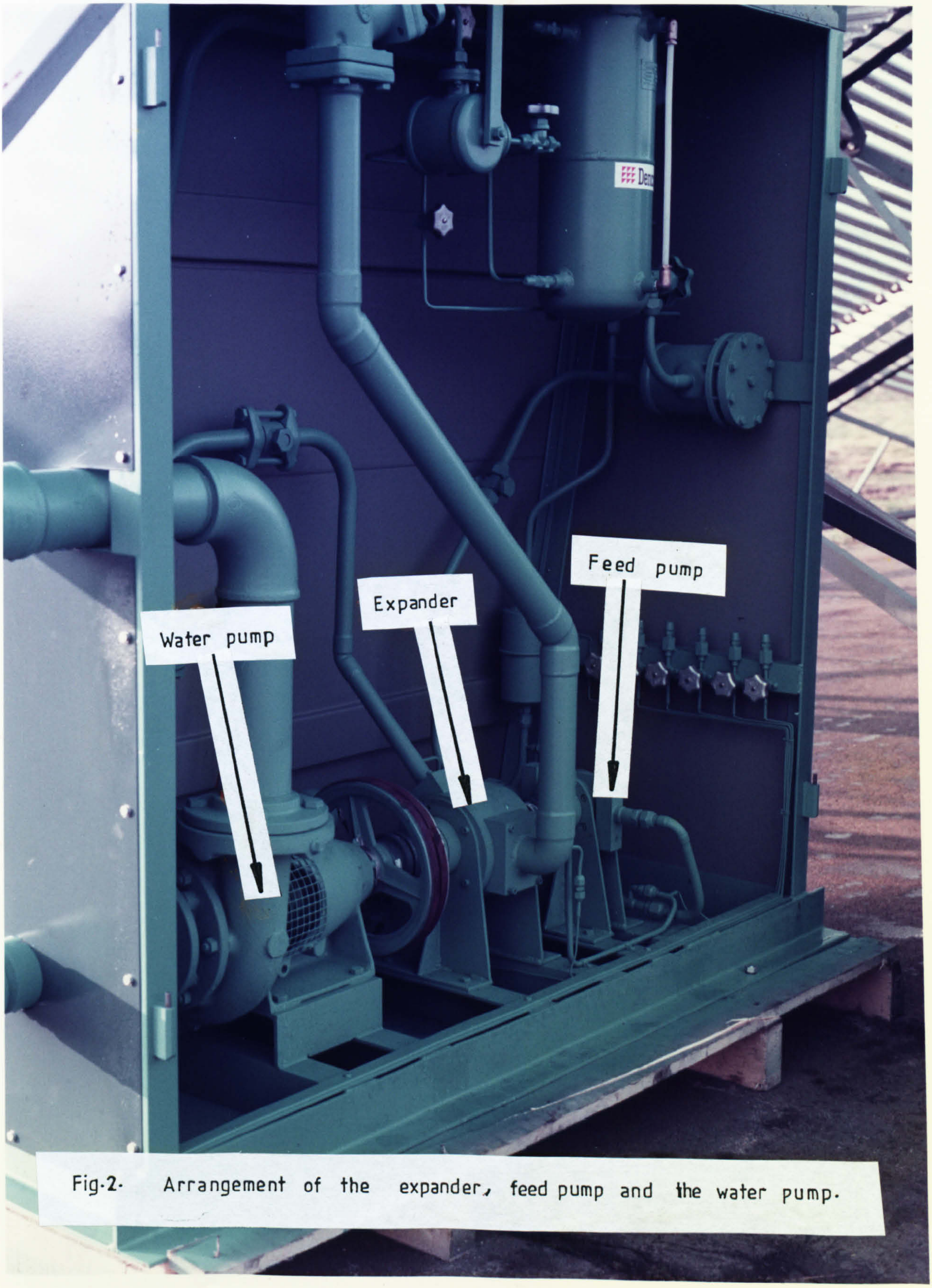

Fig.2. Arrangement of the expander, feed pump and the water pump.

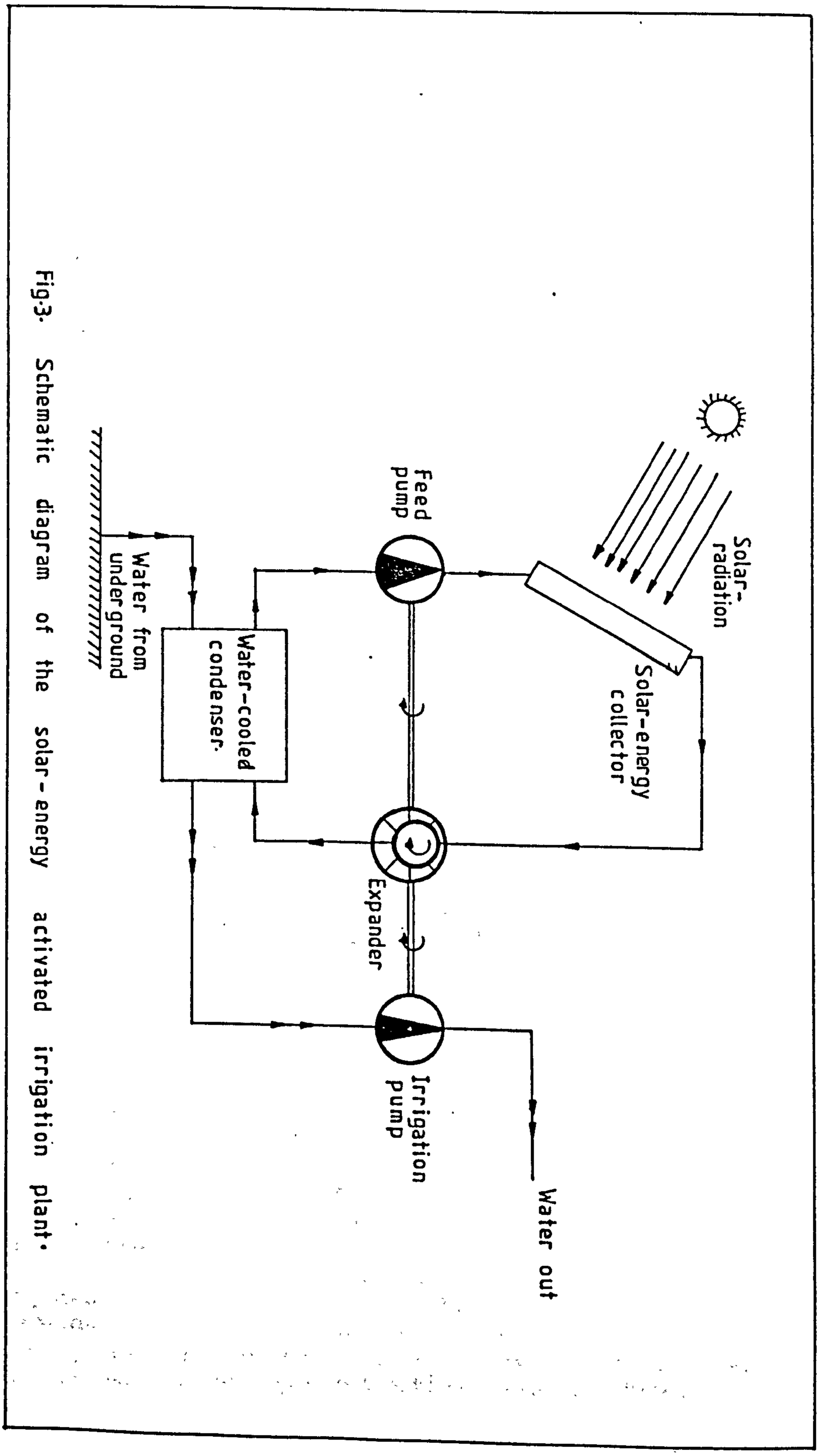

Fig.3. Schematic diagram of the solar-energy activated irrigation pump plant.

CHAPTER TWO

THE SOLAR-ENERGY COLLECTOR.

2.1 DESCRIPTION.

The collector is an array of gravity-assisted heat-pipes each enclosed within a 65mm evacuated pyrex tube-see fig.4. They were manufactured by the General Electric company, U.K. The high-vacuum which is to minimize thermal losses through convection and conduction is of the order of 10^{-4} torr. The heat-pipe's body and working fluid are 15mm black chrome-coated-copper tube and water respectively. A truncated compound parabolic reflector of designed acceptance angle of 60° is incorporated inside the glass tube so as to concentrate the Sun's rays on to the heat-pipe (see fig.5 for the reflector and Appendix A for the design parameters). A concentrator is employed because of the high ratio of beam to total insolations in Egypt (Ref.3). The tubes are oriented along the east-west direction and inclined at an angle of about 5° to the horizontal to allow for the thermo-syphon action to occur within the heat-pipes. The heat-pipes are joined orthogonally to the manifold via ball-and-socket joints. Such a joint would provide flexibility and also facilitate the replacement of a tube should it break, without loss of the Rankine-cycle working fluid and concomittant disruption of the entire plant. The array of tubes is inclined from the horizontal at an optimal angle of 30°, facing south. This 30° tilt and 60° acceptance angle of the reflector would theoretically allow the collection of direct solar rays within at least 2.8 hours before and after solar-noon each day of the year, without any need for tracking — see Appendix B for details.

2.2 MATHEMATICAL SIMULATION OF THE COLLECTOR STEADY-STATE THERMAL PERFORMANCE.

2.2.1 Assumptions.

(1)Steady-state conditions are considered to apply.
(2)For simplicity, the effect of the reflector on the thermal energy exchanges between the receiver and the glass tube is assumed negligible.
(3)The vacuum of 10^{-4} torr within the annulus is sufficient to suppress completely any convection and conduction via the residual air within the annulus(ref.4).
(4)The glass tube and receiver have lambertonian surfaces, i.e. they exhibit isotropic reflection characteristics.

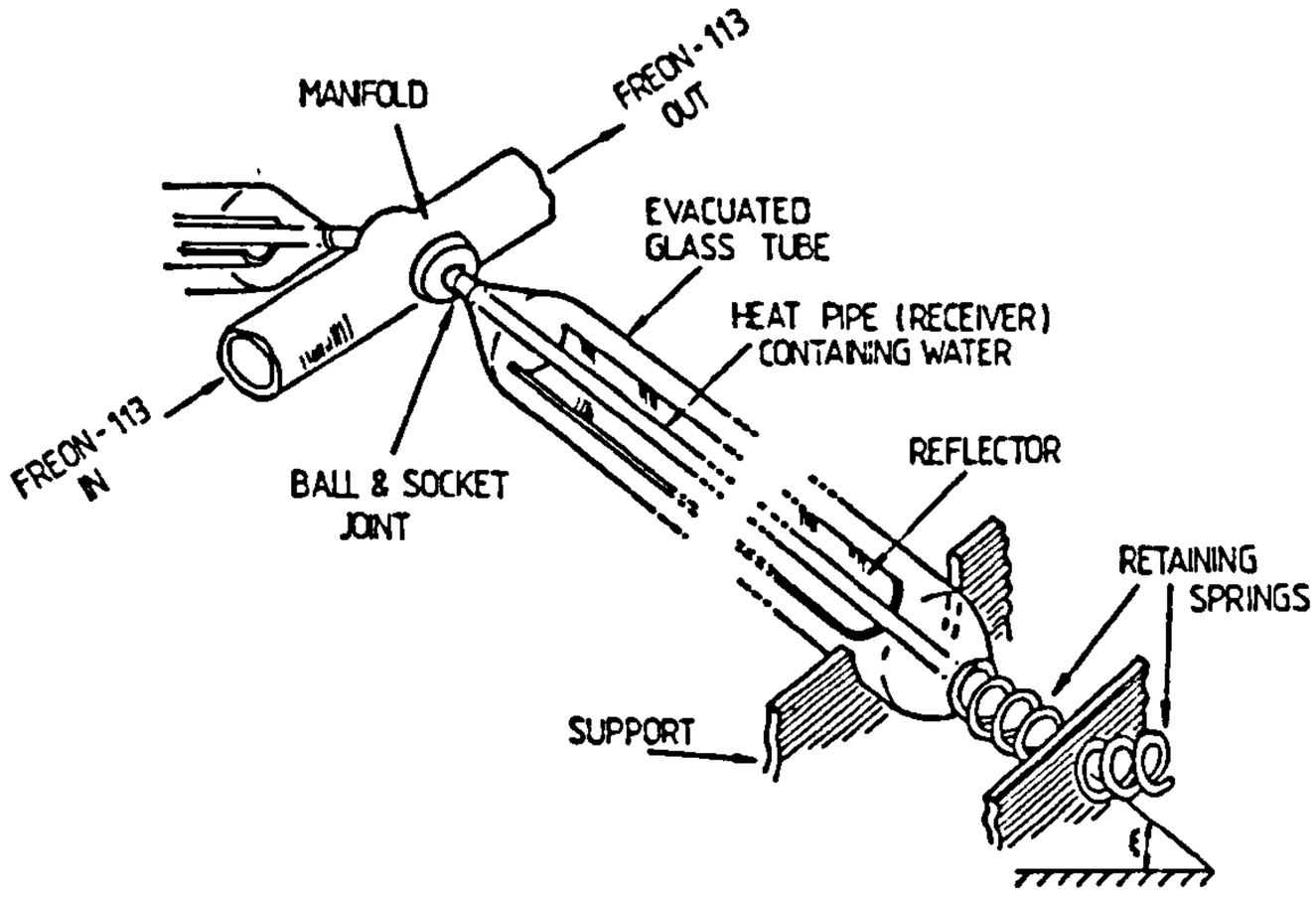

Fig. 4. Details of the solar-energy collector. The manifold is inclined in a north–south plane at an angle of 30° to the horizontal, its southerly end being lowest. The heat pipe collectors are inclined at about 5° to the horizontal and are orthogonal to the manifold, which is connected to their highest ends.

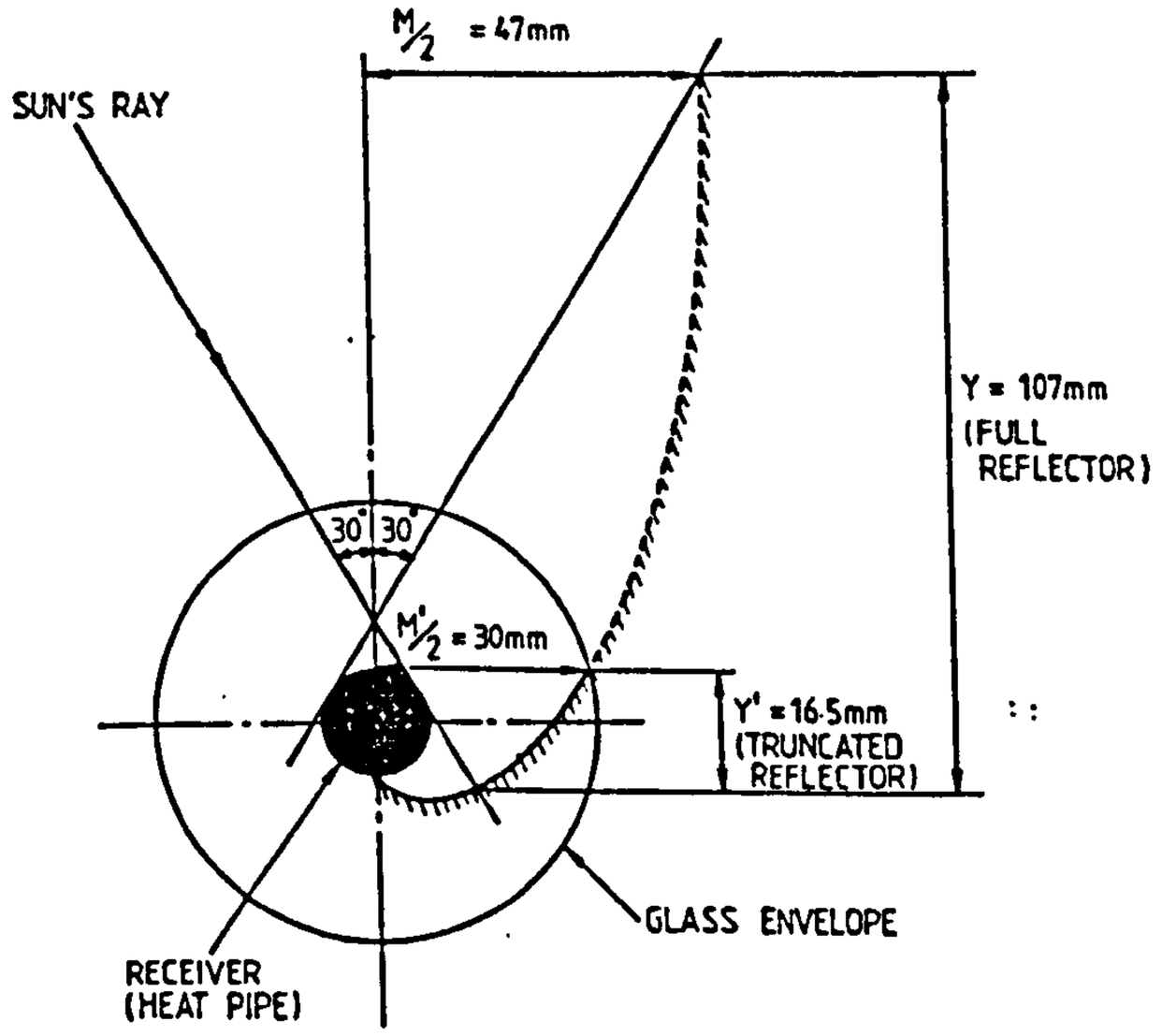

ACCEPTANCE HALF ANGLE = 30°
GLASS ENVELOPE DIAMETER D_g = 65mm
RECEIVER DIAMETER D_r = 15mm

UNTRUNCATED	CONCENTRATION RATIO = 2·00
TRUNCATED	CONCENTRATION RATIO = 1·27

Fig. 5. Section through the full and truncated compound parabolic reflector.

2.2.2 Thermal losses(Electrical analogue method)

The equivalent thermal circuit is shown in fig.6 and the component resistances evaluated according to standard practice(Ref.5 and 6). The resistance R_1 to radiative heat transfers between the receiver and the glass tube is given by:

$$R = \frac{1}{h_1 A_r} \tag{1}$$

where,

$$h_1 = \frac{\sigma (T_r^2 + T_g^2)(T_r + T_g)}{\left[\frac{1}{\varepsilon_r} + \frac{(1-\varepsilon_g)}{\varepsilon_g}\frac{D_r}{D_g}\right]} \tag{2}$$

The resistance R_2 to radiative heat transfers between the glass tube and the surrounding environment is given by:-

$$R_2 = \frac{1}{h_2 A_g} \tag{3}$$

where,

$$h_2 = \sigma \varepsilon_g (T_g^2 + T_a^2)(T_g + T_a) \tag{4}$$

The resistance R_3 to convective heat transfers from the glass tube is given by:-

$$R_3 = \frac{1}{h_3 A_g} \tag{5}$$

where,

$$h_3 = \frac{K_a \overline{Nu}}{D_g} \tag{6}$$

And $\overline{Nu} = z(Re_b)^j$ .z and j are constants dependent on the magnitude of the Reynolds number, Re_b.
The overall heat loss coefficient U for the system is given by:-

$$\frac{1}{U A_r} = \frac{1}{h_1 A_r} + \frac{1}{(h_2 + h_3) A_g} \tag{7}$$

Therefore:

$$U = \left[\frac{1}{h_1} + \frac{A_r}{(h_2 + h_3) A_g}\right]^{-1} \tag{8}$$

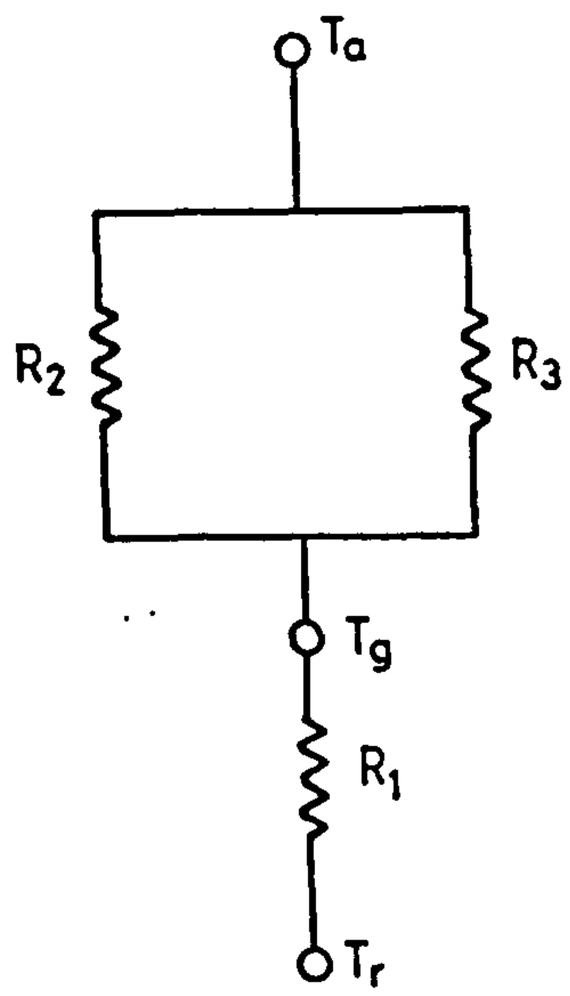

Fig. 6. Equivalent thermal circuit for steady-state heat losses from the evacuated tube, heat-pipe collector.

However, Engholm and Hertz (Ref.7) intimated that the performance of an evacuated tube solar energy collector is almost insensitive to wind conditions. This has been interpretted to mean that h_3 is much greater than h_2, such that $1/h_1$ becomes much greater than $A_r/(h_2+h_3)A_3$.
This therefore approximates equation (8) to:-

$$U \simeq h_1$$

For the steady state:-

(Rate of heat losses from the receiver to the surroundings) = (Rate of heat losses from the receiver to the glass tube)

Therefore:

$$UA_r(T_r - T_a) = h_1 A_r (T_r - T_g)$$

Therefore:

$$T_g = T_r - \frac{U}{h_1}(T_r - T_a)$$

But it was shown that U is approximately equal to h_1.
Therefore:

$$T_g \simeq T_a \tag{9}$$

Substituting $T_g \simeq T_a$ in equation (2), yields:-

$$U \simeq h_1 \simeq \frac{\sigma}{\left(\frac{1}{\varepsilon_r} + \frac{(1-\varepsilon_g)D_r}{\varepsilon_g D_g}\right)}(T_r^2 + T_a^2)(T_r + T_a) \tag{10}$$

Equation (10) can be rewritten as:-

$$U = E\sigma(T_r^2 + T_a^2)(T_r + T_a) \tag{11}$$

where E is the effective emissivity and is given by:-

$$E = \frac{1}{\left(\frac{1}{\varepsilon_r} + \frac{(1-\varepsilon_g)D_r}{\varepsilon_g D_g}\right)} \tag{12}$$

The rate of heat losses $\dot{q}_o$ from the receiver to the surroundings is given by:-

$$\dot{q}_o = U(T_r - T_a) \tag{13}$$

Insertion of the expression for U from equation (11) in equation (13), gives:-

$$\dot{q}_o = E\sigma' (T_r^4 - T_a^4) \qquad (14)$$

2.2.3 Collector gains and efficiency.

For simplicity of expressing the gains and efficiency of the collector, the receiver absorptance α for solar radiation as well as the glass tube transmittance τ are both asumed to be independent of angle of incidence of the solar radiation. From discussions with the manufacturer, i.e. the General Electric Company, it is assumed that the reflector contour imperfections and other contructional deficiencies would result in increasing the optical losses by not more than 10 percent.
The energy balance per unit receiver area can be stated as:-

(Rate of useful gains) = (Rate of absorbed solar radiation) - (Rate of thermal losses)

The rate of absorbed solar radiation per unit receiver area is the product of the solar insolation I, the glass tube transmittance τ, the receiver absorptance α, concentration ratio λ, reflectance of the reflector r and the factor ζ that accounts for the constructional deficiencies.
Therefore:

$$\dot{q}_u = I\tau\alpha r\lambda\zeta - E\sigma' (T_r^4 - T_a^4) \qquad (15)$$

Denoting $I\tau\alpha r\lambda\zeta = \Omega$, $E\sigma' T_a^4 = B$ and $(T_r / T_a) = \phi$, reduces equation (15) to:-

$$\dot{q}_u = \Omega - B(\phi^4 - 1) \qquad (16)$$

By definition, collection efficiency η_{col} is:-

$$\eta_{col} = \frac{\text{(useful gain per unit receiver area)}}{\text{(captured energy per unit receiver area)}}$$

Therefore:-

$$\eta_{col} = [\Omega - B(\phi^4 - 1)]/\lambda I \qquad (17)$$

The following numerical values for the design parameters

will be used in subsequent analysis:-
λ =1.27(concentration ratio of the truncated compound parabolic reflector as shown in fig.5).
I =800W/m^2(Average peak solar insolation in Egypt)
T_a =318 K(Peak ambient temperature in Egypt)
From discussions with the General Electric Company,the following numerical values also apply:-
ε_r=0.1, ε_g=0.9, r=0.9, τ=0.9, α=0.9, D_g=65mm and D_r=15mm.

2.2.4 Optimal surface temperature of the heat pipe element.

The optimal surface temperature of the heat pipe element will occur if the first derivative of its heat exergy with respect to temperature is zero(Ref.8). The heat exergy x, is the maximum amount of the thermal energy which is available to perform work.
The heat exergy rate $\dot{x}$ per unit receiver area is given by:-

$$\dot{x} = \frac{(T_r - T_a)}{T_r}[\Omega - B(\phi^4 - 1)] = (1 - \frac{1}{\phi})[\Omega - B(\phi^4 - 1)] \qquad (18)$$

Differentiating equation (18) with respect to ϕ, setting $\frac{d\dot{x}}{d\phi} = 0$ and rearranging, gives:-

$$4\phi^5 - 3\phi^4 - (1 + \frac{\Omega}{B}) = 0 \qquad (19)$$

The solution of equation (19), which also satisfies $\frac{d^2\dot{x}}{d\phi^2} = 0$, will reveal the optimal value $\phi^*(=T_r^*/T_a)$. Using the numerical design values mentioned earlier, a solution was obtained iteratively using the Newton-Raphson method(Ref.9). Hence it has been deduced that ϕ^* =1.453, and so T_r^*=462K(=189°C). Substituting the value of ϕ^*, so deduced, in equations (16) and (17) gives $\dot{q}_u^*$ =466.7W/m^2 and η_{col}^*=0.46 respectively.

2.3. CONCLUSIONS

For the design values used,the preceeding analysis reveals that the heat-pipe is capable of attaining an optimal surface temperature of 189°C, at which the maximum rate of thermal energy available to perform work will be maximized. This will occur when the rate of solar-energy retained by the collector is 466.7W for each square meter of the heat-pipe's surface area.
However, because of the occurrence of thermal resistance at the ball-and-socket joint, some exergy will be lost and only a fraction will be transferred to the Rankine-cycle working fluid inside the manifold.

CHAPTER THREE

OVERALL SYSTEM BEHAVIOUR

3.1 EFFICIENCY

The theoretical maximum efficiency for conversion of heat energy to mechanical work was first defined by Carnot as $(T_h - T_c)/T_h$. Where T_h and T_c are the absolute temperatures of the heat source and sink respectively. This defination means that the greater the temperature difference between the heat source and the heat sink, the greater will be the thermal efficiency of the heat engine. Unfortunately, however, the efficiency of a solar-energy collector decreases with increases in the temperature difference between its output temperature and that of the surroundings. This arises from the fact that solar-energy collector heat losses increase in proportion to the temperature difference between the absorber and the surroundings.

In order words, the requirement for a high heat engine efficiency is the reverse of that for the solar energy collector efficiency.

By a simple definition, the overall efficiency of a solar-energy collector and a heat engine system is the product of their respective efficiencies. As a result of the conflicting high efficiency requirements, there will exist an output collector temperature for any such system that maximizes the overall efficiency.

It will be assumed from the performance tests conducted(Ref.2), that the prime mover has an average efficiency equal to 60 percent that of ideal Carnot engine operating between the same temperatures.

Because of the occurrence of thermal resistance at each ball-and-socket joint, the temperature T_f of the Rankine-cycle working fluid at the collector output would be less(by ΔT) than the receiver surface temperature, T_r -- see fig.7, i.e.

$$T_f = T_r - \Delta T \qquad (20)$$

The engines efficiency η_E, is by definition given by:-

$$\eta_E = 0.6(T_f - T_c)/T_f \qquad (21)$$

where T_c is the condenser temperature.

Substituting the expression for T_f from equation (20) in equation (21), gives the engines efficiency in terms of T_r as:-

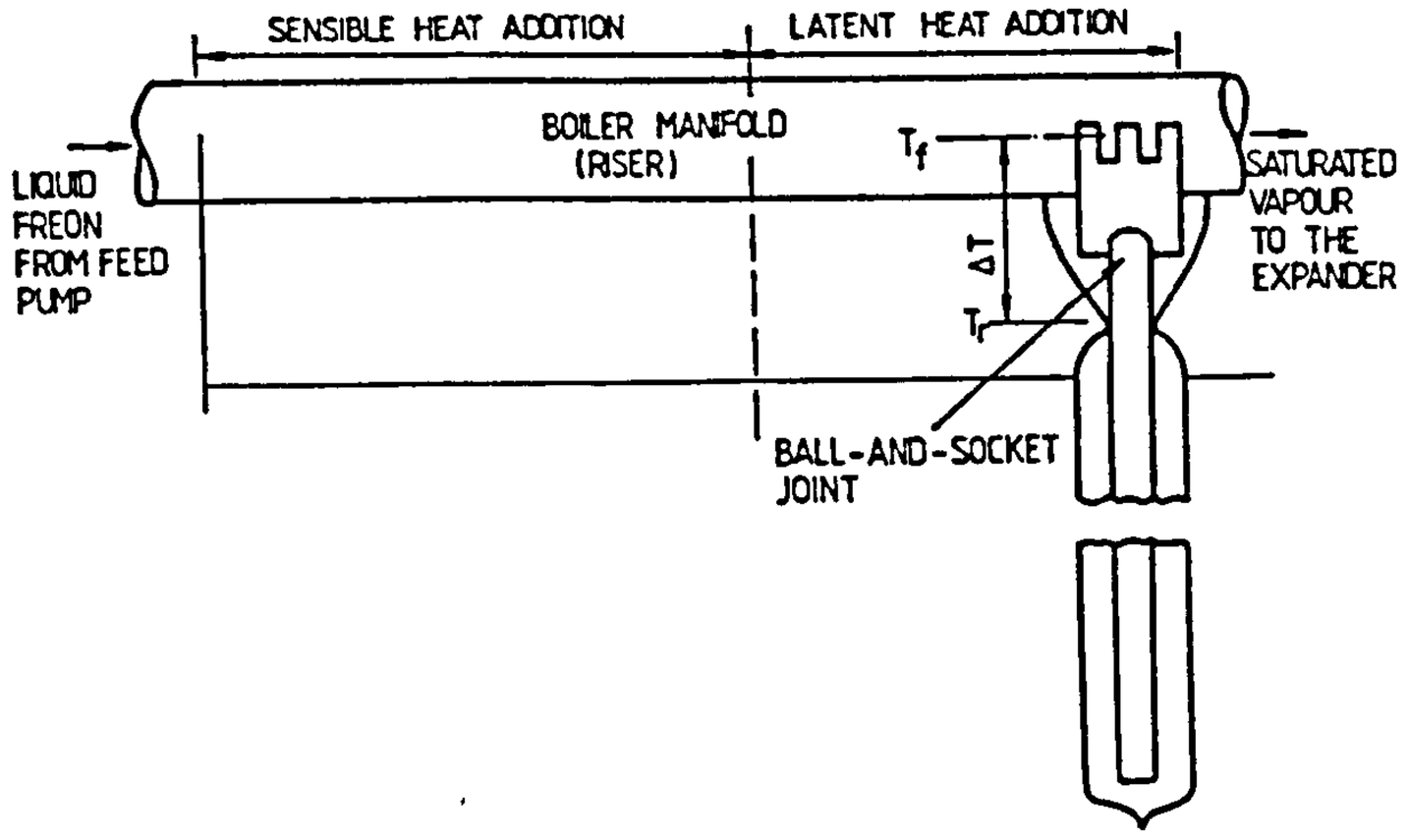

Fig. 7- Schematic diagram indicating the temperature difference between one of the heat pipe condensers and the bulk of the Freon-113 within the manifold.

$$E=\emptyset.6\frac{(T_r-\Delta T-T_c)}{(T_r-\Delta T)}=\emptyset.6\frac{[(T_r/T_c)-(\Delta T/T_c)-1]}{[(T_r/T_c)-(\Delta T/T_c)]} \quad (22)$$

However, as mentioned previously, the overall efficiency, η_G is given by:-

$$\eta_G=\eta_{col}\times\eta_E \quad (23)$$

From equations (17) and (22), the overall efficiency can therefore be expressed as:-

$$\eta_G=\emptyset.6\frac{[\Omega-B(\phi^4-1)]}{\lambda I}\frac{[(T_r/T_c)-(\Delta T/T_b)-1]}{[(T_r/T_c)-(\Delta T/T_c)]} \quad (24)$$

In practice, it is desirable that η_G should be maximized. Two cases which could occur in practice are considered. The first case considers when the condenser is air cooled. Here, the condenser temperature is considered to be the same as that of the surroundings. The second case considers the situation when the condenser is cooled by the underground water. It is expected that the temperature of the underground water would be lower than that of the surroundings.

3.2 OPTIMIZATION: IF THE CONDENSER TEMPERATURE EQUALS THAT FOR THE SURROUNDINGS ($T_c = T_a$).

In this case, the overall efficiency can then be expressed as:-

$$\eta_G=\emptyset.6\frac{[\Omega-B(\phi^4-1)]}{\lambda I}\frac{[(T_r/T_a)-(\Delta T/T_a)-1]}{[(T_r/T_a)-(\Delta T/T_a)]} \quad (25)$$

But $(T_r/T_a)=\phi$. Denoting $(\Delta T/T_a)=\delta$, gives:-

$$\eta_G=\emptyset.6\frac{[\Omega-B(\phi^4-1)]}{\lambda I}\frac{[\phi-\delta-1]}{[\phi-\delta]} \quad (26)$$

Differentiating equation (26) with respect to ϕ and setting $\frac{d\eta_G}{d\phi}=0$ and rearranging, results in:-

$$4\phi^5-(8\delta+3)\phi^4+4(\delta^2+\delta)\phi^3-(1+\Omega/B)=\emptyset \quad (27)$$

The solution of equation (27) for a given value of δ, will give the corresponding optimal value $\phi^{**}(T_r^{**}/T_a)$ that leads to a maximum value of η_G. From equation (20):-

$$T_f^{**}=T_r^{**}-\Delta T \quad (28)$$

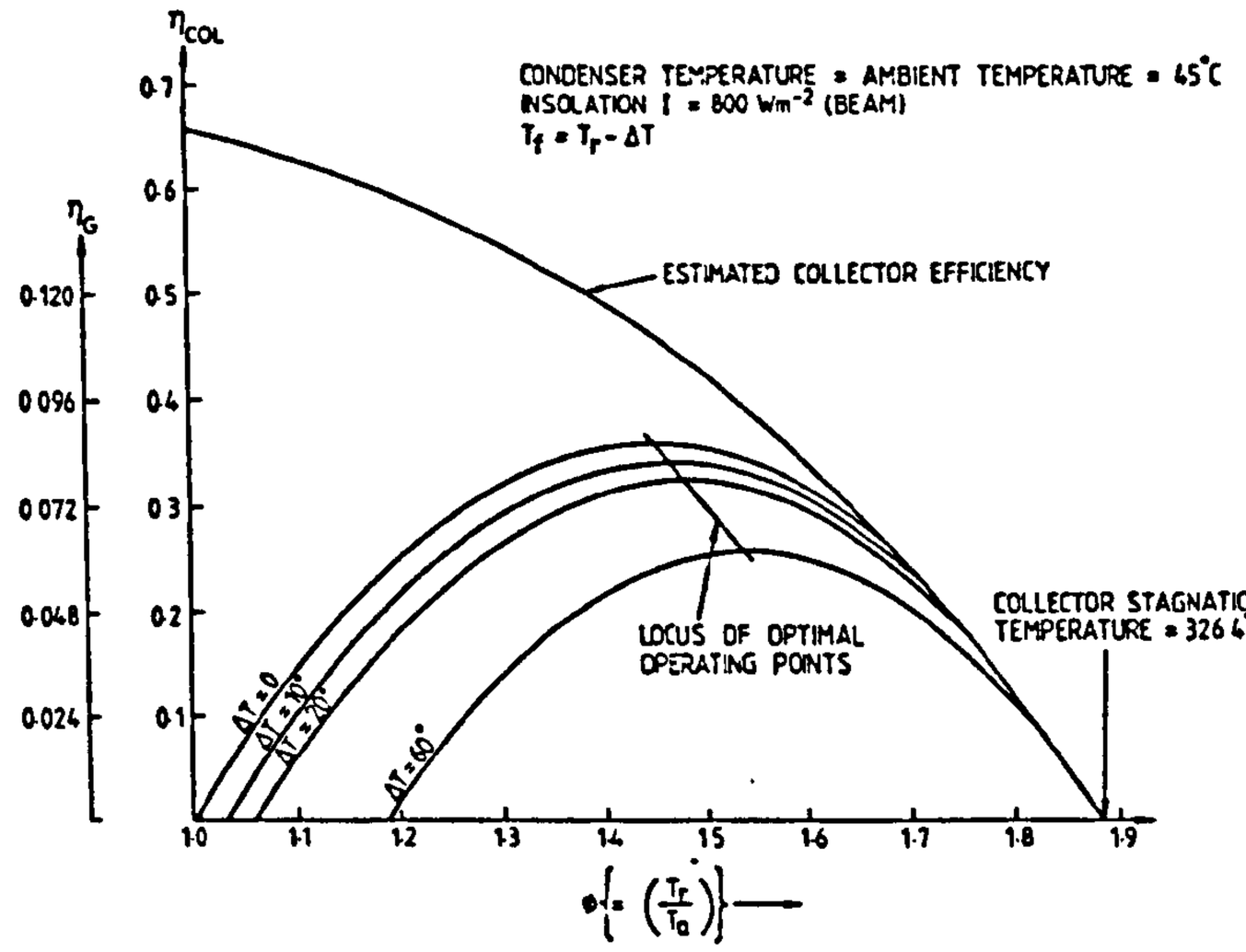

Fig. 8. Predicted variations of efficiencies of the system with temperature difference across the socket; condenser temperature, 45 °C.

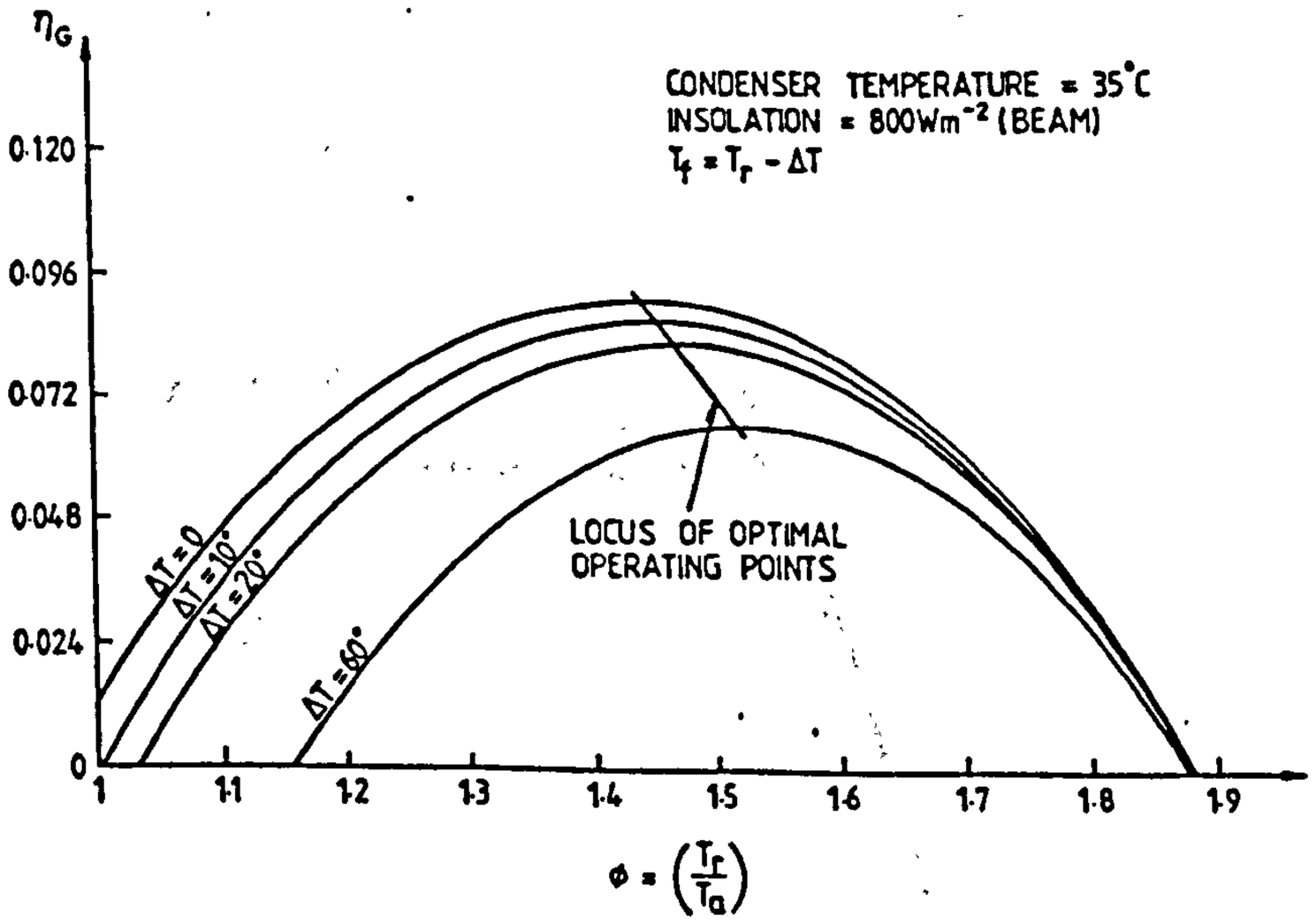

Fig. 9. As for Fig. 8, except that the condenser temperature is 35 °C.

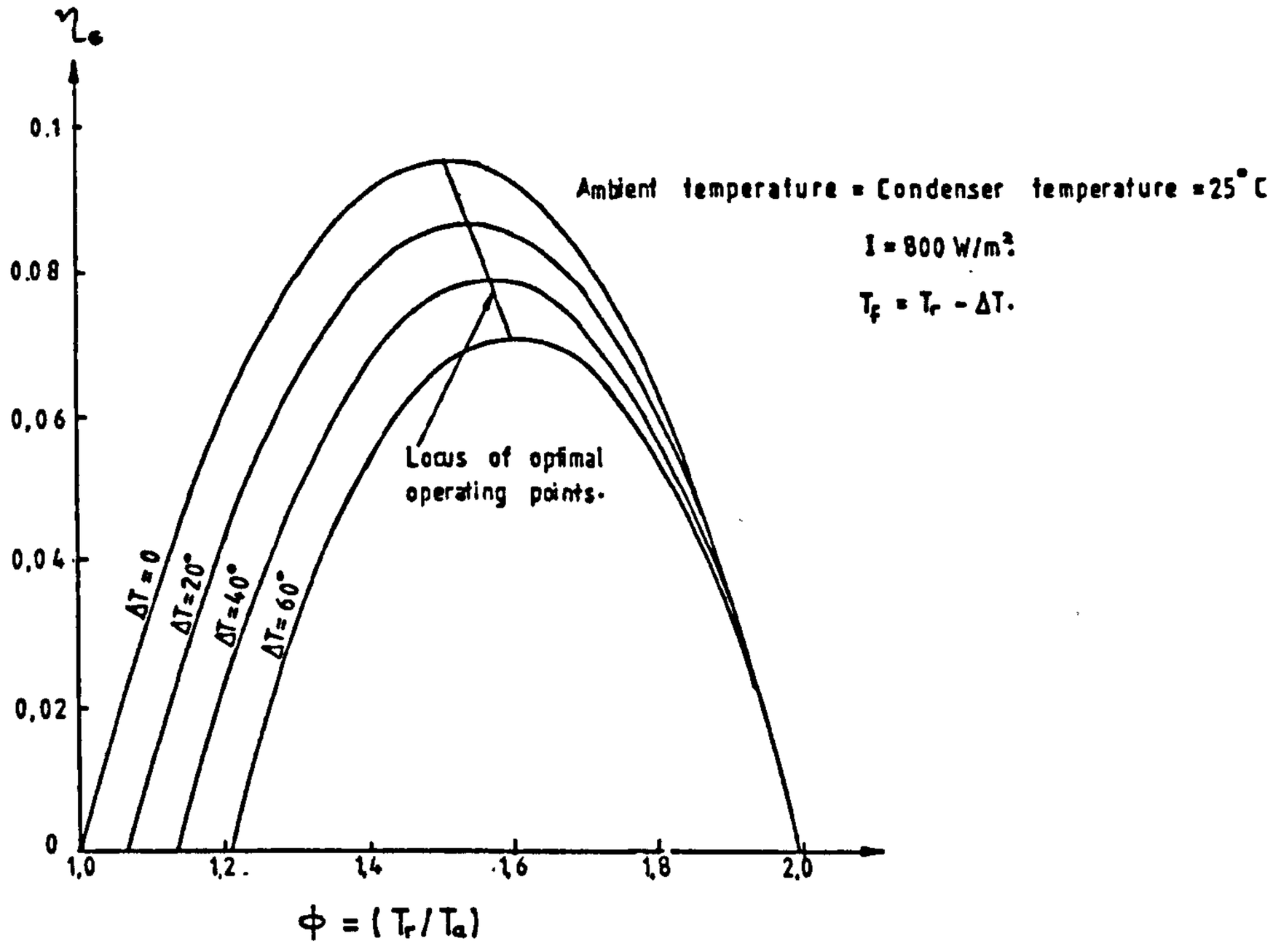

Fig 10. As for fig. 8, except that the ambient temperature is 25°C.

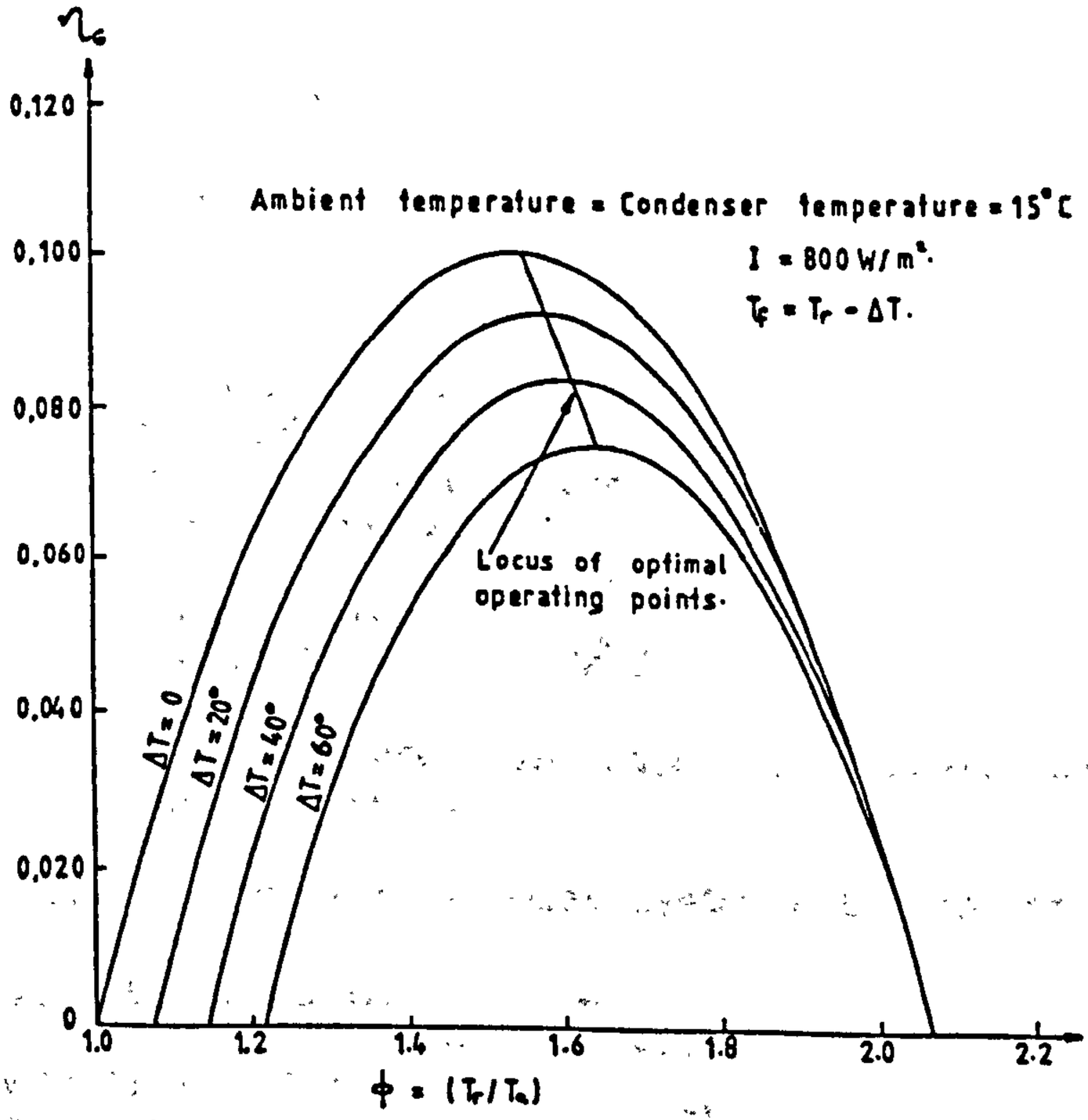

Fig.11. As for fig. 8, except that the ambient temperature is 15°C.

Figs 8, 10 and 11 show the effect of ΔT on the system's optimal performance under this case, for ambient temperatures of $45^{\circ}C$, $25^{\circ}C$ and $15^{\circ}C$ respectively.

3.3 OPTIMIZATION: IF THE CONDENSER TEMPERATURE T_c, IS LESS THAN THE AMBIENT TEMPERATURE T_a.

In this case, the overall efficiency becomes:-

$$\eta_{G=0.6}\frac{[\Phi-\delta-\Psi]}{(\Phi-\delta)}\frac{[\Omega-B(\Phi^4-1)]}{\lambda I} \qquad (29)$$

where,

$$\Psi\,(=(T_c/T_a))<1.$$

Differentiating equation (29) with respect to Φ and setting $\frac{d\eta_G}{d\Phi}=0$, and rearranging, gives:-

$$4\Phi^5-(8\delta+3\Psi)\Phi^4-4(\delta^2+\delta\Psi)-(1+\Omega/B)\Psi=0 \qquad (30)$$

The solutions of equation (28) for various values of δ, and for a condenser temperature of $35^{\circ}C$, have been obtained. The results are presented in fig.9.

3.4 COST ESTIMATES DERIVED FROM PRECEEDING ANALYSIS.

In deriving these cost estimates, the following specifications apply:-

Required system output power	=5KW
Length of each reflector	=1.7m
Aperture width of reflector	=60mm
Cost of each solar-energy collector tube.	=£w
Maximum allowable value of temperature drop ΔT.	$=20^{\circ}C$.

Data from fig.8 are used in case I, whereas those from fig.9 are used in caseII.

3.4.1 CaseI: Condenser temperature=Ambient temperature($=45^{\circ}C$)

For'optimal'operation:

$\Phi^{**}=1.48$ and $\eta^{**}_G=0.078$

The temperature of the vapour at the collectors exit	$=(\Phi^{**}\times T_a-20)$	$=178^{\circ}C$
Required rate of solar-energy	$=5000/0.078$	=64103W
Power collected per tube	$=(800)(0.06)(1.7)$	=81.7W

Therefore:

Number of tubes required	=64103/81.6	=786

Therefore:
Capital cost of the necessary collector tubes = £786w

<u>For 'off optimal'operation:</u>
The temperature of vapour
at the collectors exit =120°C(say)
Therefore:
Surface temperature of the receiver =140°C
Therefore:
ϕ =1.3 and η_G=0.063
Therefore:
Required rate of solar-energy=5000/0.063 =79365W
Therefore:
Number of tubes required =79365/81.6 =973
Therefore:
Capital cost of necessary collector tubes = £973w

It should be noted that the cost difference for these two scenarios is £187w.

3.4.2 CaseII: Condenser temperature=35°C.

<u>For'optimal'operation;-</u>
ϕ^{**} =1.466 and η^{**}_G=0.084
Therefore:
Temperature of the vapour at collector exit =173°C
Required rate of solar-energy =59524W
Therefore:
Number of tubes required =730
Therefore:
Capital cost of the necessary collector tubes = £730w

<u>For 'off optimal'operation:</u>
Temperature of vapour at collectors exit =120°C(say)
Therefore:
ϕ =1.3 and η_G=0.072
Required rate of solar-energy =69445W
Therefore:
Number of tubes required =852
Therefore:
Capital cost of the necessary collector tubes = £852w

It should also be noted that for the 'off optimal' operation, scenerio caseII leads to a saving of £121w because of 10° difference in the condenser temperature. The savings, however, falls to £56w (approximately halved) for the 'optimal'cases.

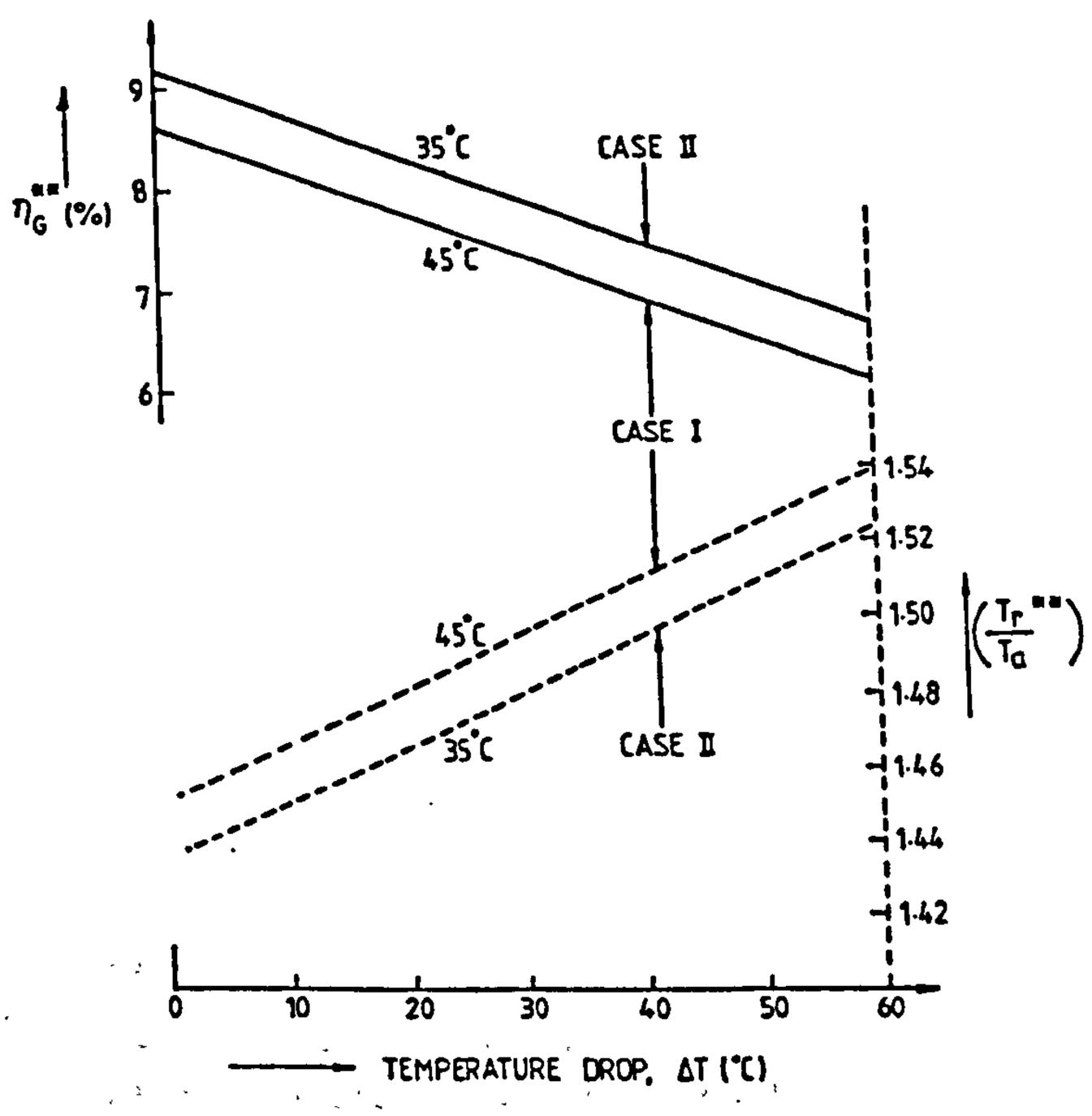

Fig.12 Variations of the optimal overall efficiency and optimal operating temperature with temperature drop.

3.5 CONCLUSIONS

It has been shown that for a solar-energy activated power system operating in a thermodynamic cycle, operation at optimal temperatures could result in to higher efficiencies and consequently lower capital costs per unit power harnessed. However, the basic problem remains: 'How can optimal conditions of operation be attained in practice?'. The collector, engine and the feed pump would usually have the working fluid in common. If the mass flow rate is very small, the temperature of the collector will rise to an extent that heat losses become excessive, so resulting in low collector efficiencies. However, high mass flow rates may inhibit adequate temperature rises for the engine to operate effectively. It may therefore be wise to use an efficient feed pump that would deliver flows at rates that will enable the solar-energy collector to concentrate sufficient exergy so as to deliver the working fluid at the temperature T_f^{**} .

It has also been shown that the drop in exergy between the heat-pipe condenser and the cycle's working fluid because of the occurrence of thermal resistances, does shift the optimal operating temperatures of the overall system away from that of the collector. However, the collector and the overall system could have the same optimal temperatures only when both reject heat to the same sink and also $\Delta T=0$. In practice, however, ΔT would be greater than zero. Hence, fig.12 shows that as ΔT increases from zero, (i) the value of $\Phi = \Phi^{**}$ that maximizes the overall efficiency increases, whereas (ii) the optimal overall efficiency decreases. This inevitably would affect the size of the collector for a desired power output and consequently, the overall capital cost.

The use of the cooler underground water in the condenser would obviously be desirable as is also shown in fig.12. It shows that, lowering the condenser temperature relative to that of the surroundings could result in a higher overall efficiency and a lower value of T_f^{**} for the same temperature drop, ΔT.

CHAPTER FOUR

SOLAR-ENERGY COLLECTOR TILT-ANGLE OPTIMIZATION

4.1 INTRODUCTION

In order to maximize the amount of solar radiation reaching the absorber of a solar energy collector, it is desirable that the Sun's relative motion be tracked. However, in a large collector unit such as in the power generation unit envisaged in this study,practical problems would arise even when seasonal tracking is involved. Tracking mechanisms could also be expensive. A compromise is to employ the collector stationary but tilted at the optimal angle which would maximize the total amount of solar radiation incident to the collector aperture, during the operational period. The present study seeks to determine this optimal angle for the location latitude 30°N in Egypt.

Two operational periods were studied. (i)For operation throughout the year and (ii)for operation between the months of March and September, i.e. when the Sun is in the northern hemisphere. Estimated monthly means of daily direct and diffuse insolations were employed. It is preferable to use measured data averaged over a number of years, e.g. as supplied by the Egyptain local weather bureau, because such imformation would take into account the local variations in cloud cover, humidity and dust in the atmosphere. However, the only available documented data for Egypt are the monthly means of daily total insolations as reported by Harb(Ref.3). A means of estimating the relevant radiation data(i.e. direct and diffuse) from the available monthly means of daily total observations became necessary.

Correlations relating diffuse to total radiation was first obtained by Liu and Jordan in 1960(Ref.10). However, questions have been raised by Choudhary(Ref.11), Stanhill(Ref.12), Ruth and Chant(Ref.13) and Orgill and Hollands(Ref.14) about the general validity of the correlations. In 1979, Manuel and Rabl(Ref.15), recalibrated Liu and Jordans correlations, and its general validity has been accepted except where measured data are available to prove otherwise(Ref.16). Manuel and Rabl intimated that their correlation relating daily diffuse to hemispherical insolations agrees with the results reported for India, Israel and Canada. Therefore, for the purpose of this study, their correlation which relates monthly mean

daily diffuse to total insolations has been used to estimate the monthly means of daily beam and diffuse insolations from Harb's measured total insolation data.

It is pertinent to mention that the 'King Tut' solar-energy harnessing system has peak insolation as one of the design parameters(Ref.2). Because peak insolation occurs at solar-noon, the optimization was therefore done with respect to this time on the average day of each month. The average day of a month is that day which has extra-terrestrial radiation closest to the average of the month(Ref.16).

4.2 ESTIMATING THE MONTHLY MEAN OF DAILY DIRECT AND DIFFUSE INSOLATIONS.

4.2.1 Correlation for the ratio of monthly mean of daily diffuse to daily total insolations.

The correlation by Manuel and Rabl(Ref.15) relating the monthly averages of the daily diffuse and total insolations is given by:-

$$H_d/H_t = \left[\begin{array}{l} 0.775 + 0.347(\omega_s - \pi/2) - \\ [0.505 + 0.261(\omega_s - \pi/2)]\cos[2(k-0.9)] \end{array}\right] \qquad (31)$$

where,
k = The long term clearness index (= H_t/H_e).
H_t = The long term monthly mean of daily total radiation on a horizontal plane(MJ/m^2)
H_e = The monthly mean of daily extra-terrestrial radiation(MJ/m^2)
H_d = The long term monthly mean of daily diffuse radiation on a horizontal plane(MJ/m^2)
ω_s = The sunset hour angle(Degrees).

4.2.2 Harb's observed monthly mean of daily total insolation and sunshine hours at Tahir in Egypt, i.e. latitude 30° N.

Harb(Ref.3) reported on the monthly mean of daily total solar radiation as well as sunshine hours, averaged over a period of five years, i.e. 1972 to 1976. He presented the data in C·g·S units, i.e. gram cal/cm^2.The data were therefore converted to MJ/m^2 using the conversion factor of 1 gram cal/cm^2 =0.041855 MJ/m^2 (Ref.17) and are presented in Table 1.

Table 1. Monthly averages of daily total solar insolation at Tahir in Egypt, MJ/m^2

Jan	Feb	Mar	April	May	June	July	Aug	Sept	Oct	Nov	Dec
12.64	15.78	19.88	23.27	26.79	28.25	27.75	25.49	23.27	18.25	13.18	11.84

Table 2. Monthly averages of daily periods of sunshine at Tahir in Egypt, hrs.

Jan	Feb	Mar	April	May	June	July	Aug	Sept	Oct	Nov	Dec
7.4	7.9	8.8	9.8	11.0	12.2	12.2	11.8	10.6	9.6	7.8	7.2

Table 3. Monthly averages of daily extra-terrestrial radiation H_e, for the location latitude 30° N, MJ/m^2.

Jan	Feb	Mar	April	May	June	July	Aug	Sept	Oct	Nov	Dec
21.1	25.5	31.2	36.4	39.6	40.7	40.0	37.5	32.9	27.1	22.0	19.7

4.2.3 Monthly means of daily extra-terrestrial radiation, H_e.

Table 3 is an extract from Duffie and Beckman(Ref.16), of the monthly averages of daily extra-terrestrail radiation for the location latitude 30° N. The data was obtained on the basis of a solar constant of 1353W/m². Solar constant is the flux of solar radiation at the outer boundary of the Earth's atmosphere, that is received on a surface held perpendicular to the Suns direction at the mean distance between the Earth and the Sun(Ref.17).

4.2.4 The long term clearness indexes,k.

The long term clearness index is defined as the ratio of the long term monthly mean of daily total radiation, H_t, to the monthly mean of daily extra-terrestrail radiation, H_e. It was therefore calculated from the monthly average values in tables 1 and 3, and are presented in table 4.

4.2.5 Ratios of monthly averages of daily diffuse to total insolations.

In order to estimate these ratios, the sunset hour angles on the average day of each month would have to be calculated. The sunset hour angle is given by(Ref.16):-

$$\cos\omega_s = -\tan L \tan d \qquad (32)$$

where, $d = 23.5 \sin\left[\frac{360(284+N)}{365}\right]$ and

N is the day of the year, i.e. N=1 on first January.
Because the tilt-angle optimization would be undertaken with respect to the average day of each month, the declinations were therefore evaluated on these days. Table 5 is an extract also from Duffie and Beckman(Ref.16), of the recommended average day of each month and the corresponding values of N.
For each month of the year, ω_s was evaluated.This, in conjunction with the values of k from table 4, were then used to compute the ratios H_d/H_t from equation (31). These are presented in table 6.

4.2.6 Monthly averages of daily diffuse and direct insolations.

With H_d/H_t evaluated and H_t known, the monthly mean of daily diffuse radiation was obtained from:-

$$H_d = [(H_d/H_t) \times H_t]$$

Table 4. Long term clearness indexes K, at Tahir.

Jan	Feb	Mar	April	May	June	July	Aug	Sept	Oct	Nov	Dec
0,559	0,619	0,637	0,639	0,677	0,694	0,694	0,680	0,677	0,673	0,599	0,601

Table 5. Recommended average day of each month and its corresponding day of the year.

	Jan	Feb	Mar	April	May	June	July	Aug	Sept	Oct	Nov	Dec
Average day.	17th	16th	16th	15th	15th	11th	17th	16th	15th	15th	14th	10th
Day of the year, N.	17	47	75	105	135	162	198	228	258	288	318	334

Table 6. Ratio of monthly averages of daily diffuse to daily total insolations H_d/H_t, at Tahir.

Jan	Feb	Mar	April	May	June	July	Aug	Sept	Oct	Nov	Dec
0,331	0,330	0,335	0,345	0,341	0,340	0,337	0,334	0,323	0,311	0,332	0,326

The direct component was then evaluated by subtracting the diffuse component from the total, i.e. $H_b = H_t - H_d$. Table 7 shows these monthly values in MJ/m^2. In order to convert these values into W/m^2, they were divided by the measured monthly averages of daily sunshine periods from table 2. Table 8 shows the monthly values in W/m^2.

4.3 ANALYSIS OF SOLAR-RADIATION FALLING NORMAL TO AN INCLINED COLLECTOR.

The following quantities are defined with respect to fig.13:-

I_Φ = Sum of direct and diffuse solar radiation falling normal to a collector inclined at an angle Φ to the horizontal (W/m^2).

β_z =Zenith angle, i.e. the angle subtended by a vertical line to the zenith and the line of sight to the sun (Degrees).

β_A =Solar altitude angle, i.e. the angle between the direct solar ray from the sun and the horizontal (Degrees).

It would be assumed that the diffuse radiation is isotropic, i.e. of equal intensity in all directions.
From traingles ABC and ADC of fig.13, we have:-

$$I_b / \mathrm{Sin}\beta_A = (I_\Phi - I_d) / \mathrm{Sin}(\Phi + \beta_A)$$

Therefore:-

$$I_\Phi = I_b \frac{\mathrm{Sin}(\Phi + \beta_A)}{\mathrm{Sin}\,\beta_A} + I_d \qquad (33)$$

But $\beta_A = 90 - \beta_z$, whereas from reference 16,

$$\mathrm{Cos}\beta_z = \mathrm{Sin}\,d\,\mathrm{Sin}\,L + \mathrm{Cos}\,d\,\mathrm{Cos}\,L\,\mathrm{Cos}\,\omega \qquad (34)$$

where ω is the hour angle, i.e. the angular displacement of the Sun, east or west of the local meridian due to rotation of the Earth on its axis at 15° per hour. Therefore ω can be expressed as:-

$$\omega = 15t \qquad (35)$$

where t is the sun time, i.e. hours before or after

Table 7. Monthly means of daily diffuse and direct insolations at Tahir, MJ/m^2

	Jan	Feb	Mar	April	May	June	July	Aug	Sept	Oct	Nov	Dec
Diffuse insolation, H_d.	4.18	5.21	6.66	8.03	9.14	9.66	9.35	8.51	7.19	5.68	4.38	3.86
Direct insolation, H_b	8.46	10.57	13.22	15.23	17.66	18.64	18.40	16.98	15.08	12.57	8.80	7.78

Table 8. Monthly averages of daily diffuse and direct radiations at Tahir, W/m^2.

	Jan	Feb	Mar	April	May	June	July	Aug	Sept	Oct	Nov	Dec
Diffuse radiation, I_d	156,91	183.19	210.28	227,61	230,81	218,81	212,89	200,23	188.42	164,35	155.98	148.92
Direct radiation, I_b	317.57	371.66	417.30	431.97	445,96	424,41	418.94	399.72	395.18	363.74	313.39	300.15

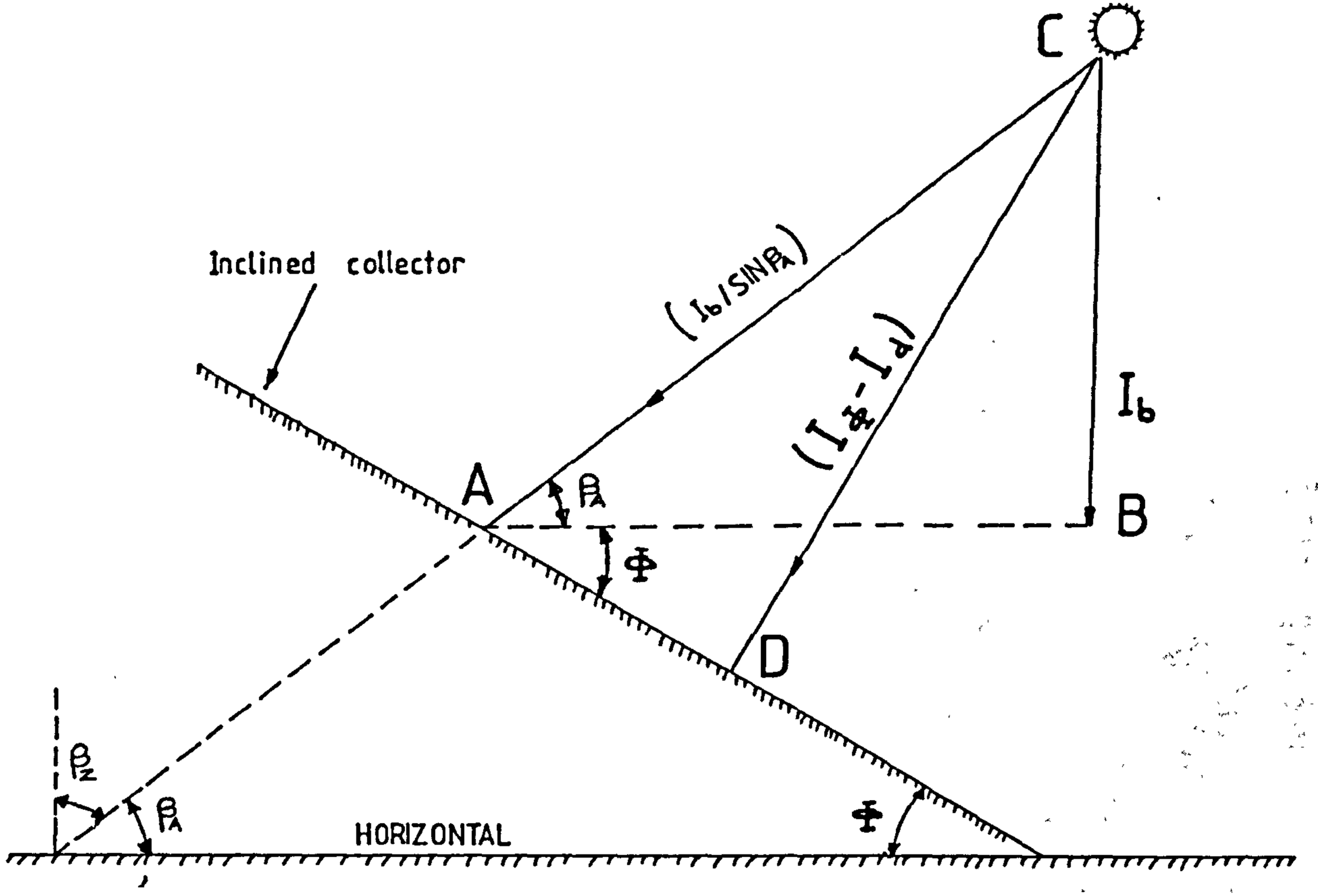

Fig.13. Geometric analysis of solar-radiation falling normal to an inclined collector.

solar-noon. Because optimization is undertaken with respect to solar-noon for the reason previously discussed, t=Ø and:-

$$\text{Cos}\,\beta_z = \text{Sin d Sin L} + \text{Cos d Cos L} = \text{Cos}(L-d)$$

Therefore:

$$\beta_z = (L-d) \qquad (36)$$
$$\beta_A = (90-L+d)$$

Substituting $\beta_A = (90-L+d)$ in equation (33) gives:-

$$I_\Phi = I_b \frac{\text{Sin}(\Phi+90-L+d)}{\text{Sin}(90-L+d)} + I_d \qquad (37)$$

The solar radiation falling normal on the collector at solar-noon has therefore been expressed in terms of the direct and diffuse components as well as the latitude of the site, solar declination and the collector tilt-angle.

4.4 OPTIMIZATION PROCEDURE.

The objective as previously stated is to determine the angle Φ that maximizes I_Φ in equation (37) during the periods, January to December and March to September. Let us consider the year round operation first, i.e.:-

Maximize $\sum_{i=1}^{i=12} (I_\Phi)_i$.

From equation (33):-

$$\sum_{i=1}^{i=12} (I_\Phi)_i = \sum_{i=1}^{i=12} \left[I_{bi} \frac{\text{Sin}(\Phi+\beta_{Ai})}{\text{Sin}\beta_{Ai}} + I_{di} \right]$$

But $\frac{\text{Sin}(\Phi+\beta_{Ai})}{\text{Sin}\,\beta_{Ai}} = \text{Sin}\Phi\,\text{Cot}\beta_{Ai} + \text{Cos}\Phi$

Therefore:

$$\sum_{i=1}^{i=12} (I_\Phi)_i = \sum_{i=1}^{i=12} I_{bi} (\text{Sin}\Phi\,\text{Cot}\beta_{Ai} + \text{Cos}\Phi) + \sum_{i=1}^{i=12} I_{di} \qquad (38)$$

It should be noted that I_d has been assumed to be isotropic and so independent of direction. Therefore, differentiating equation (38) with respect to Φ, setting the resultant equal to zero and rearranging, gives:-

$$\sum_{i=1}^{i=12} I_{bi} \tan\Phi = \sum_{i=1}^{i=12} I_{bi} \text{Cot}\,\beta_{Ai}$$

From which:

$$\tan\Phi = \frac{\sum_{i=1}^{i=12} I_{bi} \operatorname{Cot} \beta_{Ai}}{\sum_{i=1}^{i=12} I_{bi}} \qquad (39)$$

Substituting $\beta_A = (90-L+d)$ from equation (36), into equation (39) and solving for $\Phi = \Phi^*$, gives:-

$$\Phi^* = \tan^{-1}\left[\frac{\sum_{i=1}^{i=12} I_{bi} \operatorname{Cot}(90-L+d_i)}{\sum_{i=1}^{i=12} I_{bi}}\right] \qquad (40)$$

The numerical values for the parameters which determine the optimal tilt-angle at solar-noon (for the location latitude 30°N in Egypt), are as shown in table 9. From table 9 therefore:-

$$\sum_{i=1}^{i=12} I_{bi} \operatorname{Cot}(90-L+d_i) = 2756 \text{ W/m}^2$$

$$\sum_{i=1}^{i=12} I_{bi} = 4600 \text{ W/m}^2$$

Therefore:

$$\Phi^* = \tan\left(\frac{2756}{4600}\right) = 30.93^\circ$$

The second derivative of $\sum_{i=1}^{i=12}(I_\Phi)_i$ with respect to Φ is:

$$\frac{d^2}{d\Phi^2}\sum_{i=1}^{i=12}(I_\Phi)_i = -\left[\sum_{i=1}^{i=12} I_{bi} \operatorname{Cot}(90-L+d_i)\operatorname{Sin}\Phi + I_{bi}\operatorname{Cos}\Phi\right]$$

The second derivative at $\Phi^* = 30.93^\circ$ is negative because $\operatorname{Cos}\Phi^*$, $\operatorname{Sin}\Phi^*$, I_{bi} and $\operatorname{Cot}(90-L+d_i)$ are all positive quantities. Therefore this method indicates 30.93° as the optimal tilt-angle that would maximize the collection of solar-energy at solar-noon throughout the year. However, if operation were to be needed only when the Sun is in the northern hemisphere, i.e. March to September operation, the optimal angle changes to 18°.

Table 9. Numerical values for the parameters which determine Φ^* at Tahir in Egypt.

	Jan	Feb	Mar	April	May	June	July	Aug	Sept	Oct	Nov	Dec
i	1	2	3	4	5	6	7	8	9	10	11	12
I_{bi}	317.57	371.66	417.30	431.97	445.96	424.41	418.94	399.72	395.18	363.72	313.29	300.15
d_i	−20.96	−12.98	−2.42	9.43	18.83	23.14	21.23	13.48	2.22	−9.62	−18.95	−23.10
$(90-L-d_i)$	39.04	47.01	57.58	69.43	78.83	83.14	81.23	73.48	62.22	50.38	41.05	36.90
$I_{bi}\,Cot(90-L-d_i)$	391.61	346.34	265.03	162.11	88.06	51.06	64.63	118.55	208.18	301.11	359.88	399.76

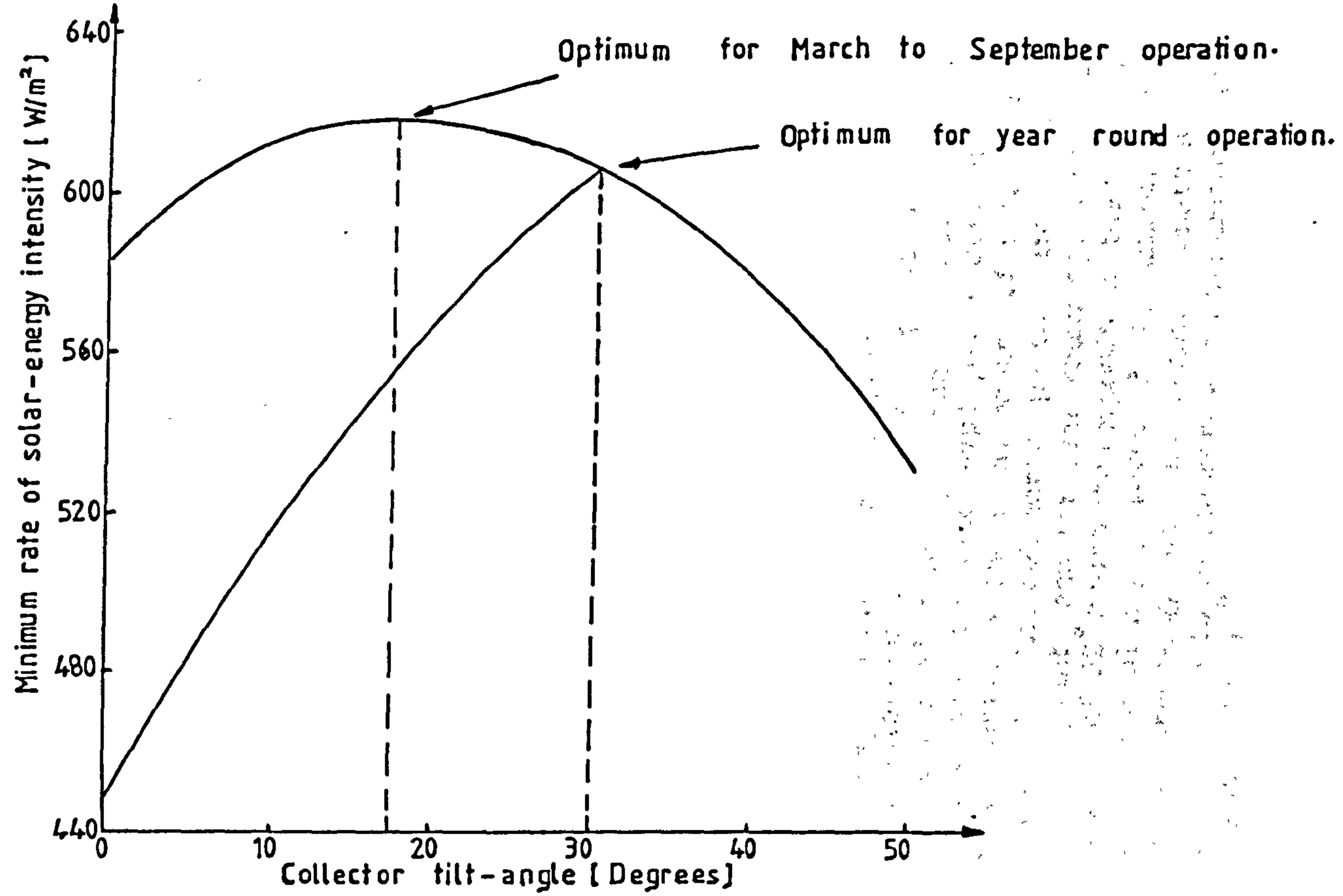

Fig.14. Variation of the minimum rate of solar-energy intensity falling normal to a collector aperture surface at solar-noon, with collector tilt-angle, for the location latitude 30 N in Egypt.

As a check on the preceeding method, another concept was used which is also considered to give the criterion for choosing a design solar insolation value. For tilt-angles between 0° and 90°, I_{Φ} was evaluated on the average day of each of the months within the operational period. The minimum value of $I_{\Phi} = (I_{\Phi})_{min}$ at each angle, out of the monthly values, were obtained. The values of $(I_{\Phi})_{min}$ were then plotted against the corresponding values of Φ, to reveal the values of Φ^{*} and $(I_{\Phi^{*}})_{min}$ —see fig.14. The values of Φ^{*} at solar-noon were again found to be $30^{\circ} \pm 1^{\circ}$ for the year round operation, and $18^{\circ} \pm 1^{\circ}$ for the March to September operation. The corresponding values of $(I_{\Phi^{*}})_{min}$ were considered to give the design solar insolation values. It is, however, significant to mention that the values of $(I_{\Phi})_{min}$ were employed instead of those of $(I_{\Phi})_{max}$, because it was thought that, for the required demand to be met by a solar-energy system during the month less favoured by tilting the collector at an angle Φ, the minimum value of I_{Φ} which occurs at that month need be considered. It should be noted that if Φ^{*} is substituted in equation (37), the optimal value $I_{\Phi^{*}}$ revealed would be $(I_{\Phi^{*}})_{max}$. The only way found of revealing $(I_{\Phi^{*}})_{min}$ was by inspection of the value of $(I_{\Phi})_{min}$ amongst the monthly values.

4.5 CONCLUSIONS

A method has been outlined which reveals the optimal tilt-angle for a solar-energy collector employed stationary within a desired period. Monthly averages of daily diffuse and direct solar insolations were employed to determine the tilt-angle that maximizes the total amount of solar-energy incident normal on to the collector aperture area. For the 'King Tut' pilot plant and for year round operation, an optimal tilt-angle of 30° (which corresponds to the latitude of the site of the plant) is revealed to maximize the collection of solar-energy at solar-noon. Whereas for operation when the Sun is in the northern hemisphere, the tilt-angle changes to 18°.

CHAPTER FIVE

THE SLIDING-VANES PUMP.

5.1 DESCRIPTION

In fig.15 is shown a schematic diagram of the sliding-vanes pump. It consists basically of a rotor from which sliding vanes actuated by centrifugal forces project to make contact with the stator. The stator is made out of two dissimilar circular arcs. The fluid flows in through the intake, filling the space between the rotating vanes. The confined liquid is transported bodily from intake to the discharge port, where the vanes retract into the rotor through the slots. The liquid is therefore forced through the discharge port at a higher pressure.

5.2 EFFECT OF CHOICE OF WORKING FLUID ON THE PERFORMANCE OF A SLIDING-VANE PUMP.

The effective overall efficiency of the Rankine-cycle power unit is defined as the ratio of the effective shaft power to the power input into the cycle. The effective shaft power is the difference between the total power developed by the expander and that used up by the feed pump in circulating the working fluid through the cycle. This therefore means that the greater the feed pump pumping power requirements, the lower will be the effective overall efficiency of the cycle.

The pumping power requirements for a given speed and pressure head for the pump, would depend upon the type of liquid being pumped. It was therefore required to decide which of the then two available organic working fluids (i.e. R-11 and R-113), would give the better performance with the sliding-vanes pump. This,amongst other factors (i.e. as discussed in Appendix C), was to help determine which working fluid should be adopted for the cycle. Simultaneously, the prime mover was also tested. Because of the use of Clavus oil 68 for lubrication purpose in the multi-vane expander, the two working fluids were therefore mixed with 10 percent Clavus oil by mass in testing the pump.

In accomplishing this investigation, an off-the-shelf sliding-vanes pump (serial no.18181020), manufactured by Sperry Vickers, U.S.A. was adopted.

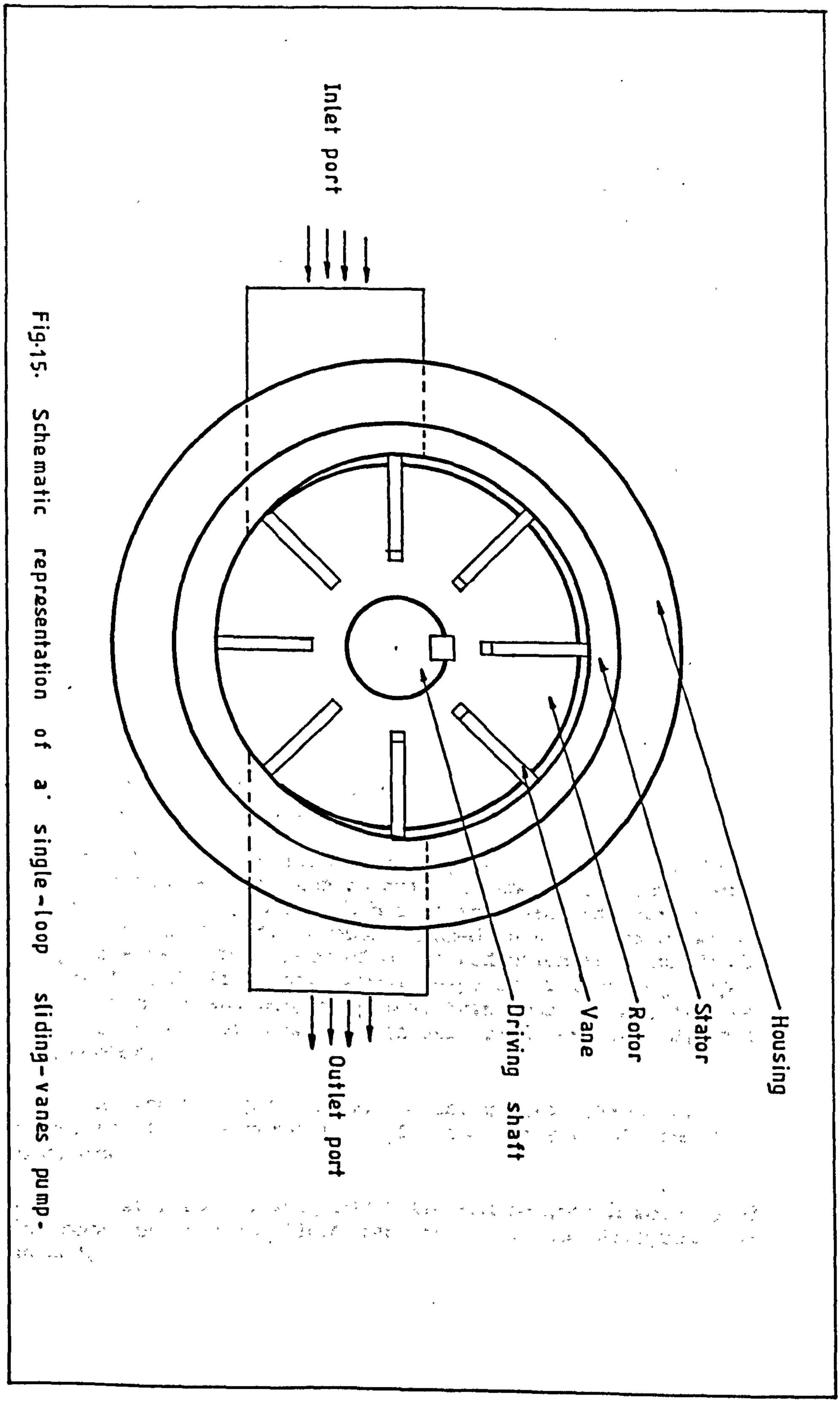

Fig.15. Schematic representation of a single-loop sliding-vanes pump.

5.2.1 The feed pump test rig.

The schematic flow diagram for the test rig used is as shown in fig.16. The working fluid was admitted into the system through D. The pump which was driven by the electric motor, pumped the fluid through the flowmeter which indicated the flow rate as a percentage of its maximum capacity. Valve E was used to control the pumps discharge pressure. A high-pressure safety switch was incorporated to turn-off the motor, should an excessive pressure arise that would damage the system. In order to maintain constant temperature and pressure at the low-pressure side, cooling water was provided through the heat exchanger (which also served as a reservoir). At times, the cooling-water flow rate was insufficient to maintain a constant pressure. It was then necessary to open up valve F, so that the reservoir was exposed to atmospheric pressure. Under such circumstances, cooling-water was run through the heat exchanger in D, so that escaping fluid vapour could condense and drip back. When admitting the fluid into the system, vent G was opened to allow displaced air to escape. Drain B provided a passage for the quick emptying of the system, whereas drain A located at the bottom-most part of the reservoir provided a means of draining the last bit of the fluid. Auxiliary instruments used with the test rig included:-

(i) Wattmeter: This was connected to the electric motor to measure the power input.

(ii)Reflective opto-switch and digital speedometer: These were used in measuring the rotational speed of the pump. The reflective opto-switch has an infra-red emitter diode and a photo-transistor sensor housed in a moulded package. The photo-transistor responded to radiation from the diode when reflected from six equally-spaced reflecting tapes round the motor and pump coupling. This was then converted to revolutions per minute which was read on the digital speedometer.

(iii) A thermocouple attached just before valve E, for measuring the temperature of the fluid at the pump discharge.

(iv) A stop watch, weighing-scale and pan,which were used in recalibrating the flowmeter to read in Kilograms per second.

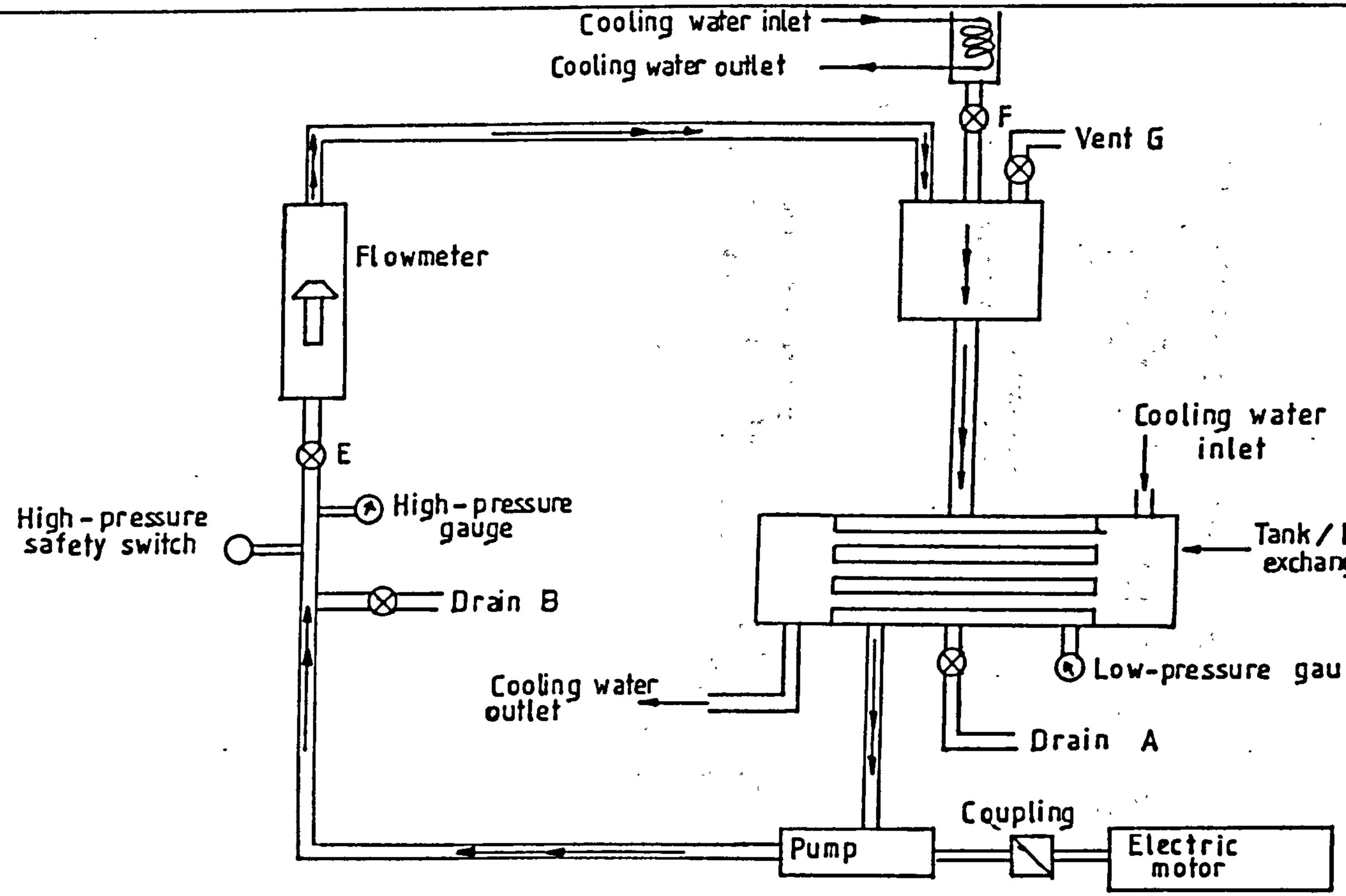

Fig.16. Schematic representation of the feed pump test rig.

5.2.2 Flowmeter recalibration.

As mentioned previously, the flowmeter (serial no. FP1-35-G-10/83 with float serial no. 1-GSVGT-68) was calibrated in percentages of its maximum capacity. However, the maximum flow would depend on the type of fluid being used. It therefore became necessary to recalibrate it, to read in kilograms per second using all the fluids to be tested. At each of certain selected flowmeter marks, the amount of liquid pumped was collected in a pan within a measured time. It was then weighed. The corresponding mass flow rate found by taking the ratio of the mass and the time -see figs.17 and 18 for the recalibration graphs.

5.2.3 Test procedure.

With the fluid admitted into the system, the pump was then driven by a variable-speed electric motor. For a fixed speed, the pump was run under varying discharge pressures. After a steady-state was attained, for each speed and discharge pressure, readings of the intake pressure, discharge pressure and temperature, flow rate and input power were then taken. The range of speeds run was from 1000 r.p.m. to 3500 r.p.m. Whereas, the pressure differential at each of the speeds was varied from zero to a maximum of about 20.7 bar, beyond which the safety cut-off switch stopped the system.

5.2.4 Density of the mixture of the freon and lubricant.

Let V_f be the volume of freon liquid with mass m_f , and V_L be the volume of lubricant with mass m_L . The densities of the freon liquid ρ_f , and lubricant ρ_L , can be expressed as:

$$\rho_f = m_f / V_f$$
$$\rho_L = m_L / V_L \qquad (41)$$

Assuming no chemical reaction occurs*, the density of the mixture ρ_{mix} , can therefore be expressed as:-

$$\rho_{mix} = \frac{(m_f + m_L)}{(V_f + V_L)} = \frac{(m_f + m_L)}{(m_f/\rho_f) + (m_L/\rho_L)} = \left[\frac{1}{\rho_f} \frac{m_f}{m_f + m_L} + \frac{1}{\rho_L} \frac{m_L}{m_f + m_L} \right]^{-1} \qquad (42)$$

But the mass of the lubricant added was 10 percent that of the freon. Therefore:

$$m_L = 0.1\, m_f \qquad (43)$$

---

* The thermal stability limit for R-113 in the presence of Clavus oil, is about 140°C (Ref-19).

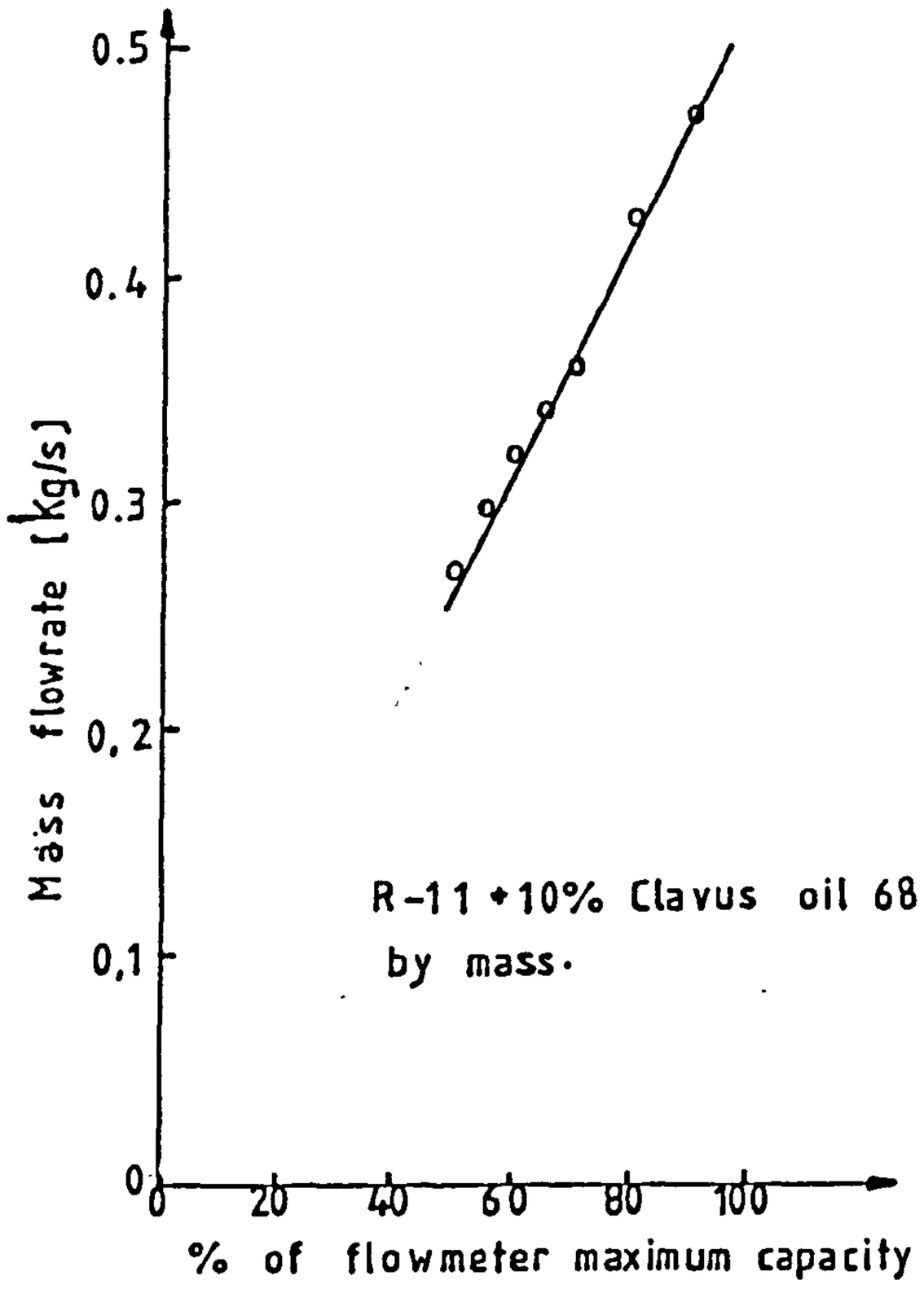

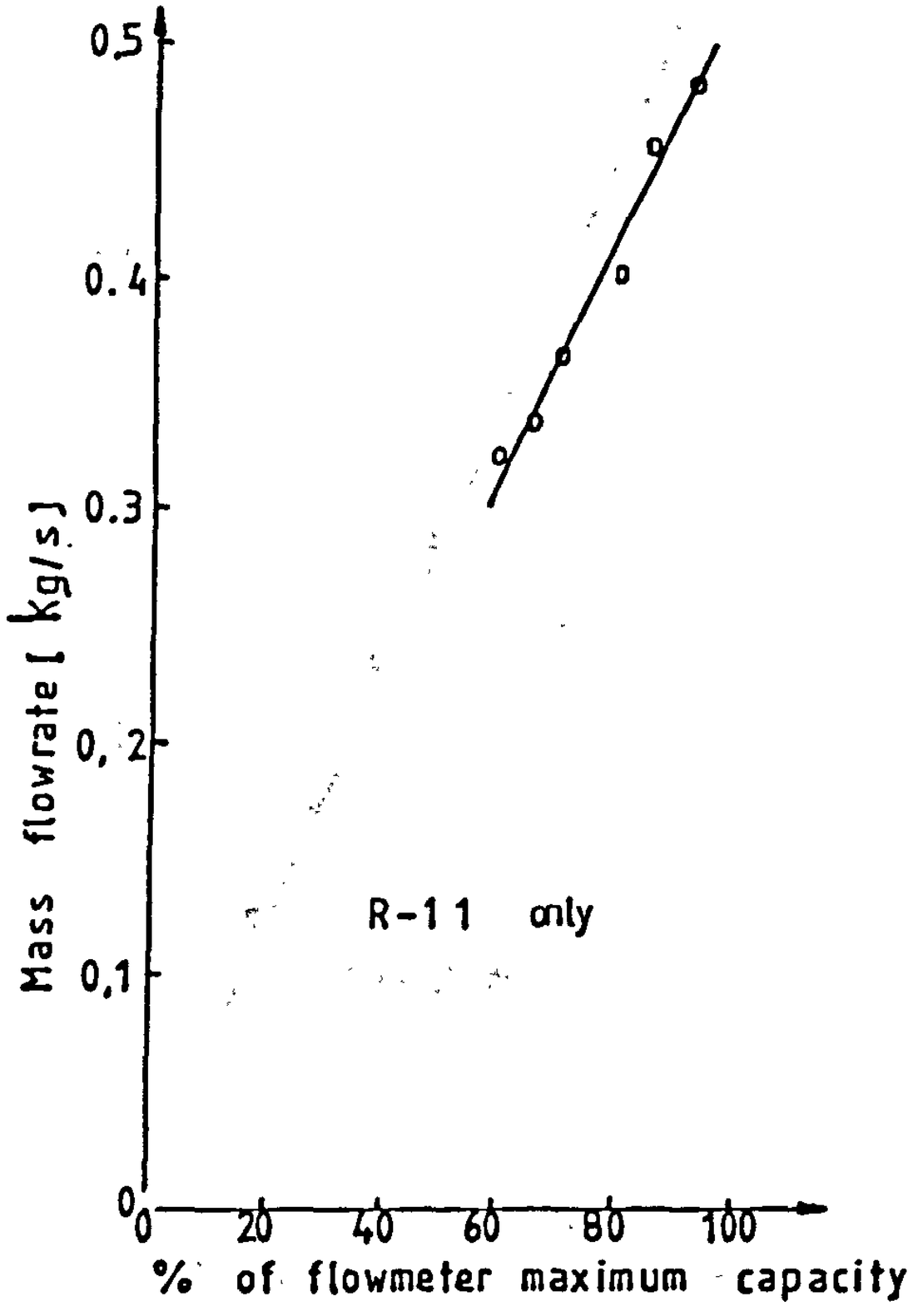

Fig.17. Flowmeter recalibration graphs with R-11.

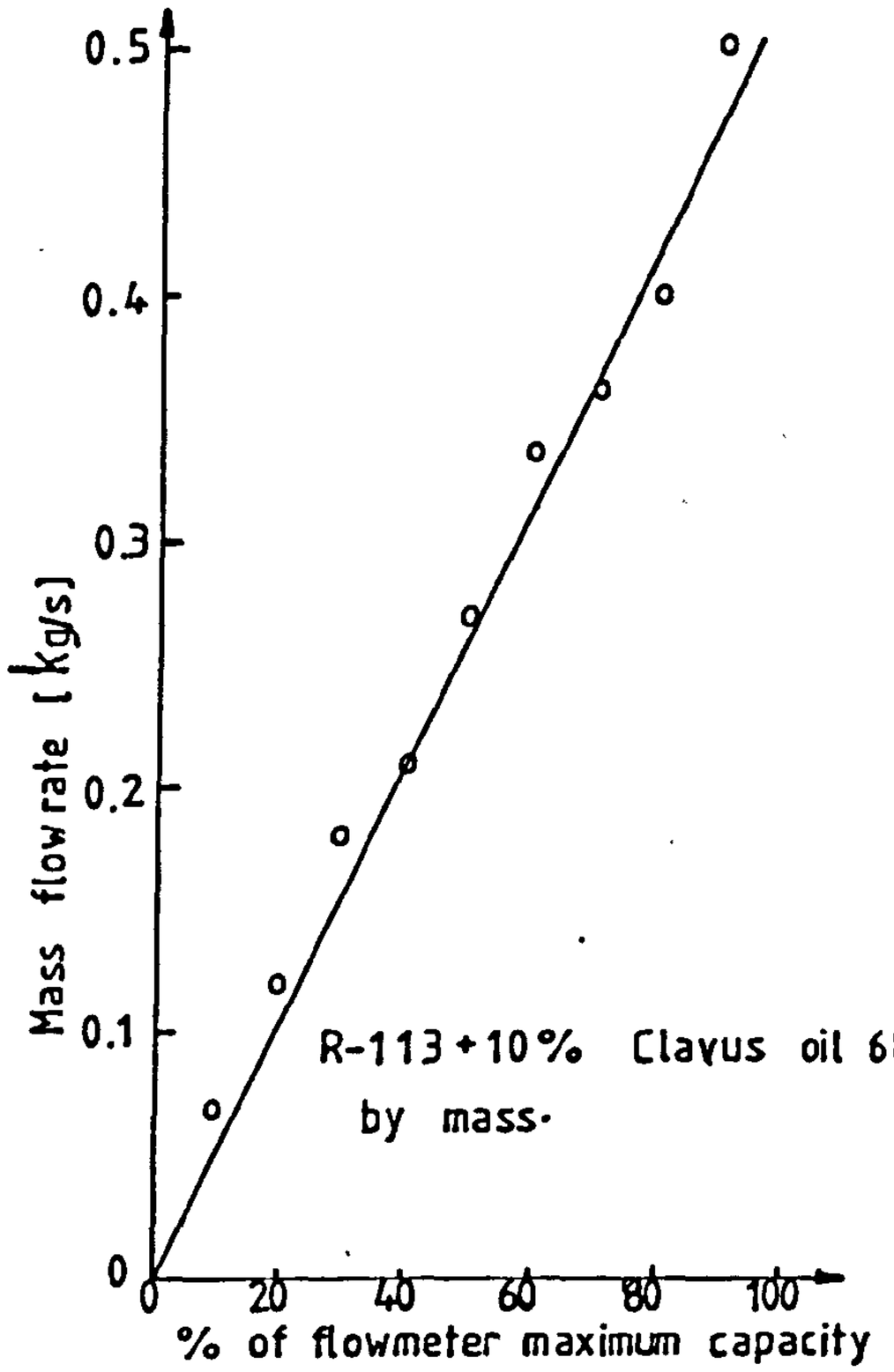

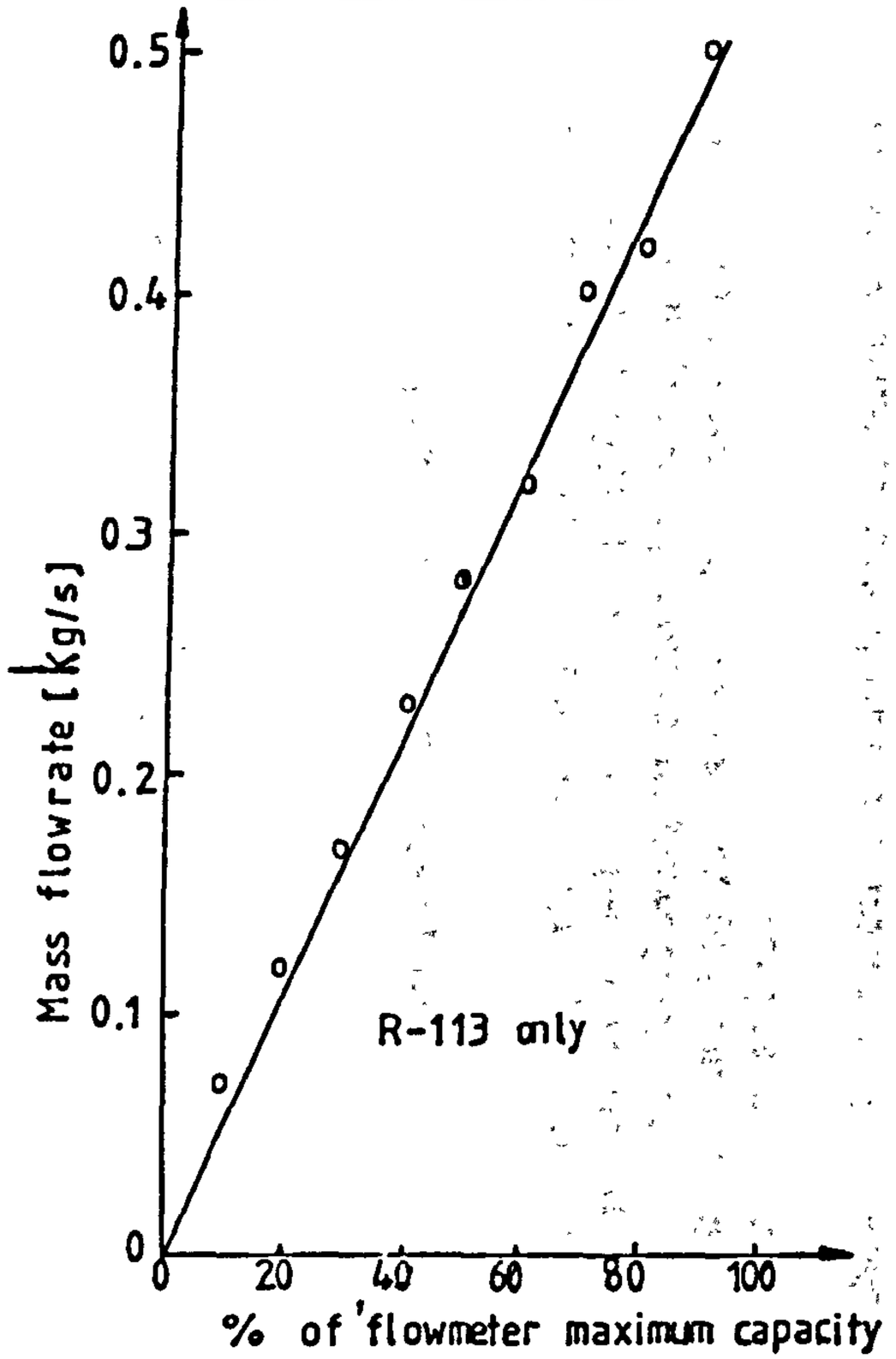

Fig.18. Flowmeter recalibration graphs with R-113+10% Clavus oil 68 by mass and R-113 only.

Therefore:

$$\rho_{mix} = \left[\frac{\text{Ø.91}}{\rho_f} + \frac{\text{Ø.Ø91}}{\rho_L}\right]^{-1} \qquad (44)$$

Equation (44) was therefore used in evaluating the densities of the mixture of R-11 and R-113 plus lubricant respectively.

5.2.5 Data reduction and results.

Because the objective is to investigate which of the fluids gives a better performance characteristics with the pump, the data taken were therefore reduced in such a manner that the end results showed relative pump efficiency against mass flow rate graphs.

For a given speed, and pressure differential Δp, mass flow rate $\dot{m}$, the volume flow rate $\dot{V}$ was evaluated from:

$$\dot{V} = \dot{m}/\rho_{mix}. \qquad (45)$$

The output power P_{out} , of the pump was then calculated from:

$$P_{out} = \dot{V}\Delta p \qquad (46)$$

The relative efficiency of the pump η_p, was evaluated from:

$$\eta_p = \frac{P_{out}}{P_{in}} \qquad (47)$$

where P_{in} , is the measured power that was used up by the electric motor.

Fig.19 shows graphically the relative performance of the sliding-vanes pump run with R-11 only, R-11+10%lubricant by mass, R-113 only and R-113+10%lubricant by mass, all at a pump speed of 3000 r.p.m. Fig.20 shows the mass flow rate versus speed characteristics.

The results show that between the two basic organic working fluids tested, R-113 gave a better pump performance than R-11. The addition of 10% Clavus oil 68 by mass, into the fluid further improved the performance.

The mass flow rate versus speed characteristics suggest that, for a fixed pressure differential, the mass flow rate varied linearly with the speed. This, however, occurred beyond a certain speed, below which no discharge could be

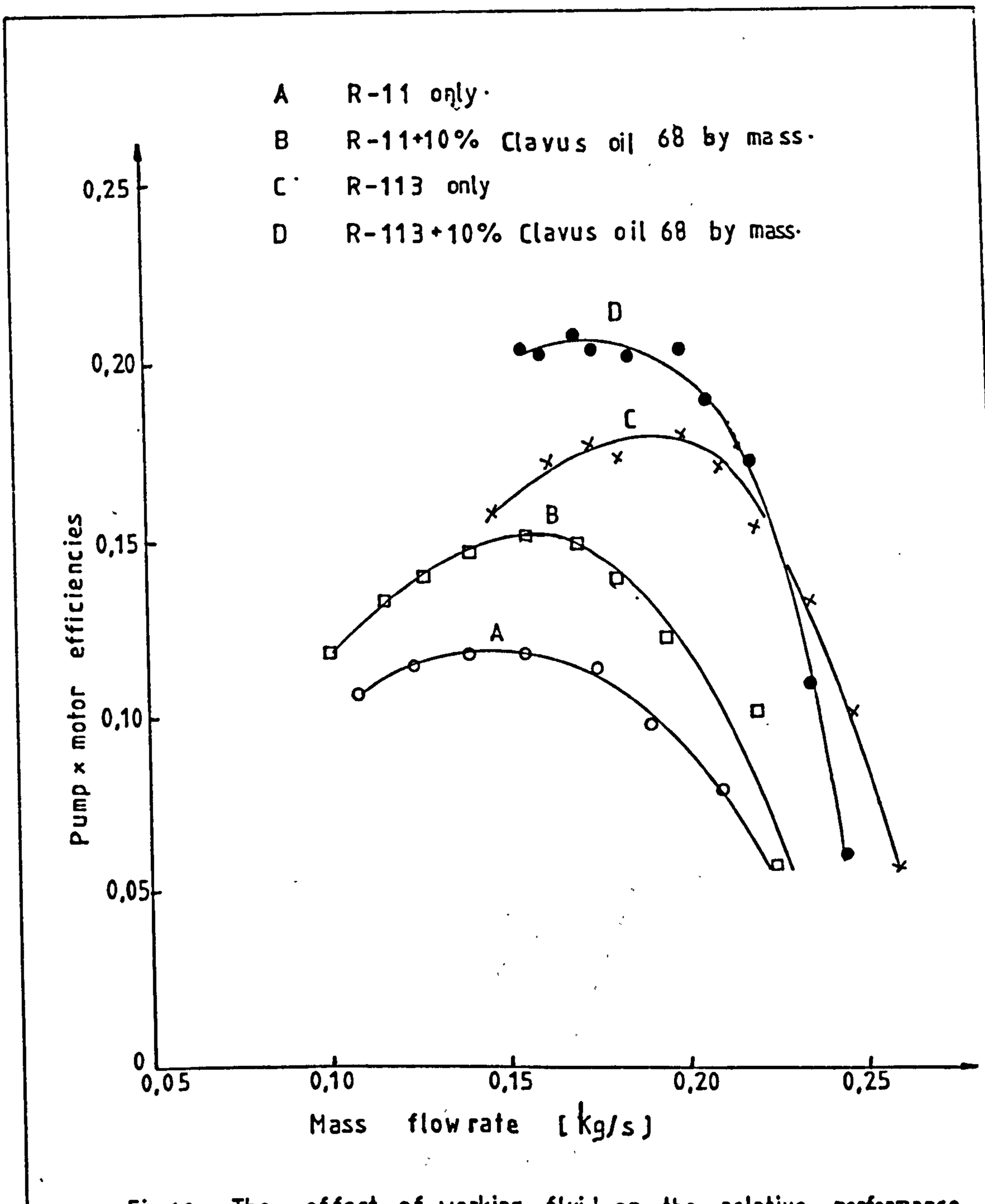

Fig.19. The effect of working fluid on the relative performance of the sliding-vanes pump at a speed of 3000 r.p.m. (For the Sperry Vickers pump.)

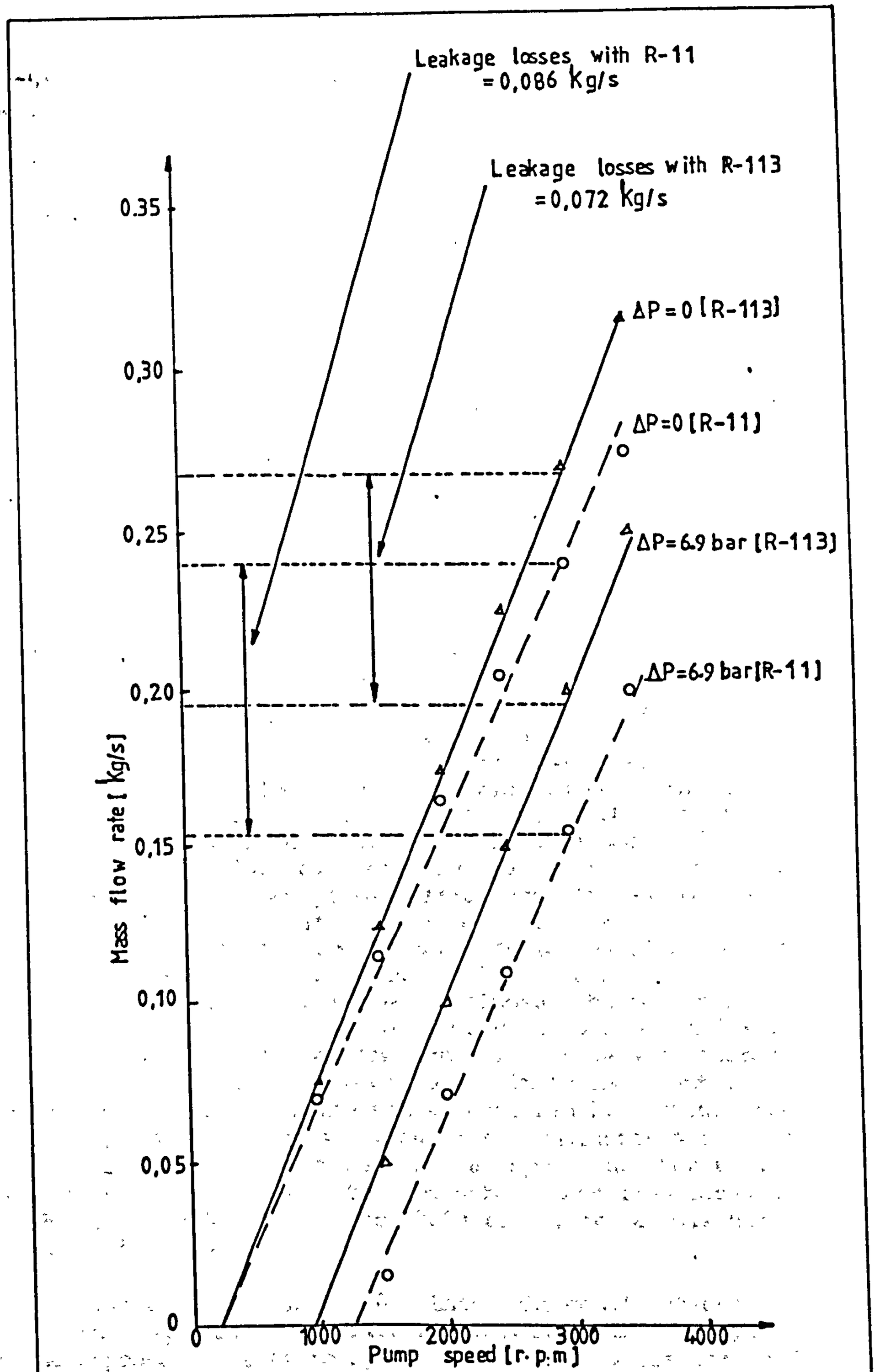

Fig.20 Variation of the mass flow rate with speed, for the sliding-vane pump run with R-11 and R-113 organic fluids.

obtained. At this stage, the power into the pump was perhaps used up in overcoming leakages(Ref.18).

It is pertinent to mention that R-113 was found to give higher expander isentropic efficiencies than R-11 (Ref.19). This, and the facts that R-113 out performed R-11 in the feed pump tests and its higher thermal stability especially in the presence of a lubricant (as indicated in Appendix C), led to its choice as the Rankine-cycle working fluid.

5.3 TESTS FOR 'FLOW RATE MATCHING'.

For the 'King Tut'project design parameters (Ref.2), and with R-113 established as the candidate working fluid, it was required that the Rankine-cycle feed pump should deliver the fluid at a rate of about 0.30 Kg/s at a discharge pressure of about 7 bar, in order to achieve the design 5KW output power at a speed of about 3000 r.p.m. So the sliding-vanes pump developed by Denco Ltd., were tested for 'flow rate matching'.

Fig.21 shows a simple representation of the first single-loop, sliding-vanes pump developed by Denco Ltd. It has a rotor of 22mm span and is cantilevered, i.e. supported at the end farther away from the end-plate. It was tested on the same test rig described earlier, and driven by a single-speed electric motor with known efficiency at 1500 r.p.m. Fig.22A shows its efficiency versus mass flow rate characteristic at a speed of 1500 r.p.m., with R-113+10% Clavus oil by mass*. It is evident that the pump has acceptable efficiency. It was, however, oversized. Secondly, it developed vibrations between discharge pressures of 7 and 14 bar. These therefore led to the second, modified pump schematically shown in fig.23. The basic modifications effected, included the reduction in capacity (i.e. by reducing the rotor span to 15mm) and also supporting the rotor on the end-plate side with another bearing. The latter intended to eliminate the cantilever effect thought to cause the vibrations. Fig.22B shows its efficiency versus mass flow rate characteristic with R-113+10 Clavus oil by mass, at a speed of 1500 r.p.m. Whereas table 10 shows the measured mass flow rates at speeds from 1000 r.p.m. to 3000 r.p.m, at a discharge pressure of 6.9 bar.

It is evident, from table 10, that the modifications did match the required mass flow rate.However, this happened at the expense of efficiency. Secondly, the vibrations did persist though relatively reduced, with the elimination of the cantilever effect. It is therefore thought that the

---

* Pump efficiency was obtained using the motor efficiency curve obtained from Mohey(Ref.1).

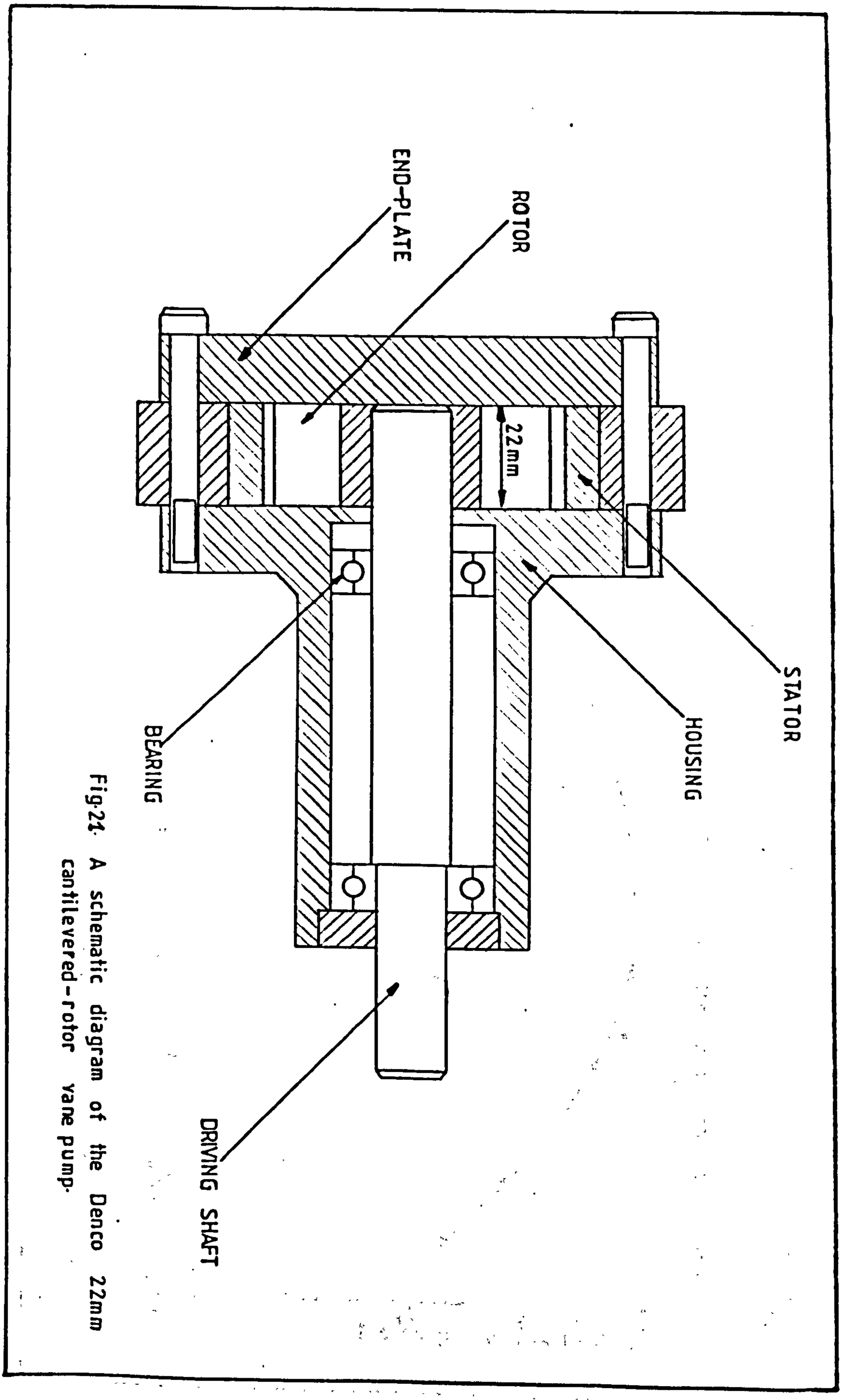

Fig.24. A schematic diagram of the Denco 22mm cantilevered-rotor vane pump.

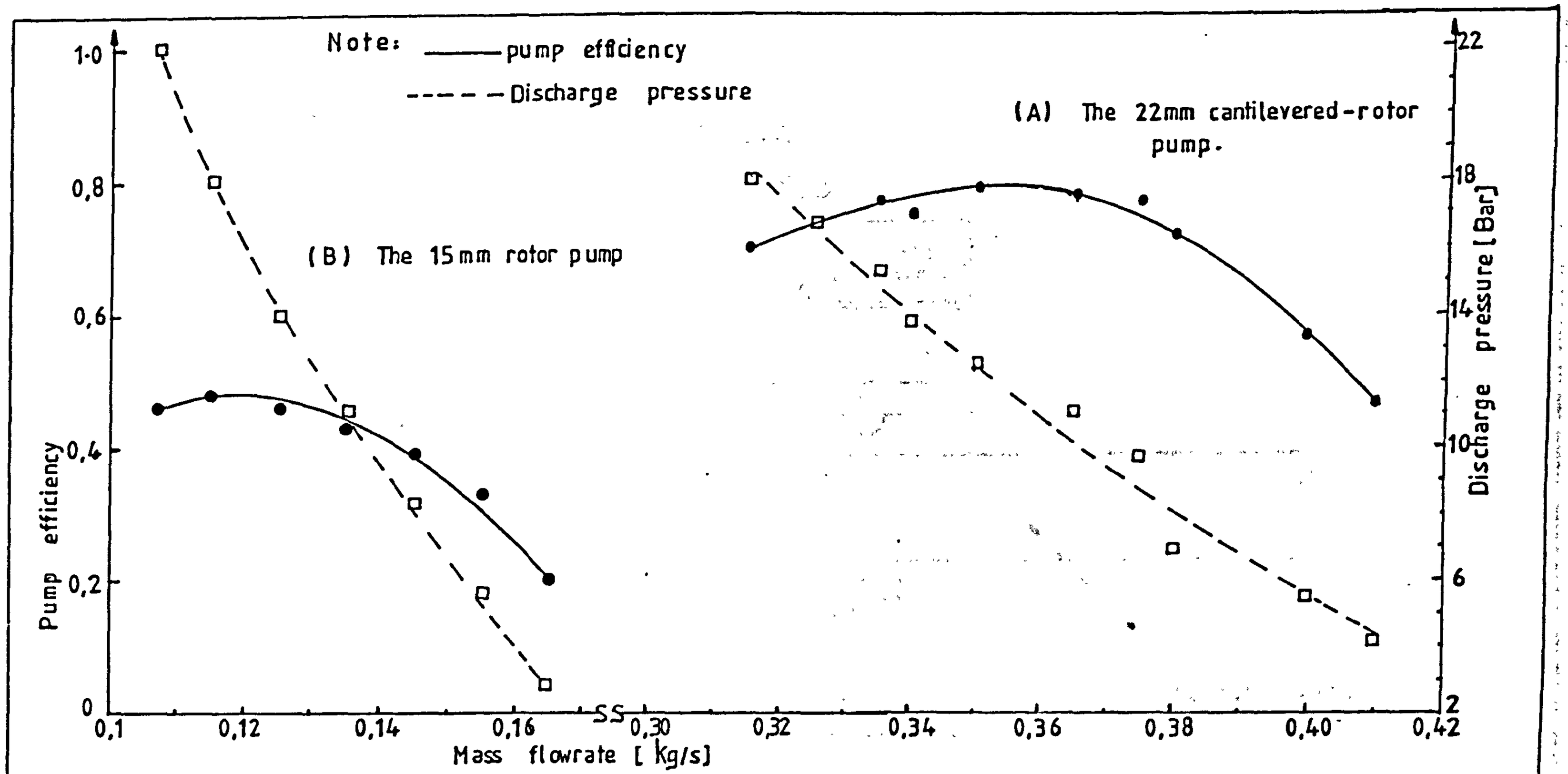

Fig.22. Characteristics of Denco pumps run with R-113 +10 % Clayus oil 68 by mass, at a speed of 1500 r·p.m

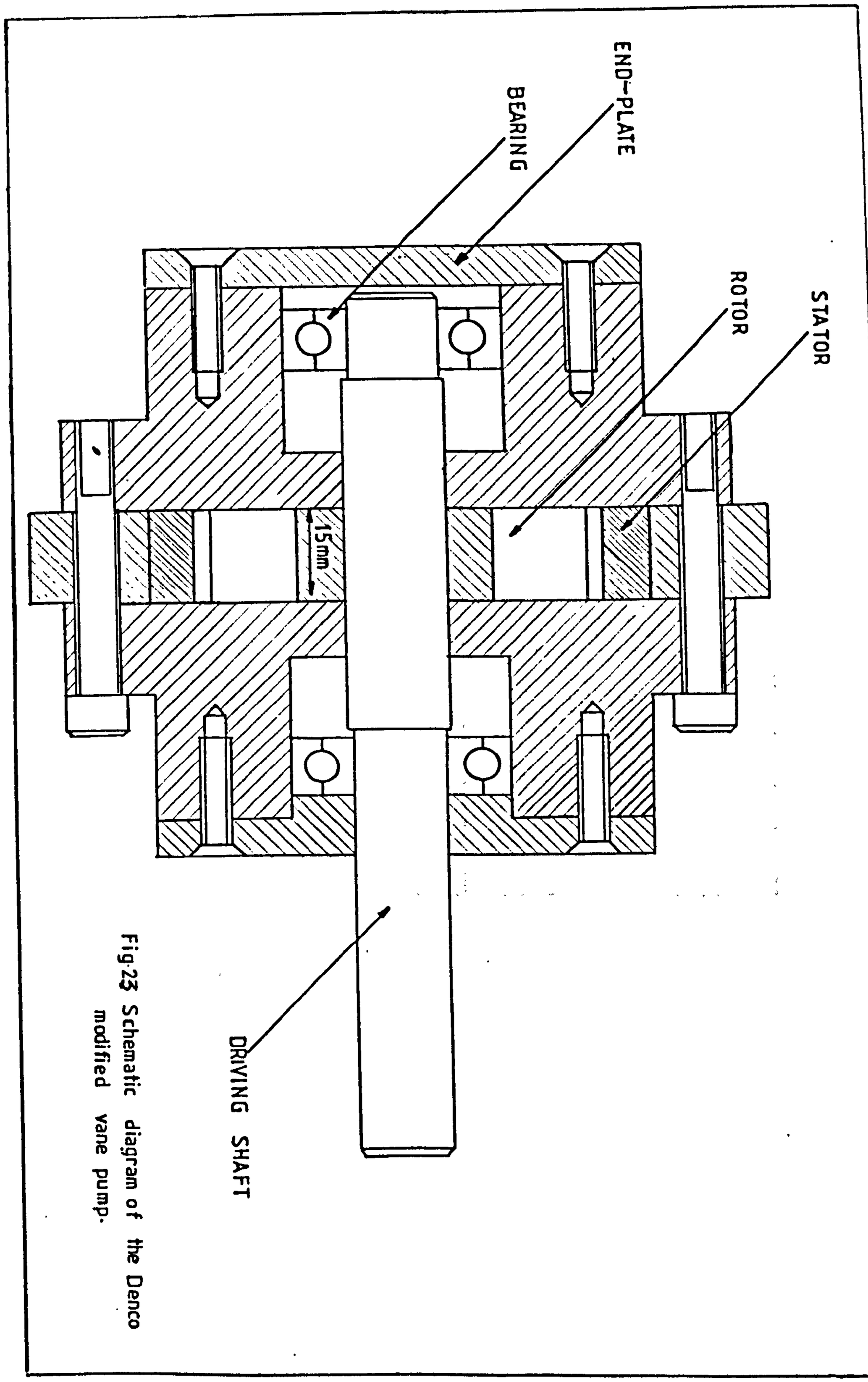

Fig.23 Schematic diagram of the Denco modified vane pump.

Table 10. Measured mass-flow rate against speed for the modified Denco pump, run with freon-113+10% Clavus oil 68 by mass, at a discharge pressure of 6.9 bar.

Pump speed (r.p.m.)	Mass flow-rate (kg/s)
1000	0.09
1500	0.155
2000	0.220
3000	0.310

vibrations are as a result of the unbalanced pressure forces in the pump, which might be minimized through 'double-loop' construction of the rotor. Because of the reduction in efficiency, a 15mm cantilevered rotor was finally adopted.*

5.4 CONCLUSIONS

It has been shown that a sliding-vanes pump performed better with R-113 than with R-11. The addition of Clavus oil 68 into the fluid further improved the pump's performance. Possible explanations are:-

(i) There were smaller leakage and frictional losses with R-113 because of its higher viscosity. For example, R-113 has a viscosity of 619×10^{-6} Ns/m^2 at 30°C, whereas R-11 has a viscosity of 405×10^{-6} Ns/m^2 at the same temperature.

(ii) The quantity of vapour entrained into the pump could be higher with R-11 than with R-113, because of its lower boiling point at the same pressures. For example, R-113 has a boiling point of 47.6°C at one atmosphere, whereas R-11 boils at 23.8°C at the same pressure. This being the case, more power would be required to pump R-11 than the same mass of R-113 at identical speed and discharge pressure, because vapours require higher pumping powers than liquids.

(iii) The improvement brought about by the added Clavus oil is thought to have resulted from further lowering of the losses because of its lubrication effect.

---

* It was not possible to test this pump because it formed an integral part of the system sent to Egypt for on site tests.

CHAPTER SIX

CONCLUSIONS

The steady-state thermal performance of the high-vacuum collector was simulated. It was predicted that the collector would be capable of attaining an optimal mean surface temperature of 189°C, at which the maximum rate of thermal energy avialable to perform work would be maximized. This would occur when the rate of thermal-energy retained by the collector would be about 466.7 W, for every square meter of the heat-pipe's surface area. The corresponding optimal efficiency of the collector would be about Ø.46.

The collector surface and output temperatures were related by a temperature difference which results into the loss of exergy. This is expected to occur because of the occurrence of thermal resistance between the heat-pipe's surface and the Rankine-cycle working fluid inside the manifold. The major part of the resistance is expected to occur across the ball-and-socket joint. The effect of the temperature difference on the overall system optimal efficiency and operating temperature was predicted. It was found that the higher the value of the temperature difference, the higher the optimal operating temperature would be, relative to that for the collector. Whereas, the overall optimal efficiency decreases relative to that for the zero temperature difference. The extent of these consequences would, however, depend upon the condenser temperature. Two cases which could occur in practice were considered:-

(i) When the condenser is air cooled, i.e. the collector and heat engine both reject heat to the same heat sink.

(ii) When the condenser is water cooled, i.e. the collector and heat engine have different heat sinks.

For the same temperature difference between the heat-pipe's surface and the fluid bulk inside the manifold, case(ii) was found to result into a lower overall optimal operating temperature and a higher overall optimal efficiency than for case(i).

A method, based on measured radiation data, which indicates an optimal collector tilt-angle as well as the optimal design solar insolation value was clearly outlined. For the 'King Tut' project, an optimal tilt-angle of about 30° (which corresponds to the latitude of the site for the project) was revealed, for the year round operation. Whereas for March to September operation (i.e. when the Sun is in the northern hemisphere), the optimal tilt-angle

changes to about 18°.

The relative performance of a sliding-vane pump was investigated with R-11 and R-113 working fluids. It was found that the sliding-vane pump performed better with R-113 than with R-11. The addition of 10% Clavus oil 68 by mass into the fluids did improve the pump's performance. The result obtained contributed in establishing R-113 as a better working fluid than R-11 for the Rankine-cycle power plant.

The sliding-vane pumps developed by Denco Ltd. were therefore tested with R-113 working fluid. The 22mm span and cantilevered-rotor pump was found to have a desirable optimal efficiency of about 78% at a speed of about 1500 r.p.m. It was, however, oversized and developed vibrations between discharge pressures of 7 and 14 bar. Modifications were therefore made which included the reduction of the rotor span to 15mm and the elimination of the cantilever effect. The modifications did give the required mass flow rate of about 0.30 Kg/s at a speed of about 3000 r.p.m. and a discharge pressure of about 7bar. However, this occurred at the expense of efficiency. For example, at the speed of 1500 r.p.m., the optimal efficiency was found to be about 50%. Secondly, the vibrations did persist though relatively reduced. It was therefore thought that the vibrations were as a result of unbalanced pressure forces in the pump, which could be minimized through 'double loop' construction of the rotor. Because of the reduction in efficiency, a 15mm cantilevered rotor was finally adopted.

REFERENCES

1. Mohey Hussein.
'Low-grade energy engine'.
Ph.D thesis, School of Mechanical Engineering,Cranfield,U.K(1981).

2. O'Callaghan, P. W., Mohey, H., Whitehouse, J. and Pollard, D.
King Tut Project Document,Cranfield,U.K(1981).

3. Harb, S.
'Characteristic features of radiation field in Egypt'.
Released by the Ministry of Electricity and Energy, Egyptian Solar Energy Commission, Feb.(1978).

4. Speyer, E.
'Solar-energy collection in evacuated tubes'.
Trans. ASME, J. of Power,87,pp270-276(1965).

5. Duffie, J. A. and Beckman, W. A.
Solar Energy Thermal Processes, John Wiley, New York(1976).

6. Kreith, F.
Principles of Heat Transfer, 3 Edition, Harper and Row, New York(1976).

7. Engholm, G. and Hertz, J.
'Performance of vacuum tube solar collector system'.
Trans. ASHRAE,84,2,pp419-434(1978).

8. O'Callaghan, P. W. and Probert, S. D.
'Exergy and economics'.
Applied Energy,8,pp227-243(1981).

9. Kreyszig, E.
Advanced Engineering Mathematics,4 Edition, Wiley Publishers,New York(1979).

10. Liu, B. Y. K. and Jordan, R. C.
'The interrelationship and characteristic distribution of direct,diffuse and total solar radiation'.
Solar Energy,4,3,ppl-19(1960).

11. Choudhury, N. K. O.
'Solar radiation at New Delhi'.
Solar Energy,7,pp44-52(1963).

12. Stanhill, G.
'Diffuse sky and cloud radiation in Israel'.
Solar Energy,10,pp96-101(1966).

13. Ruth, D. W. and Chant, R. E.
'The relationship of diffuse radiation to total radiation in Canada'.
Solar Energy,18,pp153-156(1976).

14. Orgill, J. F. and Hollands, K. G. T.
'Correlation equation for hourly diffuse radiation on a horizontal surface'.
Solar Energy,19,pp357-359(1979).

15. Manuel, C. P. and Rabl, A.
'The average distribution of solar radiation - correlations between diffuse and hemispherical and between daily and hourly insoaltion values'.
Solar Energy,22,2,pp155-164(1979).

16. Duffie, J. A. and Beckman, W. A.
Solar Engineering of Thermal Processes,
Wiley Interscience,New York(1980).

17. Sellers, W. A.
Physical Climatology,The University of Chicago Press,Chicago,U.S.A.(1965).

18. Wilson, W. E.
'Rotary pump theory'.
Trans.ASME,68,4,pp371-384(1967).

19. O, Badr, M.Hussein, S.D.Probert and P.W.Ocallaghan.
"Thermal stabilities of mixtures of trichloro-fluoroethane and lubricating fluids contained in copper sealed tubes."
Applied Energy 16,pp41-52(1984).

20. Private communication with Badr, O.M (Ph.D student, Cranfield), who was involved in testing the expander.

APPENDIX A

DESIGN OF THE COMPOUND PARABOLIC CONCENTRATOR EMPLOYING A CYLINDRICAL RECEIVER.

Fig.A1. shows the cross-section of a compound parabolic reflector with half acceptance angle θ and a cylindrical receiver of diameter D_r. The acceptance angle is the angle within which any ray entering the aperture of the reflector will reach the receiver. With reference to fig.A1., the basic design requirements as pointed out by Ortabasi and Buehl (Ref.A1.) are that:-

(i) Point F is a demarcation point such that a critical ray tangent to the cylindrical receiver intersects the reflector at this point. A critical ray is a ray entering the aperture at an angle θ with the plane of symmetry of the reflector.

(ii) The portion EF of the reflector is a convolute such that any normal to the reflector at this portion is tangent to the cylindrical receiver.

(iii) Portion FG of the reflector is such that a critical ray striking the reflector at a point on this section is reflected tangentially to the cylindrical receiver.

Generalized X and Y coordinates of a point on the reflector.

With reference to the geometric analysis in fig.A2., a point (X,Y) on the reflector can be generally defined by:-

$$X = 1/2\ D_r \sin\theta - S\cos\theta$$

$$Y = -1/2\ D_r \cos\theta - S\sin\theta \qquad \text{(A1)}$$

where S defines the length of a line from the point (X,Y) on the reflector and tangential to the point $(1/2\ D_r, \theta)$ on the receiver.

Expression for S along section EF of the reflector.

The orientation of a tangent $\vec{n}$ at point (X,Y) on the reflector is expressed vectorially by Boas (Ref.A2.) as:-

$$\vec{n} = \vec{i}\frac{dX}{d\theta} + \vec{j}\frac{dY}{d\theta} \qquad \text{(A2)}$$

The vector $\vec{S}$ from the point (X,Y) on the reflector and tangent onto the receiver at point $(1/2\ D_r, \theta)$ can be

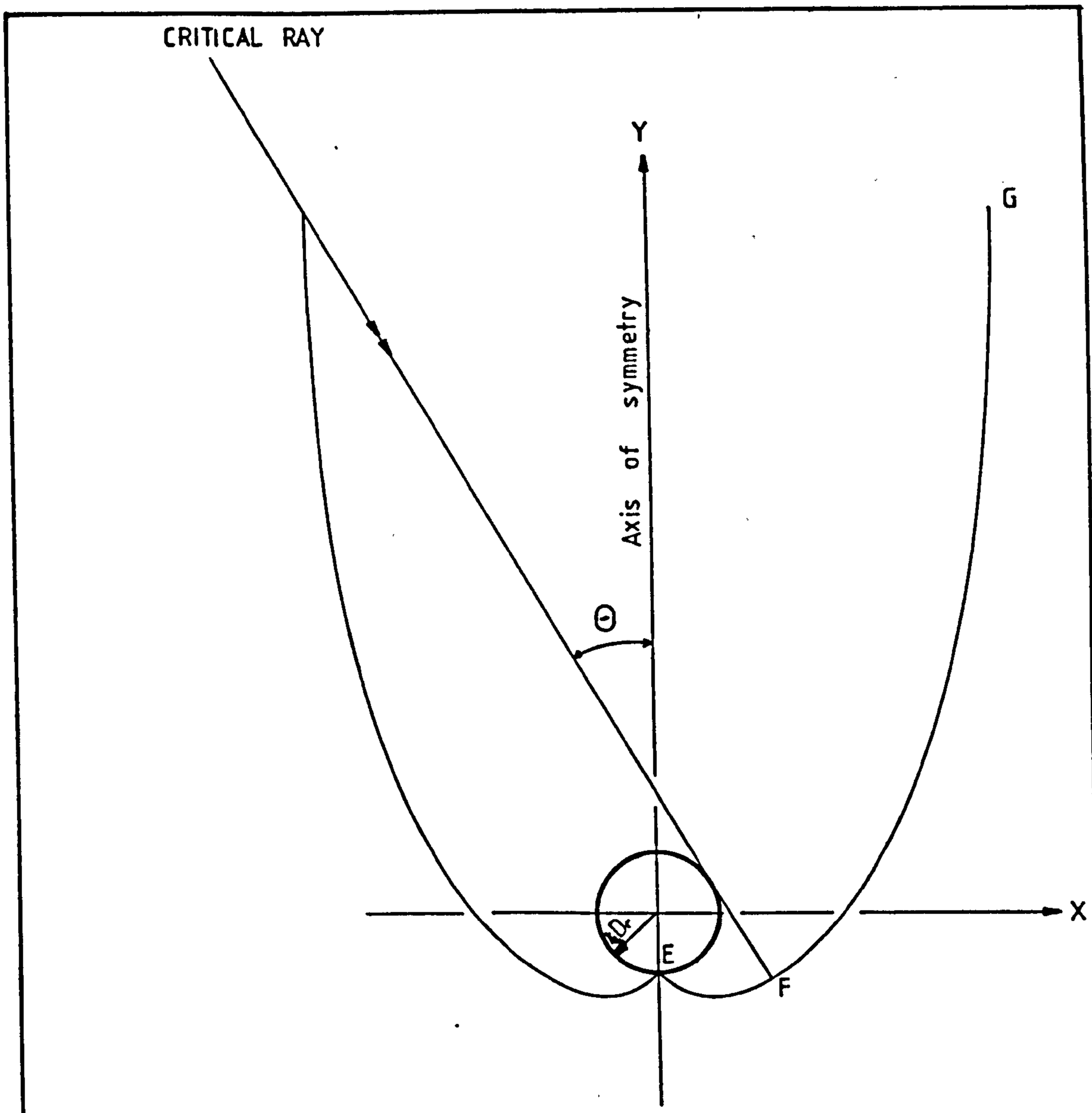

Fig. A1. Cross-sectional view of a compound parabolic reflector employing a cylindrical receiver.

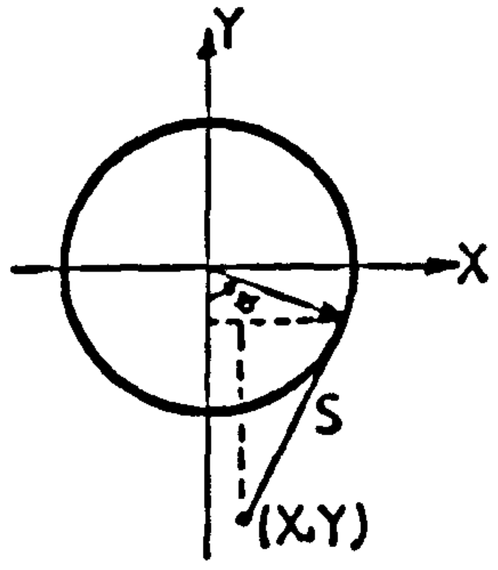

$X = \frac{1}{2} D_r \sin\theta - S \cos\theta$

$Y = -\frac{1}{2} D_r \cos\theta - S \sin\theta$

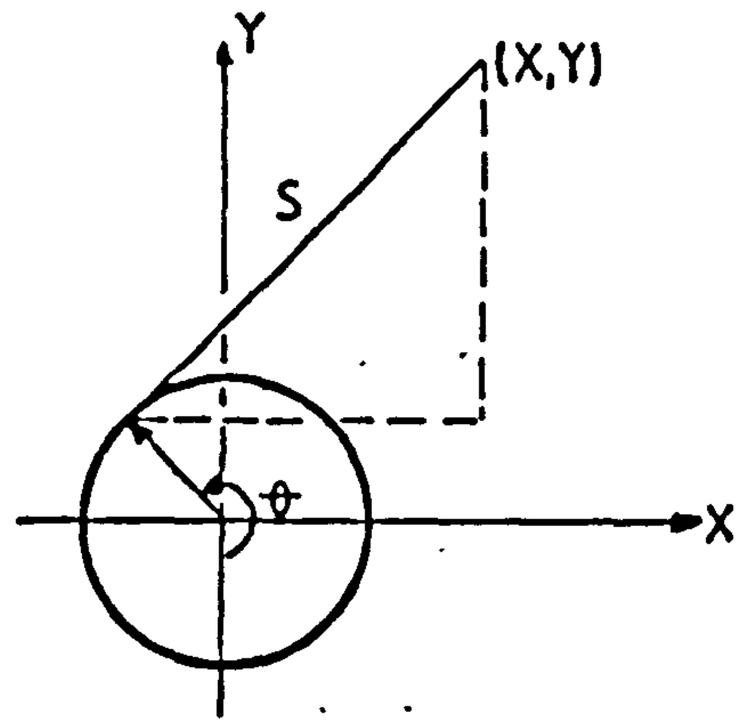

$X = S \cos(\theta - 180) - \frac{1}{2} D_r \sin(\theta - 180)$

$Y = \frac{1}{2} D_r \cos(\theta - 180) + S \sin(\theta - 180)$

Note:

$\cos(\theta - 180) = -\cos\theta$

$\sin(\theta - 180) = -\sin\theta$

Therefore:

$X = \frac{1}{2} D_r \sin\theta - S \cos\theta$

$Y = -\frac{1}{2} D_r \cos\theta - S \sin\theta$

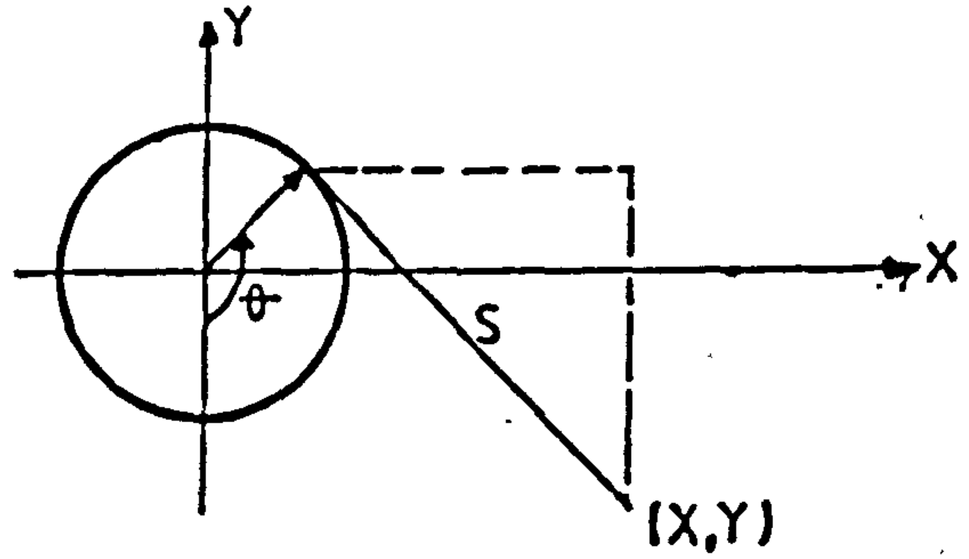

$X = \frac{1}{2} D_r \sin(180 - \theta) + S \cos(180 - \theta)$

$Y = -\left[S \sin(180 - \theta) - \frac{1}{2} D_r \cos(180 - \theta)\right]$

Note:

$\cos(180 - \theta) = -\cos\theta$

$\sin(180 - \theta) = \sin\theta$

Therefore:

$X = \frac{1}{2} D_r \sin\theta - S \cos\theta$

$Y = -\frac{1}{2} D_r \cos\theta - S \sin\theta$

Fig. A2. Generalized X and Y coordinates of a point on the compound parabolic reflector.

expressed as:-

$$\vec{S} = \vec{i}\,\mathrm{Cos}\theta + \vec{j}\,\mathrm{Sin}\theta \qquad \text{(A3)}$$

However, the basic design requirement along section EF of the reflector demands that the dot product of $\vec{S}$ and $\vec{n}$ be zero, i.e. $\vec{n}.\vec{S}=\emptyset$. Therefore:-

$$\vec{n}.\vec{S} = \frac{dX}{d\theta}\mathrm{Cos}\theta + \frac{dY}{d\theta}\mathrm{Sin}\theta = \emptyset \qquad \text{(A4)}$$

From equation(A1), $dX/d\theta$ and $dY/d\theta$ can be expressed as:-

$$\frac{dX}{d\theta} = 1/2\ D_r\mathrm{Cos}\theta + S\ \mathrm{Sin}\theta - \frac{dS}{d\theta}\mathrm{Cos}\theta$$

$$\frac{dY}{d} = 1/2\ D_r\mathrm{Sin}\theta - S\ \mathrm{Cos}\theta - \frac{dS}{d}\mathrm{Sin}\theta \qquad \text{(A5)}$$

Substitution of $dX/d\theta$ and $dY/d\theta$ from equation (A5) into equation (A4) and noting that $\mathrm{Cos}^2\theta + \mathrm{Sin}^2\theta = 1$, yields:-

$$1/2\ D_r - \frac{dS}{d\theta} = \emptyset \qquad \text{(A6)}$$

Integrating equation (A6) and noting that at $\theta = \emptyset$, $S=\emptyset$, yields:

$$S = 1/2\ D_r\theta \qquad \text{(A7)}$$

Substitution of S from equation (A7) in equation (A1), gives the expression that describes the section EF of the reflector, i.e.,

$$X = 1/2\ D_r[\mathrm{Sin}\theta - \theta\ \mathrm{Cos}\theta]$$

$$Y = -1/2\ D_r[\mathrm{Cos}\theta - \theta\ \mathrm{Sin}\theta] \qquad \text{(A8)}$$

Upper limit of θ that describes section EF of the reflector.

In order to determine the upper limit of θ within this section, the relationship amongst the angles Θ, i and θ as defined in fig.A3 must first be established. From triangle PQR of fig.A3, we have:-

$$(\theta - \pi/2) + \pi/2 + (\pi/2 - 2i - \ ) = \pi \qquad \text{(A9)}$$

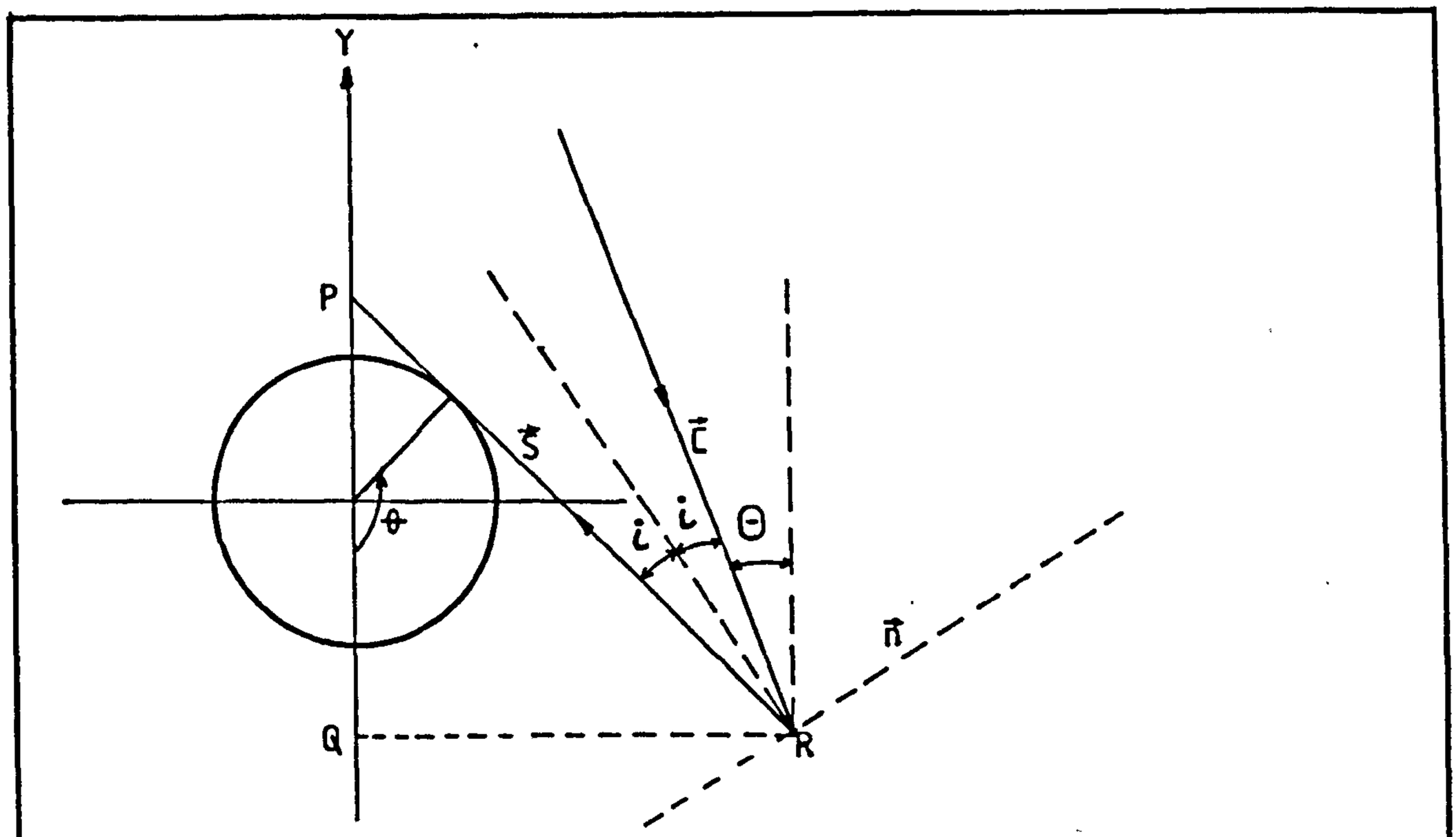

NOTE:

ANGLE $R\hat{P}Q = (\theta - \pi/2)$

ANGLE $P\hat{R}Q = (\pi/2 - 2i - \Theta)$

Fig. A3 Geometric relationship amongst angles θ, i and Θ.

Therefore:

$$i = 1/2[\theta - (\pi/2 + \Theta)] \qquad (A10)$$

But at point F, the incident ray is required to reflect along the same path, i.e. i=Ø. This requirement therefore demands that the upper limit of $\theta = \theta_F$ be:

$$\theta_F = (\pi/2 + \Theta) \qquad (A11)$$

Expression for S along section FG of the reflector.

The critical ray $\vec{C}$ can be vectorially expressed as:

$$\vec{C} = \vec{i}\,\mathrm{Sin}\Theta - \vec{j}\,\mathrm{Cos}\Theta \qquad (A12)$$

At this section of the reflector, it is required that the reflected critical ray be tangential to the cylindrical absorber, i.e. the reflected ray be $\vec{S}$. Because $\vec{C}$ and $\vec{S}$ are unit vectors, their dot products with $\vec{n}$, i.e. the tangent to the reflector, must be equal.

$$\vec{n}.\vec{C} = \vec{n}.\vec{S} \qquad (A13)$$

where,

$$\vec{n}.\vec{C} = \frac{dX}{d\theta}\mathrm{Sin}\Theta - \frac{dY}{d\theta}\mathrm{Cos}\Theta$$

and,

$$\vec{n}.\vec{S} = 1/2\ D_r - \frac{dS}{d\theta}$$

The former obtained from equations (A2) and (A12), whereas the latter obtained as in equations (A4) to (A6). Therefore equation (A13) reduces to:

$$\frac{dX}{d\theta}\mathrm{Sin}\Theta - \frac{dY}{d\theta}\mathrm{Cos}\Theta = 1/2\ D_r - \frac{dS}{d\theta} \qquad (A14)$$

Integration of equation (A14) yields:-

$$X\,\mathrm{Sin}\Theta - Y\,\mathrm{Cos}\Theta = 1/2\ D_r\theta - S + \text{constant} \qquad (A15)$$

Substitution of X and Y from equation (A1) into equation (A15) gives:-

$$\left\{\begin{matrix} 1/2\ D_r\mathrm{Cos}(\theta-\Theta)\ + \\ S\ \mathrm{Sin}(\theta-\Theta)\ +\ S \end{matrix}\right\} = 1/2\ D_r\theta + \text{const.} \qquad \text{(A16)}$$

The constant of integration can be obtained from the boundary condition that, at point F, $\theta = \theta_F = (\pi/2 + \Theta)$ when $S = 1/2\ D_r\theta$. This therefore reduces equation (A16) to:-

$$\left\{\begin{matrix} 1/2\ D_r\mathrm{Cos}(\theta-\Theta)\ + \\ S\ \mathrm{Sin}(\theta-\Theta)\ +\ S \end{matrix}\right\} = 1/2\ D_r\theta + 1/2\ D_r\ (\pi/2 + \Theta) \qquad \text{(A17)}$$

From which S can be obtained as:-

$$S = 1/2\ D_r \frac{[\pi/2 + \Theta + \theta - \mathrm{Cos}(\theta-\Theta)]}{[1 + \mathrm{Sin}\ (\theta-\Theta)]} \qquad \text{(A18)}$$

Substitution of S from equation (A18) into equation (A1) gives the X and Y coordinates within section FG as:-

$$X = 1/2\ D_r\left\{\mathrm{Sin}\theta - \frac{[\pi/2 + \Theta + \theta - \mathrm{Cos}(\theta-\Theta)]\mathrm{Cos}\theta}{[1 + \mathrm{Sin}(\theta-\Theta)]}\right\} \qquad \text{(A19)}$$

$$Y = -1/2\ D_r\left\{\mathrm{Cos}\theta + \frac{[\pi/2 + \Theta + \theta - \mathrm{Cos}(\theta-\Theta)]\mathrm{Sin}\theta}{[1 + \mathrm{Sin}(\theta-\Theta)]}\right\} \qquad \text{(A2Ø)}$$

Upper limit of θ within section FG of the reflector.

The upper limit of θ within this section of the reflector would occur at the aperture, when $dX/d\theta = Ø$, i.e.:

$$1/2\ D_r\mathrm{Cos}\theta + S\ \mathrm{Sin}\theta - \frac{dS}{d\theta}\mathrm{Cos}\theta = Ø \qquad \text{(A21)}$$

From equation (A18), $dS/d\theta$ can be expressed as:-

$$\frac{dS}{d\theta} = \frac{\left\{\begin{matrix} 1/2\ D_r[1 + \mathrm{Sin}(\theta-\Theta)]\ - \\ 1/2\ D_r\ [\pi/2 + \Theta + \theta - \mathrm{Cos}(\theta-\Theta)]\mathrm{Cos}(\theta-\Theta) \end{matrix}\right\}}{[1 + \mathrm{Sin}(\theta-\Theta)]^2}$$

Substituting the expression for $dS/d\theta$ in equation (A21) and solving for $\theta = \theta_{max}$, yields:-

$$\theta_{max} = [3\pi/2 - \Theta] \qquad \text{(A22)}$$

SUMMARY OF THE DESIGN EQUATIONS.

The equations for the design of a full compound parabolic concentrator with half acceptance angle Θ and a cylindrical receiver of diameter D_r are:-

(i) For $\emptyset \leq \theta \leq (\pi/2 + \Theta)$,

$$X = 1/2\ D_r[\sin\theta - \theta\cos\theta]$$

$$Y = -1/2\ D_r[\cos\theta + \theta\sin\theta]$$

(ii) For $(\Theta + \pi/2) \leq \theta = (3\pi/2 - \Theta)$,

$$X = 1/2\ D_r\left\{\sin\theta - \frac{[\pi/2 + \Theta + \theta - \cos(\theta - \Theta)]}{[1 + \sin(\theta - \Theta)]}\cos\theta\right\}$$

$$Y = -1/2\ D_r\left\{\cos\theta + \frac{[\pi/2 + \Theta + \theta - \cos(\theta - \Theta)]}{[1 + \sin(\theta - \Theta)]}\sin\theta\right\}$$

REFERENCES.

A1. Ortabasi, U and Buehl, W. M.,
'An internal cusp reflector for an evacuated tubular heat pipe solar thermal collector'.
Solar Energy,25,pp67-78(1980).

A2. Boas, M. L,
Mathematical Methods in the Physical Sciences,John Wiley and Sons,
New York(1966).

APPENDIX B

COLLECTION TIMES FOR EAST-WEST ORIENTED COMPOUND PARABOLIC CONCENTRATOR.

The use of a concentrator in a solar-energy collector is desirable in the sense that, it helps to increase the intensity of solar radiation reaching the absorber, and thus minimizes the area from which thermal losses could occur. A concentrator has an acceptance angle 2Θ defined as that angle within which any beam solar radiation entering the aperture will be specularly reflected to the receiver.

Rabl (Ref.B1) intimated that the concentration ratio of an ideal compound parabolic reflector is a function of its acceptance angle, i.e. $\lambda = 1/\sin\Theta$. This means that the smaller the acceptance angle, the higher the concentration ratio. However, for a compound parabolic reflector employed stationary, a higher concentration ratio, i.e a smaller acceptance angle, would mean a shorter duration within which solar energy would be collected.

An analytical procedure is thus given which yields the daily collection periods of solar radiation with respect to the acceptance angle for an east-west oriented compound parabolic reflector, south facing and inclined above the horizontal at an angle equal to to the latitude of its site.

The geometric relationship between a plane passing through a point (Ø,Ø,Ø) on the surface of the Earth and the incoming beam solar radiation is given by Benford and Bock(Ref.B2) as:-

$$\begin{aligned}\cos i = {} & \sin d \sin L \cos\Phi - \sin d \cos L \sin\Phi \cos\gamma \\ & + \cos d \cos L \cos\Phi \cos\omega + \\ & \cos d \sin L \sin\Phi \cos\gamma \cos\omega + \\ & \cos d \sin\Phi \sin\gamma \sin\omega. \end{aligned} \qquad \text{(B1)}$$

Equation (B1) will be used to determine the direction cosines of a unit vector SV (i.e. Sun vector) which locates the Sun with respect to the point (Ø,Ø,Ø) on the surface of the Earth at latitude L in the northern hemisphere- see fig.B1. With reference to fig.B1, $\cos\beta_4$ can be expressed from equation (B1) when $\Phi = Ø$, i.e.,

$$\cos\beta_4 = \sin d \sin L + \cos d \cos L \cos\omega \qquad \text{(B2)}$$

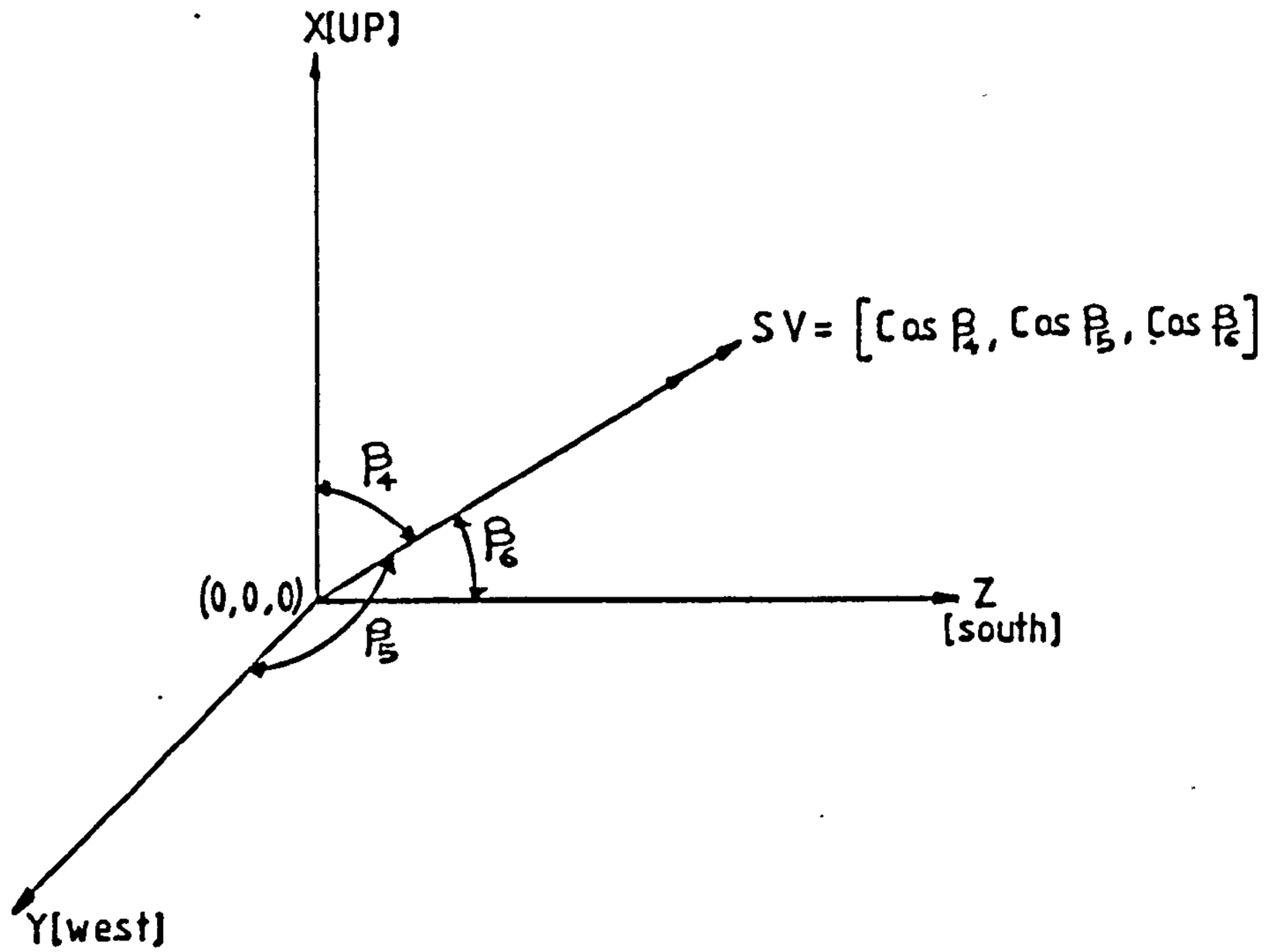

Fig. B1. Locating the Sun vector with respect to the defined X, Y and Z axes.

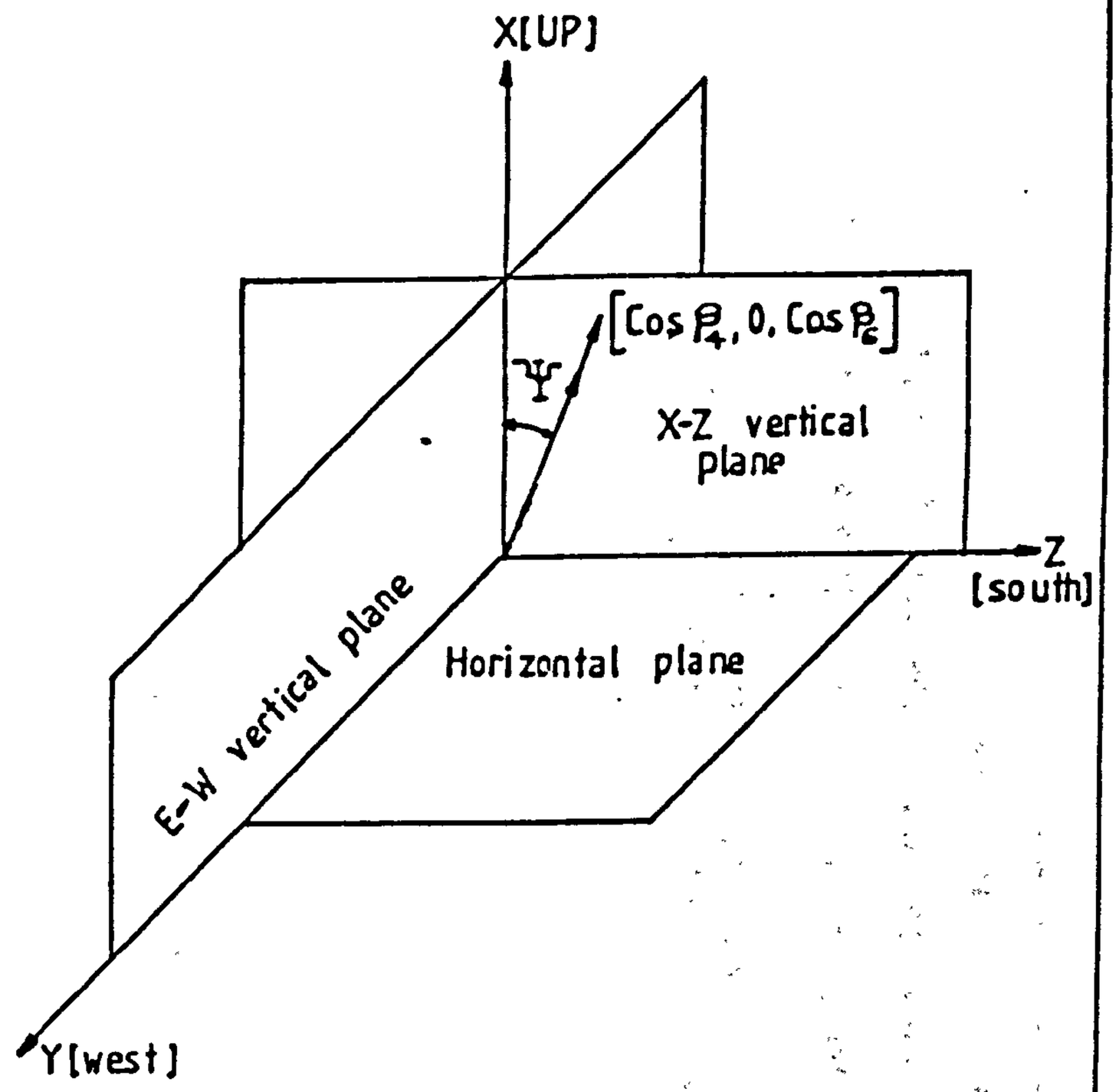

Fig. B2. Geometric representation of the east-west vertical altitude swing angle, Ψ.

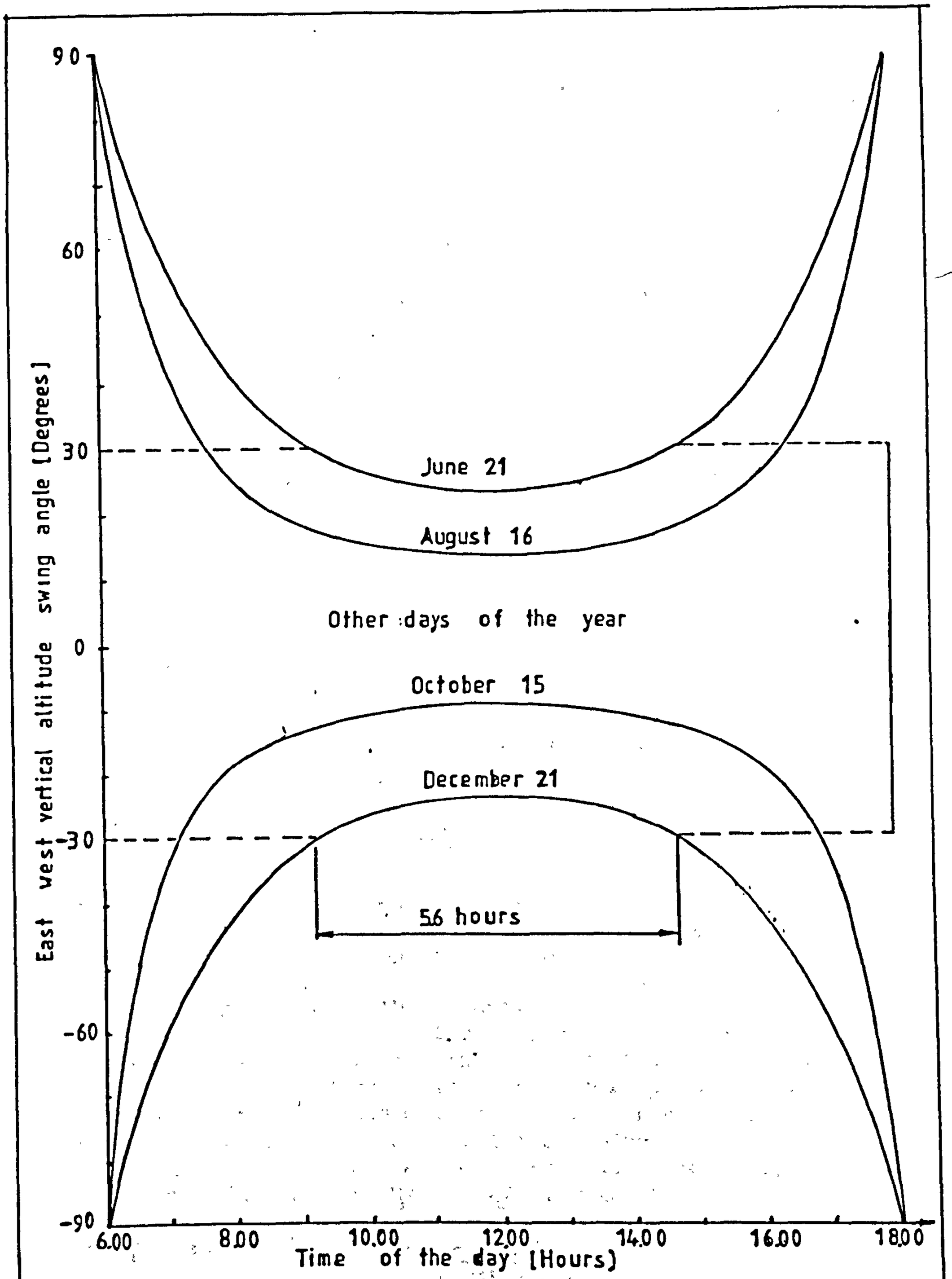

Fig. B3. The east west vertical altitude swing angle (reference to the equatorial plane) against time of the day.

Similarly, $\cos\beta_5$ and $\cos\beta_6$ can be expressed from equation (B1) when $\Phi = 90°$, $\gamma = -90°$ and $\Phi = 90°$, $\gamma = 0°$ respectively, i.e

$$\cos\beta_5 = -\cos d \sin\omega \qquad (B3)$$

$$\cos\beta_6 = -\sin d \cos L + \cos d \sin L \cos\omega \qquad (B4)$$

From fig.B1 and equations (B2) to (B4), the sun vector SV can therefore be expressed as:-

$$SV = (\sin d \sin L + \cos d \cos L \cos\ ),\ (-\cos d \sin\omega),\ (\cos d \sin L \cos\omega - \sin d \cos L) \qquad (B5)$$

By projecting SV on the X-Z vertical plane, $\cos\beta_5$ becomes zero and the projection can be defined by $(\cos\beta_4, 0, \cos\beta_6)$ at an angle ψ with the east-west vertical plane through the point (0,0,0)- see fig.B2. The angle ψ is called the east-west vertical altitude swing angle by Tabor(Ref.B3). With reference to fig.B2, the angle ψ can be expressed as:

$$\tan\psi = \frac{\cos\beta_c}{\cos\beta_4} \qquad (B6)$$

On substitution of $\cos\beta_4$ and $\cos\beta_6$ from equation (B2) and (B4) into equation (B6), gives:-

$$\tan\psi = \frac{\cos d \sin L \cos\omega - \sin d \cos L}{\cos d \cos L \cos\omega + \sin d \sin L} \qquad (B7)$$

The angle ψ is the angle of interest when considering the acceptance of solar beam radiation by a compound parabolic concentrator with horizontal east-west longitudinal axis. If ψ lies within half the acceptance angle of the concentrator, then the Sun's beam radiation will theoretically get to the receiver. However, if the reflector is inclined from the horizontal at an angle equal to the latitude of its site, then a new plane along the east-west direction normal to the reflector's aperture plane will be parallel with the equitorial plane. The angle $\hat{\psi}$ that the projection of the sun vector will make with this new plane will then be $\hat{\psi} = L - \psi$. From which,

$$\tan\hat{\psi} = \tan(L - \psi) = \frac{(\tan L - \tan\psi)}{(1 + \tan\psi \tan L)} \qquad (B8)$$

On substitution of $\tan\psi$ from equation (B7) in equation (B8) and rearranging, gives:

$$\tan\hat{\Psi} = \frac{\tan d}{\cos \omega} \qquad \text{(B9)}$$

It should be noted that ω is the angular displacement of the Sun, east or west of the local meridian due to rotation of the Earth on its axis at 15° per hour. This therefore means that:

$$\omega = 15t \qquad \text{(B10)}$$

where t is the sun time in hours. As a sign convention, morning is positive, afternoon negative and t at solar-noon is zero. Equation (B9) therefore reduces to:-

$$\tan\hat{\Psi} = \frac{\tan d}{\cos 15t} \qquad \text{(B11)}$$

Fig.B3 shows the plot of $\hat{\Psi}$ against time of the day, i.e. solar time. It is evident that a compound parabolic reflector or any trough-type solar collector with a 60° acceptance angle and inclined from the horizontal at an angle equal to the latitude of its site will theoretically collect the Sun's rays for about 5.6 hours during the solstices and for even longer periods during any other day of the year.

REFERENCES

B1. Rabl, A.
'Solar concentrators with maximal concentration for cylindrical absorbers'.
Applied Optics,15,7,pp1871-1873(1975).

B2. Benford, F. and Bock, J. E.
'A time analysis of sunshine'.
Trans. Am. Illum. Engng. Soc.,34,
pp200-218(1939).

B3. Tabor, H.
'Stationary mirrow systems for solar collectors'.
Solar Energy,2,pp27-33(1958).

APPENDIX C

SOME CONSIDERATIONS IN THE CHOICE BETWEEN R-11 AND R-113 ORGANIC WORKING FLUIDS FOR A SOLAR-ENERGY ACTIVATED RANKINE CYCLE.

(1) Safety considerations:

Both R-11 and R-113 are reported (Ref.C1) to be non-flammable. Their liquids and vapours are non-hazardous.

(2) Saturation vapour temperature and pressure relationship:

Fig.C1 compares the saturation temperature-pressure curves for the two fluids. It shows that R-11 has a lower saturation temperature than R-113 at identical pressures.

(3) Rankine cycle efficiency considerations:

Fig.C2 shows the theoretically calculated Rankine cycle efficiency with the two fluids as compared with the ideal Carnot efficiency. A condenser temperature of 35°C, saturated conditions and isentropic processes are assumed in evaluating the theoretical efficiencies as a function of the expander inlet temperature. It shows that that R-113 would give lower cycle efficiencies than with R-11. However,the reverse could occur in practice because of higher pump efficiencies (from my results in chapter five) and higher expander isentropic efficiencies (Ref.C2) with R-113.*

(4) Slope of the saturated vapour temperature-entropy curves:

Fig.C4 shows the temperature-entropy curves for the two working fluids(Ref.C3). At a given expander inlet pressure, fig.C4 shows that in order to achieve dry expansion with R-11, its vapour must be superheated to a certain degree prior to the expansion. whereas, for the same expander inlet pressure, dry expansion could be achieved with R-113 even when its vapour is saturated prior to expansion. This wetting nature of R-11 could eliminate the possibility of a regenerative heat exchanger to be incorporated in the cycle, so as to transfer thermal energy from the expander exhaust to the boiler feed.

(5) Maximum heat flux rate:

It is desirable to know the maximum rate of heat flux

---

* This is indicated in fig. C3.

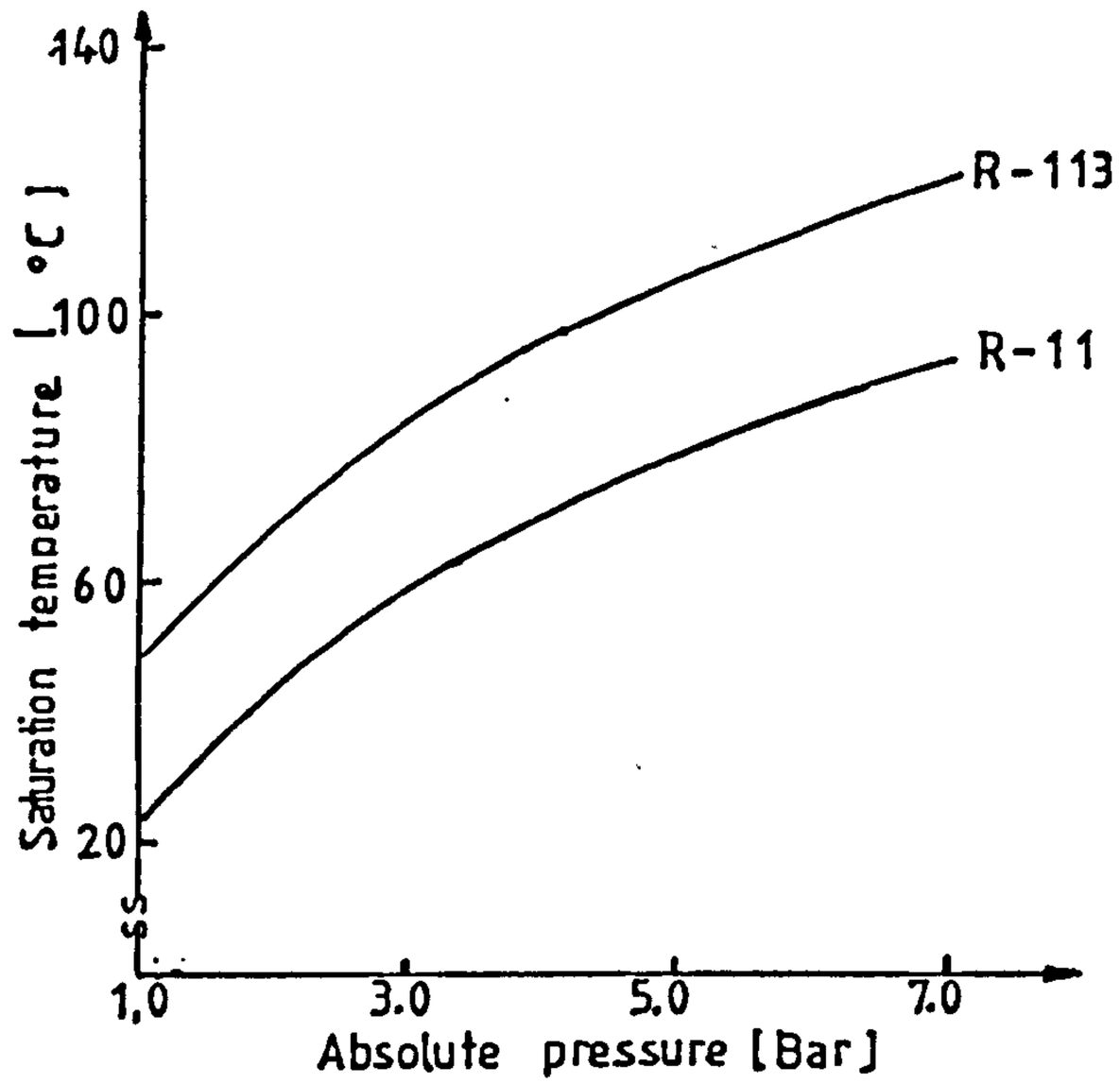

Fig. C1. Saturation temperature versus pressure curves for R-11 and R-113 organic fluids.

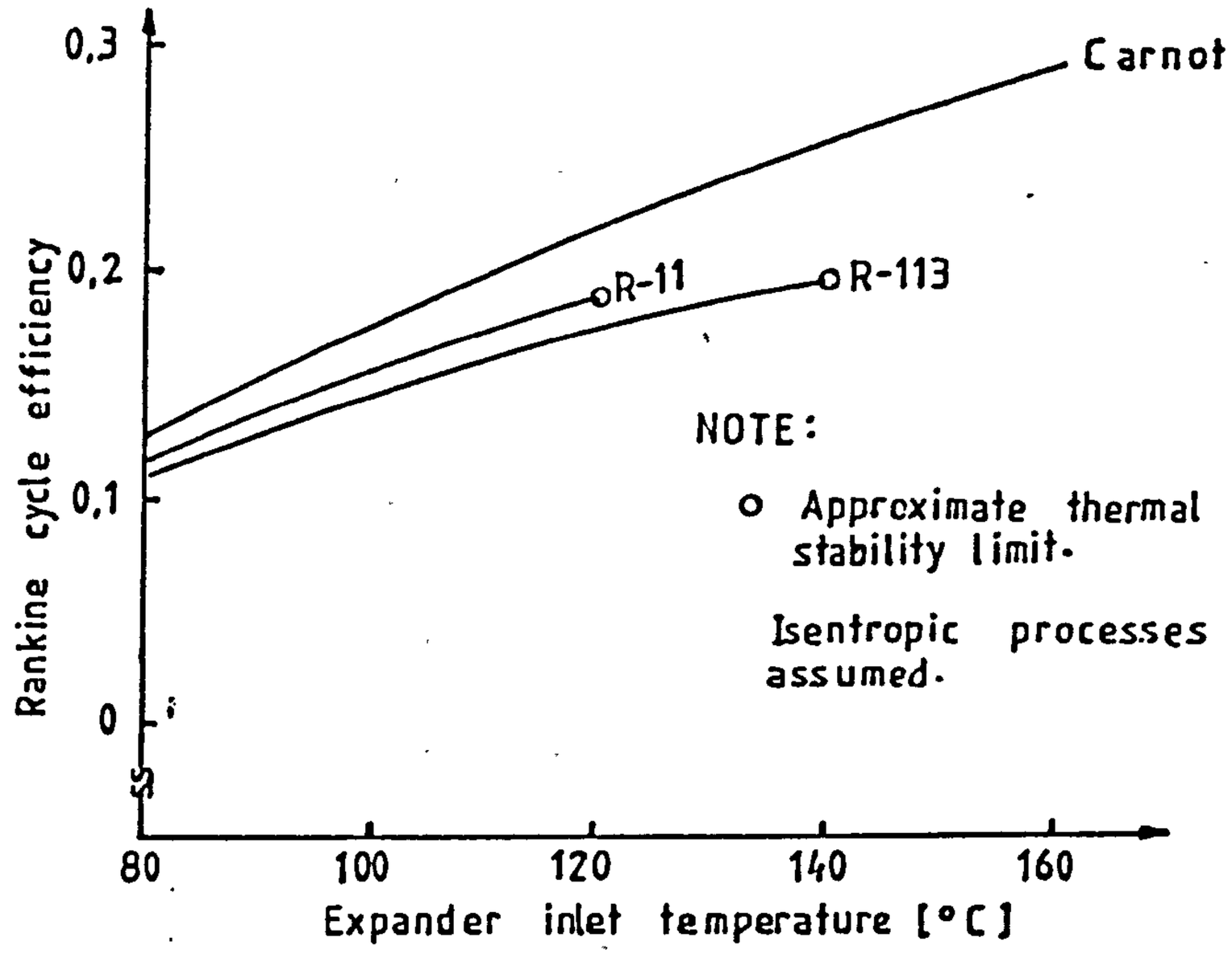

Fig. C2. Theoretical Rankine cycle efficiency against expander inlet temperature, for a condenser temperature of 35°C.

NOTE:

o Approximate thermal stability limit

	Isentropic efficiencies	
	Expander	Feed pump
With R-113	70 %	60 %
With R-11	60 %	50 %

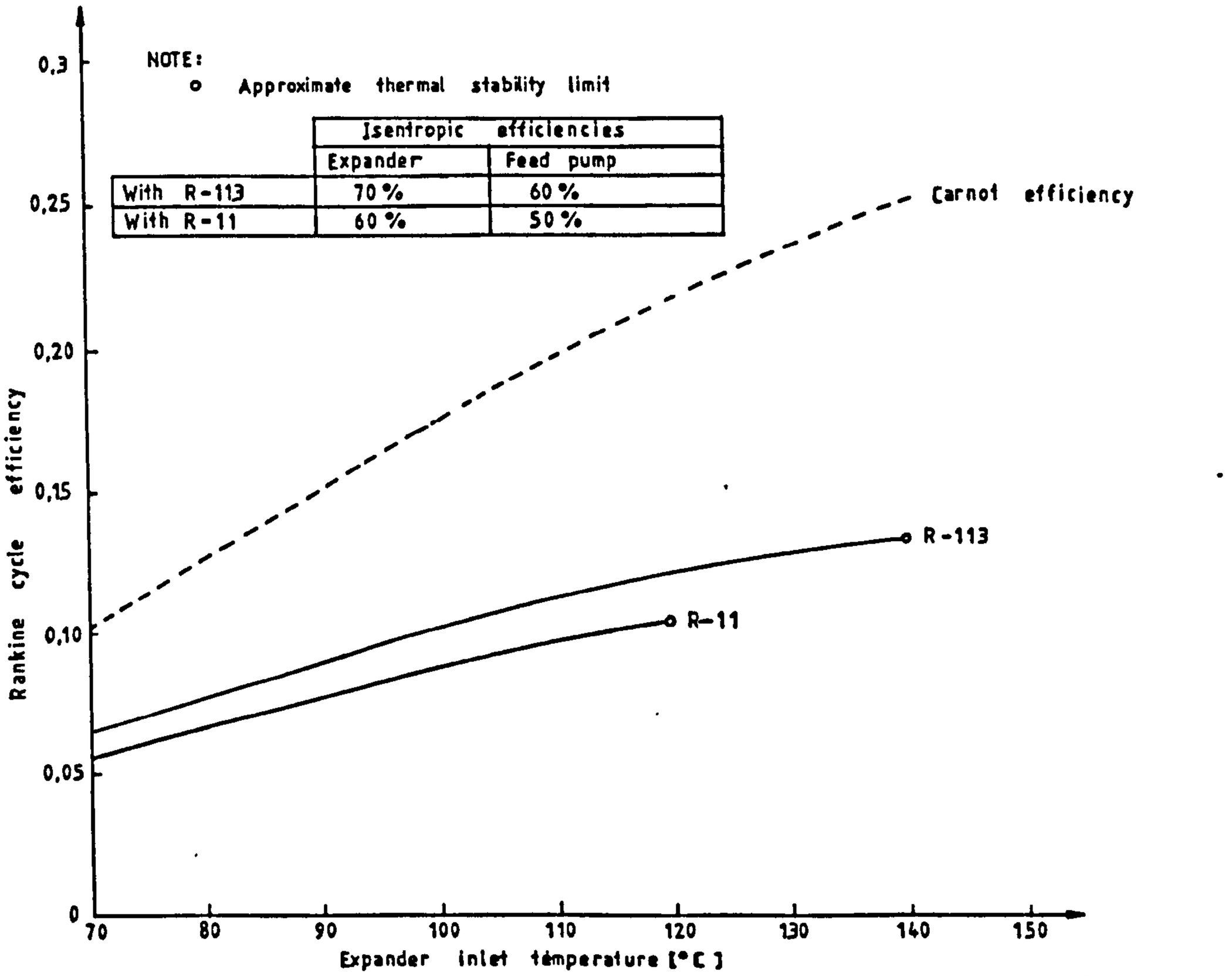

Fig. C3. As for fig. C2, except that the expander and the pump isentropic efficiencies are as indicated above.

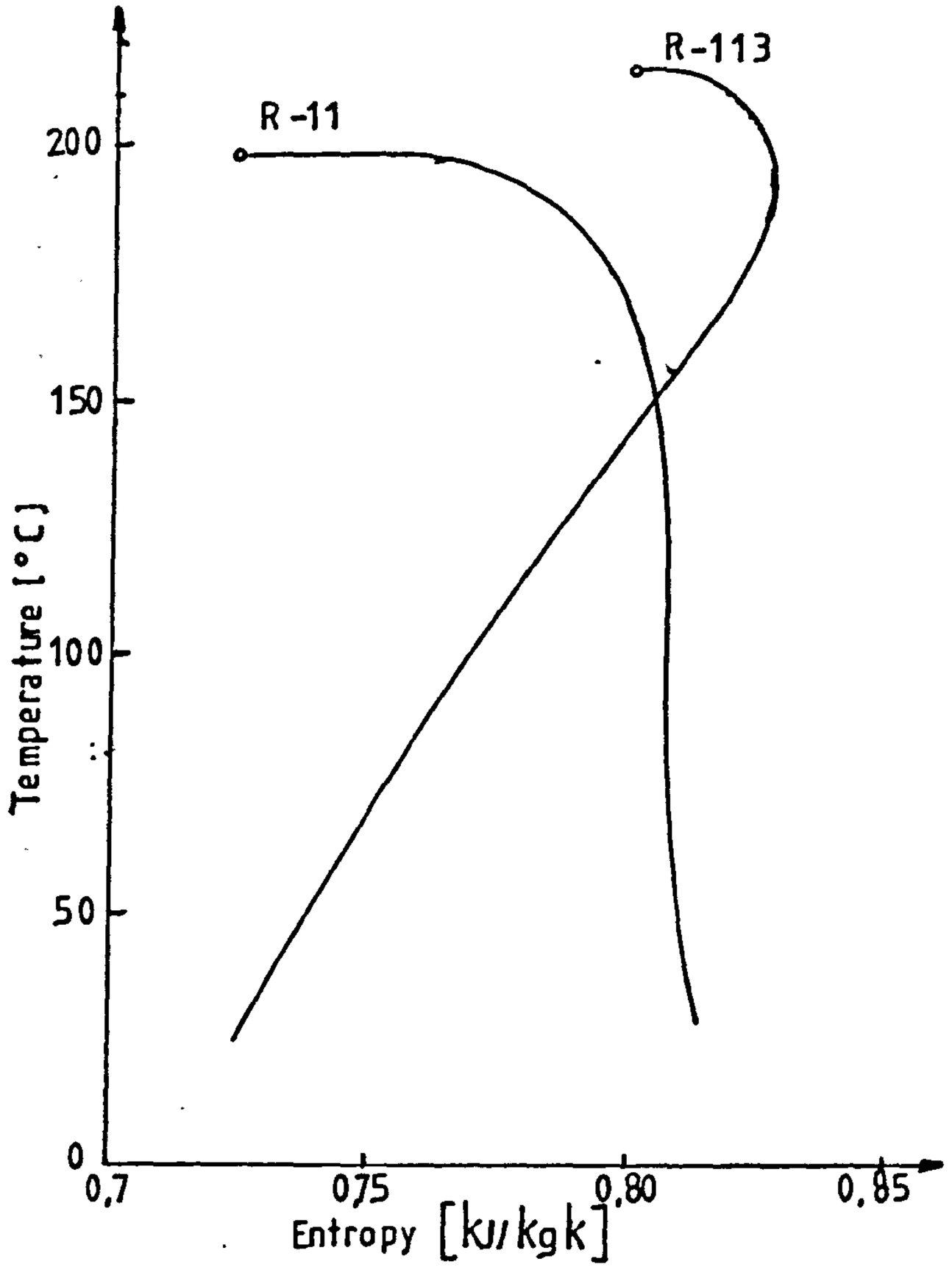

Fig. C4. Saturated vapour curves plotted on temperature against entropy basis.

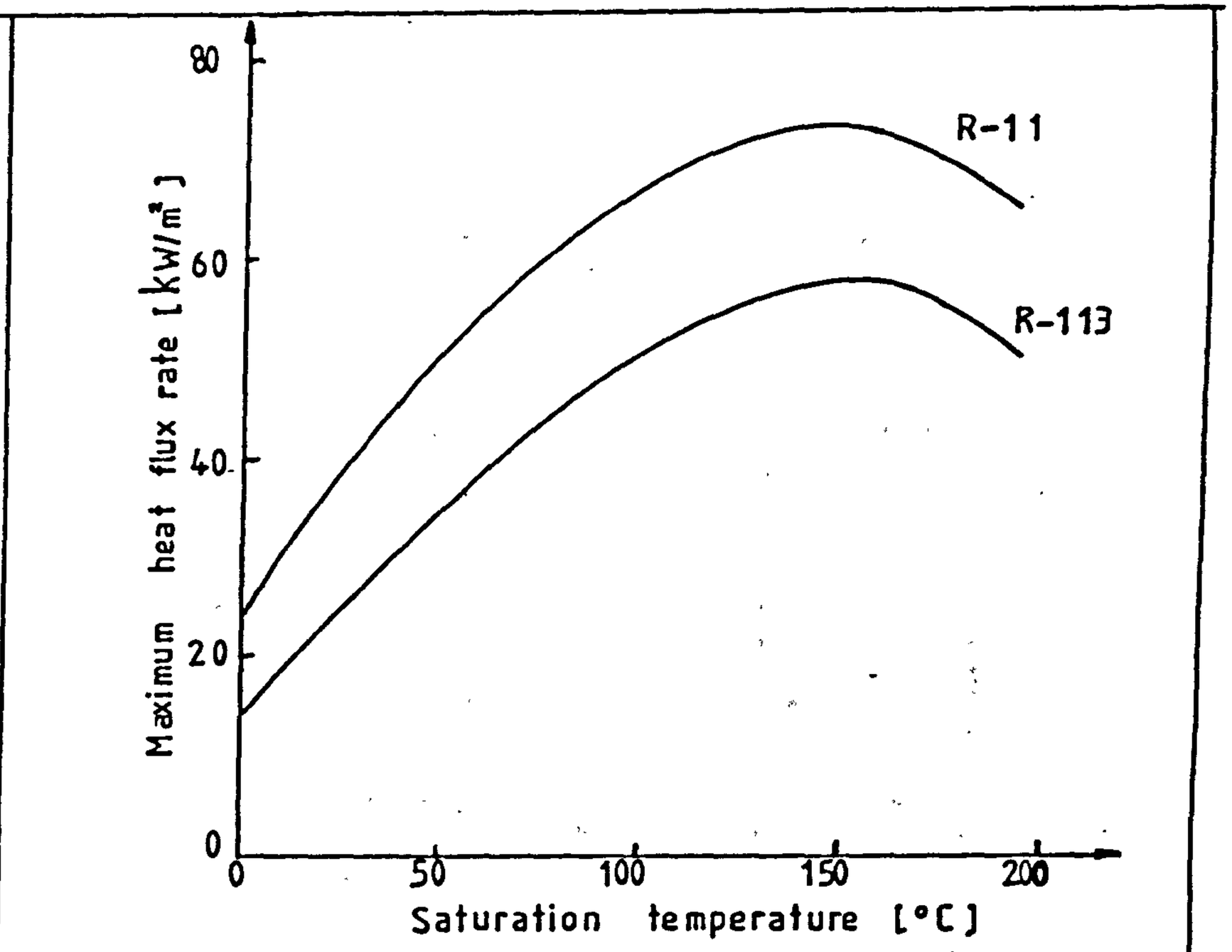

Fig. C5. Maximum heat flux at nucleate boiling against saturation temperature.

attainable at nucleate boiling, for efficient heat transfer and operation of the boiler. The maximum heat flux rate at nucleate boiling can be obtained from (Ref.C4):

$$\left(\frac{\dot{q}}{A}\right)_{max} = \frac{\pi}{24} h_{fv} \rho_v \left[\gamma_s g(\rho_f - \rho_v)\right]^{0.25} \left[1 + \frac{\rho_v}{\rho_f}\right]^{0.5}$$

where,

h_{fv} = Latent heat of vapourization (KJ/Kg)
ρ_v = Density of the vapour (Kg/m^3)
ρ_f = Density of the liquid (Kg/m^3)
γ_s = Surface tension (KN/m)
g = Acceleration due to gravity (m/s^2)

Fig.C5 shows the maximum rate of heat flux as a function of saturation temperature for the two working fluids (Ref.C3). It shows that R-11 has a higher maximum rate of heat flux than R-113 at identical saturation temperatures.

(6) Thermal stability considerations:

A candidate fluid should be chemically stable at the maximum expected cycle temperature, and in contact with the engine and piping materials as well as the lubricating oil. The table below shows data for some static stability tests undertaken by Parmelee (Ref.C5).

Fluid	Temperature	Duration	Degree of decomposition	
			Copper container	Steel container
R-113 only	149	2yrs.	Ø.13%	Ø.Ø42%
R-11 only	149 C	2yrs	Ø.6Ø %	Ø.72%
R-113+ equal volume of oil	149 C	52 days	Ø.42%	23.Ø %
R-11+ equal volume of oil	149 C	52 days	Ø.77	burst container

REFERENCES

C1. Du Pont,E.I. and Company.
Fluorocarbons Bulletin,B-2(1969)

C2. Private communications with Ossama B.(Ph.D student,Cranfield), who was involved in testing the expander.

C3. Ezzat,W.
'Optimum working fluids for solar Rankine cycle cooling of buildings'.
Solar Energy,25,3,pp235-241(1980).

C4. Zuber,N.
'On the stability of boiling heat transfer'
Trans. ASME,80,pp711-720(1958).

C5. Parmelee,H.M.
'Sealed tube stability tests on refrigeration materials'.
Du Pont Bulletin,RT-42,Apr.(1976).

PART B

CONTENTS

NOMENCLATURE

A_x	Air-cell aspect ratio (=W/L) — see fig.1.
A_p	Plan aspect ratio (=Z/W) — see fig.1
A_s	Spacer aspect ratio (=t/L) — see fig.1
A_z	Horizontal aspect ratio (=Z/L) —see fig.1
A'	Area (m^2)
B	Over-relaxation factor.
C_p	Specific heat at constant pressure (J/Kg K)
d	Thickness of the back insulation on the receiver of the solar-energy collector (m).
D	Denotes the derivative of a variable.
F	Cell coupling factor ($=K_a \Delta X_s / K_s \Delta X$)
FS	Fringe shift ($= \Delta OPD/\lambda$)
g	Acceleration due to gravity (m/s^2)
h	Heat transfer coefficient ($W/m^2 K$)
I	Solar insolation (W/m^2)
K	Thermal conductivity (W/m K)
L	Height of the convection suppression device(m)
m	Number of air-cells.
n	Refractive index of air.
N	Upper limit of the suffix i, i.e. i=2,3,4...N
Ns	Upper limit of the suffix k, i.e. k=2,3,4...Ns
Nu	Nusselt number ($=hL/K_a$)
OPD	Optical path length (m)
p	Absolute pressure (N/m^2)
P	Dimensionless pressure ($=pL^2/\rho\alpha\mu$)
Pr	Prandtl number for air ($= \mu C_p / K_a$)
$\dot{q}$	Rate of heat losses per unit area (W/m^2)
$\dot{Q}$	Rate of heat losses (W)
r	Ratio $\Delta X/\Delta Y$
r_s	Ratio $\Delta X_s/\Delta Y$
Ra	Rayleigh number ($=\frac{\rho\beta}{\mu\alpha}\Delta T\ g\ L^3/\nu^2$)
R	Thermal resistance (K/W)
t	Thickness of a spacer (m)
T	Absolute temperature (K)
u	Velocity in the x-direction (m/s)
U	Dimensionless velocity in the X-direction (=uL/α). Also used to denote overall heat transfer coefficient in chapter six ($W/m^2 K$).
v	Velocity in the y-direction (m/s).
V	Dimensionless velocity in the Y-direction(=vL/α).
W	Width of the air-cell or collector unit —see fig.1 and 2 (m).
x	Distance along the x-direction, i.e. $\emptyset \leq x \leq W$ (m).
X	Dimensionless distance along the X-direction, i.e. $X = x/L$ and $\emptyset \leq X \leq A_x$.
y	Distance along the y-direction, i.e. $\emptyset \leq y \leq L$ (m).

Y	Dimensionless distance along the Y-direction, i.e. Y = y/L and $0 \leq Y \leq 1.0$
Z	Length of the air-cell along the east-west direction (m).

Greek alphabet

α	Thermal diffusivity, i.e $= K_a/\rho C_p$ (m^2/s).
β	Also used to denote absorptivity in chapter six.
β_o	Coefficient of volume expansion for air (K^{-1}).
ΔT	Temperature difference (°C).
ΔOPD	Change in optical path length (m).
ΔX	Grid size along the X-direction — see fig.4.
ΔY	Grid size along the Y-direction — see fig.4.
ε	Emissivity.
η	Efficiency.
ϕ	Dimensionless temperature (= $[T-T_c]/[T_h-T_c]$).
λ	Wavelength of laser light (m).
μ	Dynamic viscosity for air (Ns/m^2).
ν	Kinematic viscosity for air, i.e. $= \mu/\rho$ (m^2/s).
ρ_a	Density of air (Kg/m^3).
σ	Stefan-Boltzman constant (W/m^2K^4).
Φ	Tilt-angle above the horizontal (Degrees).
τ	Transmissivity.
ψ	Dimensionless streamfunction ($=\Psi/\alpha$).
Ψ	Streamfunction (m^2/s).
ω	Dimensionless vorticity function ($=\Omega L^2/\alpha$).
Ω	Vorticity function (Rad/s).

Subscripts

a	Refers to air
b	Refers to the insulation at the back of the receiver.
c	Refers to the cold plate.
col	Refers to the collector unit.
f	Refers to heat removing fluid mean conditions.
g	Refers to the glazing.
h	Refers to the hot plate.
in	Refers to heat removing fluid inlet conditions.
i,j	Quantity at the grid-point defined by (i,j).
k,j	Quantity at the grid-point defined by (k,j).
o	Refers to property evaluated at the reference temperature T_o.
op	Optical.
out	Refers to the heat removing fluid outlet conditions.
ov	Refers to overall convective heat transfer coefficient.

r	Refers to the receiver of the collector.
s	Refers to the spacers.
1	Refers to radiation from the receiver to the glazing.
2	Refers to conduction via the air-gap.
3	Refers to conduction through the spacers.
4	Refers to forced convection over the glazing.
5	Refers to radiation from the glazing to the surroundings.
6	Refers to conduction through the insulation at the back of the receiver.

Superscript

-	Average value.

GLOSSARY

CSD — Abbreviation for convection suppression device, i.e. structures inserted within an air-layer so as to retard the convection phenomena.

LTG — Abbreviation for linear temperature gradient. It signifies the boundary condition when the spacer is assumed to be made of a perfectly conducting material.

Teflon FEP — A fluorocarbon resin manufactured by Du Pont company.

ZHF — Abbreviation for zero heat flux. It signifies the boundary condition when the spacer is assumed to be made of a perfectly insulating material.

CHAPTER ONE

INTRODUCTION

1.1 BACKGROUND:

The evacuated tube solar-energy collector employed in the solar-energy activated Rankine-cycle pilot power plant, has an adequate thermal performance as predicted in the first part of this thesis. However, as in any desert area, dust will constitute a problem, impeding the continuous exposure of the collector array to the Sun's rays. Regular cleaning would therefore be essential. Cleaning a large array of (≈1000) of such fragile tubes in situ is unlikely to be accomplished without cracks and breakages occurring. This perhaps means that the high vacuum which is essential for collectors continued adequate thermal performance could be easily lost. This, and the fact that the maximum anticipated working temperature in the organic Rankine cycle would be about 120°C, prompted the study of a means other than evacuation, of reducing thermal losses from the absorber of a flat-plate solar-energy collector.

Flat-plate collectors are easier to clean and should also be expected to be more cost effective. Moreover, the annual average solar radiation distribution in Egypt is such that 30 percent of the total available radiation is diffuse (Ref.1). A flat-plate collector would utilize a greater proportion of this component. However, the efficiency of a given collector depends upon its optical and thermal losses. The optical losses are calculated as the difference between the amount of solar radiation incident at the collector aperture and that reaching the absorber. The main forms of thermal losses occur by radiation and convection from the surface of the receiver exposed to solar-radiation. The radiation losses can be reduced effectively by applying some selective optical coating of very low emissivity and high absorptivity on the surface of the absorber (Ref.2 and 3). The major problem, however, lies with the thermal losses due to natural convection.

1.2 LITERATURE SURVEY:

IF a horizontal fluid layer confined between two parallel isothermal surfaces is subjected to heating from below, then provided that the temperature difference between the two surfaces is greater than a critical value, convective motion will ensue. This is referred to as the Bénard

effect. In 1901 Bénard (Ref.4) found that a thin layer of spermaceti (spermateci is a white waxy material obtained from oil of the sperm whale and some other marine mammals, which is used in making ointments, cosmetics and other commercial products) which was heated from below performed a motion of a distinct regular pattern. Seen from above , the image resembled a honeycomb section. The motion occurred within prisms of which the base had a hexagonal form. The warmer fluid rose at the centre and the colder fluid descended at the boundaries.

A mathematical treatment of this phenomenon was given in 1916 by Lord Rayleigh (Ref.5). The theoretical considerations led to the conclusions that a layer of fluid, heated from below should remain at rest until the Rayleigh number reaches a certain critical value*, dependent upon the boundary conditions. When a layer is bounded by two rigid parallel planes, this critical Rayleigh number amounts to about 1700. When this value is exceeded, instability occurs and the beginning motion has the form of the regular cells already described.

De Graaf and Van der Held (Ref.6) concluded that in horizontal air layers, the air remains at rest until the Rayleigh number reaches about 2000. When this value is exceeded, the cellular motion sets in, at first in the form of hexagonal prisms but with a tendency to change into rows of tetragonal prisms when the Rayleigh number increases. These workers found, in contrast with the Bénard cells in liquids, that the air descended in the middle. A possible explanation they gave to this behaviour is that, for gases, the kinematic viscosity increases, whereas for liquids it decreases, with temperature. Assuming that the direction of flow at the outset determines the mode of motion which occurs in the cell,it will be clear that the cells observed in liquids start forming on the warmer bottom of the layer with an ascending movement. Because the warmer bottom is the region where the kinematic viscosity is smallest. For gases, however, the cooler top of the layer has the lowest kinematic viscosity, causing the flow to descend in the centre of the cells.

However,flat-plate solar-energy collectors are seldom employed horizontally. They can be likened to an inclined air enclosure bounded at the bottom and top by isothermal surfaces,i.e. the solar-energy absorber and glazing respectively. For this closed top inclined air systems heated from below, an argument put forward by Peterson(Ref.7) indicated that, regardless of the temperature difference, convective motion referred to, as

---

*The critical Rayleigh number defines the critical conditions which must be exceeded before convective motion can begin in a fluid subjected to a temperature gradient in a gravity field.

the base flow must occur. Heat transfer in the base flow is basically by conduction. Peterson's argument is based on the fact that if the stagnant fluid is assumed to exist in the inclined position, then the isotherms throughout the fluid cannot be matched to the two isotherms representing the isothermal surfaces. Distortion of the isotherms must therefore occur. This can only be achieved by convective motion of the fluid. In the immediate post-conductive regime,i.e. Rayleigh numbers greater than the critical value, the flow situation becomes unstable . Hollands et al (Ref.8) intimated that for tilt-angles less than 15°, the instabilities result into tendency of convective cells to be formed in all directions. Whereas for tilt-angles between 15° and 45°, the first incipient motion is rolls with axis along the upslope. However, there is still some tendency for transverse rolls, i.e rolls with axis normal to the upslope direction. For tilt-angles between 70° and 90°, the flow situation is more unstable to rolls with their axis along the upslope. No mention was made of angles between 45° and 70°.

A number of studies,i.e. Randal et al (Ref.10), Hollands et al (Ref.9) and Elsherbiny et al (Ref.11) on the convective heat transfer in large inclined air cavities have been carried out. Some of those applicable to the design of the conventional flat-plate collector are reviewed by Buchberg et al (Ref.12). The suppression of the convective heat transfer losses from the absorbers of flat-plate collectors is a subject of wide interest to designers of solar-energy collectors. The basic approach to this problem has involved the use of so-called convection suppression devices (usually abbreviated as CSD). The CSD are structures inserted between the absorber and the glazing, which subdivides the air in-between the glazing and the absorber into smaller air-cells. This is intended to increase the viscous drag which retards the convective motion. The name of a CSD is usually derived from the shape of the cross-section of the air-cells formed, when viewed from the top. For example,cylindrical (Ref.13), square (Ref.14), and rectangular (Ref.15). The sizes of the air-cells so formed are usually specified with respect to the ratios of their respective dimensions, i.e.width, height, and length and are referred to as the 'aspect ratios'. These aspect ratios are defined in fig.1. Arnold et al (Ref.15) studied the effect of the 'horizontal aspect ratio' on the convective heat transfer for the rectangular device, with 'air-cell aspect ratio' of about 0.25. They found that the horizontal aspect ratio had little effect upon the convective heat transfer for values greater than unity. A rectangular convection suppression device with large horizontal aspect

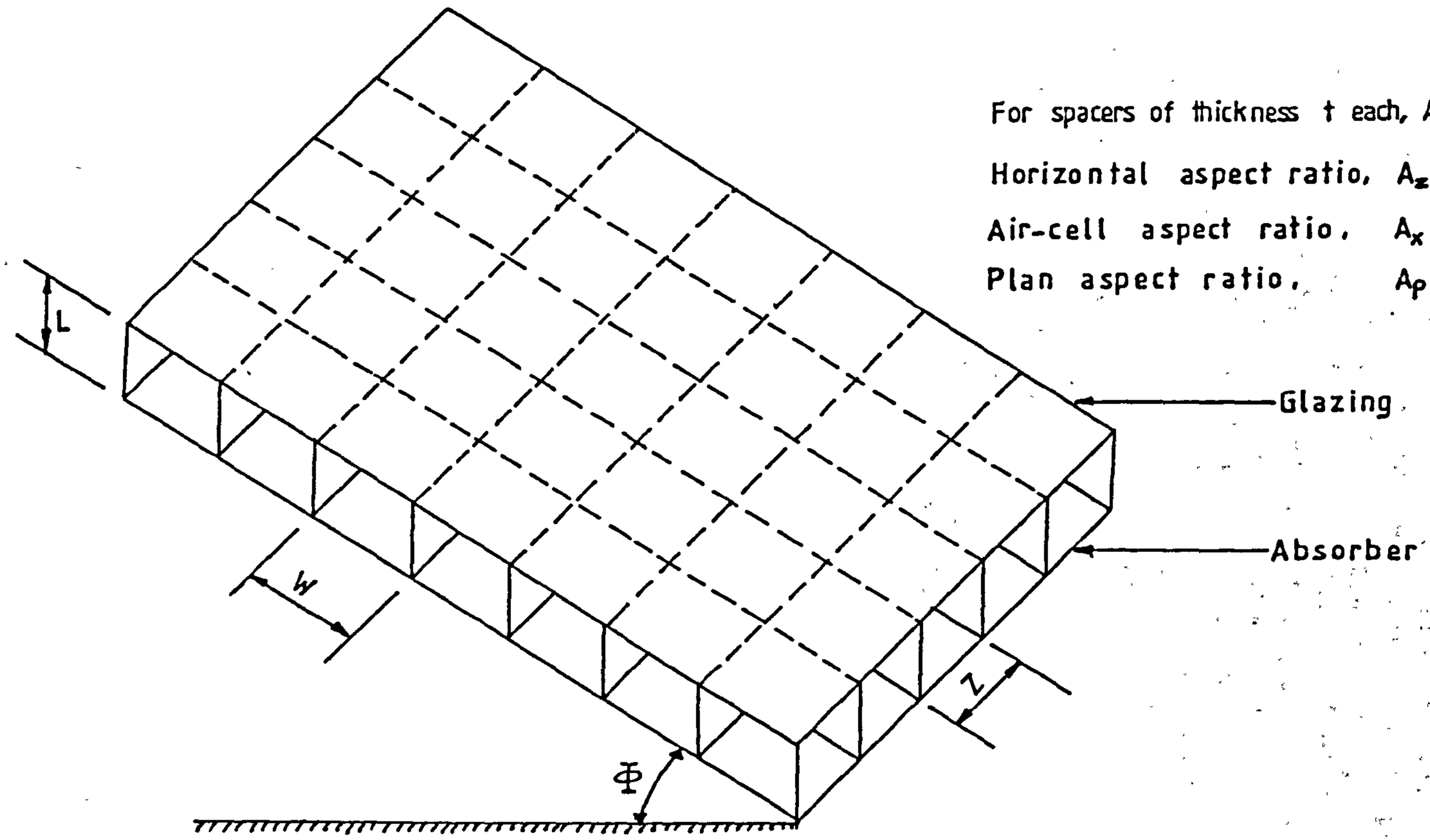

Fig. 1. Schematic diagram of a collector with a rectangular CSD.

ratio is referred to as a slatted or two-dimentional device (Ref.16). It is of interest in this study because of its simplicity. A simple schematic diagram of a collector employing such a device is shown in fig.2. It simply consists of a set of plane high transmissivity spacers forming small air-cells, oriented along the east-west direction and normal to the collector absorber and glazing.

The performance of a solar-energy collector employing a CSD, as pointed out by Hollands (Ref.17), is not only influenced by the capability of the device to minimize the convective heat losses but also the heat losses due to conduction directly through its walls as well as the amount of solar radiation it attenuates. Symons (Ref.18), however, intimated that the most desirable materials for the construction of CSD for solar energy applications are glass and FEP Teflon. They have high transmissivities of about Ø.9Ø and Ø.96 respectively, fairly good weatherability and maximum operating temperatures exceeding 2ØØ°C. Charters and Guthrie (Ref.16) also intimated that at collector output temperatures of about 1ØØ° C, the attenuation of solar-radiation caused by the CSD wall material can be compensated for by lower heat loss coefficients as a result of reduced convective and radiative heat losses.

1.3 THE PRESENT STUDY:

A numerical study by Koutsoheras (Ref.19) and experimental studies by Meyer et al (Ref.2Ø), Charters and Guthrie (Ref.16) show that the important parameter for the closed top slatted-CSD with respect to minimizing convective heat transfer, is the ratio width-to-height of the air-cells, i.e. the so-called air-cell aspect ratio. The smaller this is, i.e. less than unity, the more effective will the CSD be in reducing the convective heat transfer. This information, although very useful, is inadequate in determining the size of the air-cells for which convective heat transfer could be minimized. A criterion for choosing either the width or the height must also be stated. Thus two complementary studies (i.e. theoretical and experimental) of the convective heat transfers in a slatted CSD were undertaken. The theoretical study was used to predict the air-cell aspect ratio for which the convective heat transfer could be minimized. The approach involved seeking the solutions of the two-dimensional equations governing a laminar two-dimensional convective flow. The two-dimensional equations were derived from the three basic laws of conservation of energy, momemtum and mass. The solutions were obtained using the finite-difference

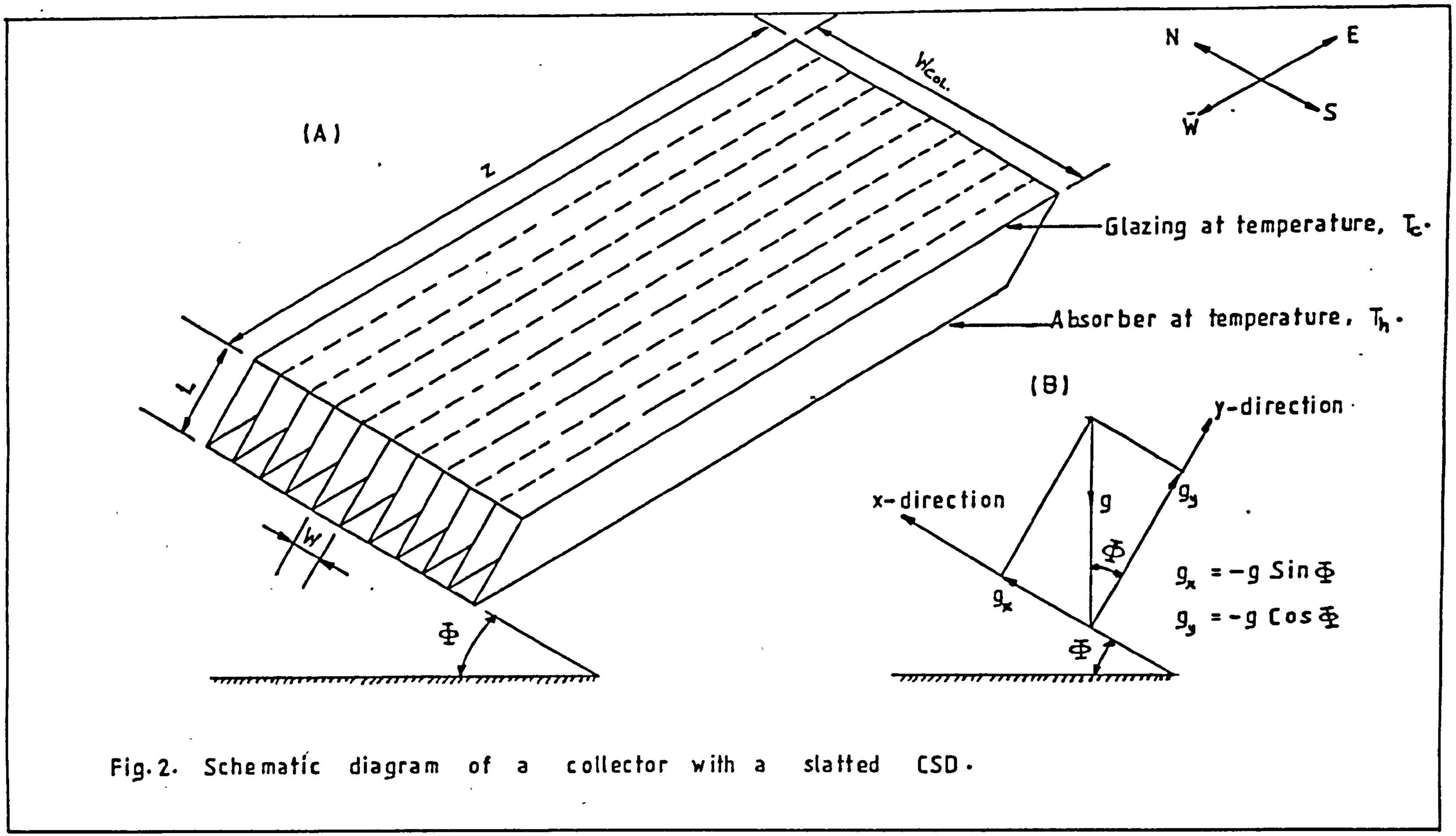

Fig. 2. Schematic diagram of a collector with a slatted CSD.

methods, with the aid of a computer program. However, as already mentioned, in order to completely define the air-cell size, the corresponding width or height must be stated. Thus the experimental study was employed to render the criterion for choosing the cell-height. It involved the investigation of the effect on convective heat transfer of decreasing the air-cell aspect ratio from unity , by varying the cell-height for constant cell-width. This was carried out using an interferometric method. From the two studies, the air-cell size was defined. The thermal performance of the flat-plate solar-energy collector employing the CSD was predicted and compared with that previously predicted for the evacuated tube collector. The two collectors were then appraised on economic grounds, if each should supply the input power requirements of the 'King Tut' organic Rankine-cycle pilot plant.

CHAPTER TWO

THE MATHEMATICAL MODEL

2.1 GOVERNING EQUATIONS IN THE CELL.

The bahaviour of air in the cells* is governed by the three basic laws, i.e. conservation of momentum, energy and mass. The equations representing these laws as applied to fluid flow have been derived and well documented (Ref.21), namely the three-dimensional Navier-Stokes, energy and mass continuity equations. Solutions of these equations in their full form are not easy to obtain. Therefore the following assumptions were made which simplify the equations (Ref.22):-

(i) No external forces other than gravity,
(ii) Constant physical and transport properties, except for the temperature effect on the density which produces a buoyancy force, i.e the Boussinesq approximation,
(iii) Negligible viscous heat dissipation,
(iv) Laminar two-dimensional flow,
(v) No internal heat source,
(vi) Negligible radiation effects,
(vii) Newtonian fluid and
(viii) Steady-state.

Applying these assumptions to the general continuity, Navier-Stokes and energy equations (Ref.21),yields:-

The continuity equation:

$$\frac{\partial u}{\partial x} + \frac{\partial v}{\partial y} = 0 \qquad (1)$$

The momentum equation:
x-direction,

$$\rho_o\left(u\frac{\partial u}{\partial x} + v\frac{\partial u}{\partial y}\right) = -\frac{\partial p}{\partial x} + \mu\left(\frac{\partial^2 u}{\partial x^2} + \frac{\partial^2 u}{\partial y^2}\right) + \rho g_x \qquad (2)$$

y-direction,

$$\rho_o\left(u\frac{\partial v}{\partial x} + v\frac{\partial v}{\partial y}\right) = -\frac{\partial p}{\partial y} + \mu\left(\frac{\partial^2 v}{\partial x^2} + \frac{\partial^2 v}{\partial y^2}\right) + \rho g_y \qquad (3)$$

The energy equation:

$$u\frac{\partial T}{\partial x} + v\frac{\partial T}{\partial y} = \alpha\left(\frac{\partial^2 T}{\partial x^2} + \frac{\partial^2 T}{\partial y^2}\right) \qquad (4)$$

---

* Refer to fig.3

2.1.1 Elimination of the variable density term.

The variable density term ρ, which produces a buoyancy force can be expressed as a power series in T, using the Taylors series expansion about a reference temperature T_o, i.e,

$$\rho(T) = \rho_o + (T-T_o)\frac{\partial \rho}{\partial T}\Big|_o + \frac{(T-T_o)^2}{2!}\frac{\partial^2 \rho}{\partial T^2}\Big|_o + \text{---+Remainder.} \qquad (5)$$

Neglecting the second and higher order terms, yields:-

$$\rho(T) = \rho_o + (T-T_o)\frac{\partial \rho}{\partial T}\Big|_o \qquad (6)$$

The coefficient of cubic expansion of air β_o, at a reference temperature T_o can be expressed as (Ref.23):

$$\beta_o = \frac{-1}{\rho_o}\frac{\partial \rho}{\partial T}\Big|_o \qquad (7)$$

Therefore:

$$\rho(T) = \rho_o [1 - \beta_o(T - T_o)] \qquad (8)$$

From fig.2B, the components of the gravity vector in the x and y directions are given by:-

$$g_x = - g \operatorname{Sin}\Phi$$
$$g_y = - g \operatorname{Cos}\Phi \qquad (9)$$

Substitution from equations (8) and (9) into the momentum equations, gives:-

$$u\frac{\partial u}{\partial x} + v\frac{\partial u}{\partial y} = -\frac{1}{\rho_o}\frac{\partial p}{\partial x} + \frac{\mu}{\rho_o}\left(\frac{\partial^2 u}{\partial x^2} + \frac{\partial^2 u}{\partial y^2}\right) - g \operatorname{Sin}\Phi[1 - \beta_o(T - T_o)] \qquad (10)$$

$$u\frac{\partial v}{\partial x} + v\frac{\partial v}{\partial y} = -\frac{1}{\rho_o}\frac{\partial p}{\partial y} + \frac{\mu}{\rho_o}\left(\frac{\partial^2 v}{\partial x^2} + \frac{\partial^2 v}{\partial y^2}\right) - g \operatorname{Cos}\Phi[1 - \beta_o(T - T_o)] \qquad (11)$$

2.1.2 Non-dimensionlized equations.

The following dimensionless quantities are defined:

$$X = x/L$$
$$Y = y/L \qquad (12)$$
$$U = u\,L/\alpha$$
$$V = v\,L/\alpha$$

$$\theta = \frac{(T - T_c)}{(T_h - T_c)} \qquad (13)$$

$$P = p\,L^2/\rho\alpha^2 \qquad (14)$$

The reference temperature T_o, is defined as:-

$$T_o = (T_h + T_c)/2 \qquad (15)$$

This implies that:-

$$(T - T_o) = (T_h - T_c)(\theta - 1/2) \qquad (16)$$

By using the chain rule in differentiation (Ref.23) in conjunction with equation (12), the continuity equation can be shown to reduce to:-

$$\frac{\partial U}{\partial X} + \frac{\partial V}{\partial Y} = 0 \qquad (17)$$

Similarly, by using the chain rule in conjunction with equations (12) to (16), the momentum equation in the X-direction can be shown to be:-

$$\frac{\alpha^2}{L}\left(U\frac{\partial U}{\partial X} + V\frac{\partial U}{\partial Y}\right) = -\frac{\alpha\mu}{L^2\rho_o}\frac{\partial P}{\partial X} + \frac{\alpha\mu}{L^2\rho_o}\left(\frac{\partial^2 U}{\partial X^2} + \frac{\partial^2 U}{\partial Y^2}\right) - g\,\mathrm{Sin}\Phi\,[1 - \beta_o(T_h - T_c)(\theta - 1/2)] \qquad (18)$$

Multiplying both sides of equation 18 by $L^3\rho_o/\alpha\mu$, and noting that:-

$$\alpha\rho_o/\mu = Pr, \quad \rho_o/\alpha\mu = Pr/\nu^2 \text{ and } \beta_o g(T_h - T_c)L^3\,Pr/\nu^2 = Ra,$$

reduces the momentum equation in the X-direction to:-

$$\frac{1}{Pr}\left(U\frac{\partial U}{\partial X} + V\frac{\partial U}{\partial Y}\right) = -\frac{\partial P}{\partial X} + \nabla^2 U - \mathrm{Sin}\Phi\,[g\,L^3/\alpha\nu^2 - Ra(\theta - 1/2)] \qquad (19)$$

where $\nabla^2 = \left(\frac{\partial}{\partial X^2} + \frac{\partial}{\partial Y^2}\right)$

Following a similar procedure, the momemtum equation in the Y-direction becomes:-

$$\frac{1}{Pr}\left(U\frac{\partial V}{\partial X} + V\frac{\partial V}{\partial Y}\right) = -\frac{\partial P}{\partial Y} + \nabla^2 V - \text{Cos}\Phi[g\ L^3/\alpha\nu - \text{Ra}(\theta - 1/2)] \quad (20)$$

On application of the chain rule again in conjunction with equations (12), (13) and (16), reduces the energy equation to:-

$$U\frac{\partial\theta}{\partial X} + V\frac{\partial\theta}{\partial Y} = \frac{\partial^2\theta}{\partial X^2} + \frac{\partial^2\theta}{\partial Y^2} \quad (21)$$

2.1.3 Elimination of the pressure term from the momemtum equation.

Differentiating the momemtum equations in the X- and Y-directions with respect to Y and X respectively and noting that $\partial U/\partial X + \partial V/\partial Y = 0$ (from the continuity equation), reduces the two momemtum equations to:-

$$\frac{1}{Pr}\left(U\frac{\partial^2 U}{\partial X\partial Y} + V\frac{\partial^2 U}{\partial Y^2}\right) = -\frac{\partial^2 P}{\partial X\partial Y} + \frac{\partial(\nabla^2 U)}{\partial Y} + \text{Ra Sin}\Phi\frac{\partial\theta}{\partial Y} \quad (22)$$

$$\frac{1}{Pr}\left(U\frac{\partial^2 V}{\partial X^2} + V\frac{\partial^2 V}{\partial X\partial Y}\right) = -\frac{\partial^2 P}{\partial X\partial Y} + \frac{\partial(\nabla^2 V)}{\partial X} + \text{Ra Cos}\Phi\frac{\partial\theta}{\partial X} \quad (23)$$

Subtracting equation (23) from equation (22), reduces the momemtum equation to:-

$$\frac{1}{Pr}\left(U\frac{\partial^2 U}{\partial X\partial Y} + V\frac{\partial^2 U}{\partial Y^2} - U\frac{\partial^2 V}{\partial X^2} - V\frac{\partial^2 V}{\partial X\partial Y}\right) = \frac{\partial(\nabla^2 U)}{\partial Y} - \frac{\partial(\nabla^2 V)}{\partial X} + \text{Ra Sin}\Phi\frac{\partial\theta}{\partial Y} - \text{Cos}\Phi\frac{\partial\theta}{\partial X} \quad (24)$$

2.1.4 Introduction of the dimensionless stream and vorticity functions.

Physically, a stream function denotes the volume rate of flow per unit distance normal to the plane of motion between a streamline in the fluid and an arbitrary reference or base streamline. Whereas the vorticity denotes twice the mean angular velocity of the fluid particle. Stream and vorticity functions have dimensions of $[length]^2[time]^{-1}$ and $[time]^{-1}$ respectively. The dimensionless vorticity ω, and the stream function ψ, are defined as follows (Ref.25):-

$$U = \frac{\partial \Psi}{\partial Y} \quad \text{and} \quad V = -\frac{\partial \Psi}{\partial X} \tag{25}$$

$$\omega = \left(\frac{\partial V}{\partial X} - \frac{\partial U}{\partial Y}\right) = -\left(\frac{\partial^2 \Psi}{\partial X^2} + \frac{\partial^2 \Psi}{\partial Y^2}\right) \tag{26}$$

It should be noted that:

$\omega = \Omega L^2/\alpha$, where Ω is the dimensioned vorticity function.
$\Psi = \Psi/\alpha$, where Ψ is the dimensioned stream function.

Substitution of equation (25) and (26) into equation (24), reduces the momentum equation to:-

$$\frac{1}{Pr}\left(\frac{\partial \Psi}{\partial X}\cdot\frac{\partial \omega}{\partial Y} - \frac{\partial \Psi}{\partial Y}\cdot\frac{\partial \omega}{\partial X}\right) = -\nabla^2\omega + Ra\,Sin\Phi\frac{\partial \theta}{\partial Y} - Ra\,Cos\Phi\frac{\partial \theta}{\partial X} \tag{27}$$

Similarly, the energy equation reduces to:-

$$\nabla^2\theta = \frac{\partial \Psi}{\partial Y}\cdot\frac{\partial \theta}{\partial X} - \frac{\partial \Psi}{\partial X}\cdot\frac{\partial \theta}{\partial Y} \tag{28}$$

2.2. BOUNDARY CONDITIONS:

With reference to fig.3,
(i) The top cold surface and bottom hot surface are considered to be isothermal, i.e.

$$\begin{aligned} &\text{At } Y=0 \text{ and for all } X, \ \theta = 1.0 \\ &\text{At } Y=0 \text{ and for all } X_s, \ \theta_s = 1.0 \\ &\text{At } Y=1 \text{ and for all } X, \ \theta = 0 \\ &\text{At } Y=1 \text{ and for all } X_s, \ \theta_s = 0 \end{aligned} \tag{29}$$

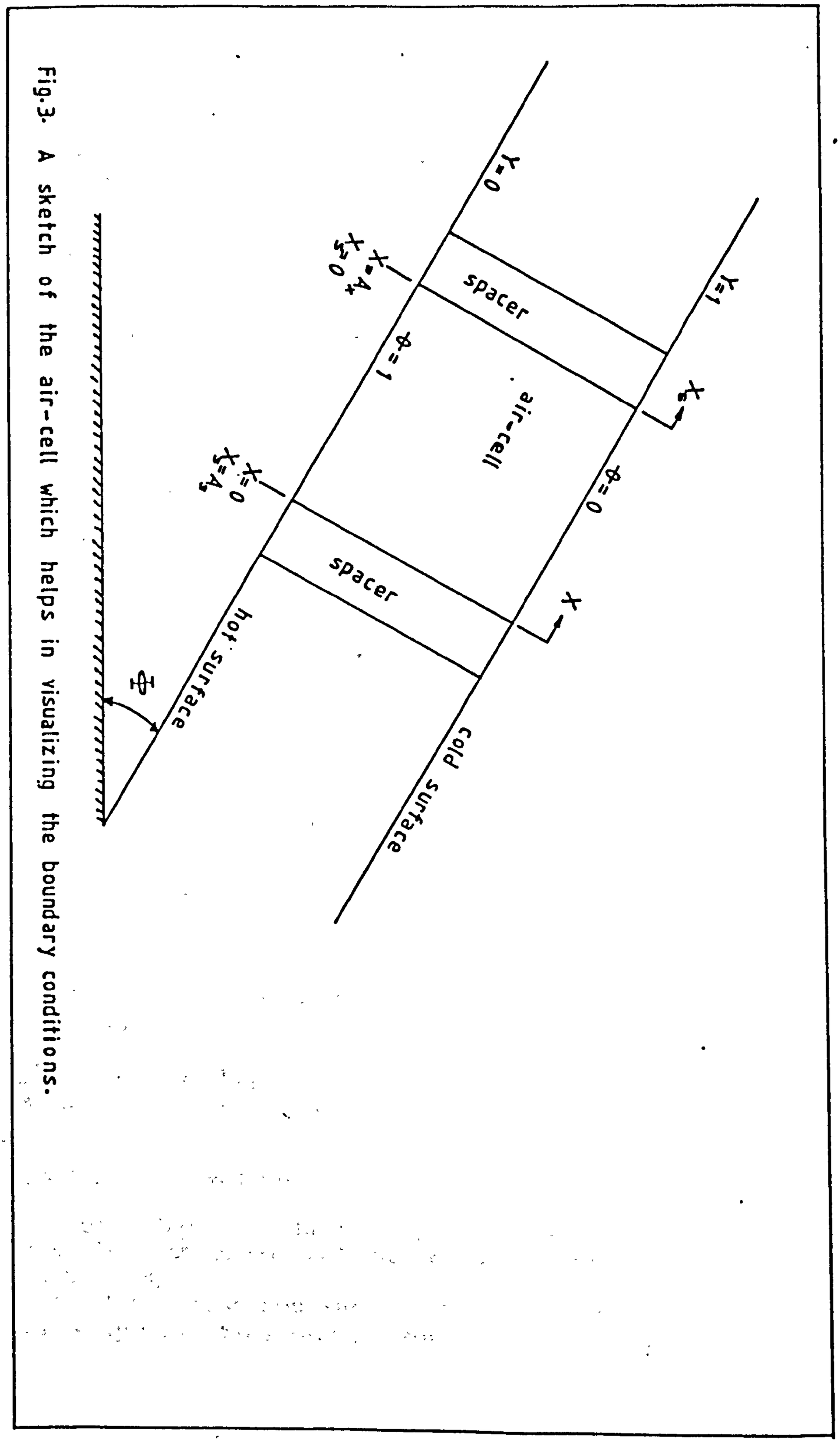

Fig.3. A sketch of the air-cell which helps in visualizing the boundary conditions.

(ii) The no-slip condition is imposed on all boundaries and no flow in or out of the boundaries, i.e.

At X=Ø for all Y, U = Ø and V = Ø
At $X=A_x$ for all Y, U =Ø and V = Ø (3Ø)
At Y=Ø for all X, U = Ø and V = Ø
At Y=1 for all X, U = Ø and V = Ø

(iii) The reference stream function is arbitrary and for convenience, is taken as zero on the boundaries.

(iV) Heat transfer between the air-cell and the spacer would occur because of the spacers finite thickness and finite value of thermal conductivity. To allow for this effect, the two-dimensional steady-state heat conduction equation, which is applicable to the spacers, has to be solved simultaneously with the cell equations, whilst matching the temperature and heat flux distributions at the boundaries between the two regions. the steady-state two-dimensional heat conduction equation can be expressed as:-

$$\frac{\partial^2 \theta_s}{\partial X_s^2} + \frac{\partial^2 \theta_s}{\partial Y^2} = \emptyset \qquad (31)$$

At the boundary between the spacer and the air, the matching of temperature distributions, gives:-

$$\theta_s\big|_{X_s=\emptyset} = \theta\big|_{X=A_x}$$

$$\theta_s\big|_{X_s=A_s} = \theta\big|_{X=\emptyset} \qquad (32)$$

Matching of the heat-flux distributions at the spacer and air boundary,gives:-

$$K_s \frac{\partial \theta_s}{\partial X_s}\Big|_{X_s=\emptyset} = K_a \frac{\partial \theta}{\partial X}\Big|_{X=A_x}$$

$$K_s \frac{\partial \theta_s}{\partial X_s}\Big|_{X_s=A_s} = K_a \frac{\partial \theta}{\partial X}\Big|_{X=\emptyset} \qquad (33)$$

However, two simplified thermal boundary conditions may be used depending on the thermal properties of the spacers (Ref.19,25 to 28).

(a) That of zero heat flux through the side boundaries, i.e. perfectly insulating spacer material. In this case,

$$\left.\frac{\partial \theta}{\partial X}\right|_{X=\emptyset} = \emptyset$$

$$\left.\frac{\partial \theta}{\partial X}\right|_{X=A_x} = \emptyset \qquad (34)$$

For brevity, this case will henceforth be referred to as the 'ZHF' case.
(b) That of a linear temperature gradient along the side boundaries,i.e. infinitely conducting spacers. In this case,

$$\theta(\emptyset,Y) = \theta(A_x,Y) = \theta_s(\emptyset,Y) = \theta_s(A_s,Y) = (1-Y) \qquad (35)$$

For brevity as well, this case will henceforth be referred to as the 'LTG' case.

2.3 HEAT TRANSFER:

A dimensionless quantity which indicates the convective heat transfer relative to that obtain by pure conduction, is the Nusselt number. For example, the Nusselt number on the hot bottom surface may be expressed as follows:-

$$Nu_h = h\,L/K_a \qquad (36)$$

$$\text{But } h(T_h - T_c) = -K_a \left.\frac{\partial T}{\partial Y}\right|_{Y=\emptyset}$$

Therefore,

$$h = \frac{-K_a}{(T_h - T_c)} \left.\frac{\partial T}{\partial Y}\right|_{Y=\emptyset} \qquad (37)$$

But $\theta = (T - T_c)/(T_h - T_c)$ and $Y = y/L$
Therefore,

$$\left.\frac{\partial T}{\partial Y}\right|_{Y=\emptyset} = \frac{(T_h - T_c)}{L} \left.\frac{\partial \theta}{\partial Y}\right|_{Y=\emptyset} \qquad (38)$$

Substitution from equation (38) into equation (37) and inserting the result in equation (36), yields:-

$$Nu_h = -\left.\frac{\partial \theta}{\partial Y}\right|_{Y=\emptyset} \qquad (39)$$

The average Nusselt number $\overline{Nu}_h$, is defined as follows:-

$$\overline{Nu}_h = \frac{1}{W}\int_0^W Nu_h\,dx \qquad (40)$$

But X = x/L. At x=Ø,X=Ø and at x=W,X=A_x.
Therefore:-

$$\overline{Nu_h} = -\frac{1}{A_x}\int_{\emptyset}^{A_x}\left.\frac{\partial\theta}{\partial Y}\right|_{Y=\emptyset} dX \qquad (41)$$

2.4 SUMMARY OF THE MATHEMATICAL EQUATIONS.

2.4.1 The air-cell:

(a) The stream function equation,

$$\frac{\partial^2\psi}{\partial X^2} + \frac{\partial^2\psi}{\partial Y^2} = -\omega \qquad (42)$$

(b) The vorticity equation,

$$\frac{1}{Pr}\left(\frac{\partial\psi}{\partial X}.\frac{\partial\omega}{\partial Y} - \frac{\partial\psi}{\partial Y}.\frac{\partial\omega}{\partial X}\right) = -\left(\frac{\partial^2\omega}{\partial X^2} + \frac{\partial^2\omega}{\partial Y^2}\right)$$

$$+ Ra\ Sin\Phi\frac{\partial\theta}{\partial Y} \qquad (43)$$

$$- Ra\ Cos\Phi\frac{\partial\theta}{\partial X}$$

(c) The temperature distribution equation,

$$\frac{\partial^2\theta}{\partial X^2} + \frac{\partial^2\theta}{\partial Y^2} = \frac{\partial\psi}{\partial Y}.\frac{\partial\theta}{\partial X} - \frac{\partial\psi}{\partial X}.\frac{\partial\theta}{\partial Y} \qquad (44)$$

2.4.2 The spacer:

The temperature distribution equation,

$$\frac{\partial^2\theta_s}{\partial X_s^2} + \frac{\partial^2\theta_s}{\partial Y^2} = \emptyset \qquad (45)$$

2.4.3 Boundary conditions.

$$\theta(X,\emptyset) = \theta_s(X_s,\emptyset) = 1$$

$$\theta(X,1) = \theta_s(X_s,1) = \emptyset \qquad (46)$$

$$U = V = \psi = \emptyset \text{ on all boundaries.} \qquad (47)$$

For the real spacer,

$$K_s \left.\frac{\partial \theta_s}{\partial X_s}\right|_{X_s=\emptyset} = K_a \left.\frac{\partial \theta}{\partial X}\right|_{X=A_x}$$

$$K_s \left.\frac{\partial \theta_s}{\partial X_s}\right|_{X_s=A_s} = K_a \left.\frac{\partial \theta}{\partial X}\right|_{X=\emptyset} \qquad (48)$$

$$\left.\theta_s\right|_{X_s=\emptyset} = \left.\theta\right|_{X=A_x}$$

$$\left.\theta_s\right|_{X_s=A_s} = \left.\theta\right|_{X=\emptyset} \qquad (49)$$

For the LTG case:

$$\theta(\emptyset,Y)=\theta_s(\emptyset,Y)=\theta(A_x,Y)=\theta_s(A_s,Y)=1-Y \qquad (50)$$

For the ZHF case:

$$\left.\frac{\partial \theta}{\partial X}\right|_{X=\emptyset} = \left.\frac{\partial \theta}{\partial X}\right|_{X=A_x} = \emptyset \qquad (51)$$

2.4.4. Heat transfer:

The local Nusselt number on the hot surface,

$$Nu_h = - \left.\frac{\partial \theta}{\partial Y}\right|_{Y=\emptyset} \qquad (52)$$

The average Nusselt number on the hot surface,

$$\overline{Nu}_h = -\frac{1}{A_x} \int_0^{A_x} \left.\frac{\partial \theta}{\partial Y}\right|_{Y=\emptyset} dX \qquad (53)$$

These governing equations form a system of coupled differential equations in ψ, θ and ω. If they can be solved simultaneously in conjunction with the boundary conditions, then the temperature gradients at the surfaces may be evaluated, from which the Nusselt numbers can be obtained. An inspection of the equations show that the Nusselt number will depend upon the following parameters:-

(i) The Rayleigh number, Ra.
(ii) The tilt-angle, Φ.
(iii) The air-cell aspect ratio, A_x.
(iv) The spacer aspect ratio, A_s.
(v) The thermal conductivity of the spacer material, K_s.
(vi) The thermal conductivity of the air, K_a.

CHAPTER THREE

THE NUMERICAL MODEL

3.1 GENERAL METHODOLOGY.

The regular shape of the slatted-CSD system facilitated the use of the finite-difference methods in seeking the solutions of the governing equations, which form a system of coupled differential equations in ψ , θ and ω. The region of solution is broken up into a finite number of grid-points. The derivatives are then approximated by finite-differences, resulting in a number of algebraic equations, which can be solved by successive iterations.

3.2 THE GRID SYSTEM.

In applying the finite-difference methods, the region of solution is broken up into a finite number of spaced lines, forming a rectangular grid system. The intersections of these mutually perpendicular lines are referred to as grid-points. The suffixes i or k and j have been used to denote the vertical and horizontal lines respectively—see fig.4. Grid-points are therefore easily identified using these suffixes. With reference to fig.4., for NDX, NDY and NDX_s grid divisions taken within the X, Y and X_s axes, there will exist correspondingly (NDX+1), (NDY+1) and (NDX_s +1) grid-points. The corresponding grid sizes will therefore be:-

$$\Delta X = \frac{A_x}{NDX} \quad , \Delta Y = \frac{1}{NDY} \quad \text{and} \quad \Delta X_s = \frac{A_s}{NDX} \tag{54}$$

Because the zero datum of X, Y and X_s axes are taken as i=2, j=1 and k=2, then correspondingly:-

$$N=(NDX+2), \; M=(NDY+1) \text{ and } Ns=(NDX_s+2) \tag{55}$$

The reason for taking the datum of suffixes i and k as 2 will be made clear later.

3.3 FINITE-DIFFERENCE APPROXIMATIONS.

3.3.1 Basic finite-difference formulae.

The basic principle in establishing a finite-difference approximation to a derivative of a dependent variable at a

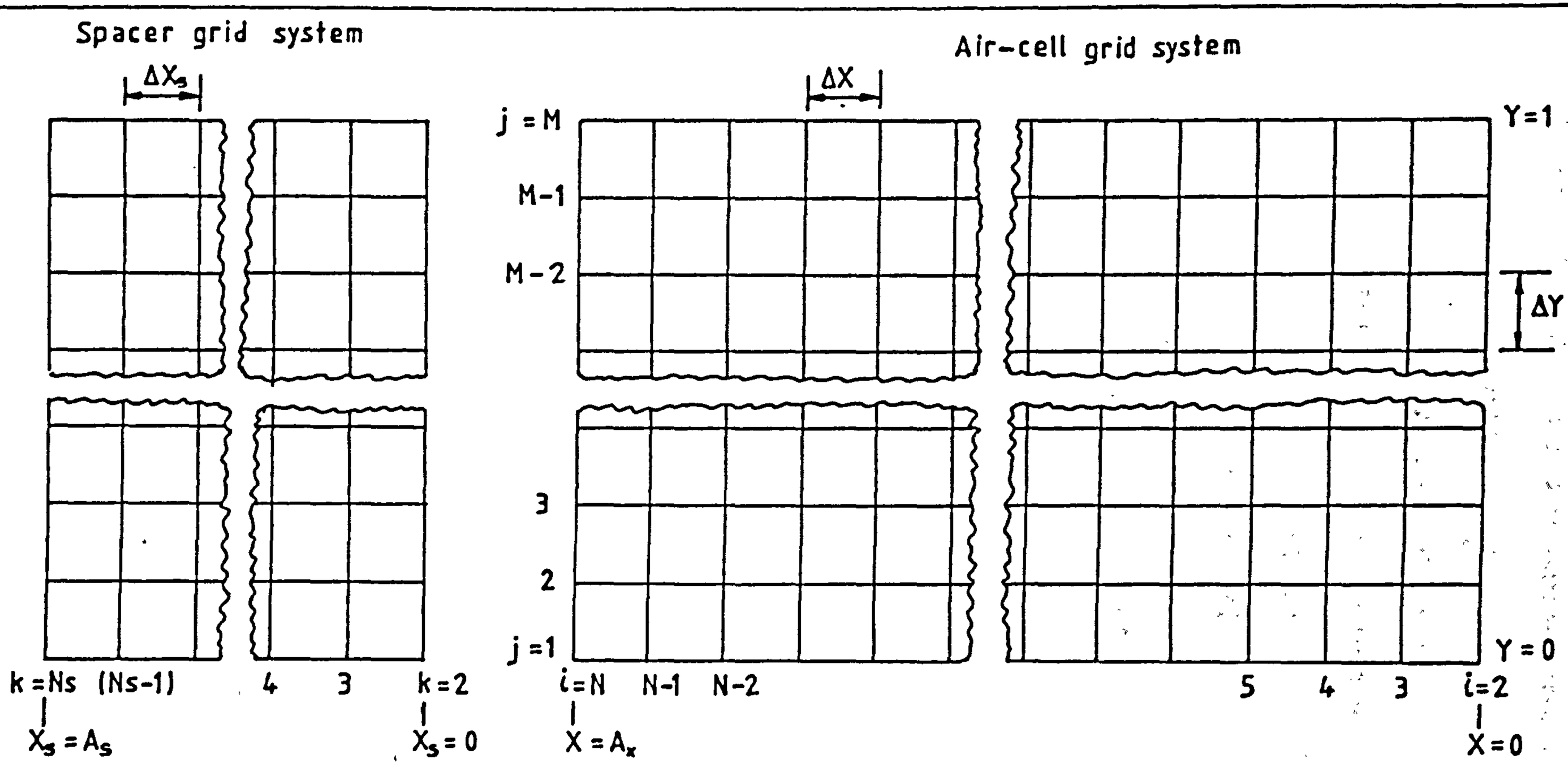

Fig.4. The grid system

point, is the application of a Taylor's series expansion at the value of that variable in the vicinity of that point. For brevity, however, the general finite-difference approximations for first and second order derivatives, which are of interest in this study, are presented as follows (Ref.29):-

(i) The two-point forward-difference approximations:

$$D_x C_{ij} = [C_{i+1j} - C_{ij}]/\Delta X \quad + O(\Delta X)$$
$$D_Y C_{ij} = [C_{ij+1} - C_{ij}]/\Delta Y \quad + O(\Delta Y) \qquad (56)$$

where C is used to denote any variable, whereas D denotes the first order derivatives with respect to X and Y. The symbol O, denotes the order of magnitude of the error in the approximation.

(ii) The two-point backward-difference approximation:

$$D_x C_{ij} = [C_{ij} - C_{i-1j}]/\Delta X \quad + O(\Delta X)$$
$$D_Y C_{ij} = [C_{ij} - C_{ij-1}]/\Delta Y \quad + O(\Delta Y) \qquad (57)$$

(iii) The two-point central-difference approximation:

$$D_x C_{ij} = [C_{i+1j} - C_{i-1j}]/2\Delta X \quad + O(\Delta X)^2$$
$$D_Y C_{ij} = [C_{ij+1} - C_{ij-1}]/2\Delta Y \quad + O(\Delta Y)^2 \qquad (58)$$

(iv) The three-point forward-difference approximation:

$$D_x C_{ij} = [-3\,C_{ij} + 4\,C_{i+1j} - C_{i+2j}]/2\Delta X \quad + O(\Delta X)^2$$
$$D_Y C_{ij} = [-3\,C_{ij} + 4\,C_{ij+1} - C_{ij+2}]/2\Delta Y \quad + O(\Delta Y)^2 \qquad (59)$$

(v) The three-point backward-difference approximation:

$$D_x C_{ij} = [3\,C_{ij} - 4\,C_{i-1j} + C_{i-2j}]/2\Delta X \quad + O(\Delta X)^2$$
$$D_Y C_{ij} = [3\,C_{ij} - 4\,C_{ij-1} + C_{ij-2}]/2\Delta Y \quad + O(\Delta Y)^2 \qquad (60)$$

(vi) The three-point central-difference approximation:

$$D_X^2 C_{ij} = [C_{i+1j} - 2\,C_{ij} + C_{i-1j}]/(\Delta X)^2 \quad + O(\Delta X)^2$$
$$D_Y^2 C_{ij} = [C_{ij+1} - 2\,C_{ij} + C_{ij-1}]/(\Delta Y)^2 \quad + O(\Delta Y)^2 \qquad (61)$$

where D^2 denotes the second-order derivative with respect to X or Y.

3.3.2 Approximations for the stream function.

A method originally developed by Greenspan (Ref.29) and later adopted by David (Ref.26), is used here for approximating the stream function. At grid-points a distance ΔX and ΔY away from the boundaries, a three-point forward- or backward-difference approximation is used. Whereas a central-difference scheme is used for the other central grid-points.

(i) Approximations at the grid-points which are a distance ΔX and ΔY away from the boundaries.

For grid-points at a distance ΔX from the boundary, defined by X=Ø for all Y, the three-point forward- difference approximation is used, to give:-

$$D_x \psi_{2,j} = (4\psi_{3,j} - \psi_{4,j} - 3\psi_{2,j}) \qquad (62)$$

Because $\psi_{2,j}$ and $D_x\psi_{2,j}$ are both equal to zero at the boundary, then:-

$$\psi_{2,j} = 1/4\ \psi_{4,j} \qquad (63)$$

For grid-points at a distance ΔX away from the boundary, defined by $X=A_x$ for all Y, the three-point backward-difference approximation is used, to give:-

$$D_x \psi_{N,j} = (\psi_{N-2,j} - 4\psi_{N-1,j} + 3\psi_{N,j}) \qquad (64)$$

Because $\psi_{N,j}$ and $D_x\psi_{N,j}$ are both equal to zero on the boundary, then:-

$$\psi_{N-1,j} = 1/4\ \psi_{N-2,j} \qquad (65)$$

Similarly, for grid-points at a distance ΔY from the boundary, defined by Y=Ø for all X,

$$\psi_{i,2} = 1/4\ \psi_{i,3} \qquad (66)$$

Whereas, for grid-points at a distance ΔY from the boundary defined by Y=1 for all X,

$$\psi_{i,M-1} = 1/4\ \psi_{i,M-2} \qquad (67)$$

(ii) Approximations at central grid-points.
By using the three-point central-difference approximation,

we have:-

$$D_x^2 \psi_{i,j} = (\psi_{i+1,j} - 2\psi_{i,j} + \psi_{i-1,j})/(\Delta x)^2 \qquad (68)$$

$$D_Y^2 \psi_{i,j} = (\psi_{i,j+1} - 2\psi_{i,j} + \psi_{i,j-1})/(\Delta Y)^2 \qquad (69)$$

Substitution from equations (68) and (69) into the stream function equation, i.e. equation (42), and solving for , gives:-

$$\psi_{i,j} = \frac{(\psi_{i+1,j} + \psi_{i-1,j} + (\psi_{i,j+1} + \psi_{i,j-1})r^2 + \omega_{i,j}(\Delta x)^2)}{2\ (1 + r^2)} \qquad (70)$$

where, $r = \Delta X/\Delta Y$

If ω, ΔX and ΔY are assumed to be known quantities, then equation (70) sets up a system of simultaneous equations in ψ, which can be solved by successive iterations. If the most recent values of ψ are used on the right hand side, then the solution procedure is the Gauss-Siedel iteration method (Ref.30). However, convergence of the solutions can be enhanced by using the successive over-relaxation method, i.e.,

$$\psi_{i,j}^m = \psi_{i,j}^{m-1} + B(\psi'_{i,j} - \psi_{i,j}^{m-1}) \qquad (71)$$

where, $\psi'_{i,j}$ is the most recent value evaluated from equation (70). B is the relaxation factor which is known to lie between 1 and 2 (Ref.30).

3.3.3 Approximations for the temperature-distribution function.

In order to maintain diagonal dominance and thus have convergence of the solutions, a method by Greenspan (Ref.29) is used here as well. The method employs the central-difference schemes in approximating the folowing derivatives:-
$D_x^2\theta$, $D_Y^2\theta$, $D_x\psi$ and $D_Y\psi$.
Whereas, depending on the signs of γ and δ (which are defined in equation (74)), the two-point backward- or forward-difference scheme is employed in approximating the followings:-
$D_x\theta$ and $D_Y\theta$.

Using the three-point central-difference scheme, we have:-

$$\Delta_x^2 \theta_{i,j} = (\theta_{i+1,j} - 2\theta_{i,j} + \theta_{i-1,j})/(\Delta x)^2$$

$$\Delta_Y^2 \theta_{i,j} = (\theta_{i,j+1} - 2\theta_{i,j} + \theta_{i,j-1})/(\Delta Y)^2 \qquad (72)$$

Using the two-point central-difference scheme, we have:-

$$\Delta_x \psi_{i,j} = (\psi_{i+1,j} - \psi_{i-1,j})/2(\Delta x)$$

$$\Delta_Y \psi_{i,j} = (\psi_{i,j+1} - \psi_{i,j-1})/2(\Delta Y) \qquad (73)$$

The quantities γ and δ are defined as follows:-

$$\gamma = (\psi_{i+1,j} - \psi_{i-1,j})$$

$$\delta = (\psi_{i,j+1} - \psi_{i,j-1}) \qquad (74)$$

(i) For $\gamma \geq 0$ and $\delta \geq 0$.

$\Delta_x\theta$ is approximated using the two-point backward-difference scheme, whereas $\Delta_Y\theta$ is approximated using the two-point forward-difference scheme, to give:-

$$\Delta_x \theta_{i,j} = (\theta_{i,j} - \theta_{i-1,j})/\Delta x$$

$$\Delta_Y \theta_{i,j} = (\theta_{i,j+1} - \theta_{i,j})/\Delta Y \qquad (75)$$

Substitution from equations (72) to (75) into the temperature- distribution equation, i.e. equation (44) and solving for $\theta_{i,j}$, gives:-

$$\theta_{i,j} = \frac{\left[\begin{array}{l} 2(\theta_{i+1,j} + \theta_{i-1,j}) + 2r^2(\theta_{i,j+1} + \theta_{i,j-1}) \\ + r(\delta\,\theta_{i-1,j} + \gamma\,\theta_{i,j+1}) \end{array}\right]}{[4(1 + r^2) + r(\delta + \gamma)]} \qquad (76)$$

(ii) For $\gamma < 0$ and $\delta < 0$.

$\Delta_x\theta$ is approximated using the two-point forward-difference scheme, whereas $\Delta_Y\theta$ is approximated using the two-point backward-difference scheme, to yield:-

$$\Delta_x \theta_{i,j} = (\theta_{i+1,j} - \theta_{i,j})/\Delta x$$

$$\Delta_Y \theta_{i,j} = (\theta_{i,j} - \theta_{i,j-1})/\Delta Y. \qquad (77)$$

Substitution from equations (72) to (74) and equation (77), into equation (44) and solving for $\theta_{i,j}$, gives:-

$$\theta_{i,j} = \frac{\left[\begin{array}{l} 2(\theta_{i+1,j} + \theta_{i-1,j}) + 2r^2(\theta_{i,j+1} + \theta_{i,j-1}) \\ -r(\delta\theta_{i+1,j} + \gamma\theta_{i,j-1}) \end{array}\right]}{[4(1 + r^2) - r(\delta + \gamma)]} \qquad (78)$$

(iii) For $\gamma \geq 0$ and $\delta < 0$.

Both $D_x\theta$ and $D_Y\theta$ are approximated by using the two-point forward-difference scheme, to give:-

$$D_x\theta_{i,j} = (\theta_{i+1,j} - \theta_{i,j})/\Delta x$$

$$D_Y\theta_{i,j} = (\theta_{i,j+1} - \theta_{i,j})/\Delta Y \qquad (79)$$

Substitution from equations (72) to (74) and equation (79), into equation (44) and solving for $\theta_{i,j}$, gives:-

$$\theta_{i,j} = \frac{\left[\begin{array}{l} 2(\theta_{i+1,j} + \theta_{i-1,j}) + 2r^2(\theta_{i,j+1} + \theta_{i,j-1}) \\ -r(\delta\theta_{i+1,j} - \gamma\theta_{i,j+1}) \end{array}\right]}{[4(1 + r) - r(\delta - \gamma)]} \qquad (80)$$

(iv) For $\gamma < 0$ and ≥ 0.

Both $D_x\theta$ and $D_Y\theta$ are approximated by using the two-point backward-difference scheme, to give:-

$$D_x\theta_{i,j} = (\theta_{i,j} - \theta_{i-1,j})/\Delta x$$

$$D_Y\theta_{i,j} = (\theta_{i,j} - \theta_{i,j-1})/\Delta Y \qquad (81)$$

Substitution from equations (72) to (74) and equation (81), into equation (44) and solving for $\theta_{i,j}$, gives:-

$$\theta_{i,j} = \frac{\left[\begin{array}{l} 2(\theta_{i+1,j} + \theta_{i-1,j}) + 2r^2(\theta_{i,j+1} + \theta_{i,j-1}) \\ +r(\delta\theta_{i-1,j} - \gamma\theta_{i,j-1}) \end{array}\right]}{[4(1 + r^2) + r(\delta - \gamma)]} \qquad (82)$$

It should be noted that in all these cases, the successive over-relaxation method also applies, i.e.,

$$\theta^m_{i,j} = \theta^{m-1}_{i,j} + B(\theta'_{i,j} - \theta^{m-1}_{i,j}) \qquad (83)$$

where $\theta'_{i,j}$ is the most recent value evaluated from amongst equations (76), (78), (80) and (82), depending on the signs of γ and δ.

3.3.4 Approximations for the vorticity function at the interior grid-points.

For the same reason as applied when approximating the temperature- distribution function, the following derivatives are approximated using the central- difference scheme:-
$D_x^2\omega$, $D_Y^2\omega$, $D_x\theta$, $D_Y\theta$, $D_x\psi$ and $D_Y\psi$.
Whereas, depending on the signs of γ and δ, the forward- or the backward- difference is used in approximating the followings:-
$D_x\omega$ and $D_Y\omega$.

Using the three-point central-difference scheme, the following approximations apply:-

$$D_x^2\omega_{i,j} = (\omega_{i+1,j} - 2\omega_{i,j} + \omega_{i-1,j})/(\Delta x)^2$$

$$D_Y^2\omega_{i,j} = (\omega_{i,j+1} - 2\omega_{i,j} + \omega_{i,j-1})/(\Delta Y)^2 \qquad (84)$$

Using the two-point central-difference scheme, the following approximations apply as well:-

$$D_x\psi_{i,j} = (\psi_{i+1,j} - \psi_{i-1,j})/2\Delta x$$
$$D_Y\psi_{i,j} = (\psi_{i,j+1} - \psi_{i,j-1})/2\Delta Y$$
$$D_x\theta_{i,j} = (\theta_{i+1,j} - \theta_{i-1,j})/2\Delta x \qquad (85)$$
$$D_Y\theta_{i,j} = (\theta_{i,j+1} - \theta_{i,j-1})/2\Delta Y$$

(i) For $\gamma \geq 0$ and $\delta \geq 0$.

$D_x\omega$ is approximated by using the two-point backward-difference scheme, whereas $D_Y\omega$ is approximated by using the two-point forward- difference scheme, to give:-

$$D_x\omega_{i,j} = (\omega_{i,j} - \omega_{i-1,j})/\Delta x$$

$$D_Y\omega_{i,j} = (\omega_{i,j+1} - \omega_{i,j})/\Delta Y \qquad (86)$$

Substitution from equations (84) to (86) into the vorticity equation, i.e. equation (43) and solving for $\omega_{i,j}$, gives:-

$$\omega_{i,j} = \frac{\left[\begin{array}{l} 2(\omega_{i+1,j} + \omega_{i-1,j}) + 2r^2(\omega_{i,j+1} + \omega_{i,j-1}) \\ +Ra\,Cos\Phi(\theta_{i+1,j} - \theta_{i-1,j})\Delta x - Ra\,Sin\Phi(\theta_{i,j+1} - \theta_{i,j-1})r\Delta x \\ +r/Pr(\gamma\omega_{i,j+1} + \delta\omega_{i-1,j}). \end{array}\right]}{[4(1 + r^2) + r/Pr(\delta + \gamma)]} \qquad (87)$$

(ii) For $\gamma < 0$ and $\delta < 0$.

$D_x\omega$ is approximated by using the two-point forward-difference scheme, Whereas $D_y\omega$ is approximated by using the two-point backward- difference scheme, to give:-

$$D_x\omega_{i,j} = (\omega_{i+1,j} - \omega_{i,j})/\Delta x$$

$$D_y\omega_{i,j} = (\omega_{i,j} - \omega_{i,j-1})/\Delta y \qquad (88)$$

Substitution from equations (84), (85) and (88) into equation (43) and solving for $\omega_{i,j}$, gives:-

$$\omega_{i,j} = \frac{\left[\begin{array}{l} 2(\omega_{i+1,j} + \omega_{i-1,j}) + 2r^2(\omega_{i,j+1} + \omega_{i,j-1}) \\ + Ra\cos\Phi(\theta_{i+1,j} - \theta_{i-1,j})\Delta x - Ra\sin\Phi(\theta_{i,j+1} - \theta_{i,j-1})r\Delta x \\ - r/Pr(\gamma\omega_{i,j-1} + \delta\omega_{i+1,j}) \end{array}\right]}{[4(1 + r^2) - r/Pr(\delta + \gamma)]} \qquad (89)$$

(iii) For $\gamma \geq 0$ and $\delta < 0$.

$D_x\omega$ and $D_y\omega$ are both approximated by using the two-point forward- difference scheme, to give:-

$$D_x\omega_{i,j} = (\omega_{i+1,j} - \omega_{i,j})/\Delta x$$

$$D_y\omega_{i,j} = (\omega_{i,j+1} - \omega_{i,j})/\Delta y \qquad (90)$$

Substitution from equations (84), (85) and (90) into equation (43) and solving for $\omega_{i,j}$, gives:-

$$\omega_{i,j} = \frac{\left[\begin{array}{l} 2(\omega_{i+1,j} + \omega_{i-1,j}) + 2r^2(\omega_{i,j+1} + \omega_{i,j-1}) \\ + Ra\cos\Phi(\theta_{i+1,j} - \theta_{i-1,j})\Delta x - Ra\sin\Phi(\theta_{i,j+1} - \theta_{i,j-1})r\Delta x \\ + r/Pr(\gamma\omega_{i,j+1} - \delta\omega_{i+1,j}) \end{array}\right]}{[4(1 + r^2) - r/Pr(\delta - \gamma)]} \qquad (91)$$

(iv) For $\gamma < 0$ and $\delta \geq 0$.

Both $D_x\omega$ and $D_y\omega$ are approximated by using the two-point backward- difference scheme, to give:-

$$D_x\omega_{i,j} = (\omega_{i,j} - \omega_{i-1,j})/\Delta x$$

$$D_y\omega_{i,j} = (\omega_{i,j} - \omega_{i,j-1})/\Delta y \qquad (92)$$

Substitution from equations (84), (85) and (92) into equation (43) and solving for $\omega_{i,j}$, gives:-

$$\omega_{i,j} = \frac{\boxed{\begin{array}{l} 2(\omega_{i+1,j} + \omega_{i-1,j}) + 2r^2(\omega_{i,j+1} + \omega_{i,j-1}) \\ + Ra\cos\Phi(\theta_{i+1,j} - \theta_{i-1,j})\Delta x - Ra\sin\Phi(\theta_{i,j+1} - \theta_{i,j-1})r\Delta x \\ - r/Pr(\gamma\omega_{i,j-1} - \delta\omega_{i-1,j}) \end{array}}}{[4(1 + r^2) + r/Pr(\delta - \gamma)]} \qquad (93)$$

By applying the successive over-relaxation method, we have:-

$$\omega^m_{i,j} = \omega^{m-1}_{i,j} + B(\omega'_{i,j} - \omega^{m-1}_{i,j}) \qquad (94)$$

where $\omega'_{i,j}$ is the most recent value. This emerges from amongst equations (87), (89), (91) and (93), depending on the signs of γ and σ.

3.3.5 Approximations to the vorticity function at the boundaries.

The vorticity function at the boundaries is not as well defined as the stream function. However, it is approximated as follows:-

(i) At the boundary defined by X=Ø for all Y, $\psi_{4,j}$ and $\psi_{3,j}$ can be expanded in a Taylor series about $\psi_{2,j}$ as follows:-

$$\psi_{4,j} = \psi_{2,j} + (2\Delta x)D_x\psi_{2,j} + \frac{(2\Delta x)^2}{2!}D_x^2\psi_{2,j} + \frac{(2\Delta x)^3}{3!}D_x^3\psi_{2,j} + O(\Delta x)^4 \qquad (95)$$

$$\psi_{3,j} = \psi_{2,j} + (\Delta x)D_x\psi_{2,j} + \frac{(\Delta x)^2}{2!}D_x^2\psi_{2,j} + \frac{(\Delta x)^3}{3!}D_x^3\psi_{2,j} + O(\Delta x)^4 \qquad (96)$$

However, the no-slip boundary condition imposed at the boundaries means that, $D_x\psi_{2,j} = Ø$. By definition $\psi_{2,j} = Ø$. Therefore, equations (95) and (96) reduce to:-

$$\psi_{4,j} = \frac{(2\Delta x)^2}{2!}D_x^2\psi_{2,j} + \frac{(2\Delta x)^3}{3!}D_x^3\psi_{2,j} + O(\Delta x)^4 \qquad (97)$$

$$\psi_{3,j} = \frac{(\Delta x)^2}{2!}D_x^2\psi_{2,j} + \frac{(\Delta x)^3}{3!}D_x^3\psi_{2,j} + O(\Delta x)^4 \qquad (98)$$

Multiplying equation (98) by 8 and subtracting from equation (97), gives:-

$$D_x^2\psi_{2,j} = (8\psi_{3,j} - \psi_{4,j})/2(\Delta x)^2 + O(\Delta x)^2 \qquad (99)$$

But from the stream function equation,

$$\omega_{2,j} = -\left(\delta_x^2 \psi_{2,j} + \delta_Y^2 \psi_{2,j}\right) \qquad (100)$$

Because $\psi = \emptyset$ for all Y along this boundary, then $\delta_Y^2 \psi_{2,j} = \emptyset$. Therefore:-

$$\omega_{2,j} = -\delta_x^2 \psi_{2,j} = \left(\psi_{4,j} - 8\psi_{3,j}\right)/2(\Delta x)^2 \qquad (101)$$

Using a similar analysis, the vorticity function at the following boundaries are approximated as follows:

(ii) At the boundary defined by $X = A_x$ for all Y:-

$$\omega_{N,j} = \left(\psi_{N-2,j} - 8\psi_{N-1,j}\right)/2(\Delta x)^2 \qquad (102)$$

(iii) At the boundary defined by $Y = \emptyset$ for all X:-

$$\omega_{i,1} = \left(\psi_{i,3} - 8\psi_{i,2}\right)/2(\Delta Y)^2 \qquad (103)$$

(iv) At the boundary defined by Y=1 for all X:-

$$\omega_{i,M} = \left(\psi_{i,M-2} - 8\psi_{i,M-1}\right)/2(\Delta Y)^2 \qquad (104)$$

3.3.6 Approximation for the temperature-distribution function in the spacer.

Using the three-point central-difference scheme, we have:-

$$\delta_{x_s}^2 \theta_{sK,j} = \left(\theta_{sK+1,j} - 2\theta_{sK,j} + \theta_{sK-1,j}\right)/(\Delta x_s)^2$$
$$\delta_Y^2 \theta_{sK,j} = \left(\theta_{sK,j+1} - 2\theta_{sK,j} + \theta_{sK,j-1}\right)/(\Delta Y)^2 \qquad (105)$$

Substitution from equation (105) in the steady-state heat conduction equation, i.e. equation (44) and solving for $\theta_{sK,j}$, gives:-

$$\theta_{sK,j} = \frac{\left\{\theta_{sK+1,j} + \theta_{sK-1,j} + r_s^2\left(\theta_{sK,j+1} + \theta_{sK,j-1}\right)\right\}}{\left[2(1 + r_s^2)\right]} \qquad (106)$$

where $r_s = \Delta X_s / \Delta Y$.
On the application of the successive over-relaxation method, we have:-

$$\theta^m_{sk,j} = \theta^{m-1}_{sk,j} + B(\theta'_{sk,j} - \theta^{m-1}_{sk,j}) \qquad (107)$$

where $\theta'_{sk,j}$ is the most recent value evaluated from equation (106).

3.3.7 Approximation for the temperature-distribution function at the spacer and air interface.

(i) If the temperature distribution is assumed to be linear, i.e. the spacers assumed to be made of a perfectly thermally-conducting material, then from equation (50),

$$\theta_{2,j} = \theta_{N,j} = [1 - (j - 1)\Delta Y] \qquad (108)$$

(ii) If no heat is assumed to cross the spacers, i.e. zero heat flux condition, then from equation (51),

$$D_x\theta_{2,j} = D_x\theta_{N,j} = 0 \qquad (109)$$

Using the three-point forward-difference scheme, we have:-

$$D_x\theta_{2,j} = (4\theta_{3,j} - \theta_{4,j} - 3\theta_{2,j})/2(\Delta x) \qquad (110)$$

But $D_x\theta_{2,j} = 0$. Therefore:

$$\theta_{2,j} = (4\theta_{3,j} - \theta_{4,j})/3.0 \qquad (111)$$

Similarly, using the three-point backward-difference scheme, we have:-

$$D_x\theta_{N,j} = (\theta_{N-2,j} - 4\theta_{N-1,j} + 3\theta_{N,j})/2(\Delta x) \qquad (112)$$

But $D_x\theta_{N,j} = 0$. Therefore:-

$$\theta_{N,j} = (4\theta_{N-1,j} - \theta_{N-2,j})/3.0 \qquad (113)$$

(iii) For the real spacer, a method used by Koutsoheras (Ref.19) and Meyer (Ref.22) is adopted in order to approximate the heat-flux boundary equation, i.e. equation (48). It involves the calculation of fictitious temperatures at each end of the spacer corresponding to k=1 and k=(Ns+1). This then enables the calculation of $\theta_{s2,j}$ and $\theta_{sNs,j}$ from equation (107). By matching the temperature distribution at the boundaries, we then have:-

$$\theta_{2,j} = \theta_{sNk,j}$$

$$\theta_{N,j} = \theta_{s2,j} \qquad (114)$$

The fictitious temperatures are obtained as follows:-
By using the two-point central-difference scheme, we have:-

$$\Delta_{xs}\theta_{s2,j} = (\theta_{s3,j} - \theta_{s1,j})/2(\Delta x_s) \qquad (115)$$

By using the three-point backward-difference scheme, we have:-

$$\Delta_x \theta_{N,j} = (\theta_{N-2,j} - 4\theta_{N-1,j} + 3\theta_{N,j})/2(\Delta x) \qquad (116)$$

Substitution from equation (115) and (116) into equation (48) and solving for $\theta_{s1,j}$, gives:-

$$\theta_{s1,j} = \theta_{s3,j} + F(4\theta_{N-1,j} - \theta_{N-2,j} - 3\theta_{N,j}) \qquad (117)$$

where $F = (K_a \Delta X_s / K_s \Delta X)$. This parameter F, will later be shown to characterize the thermal properties of the spacer. It is also referred to as the cell coupling factor because it couples the heat transfer between the spacers and the air-cell.
Similarly, by using the two-point central-difference scheme in conjunction with the three-point central-difference scheme, it can be shown that:-

$$\theta_{sNs+1,j} = \theta_{sNs-1,j} + F(4\theta_{3,j} - \theta_{4,j} - 3\theta_{2,j}) \qquad (118)$$

However, when F is greater than or equal to unity, this method leads to instabilities and the solutions diverge. In this situation, fictitious temperatures corresponding to $\theta_{1,j}$ and $\theta_{N+1,j}$ are calculated. The boundary temperatures $\theta_{2,j}$ and $\theta_{N,j}$ can then be calculated using equation (82), depending on the signs of γ and σ. The fictitious temperatures are obtained as follows:-
By using the three-point backward-difference scheme, we have:-

$$\Delta_{xs}\theta_{sNs,j} = (\theta_{sNs-2,j} - 4\theta_{sNs-1,j} + 3\theta_{sNs,j})/2(\Delta x_s) \qquad (119)$$

By using the two-point central-difference scheme, we have:-

$$\Delta_x \theta_{2,j} = (\theta_{3,j} - \theta_{1,j})/2\Delta x \qquad (120)$$

Substitution from equations (119) and (120) into equation (48) and solving for $\theta_{1,j}$, gives:-

$$\theta_{1,j} = \theta_{3,j} + (4\theta_{sNs-1,j} - \theta_{sNs-2,j} - 3\theta_{sNs,j})/F \qquad (121)$$

Similarly, by using the three-point forward-difference scheme in conjunction with the two-point central-difference scheme, it can be shown that:-

$$\theta_{N+1,j} = \theta_{N-1,j} + (4\theta_{s3,j} - \theta_{s4,j} - 3\theta_{s2,j})/F \qquad (122)$$

It should now be clear why the zero datum of suffixes i and k were taken as 2.

3.3.8 Approximation for the Nusselt number on the hot surface.

From equation (52), the local Nusselt number on the hot surface is expressed as:-

$$Nu_h = -\left.\frac{\partial\theta}{\partial Y}\right|_{Y=0}$$

At the hot surface, j=1. Therefore:-

$$Nu_{i,1} = -\frac{\partial\theta_{i,1}}{\partial Y} \qquad (123)$$

By using the three-point forward-difference scheme, we have:-

$$\Delta_Y\theta_{i,1} = (4\theta_{i,2} - \theta_{i,3} - 3\theta_{i,1})/2\Delta Y \qquad (124)$$

Therefore:

$$Nu_{i,1} = [3\theta_{i,1} - 4\theta_{i,2} + \theta_{i,3}]/2(\Delta Y) \qquad (125)$$

Recall from equation (53), that the average Nusselt number is given by:-

$$\overline{Nu}_h = \frac{1}{A_x}\int_0^{A_x} Nu_{i,1}\,dX.$$

By using the Simpson's numerical intergration rule (Ref.31), we have:-

$$\int_0^{A_x} Nu_{i,1}dx = \frac{\Delta x}{3}(Nu_{2,1} + 4Nu_{3,1} + 2Nu_{4,1} + \cdots\cdots + 4Nu_{N-1,1} + Nu_{N,1}) \qquad (126)$$

Therefore:-

$$\overline{Nu}_h = \frac{\Delta x}{3A_x}(Nu_{2,1} + 4Nu_{3,1} + 2Nu_{4,1} + \cdots\cdots + 4Nu_{N-1,1} + Nu_{N,1}) \qquad (127)$$

CHAPTER FOUR

NUSSELT NUMBER VARIATIONS WITH AIR-CELL ASPECT RATIO.

4.1 SOLUTION PROCEDURE FOR THE 'LTG' CASE.

For chosen values of tilt-angle, Raleigh number, air-cell aspect ratio and grid size, the following steps were taken:-

Step 1:

An initial guess of $\Psi = \psi^{(0)}$, $\omega = \omega^{(0)}$ and $\theta = \theta^{(0)}$ were made, i.e. $\Psi = \omega = 0$ and $\theta = 1-Y$.

Step 2:

By using equations (63) and (65) to (67), the stream functions $\psi^{(1)}$ at grid-points a distance ΔX and ΔY away from the boundaries were computed.

Step 3:

By using equations (70) and (71), the stream functions $\psi^{(1)}$ at the interior grid-points of the air-cell were computed.

Step 4:

By using equation (108), the temperatures $\theta^{(1)}$ at the spacer and air interface were computed.

Step 5:

By using equation (83) in conjunction with equations (76), (78),(80) and (82), depending on the signs of γ and σ, the temperatures $\theta^{(1)}$ at the interior grid-points of the air-cell were computed.

Step 6:

By using equations (101) to (104), the vorticity functions $\omega^{(1)}$ at the boundary grid-points of the air-cell were computed.

Step 7:

By using equation (94) in conjunction with equations (87),(89), (91) and (93), depending on the signs of γ and σ, the vorticity functions $\omega^{(1)}$ at the interior grid-points of the air-cell were computed.

Step 8:

The procedure was repeated starting from step 2 to generate $\psi^{(2)}$, $\theta^{(2)}$, and $\omega^{(2)}$. Then $\psi^{(3)}$, $\theta^{(3)}$ and $\omega^{(3)}$ and so on, until $|\psi^m - \psi^{m-1}|$, $|\theta^m - \theta^{m-1}|$ and $|\omega^m - \omega^{m-1}|$ at all grid-points converged to within a specified error.

Step 9:
Equations (125) and (127) were then used to compute the local and average Nusselt numbers.

Step 1Ø:
The Raleigh number or the air-cell aspect ratio changed and the whole process was repeated.

4.2 SOLUTION PROCEDURE FOR THE 'ZHF' CASE.

The procedure was identical to that for the 'LTG' case, except for the way in which the temperatures at the side boundaries were computed. The equation in step 4 was thus replaced with equations (111) and (113).

4.3 SOLUTION PROCEDURE FOR THE CASE OF THE REAL SPACER.

The solution procedure was also basically the same as that for the 'LTG' case, except for the additional parameters involved as a result of the spacer finite thickness and thermal conductivity. This resulted in a modified approach for computing the temperatures at the spacer and air interface. Two methods apply depending upon the magnitude of the factor F, i.e. the cell coupling factor.

For $F < 1$:
Fictitious temperatures $\theta_{s1,j}$ and $\theta_{sNs+1,j}$ were first computed using equations (117) and (118) respectively. Equation (1Ø6), in conjunction with equation (1Ø7), was then applied to compute the temperatures inside (and including the side boundaries of) the spacer. The boundary values were then equated to those of the air-cell before proceeding to calculate the temperatures at the interior grid-points of the air-cell.

For $F \geq 1$:
The spacer side boundary temperatures were first equated to those of the air-cell. The temperatures at the interior grid-points of the spacer were then computed. The fictitious temperatures $\theta_{1,j}$ and $\theta_{N+1,j}$ were calculated using equations (121) and (122), before proceeding to calculate the temperatures at all the grid-points of the air-cell, including those at the side boundaries.

These procedures replaced the procedure in step 4 of section 4.1.

4.4 RESULTS AND DISCUSSIONS.

The solution procedures described in section 4.1 to 4.3 were translated into computer Fortran language and run on the Cranfield VAX 11/780 computer -- see Appendix D for details. Grid-points of 21x21 were employed both in the cell and in the spacer as a compromise between running time and accuracy of the solutions. For example, the effect of the grid size on the values of the predicted average Nusselt numbers is shown in fig.5, for A_x= 0.8 and Φ =30°. The average Nusselt number for 21x21 grid-points, in this example, underestimates the extrapolated value for an infinite number of grid-points by about 10%. During successive iterations for the solutions, relaxation factors between 1.2 and 1.5 were, through trial and error, found to give faster convergence of the solutions. This, however, depended upon the boundary conditions. The effect of the relaxation factor on the number of iterations on convergence, is shown graphically in fig.6.

4.4.1 Nu - A_x relationships.

Fig.7 shows the numerically predicted variation of the average Nusselt number on the hot surface with the air-cell aspect ratio, for the LTG and ZHF cases. The variations for the two cases, indicate decreases in the convective heat transfers from the hot surface with decreases in the air-cell aspect ratio from unity. However, for the same Rayleigh number, the ZHF case indicates higher convective heat transfers than that shown for the LTG case. Fig.8 shows the predicted local Nusselt number distributions along the hot surface of the air-cell, for a Rayleigh number of 50000 and Φ = 30° . The dotted lines indicate loci of points which define the cross-section of the hot plate where maximum heat transfer occurs. No apparant physical reason was found to explain the shape of the loci. However, the occurrence of the maxima at x/W less than 0.5 is thought to occur from the nature of the convective motion. For example, fig.9 shows the predicted flow patterns for A_x=1.0 and 0.5 for the ZHF case. The predicted flow patterns show the formation of a big single convective roll cell, rising about the cell end defined by x/W equals unity and falling about the end defined by x/W equals zero. This being the case, it should therefore be expected that the greatest temperature gradient on the hot surface should occur within the region where the air falls, because the air in that region has lower temperature than that rising. A similar argument also holds for the cold surface, i.e. the maximum occurring within the region where the air rises. It should be recalled that the cold and hot surfaces

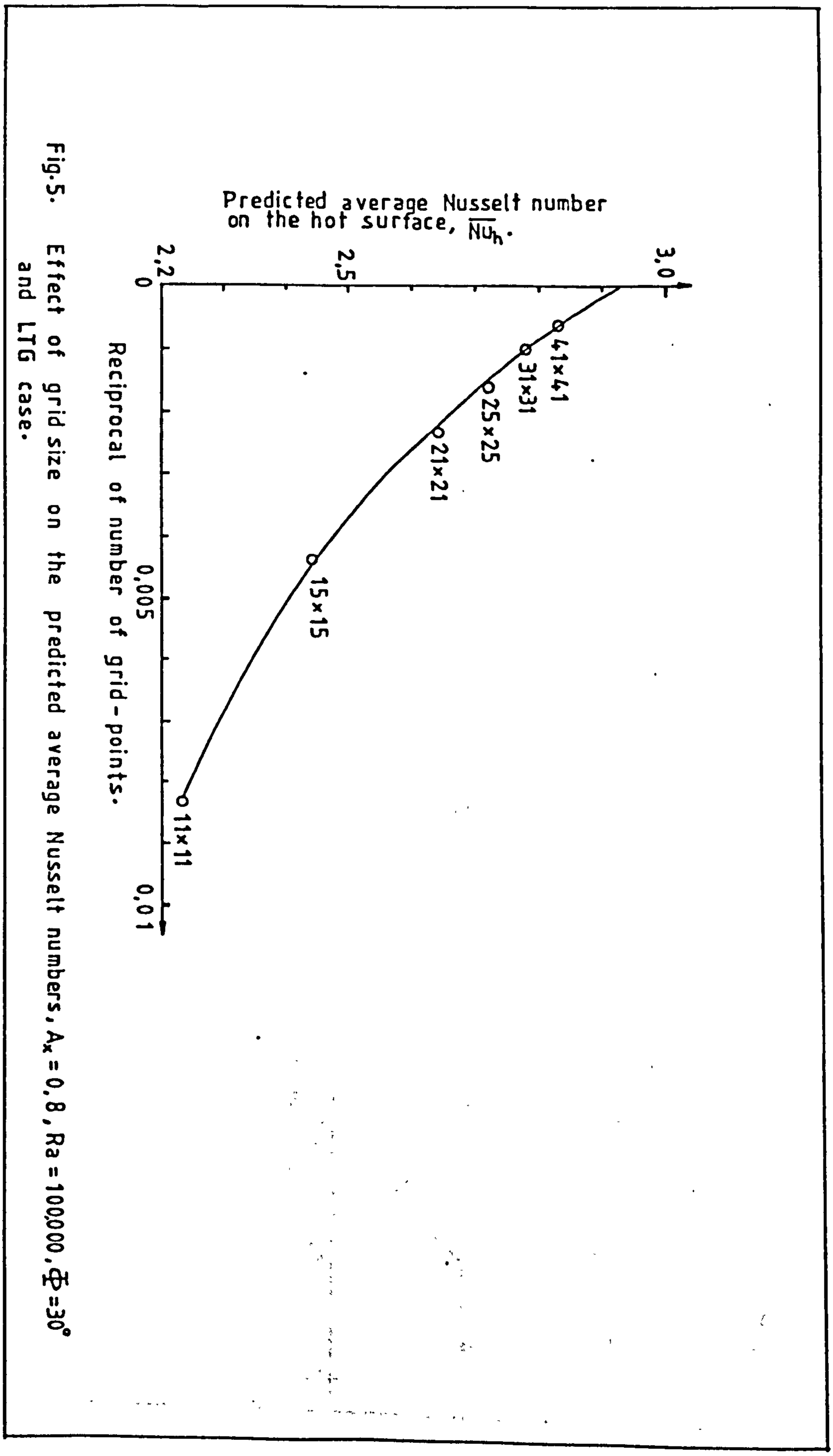

Fig.5. Effect of grid size on the predicted average Nusselt numbers, $A_x = 0,8$, Ra = 100.000, Φ=30° and LTG case.

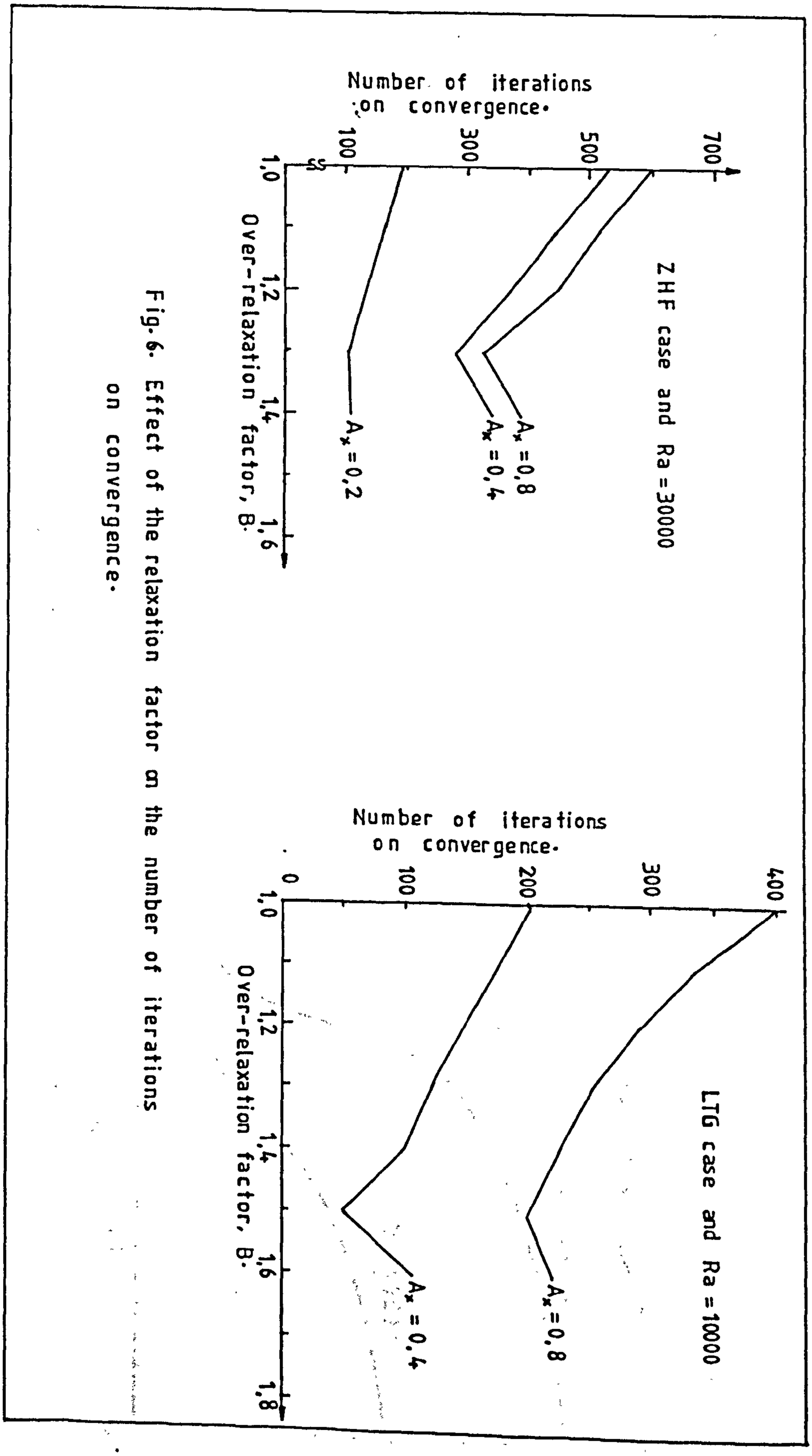

Fig. 6. Effect of the relaxation factor on the number of iterations on convergence.

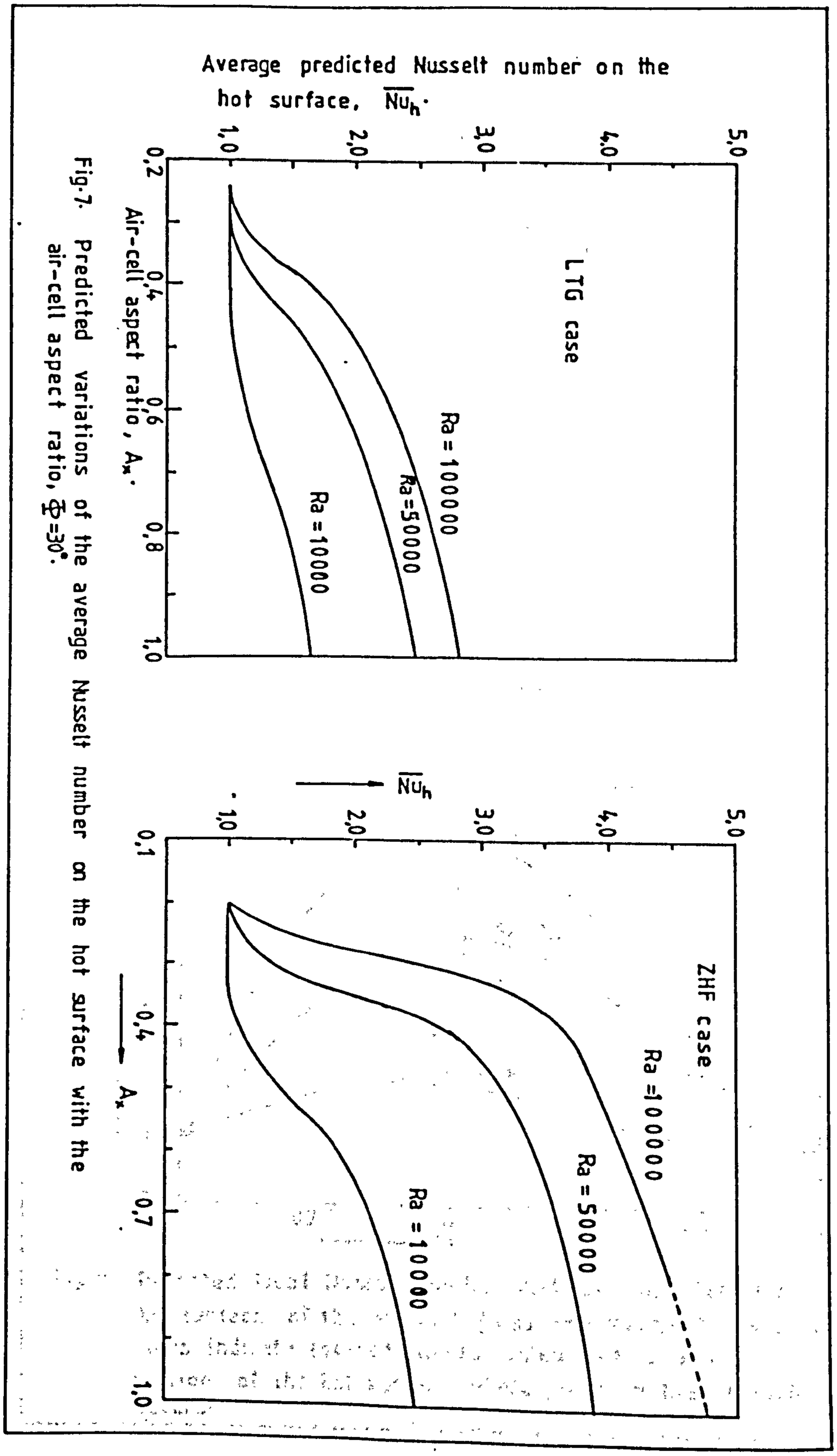

Fig.7. Predicted variations of the average Nusselt number on the hot surface with the air-cell aspect ratio, $\Phi=30°$.

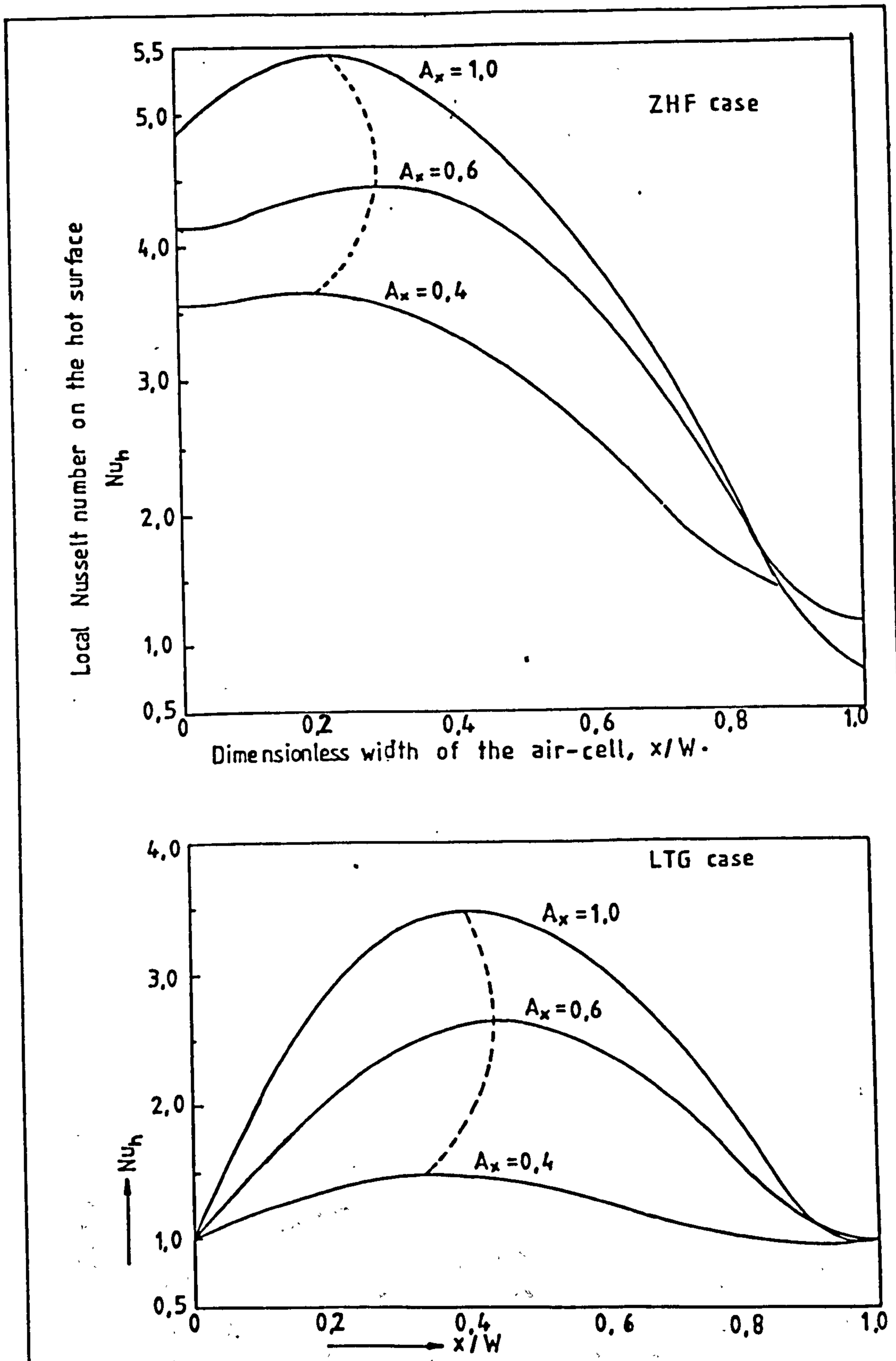

Fig.8. Predicted local Nusselt number distributions along the hot surface of the air-cell, $\Phi = 30°$ and $Ra = 5 \times 10^4$. The dotted lines indicate loci of points which define the cross-section of the hot surface where maximum heat transfer occurs.

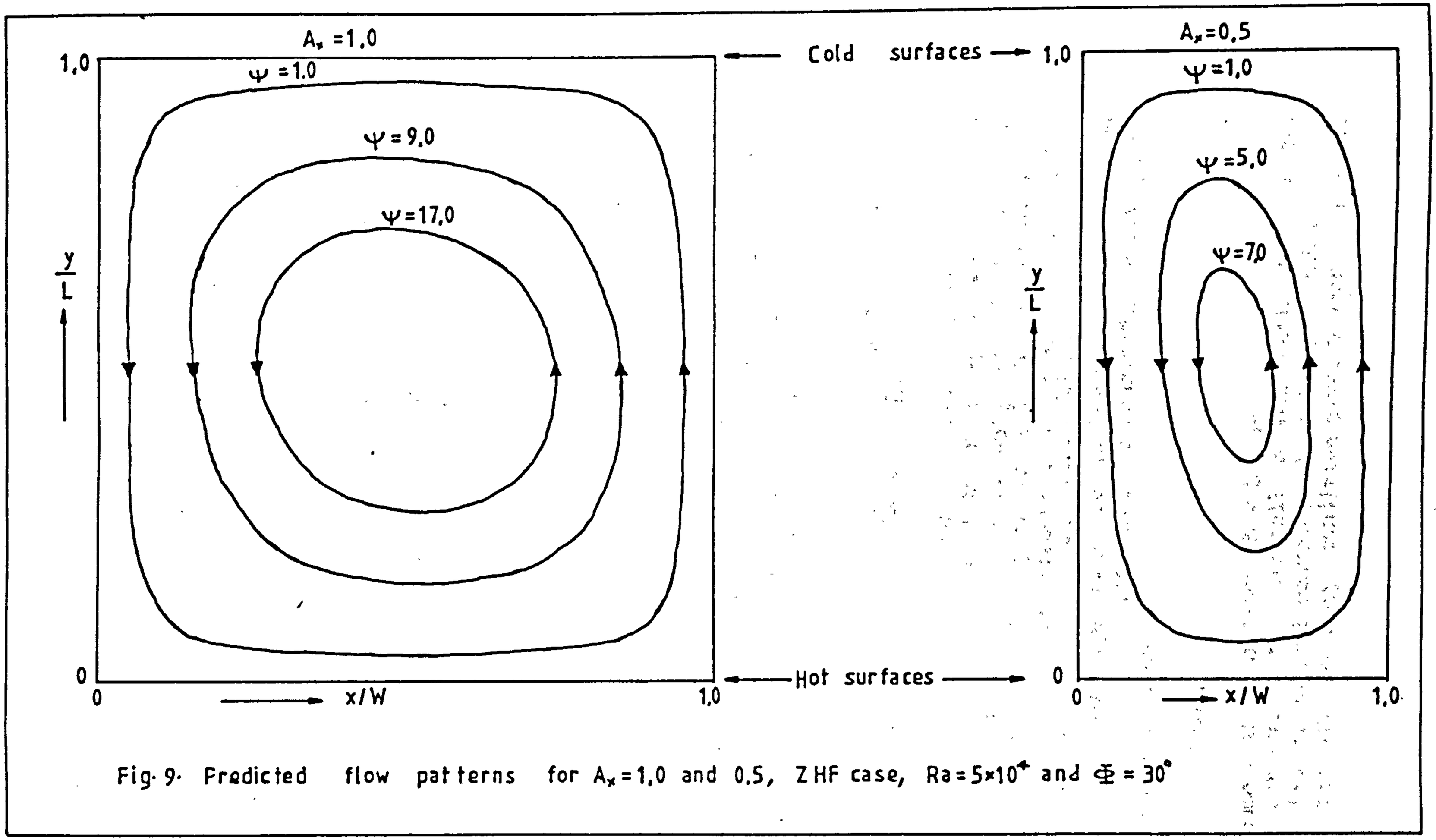

Fig. 9. Predicted flow patterns for $A_x = 1.0$ and 0.5, ZHF case, $Ra = 5 \times 10^4$ and $\Phi = 30°$

were considered isothermal. The symmetry of the solutions is indicated in fig.1Ø, where the local Nusselt number distributions on the cold and hot surfaces are shown. The results in fig.1Ø show that, the average Nusselt numbers on the cold and hot surfaces are the same. This therefore means that the overall convective heat transfer coefficient would be determined from half the average Nusselt number evaluated on any of the surfaces.

The Nu-A_x relationships for the case of the real spacer lies between that indicated for the LTG and ZHF cases, depending upon the cell coupling factor F, which characterizes the spacer's thermal properties. For example, fig.11 shows the effect of the cell coupling factor F on the local Nusselt number distribution for $A_x = 1.Ø$ and $\Phi = 3Ø°$. It shows that as F increases from zero (i.e. represented by LTG), the local Nusselt number distribution tends to approach that for the ZHF case.

4.4.2 Comparison between the numerically-predicted results in this study with other people's results.

In table 1, the numerically predicted average Nusselt number values on the hot plate for the LTG case, $A_x = 1.Ø$ and $\Phi = 9Ø°$ are compared. On the average, the results compared show that the values of this study compares with the numerically-predicted values of Meyer et al (Ref.25), David (Ref.26) and Poots (Ref.27) to within a maximum of about 1.7 percent. The percentage differences are indicated by the bracketted values and were obtained using the following relationship:-

$$\text{Percentage difference} = \frac{(\text{Reference value} - \text{This study's value})}{\text{Reference value.}}$$

The numerically-predicted local Nusselt number distributions for the case of the real spacer were compared with the experimental results of Meyer et al (Ref.2Ø and 25), for $A_x = 1.Ø$ at tilt-angles of 45°, 6Ø° and 9Ø° above the horizontal. These are presented in figs.12 and 13. The predicted local Nusselt number distributions are similar to those obtained experimentally by Meyer et al (Ref.2Ø and 25), except for the differences in magnitudes especially at the side boundaries.

4.5 CONCLUSIONS.

The numerical predictions show that:-
(i) Decreases in the air-cell aspect ratio from unity, could lead to minimal convective heat transfer rates.
(ii) The ZHF boundary condition gives higher convective

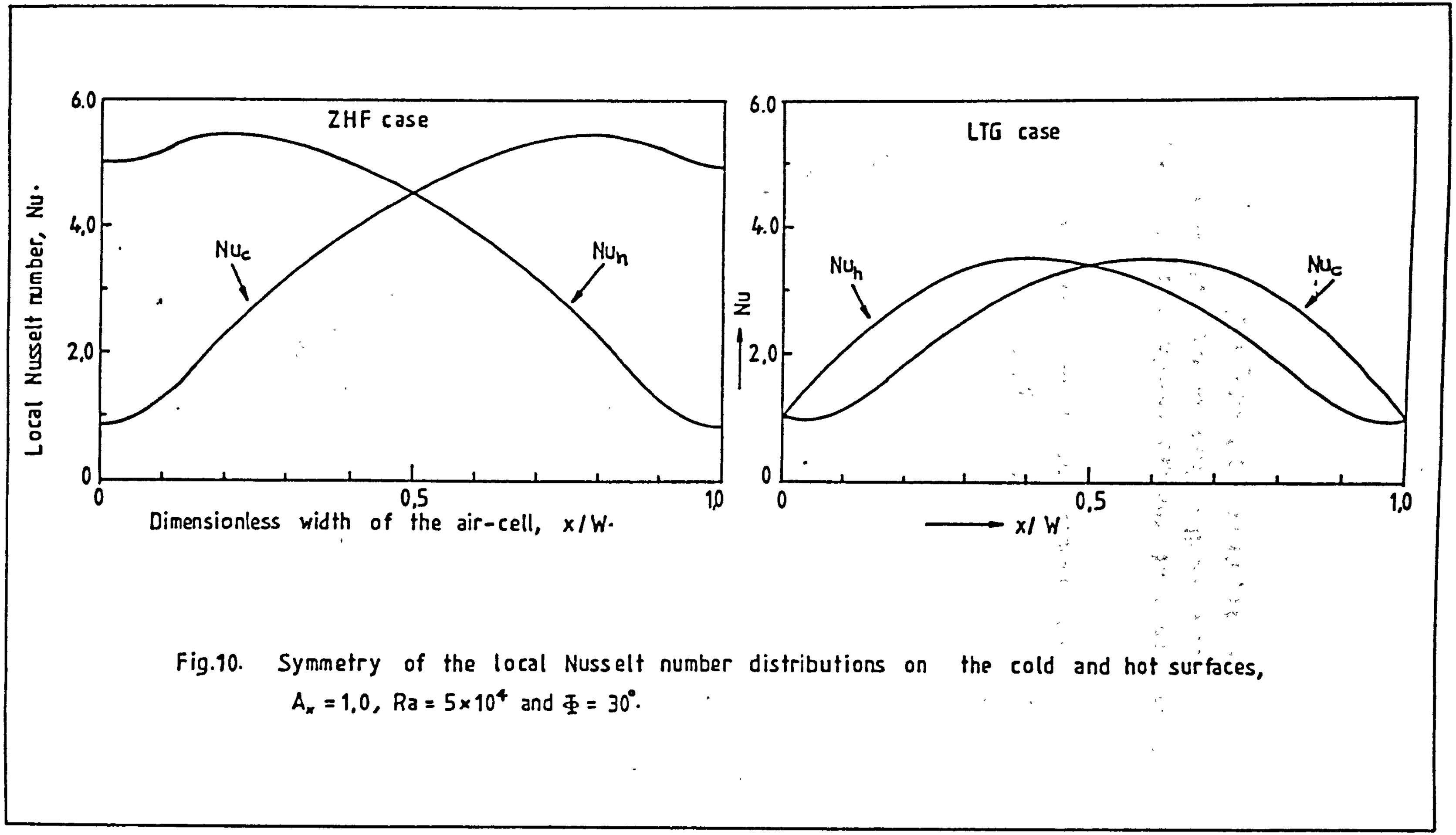

Fig.10. Symmetry of the local Nusselt number distributions on the cold and hot surfaces, $A_x = 1,0$, $Ra = 5 \times 10^4$ and $\Phi = 30°$.

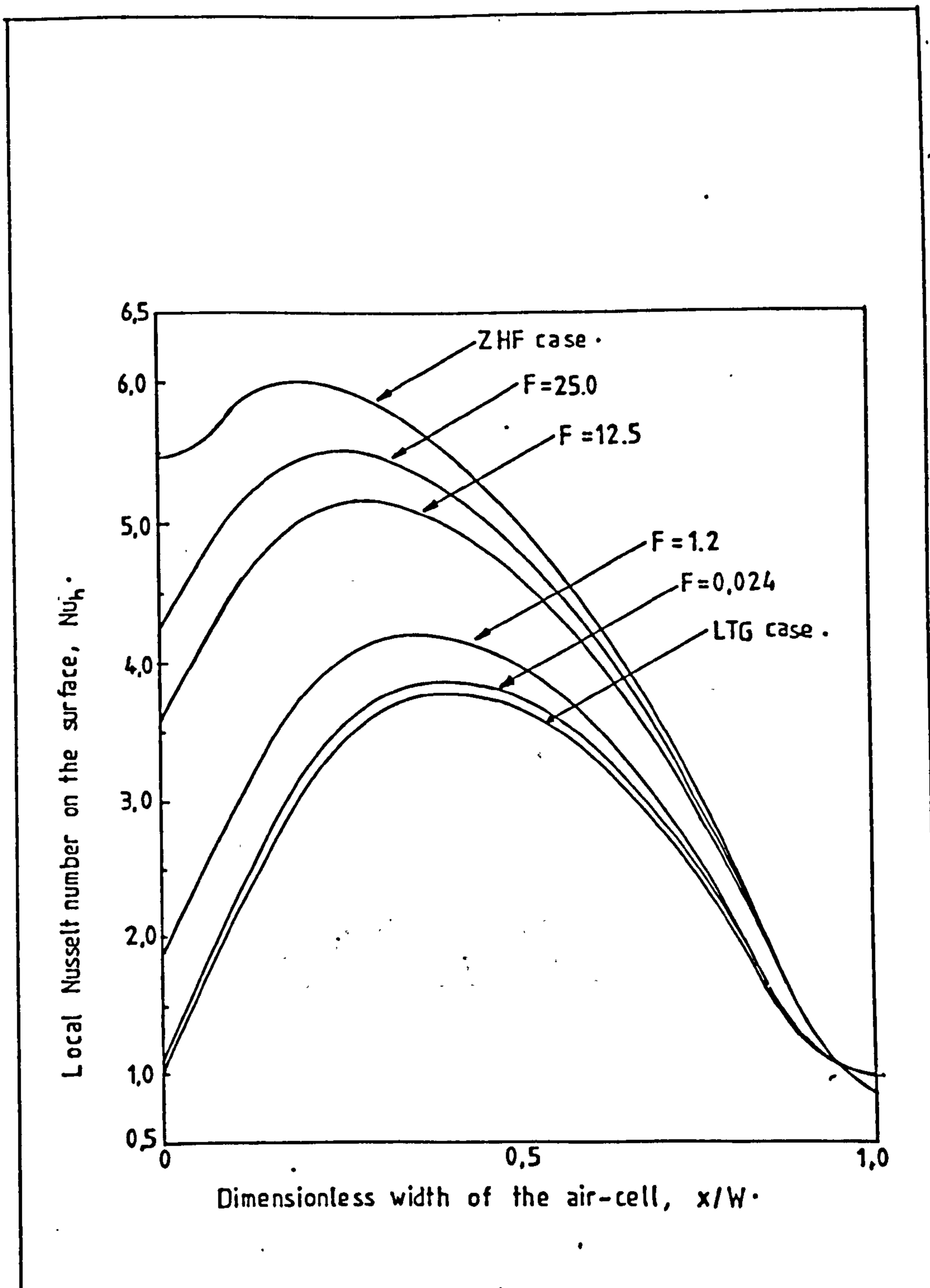

Fig.11. Effect of the cell coupling factor F, on the local Nusselt numbers on the hot surface, $A_x = 1,0$, $Ra = 7,5 \times 10^4$ and $\Phi = 30°$.

Table 1. Comparisons of the numerically predicted average Nusselt number values on the hot surface for the LTG case, $A_x = 1.0$ and $\Phi = 90$.

Rayleigh number	Average Nusselt number on the hot surface.				
	This study	Meyer et al (Ref.25)	David (Ref.26)	Poots Ref.27)	Wilkes et al (Ref.28)
500	1.014	1.015 (+0.1)	1.011 (-0.3)	1.013 (-0.1)	-
1000	1.050	1.050 (0)	1.041 (-0.9)	1.042 (-0.8)	-
2500	1.193	-	-	1.193 (0)	-
5000	1.408	1.408 (0)	1.432 (+1.7)	1.415 (+0.5)	-
5021	1.409	-	-	-	1.419 (+0.9)
10000	1.705	1.709 (+0.23)	1.717 (+0.7)	1.706 (0.06)	-

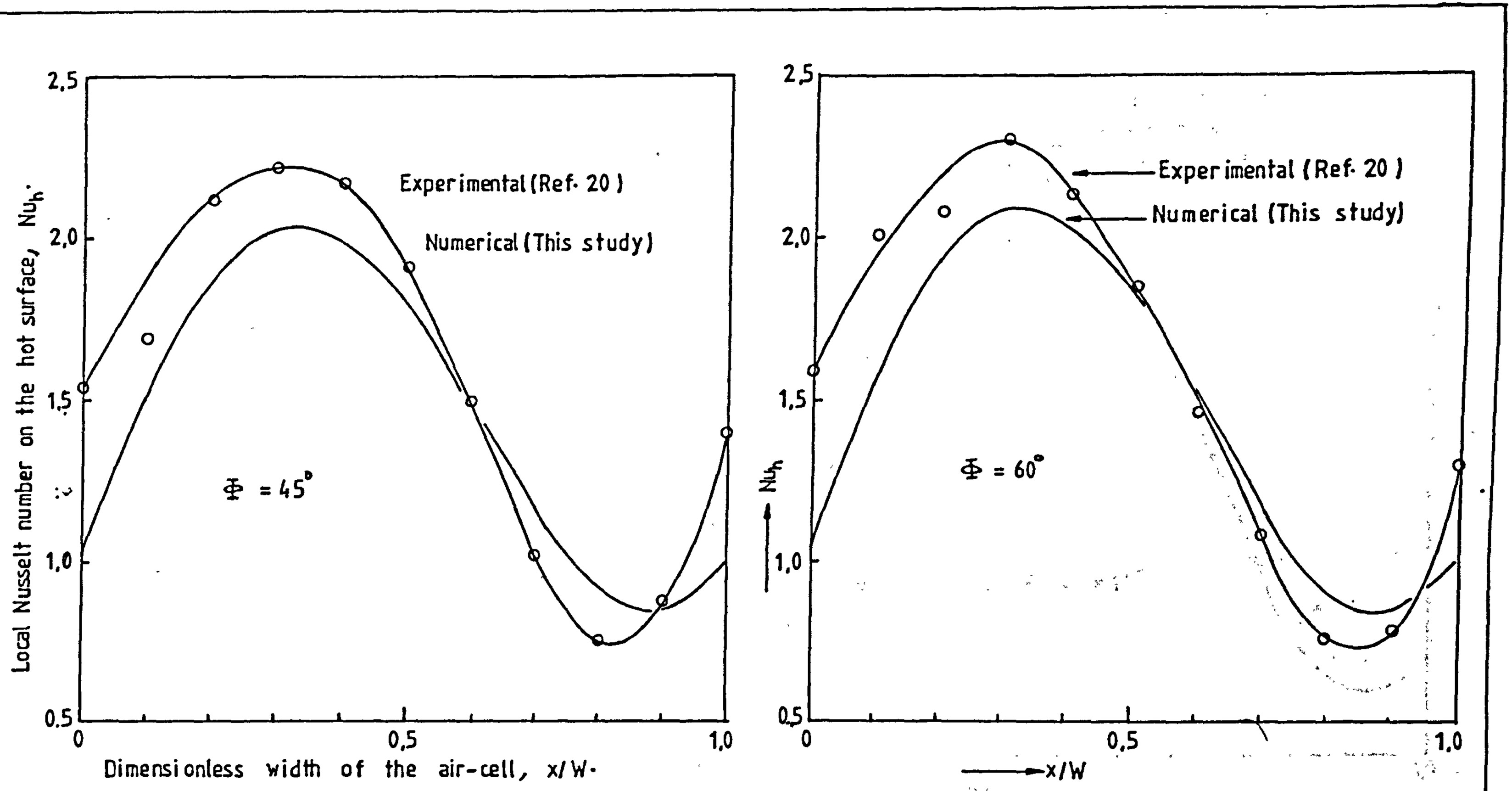

Fig. 12. Comparisons between the experimental results of Meyer et al (Ref. 20) with those numerically predicted in this study, $A_x = 1.0$, $Ra = 5.5 \times 10^5$, $A_s = 0.02$ and $K_a/K_s = 0.25$.

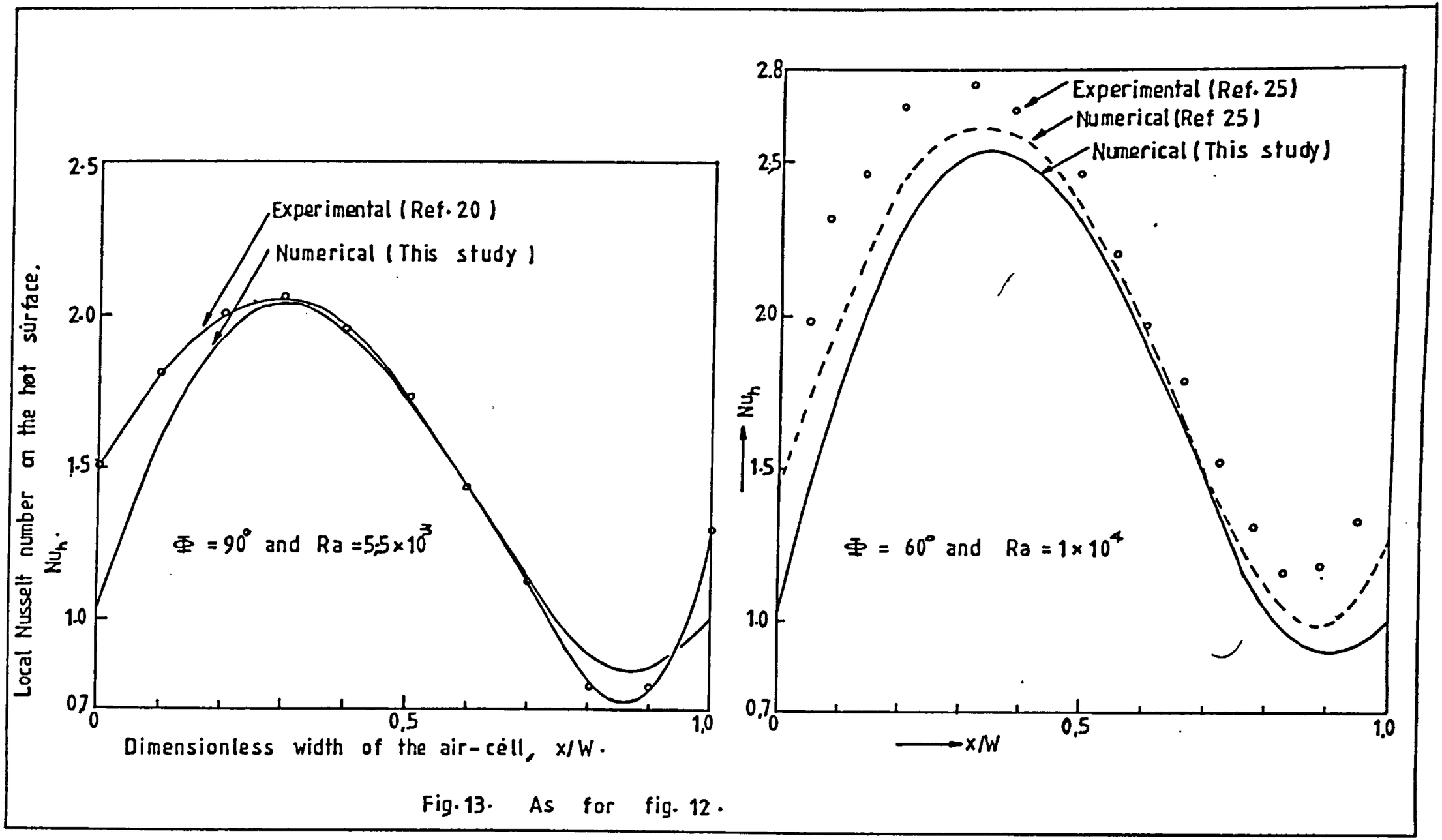

Fig. 13. As for fig. 12.

heat transfer rates than those for the LTG case, for the same Rayleigh numbers.
(iii) The average Nusselt number on the cold and hot surfaces of the air-cells, are the same. Thus the overall convective heat transfer coefficient could be determined from half the average Nusselt number value evaluated on any of the surfaces.
(iv) Air-cell aspect ratio of about Ø.2 could be capable of maintaining minimal rates of convective heat transfer. A similar conclusion was also reached by Charters and Guthrie (Ref.16), when they conducted energy loss tests by varying the spacer-to-spacer distance. They found that minimal heat loss occurred at aspect ratios of about Ø.21 and Ø.26. Because the air-cell aspect ratio is the ratio of cell width-to-height, the corresponding width or height need also be stated. This is to enable complete the definition of the size of the air-cell for which convection could be minimized.

CHAPTER FIVE

EXPERIMENTAL INVESTIGATION OF THE EFFECT ON CONVECTIVE HEAT TRANSFER OF DECREASING THE AIR-CELL ASPECT RATIO BY VARYING THE HEIGHT.

5.1 INTRODUCTION.

One of the conclusions arrived at in chapter four is that, the ratio width-to-height of about Ø.2 could minimize the rate of convective heat transfers in the air-cells created using a slatted CSD (i.e. convection suppression device). However, as previously mentioned in chapter one, the corresponding width or height also needs to be stated, in order that the size of the air-cells be adequately defined. The objective here therefore, is to investigate the effect on convective heat transfer of decreasing the air-cells aspect ratio from unity, by varying the height. An air enclosure subdivided into five smaller air-cells, each of 1Ømm width, was therefore subjected to heating from below and cooled at the top. The convective heat transfer coefficients were measured, for three heights of the air-cells.

In measuring the convective heat transfer rates across air enclosures, two basic experimental approaches are used:-
(i) The total heat transfer rate (i.e. radiative, conductive and convective through the air) in the enclosure is measured, and then the radiative and conductive components subtracted from the total. This, however, adds another dimension to the basic problem, through the quantification of the two components. In a multiple-air-cell enclosure (which is to be described later), the radiative component may not be quantified easily, unless the Rayleigh number is varied by changing the air pressure instead of temperature or the characteristic length. Such a method would involve keeping the enclosure at the lowest Rayleigh number possible (i.e. lower than the critical value) and then measuring the heat transfer across the air gap. Because the Rayleigh number is substantially below the critical value, it is then assumed that the heat flow occurs by radiation and conduction alone. Subtracting the conduction component yields the radiative heat transfer rate. This is then assumed to be the same for all Rayleigh numbers because pressure rather than temperature is used to vary the Rayleigh number.
(ii) As revealed in the mathematical model, in order to quantify the convective heat transfer alone, the temperature distribution within the air-cells has to be determined. In addition to practical difficulties, direct

temperature measurements using temperature sensors could interfere with the convective flow. An optical method, however, minimizes these problems and has therefore been used to measure temperature distibution within the air-cells.

5.2 THE MACH-ZEHNDER INTERFEROMETER.

5.2.1 Description:

The Mach-Zehnder interferometer was the optical instrument used in determining the temperature distributions, from which the Nusselt numbers were calculated. A schematic diagram of the interferometer is shown in fig. 14., whereas the photograph is shown in fig.15. The interferometer is based on a 60° angle parallelogram. The light source used was nominally a 3mW Helium-Neon gas laser ($\lambda = 0.6328 \times 10^{-6}$ m). The output from the laser, by means of a lens, produces a parallel beam of light. The parallel light beam strikes the first splitter plate SP1, which is a partially-silvered mirror, permitting half of the light to pass directly through it. The transmitted light gets to mirror M2 where it is totally reflected towards the second splitter plate SP2. The reflected light by SP1 gets to mirror M1 where it is also totally reflected towards splitter plate SP2. The splitter plate SP2 is a semi-silvered mirror. The recombined beams then pass onto the screen through a lens where it is viewed or photographed to provide a permanent record.

5.2.2 Operational theory of the Mach-Zehnder interferometer.

The Mach-Zehnder interferometer utilizes the phenomenon of light interference to measure the change of index of refraction in the interferometer test section. The index of refraction of the medium in turn, can be related to other properties of the medium; for example, the density and hence temperature of air in the present study.
According to electromagnetic theory, light is energy travelling in the form of wave trains. Two coherent light waves that strike a surface at the same point are said to interfere in the sense that their effects are combined. For example, if two light waves are 180° degrees out-of-phase when they strike a surface, their effects cancel and the surface appears dark. If the waves, however, are in-phase when they strike the surface, they reinforce each other and the surface appears bright.
In the interferometer (refer to fig. 14), the reference and test light beams are in-phase when leaving SP1. Their phase relationship when recombined at SP2 depends on the

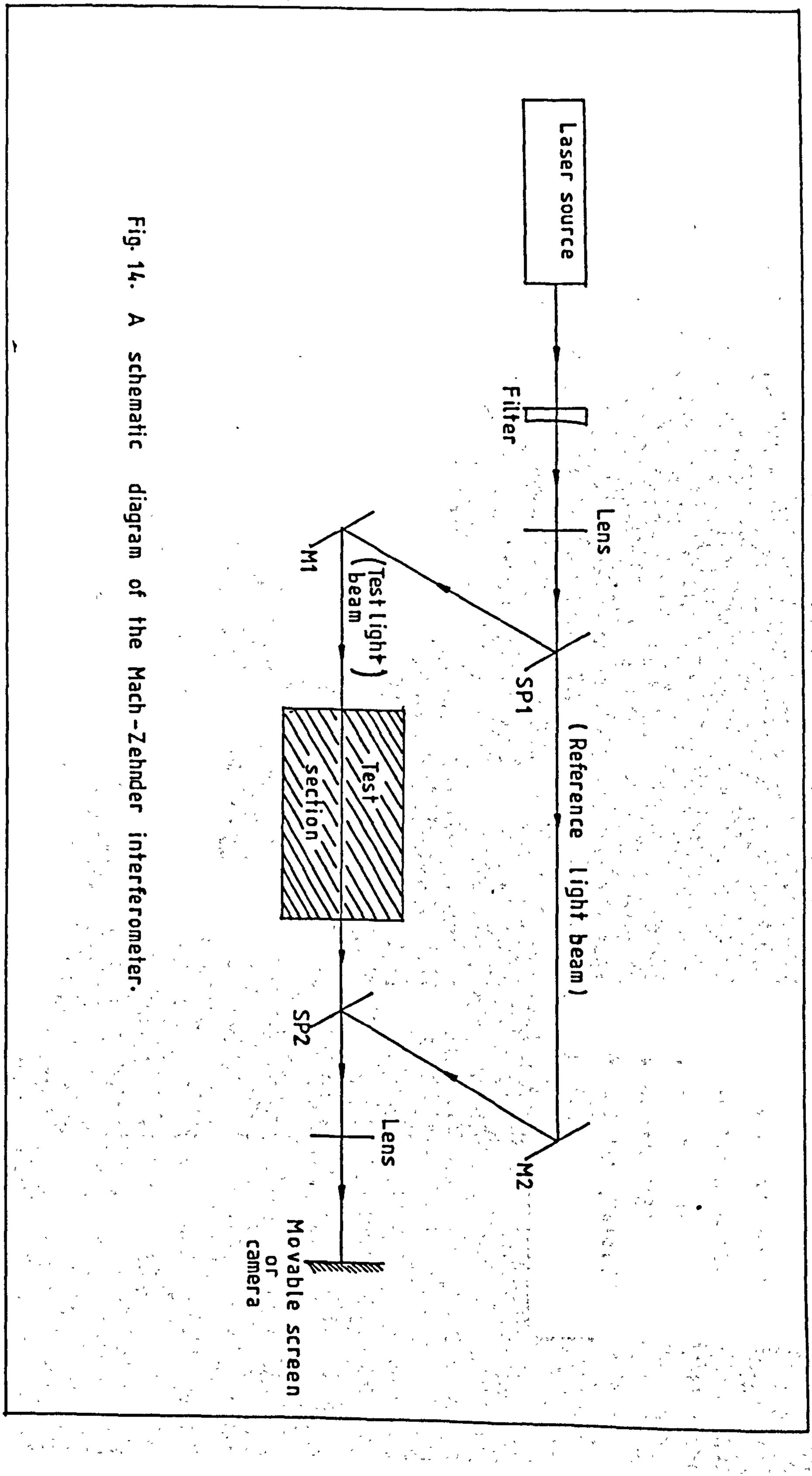

Fig. 14. A schematic diagram of the Mach-Zehnder interferometer.

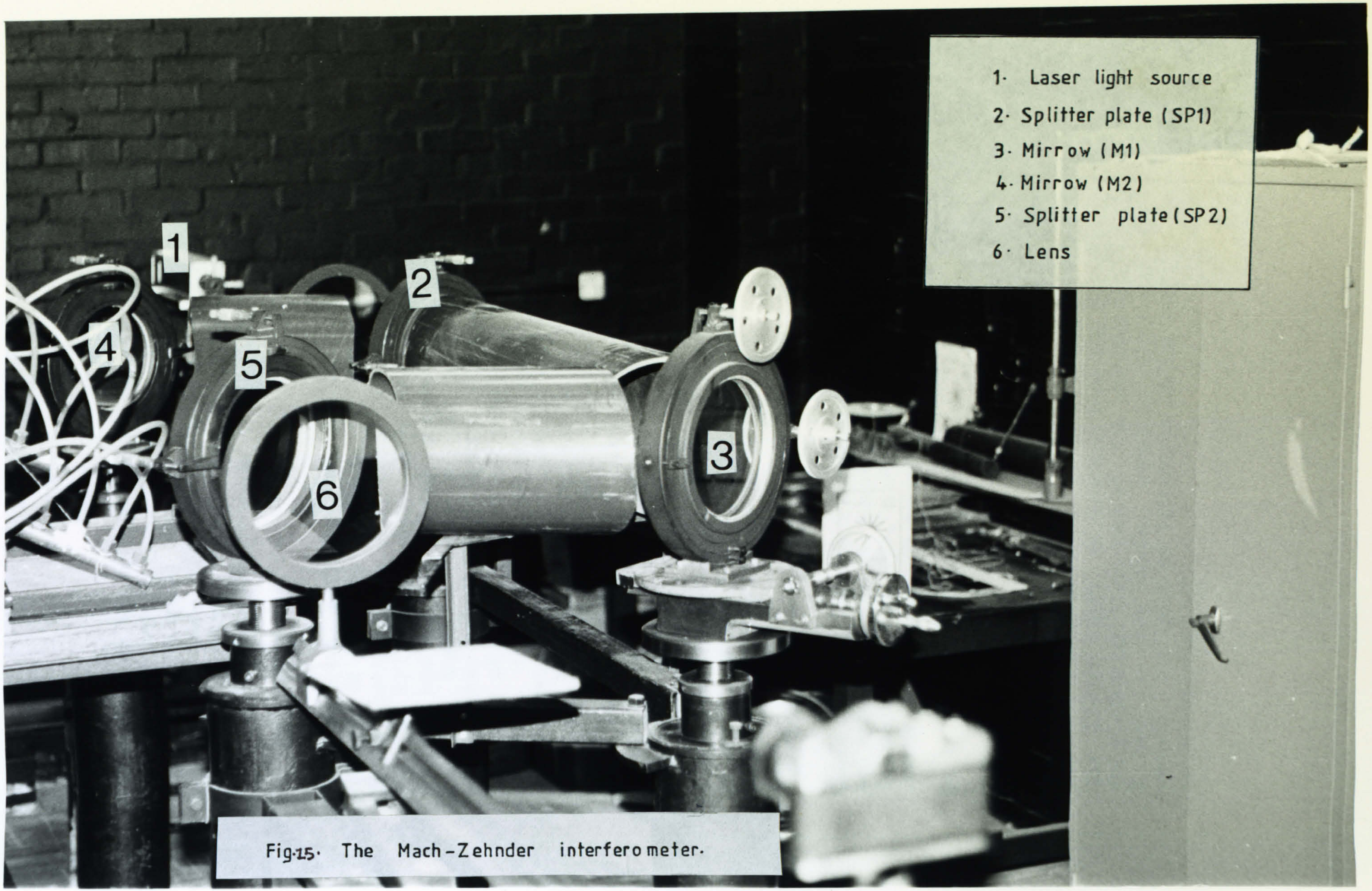

1· Laser light source
2· Splitter plate (SP1)
3· Mirrow (M1)
4· Mirrow (M2)
5· Splitter plate (SP2)
6· Lens

Fig·15· The Mach-Zehnder interferometer.

differences in the optical path lengths they travel. The optical path length (i.e. OPD), is defined as the distance that the light would travel in a vacuum during the same period of time that it takes the light to travel a specified distance Z, in a medium. It is expressed in terms of the index of refraction, n, as follows:-

$$OPD = nZ \tag{128}$$

The index of refraction is defined as the ratio of the velocity of light in vacuum to its velocity in the medium.
If both paths of the light beams (i.e. the reference path SP1, M2, SP2 and the test path SP1, M1, SP2) are the same lengths, and the four optical plates are perfectly aligned, the two beams arriving at SP2 will be in-phase and the photographic screen will appear uniformly bright, provided the index of refraction in the reference and test beams are the same. If one of the path lengths is longer by $1/2\lambda m$ (where m=1, 2, 3.....), then the screen will be uniformly dark. If, however, a disturbance is introduced in the test medium (i.e. via heating of the medium), the light at SP2 will be in-phase at some locations and out-of-phase at others thereby causing bright and dark fringes to appear on the screen.
The difference in the optical path lengths (i.e. $\Delta(OPD)$), between the reference and test beams determines the number of fringe shifts that occur. The difference in optical path lengths is expressed as follows:-

$$\Delta(OPD) = \int (n - n_o)\, dz \tag{129}$$

where n and n_o are the indexes of refraction in the test and reference medium respectively. The magnitude of the fringe shift (i.e. FS), caused by this optical path length change is expressed as follows:-

$$FS = \frac{(OPD)}{\lambda} = \int_0^Z \frac{(n - n_o)}{\lambda}\, dz \tag{130}$$

Therefore,

$$FS = Z\frac{(n - n_o)}{\lambda} \tag{131}$$

The fringe shift is measured from the fringe patterns on the photograph (i.e. called the interferogram). Thus if n_o, Z and λ are known, equation (131) provides a means whereby the index of refraction in the test cell medium can be determined.

5.2.3 Equations for temperature determination.

For air being the medium in the test cell, by relating the density and hence temperature of the air to the index of refraction, the interferometer can be used to measure temperature distribution within the test cell. The relationship between refractive index and the air density ρ, is given by the Lorenz-Lorentz equation (Ref.32), i.e.,

$$\frac{(n^2 - 1)}{(n^2 + 2)} \cdot \frac{1}{\rho} = \text{constant.} \qquad (132)$$

If the refractive index of dry air is assumed to be approximately unity, then by noting that $(n^2 - 1)$ and $(n^2 + 2)$ are approximately equal to $2(n-1)$ and 3 respectively, equation (132) therefore reduces to:-

$$\frac{(n - 1)}{\rho} = \text{constant.} \qquad (133)$$

Equation (133) is the Gladstone and Dale's law (Ref.33).
At moderate atmospheric pressures p, and temperatures T, air behaves as an ideal gas for which,

$$\rho = p/RT \qquad (134)$$

where R is the specific gas constant for air, i.e. R=287 J/Kg K.
From equation (133),
$(n - 1)/\rho = (n_o - 1)/\rho_o$
Therefore,

$$n = (n_o - 1)\rho/\rho_o + 1 \qquad (135)$$

At constant pressure, equation (134) can be reduced to:-

$$\frac{\rho}{\rho_o} = \frac{T_o}{T} \qquad (136)$$

Substitution from equation (135) and (136) into equation (131), gives the following equation for the fringe shift between a location inside the test cell at temperature T, and another location at the reference temperature T_o, i.e.

$$FS = (n_o - 1)[T_o/T - 1]\, Z/\lambda \qquad (137)$$

Solving for T, yields:-

$$T = \frac{T_o}{\left[\frac{\lambda FS}{Z(n_o - 1)} + 1\right]} \qquad (138)$$

According to an old empirical formula of Dale and Gladstone (Ref.34),

$$\frac{(n_o - 1)}{(n_e - 1)} = \frac{273}{T_o} \cdot \frac{p}{760} \qquad (139)$$

where n_e is the refractive index of air at 273 degrees Kelvin and 760mm mercury pressure. With an average value of $n_e = 1.000293$ for air (Ref.34), the reference refractive index n_o, at reference temperature T_o, can then be evaluated from:-

$$n_o = 1 + \frac{0.08}{T_o} \cdot \frac{p}{760} \qquad (140)$$

Equations (138) and (140) can thus be used to compute the temperature T, associated with each fringe, once its fringe shift FS, is measured from the surface at reference temperature T_o, on the interferogram.

5.3 THE TEST SECTION.

5.3.1 Description:

The test section was constructed to form a five air-cells enclosure with a hot bottom plate and a cold top plate. The hot and cold plates were made of 266mm×101mm×12mm aluminium alloy, joined by two 18mm thick plywood as shown in fig.16. and 17. The air-space so formed was partitioned into five smaller air-cells using Perspex sheets, each 3mm thick and thermal conductivity of 0.2 W/m K. The Perspex sheets were held in position by 3mm×2mm grooves milled into the surfaces of the cold and hot plates facing the flow field. The width of the air-cells was kept at 10mm each, whereas the height varied to 10mm, 20mm and 50mm.

The hot plate was kept at a uniform temperature using power-carrying heating element uniformly wound round a thin asbestos sheet. The heater protected from underneath using another asbestos block. The sides of the hot plate were insulated using 6mm thick asbestos held using 4BA screws.

The cold plate was kept at a uniform temperature using cooling water which circulated through channels milled within the plate --- see fig.18. It was covered with another plate of the same dimensions, held tight in position using 2BA screws.

The set up, protected along the longitudinal sides with 18mm thick plywood, was mounted on a wooden support hinged onto another wooden base to enable positioning at the required angle above the horizontal. The cavity faces

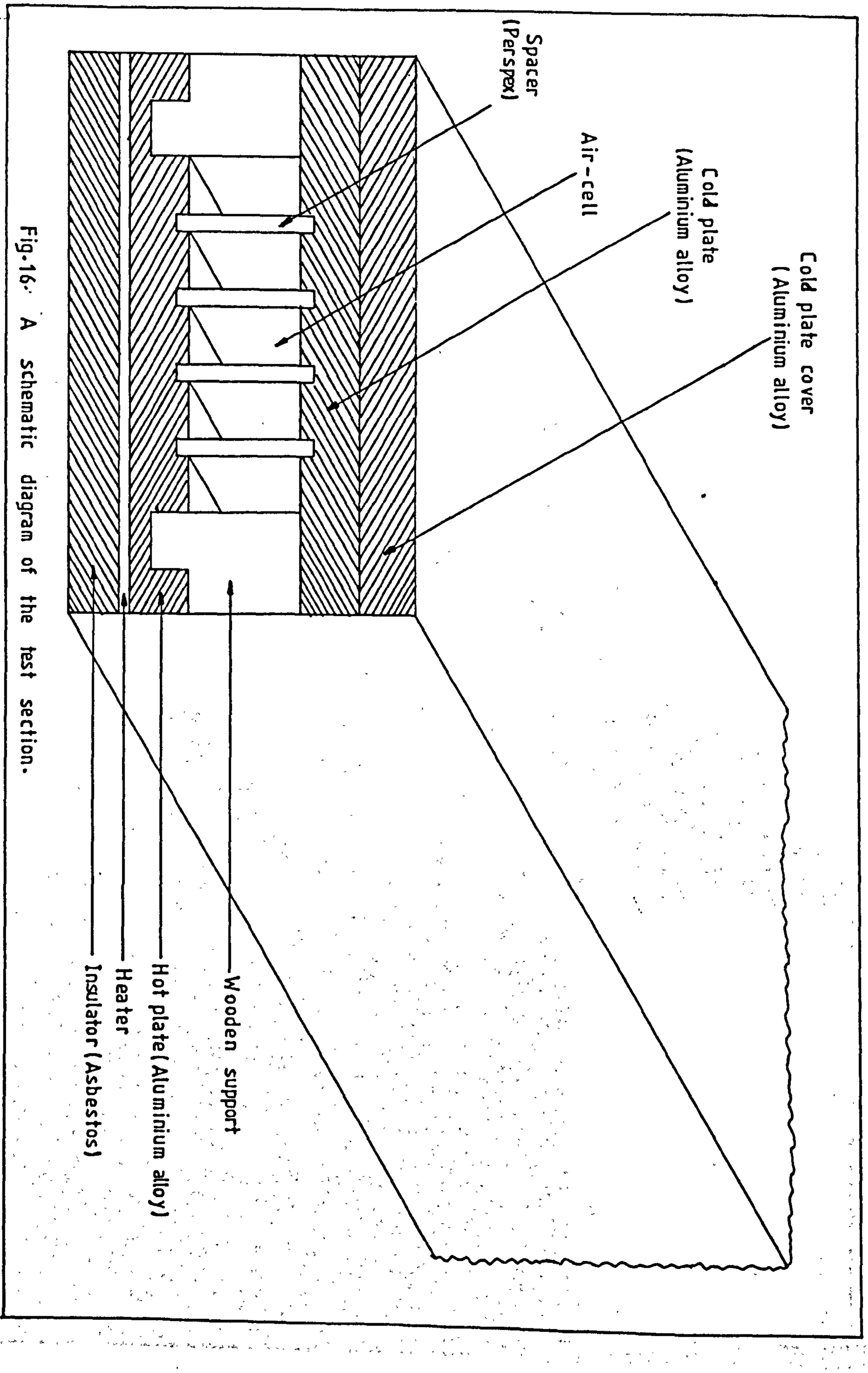

Fig.16. A schematic diagram of the test section.

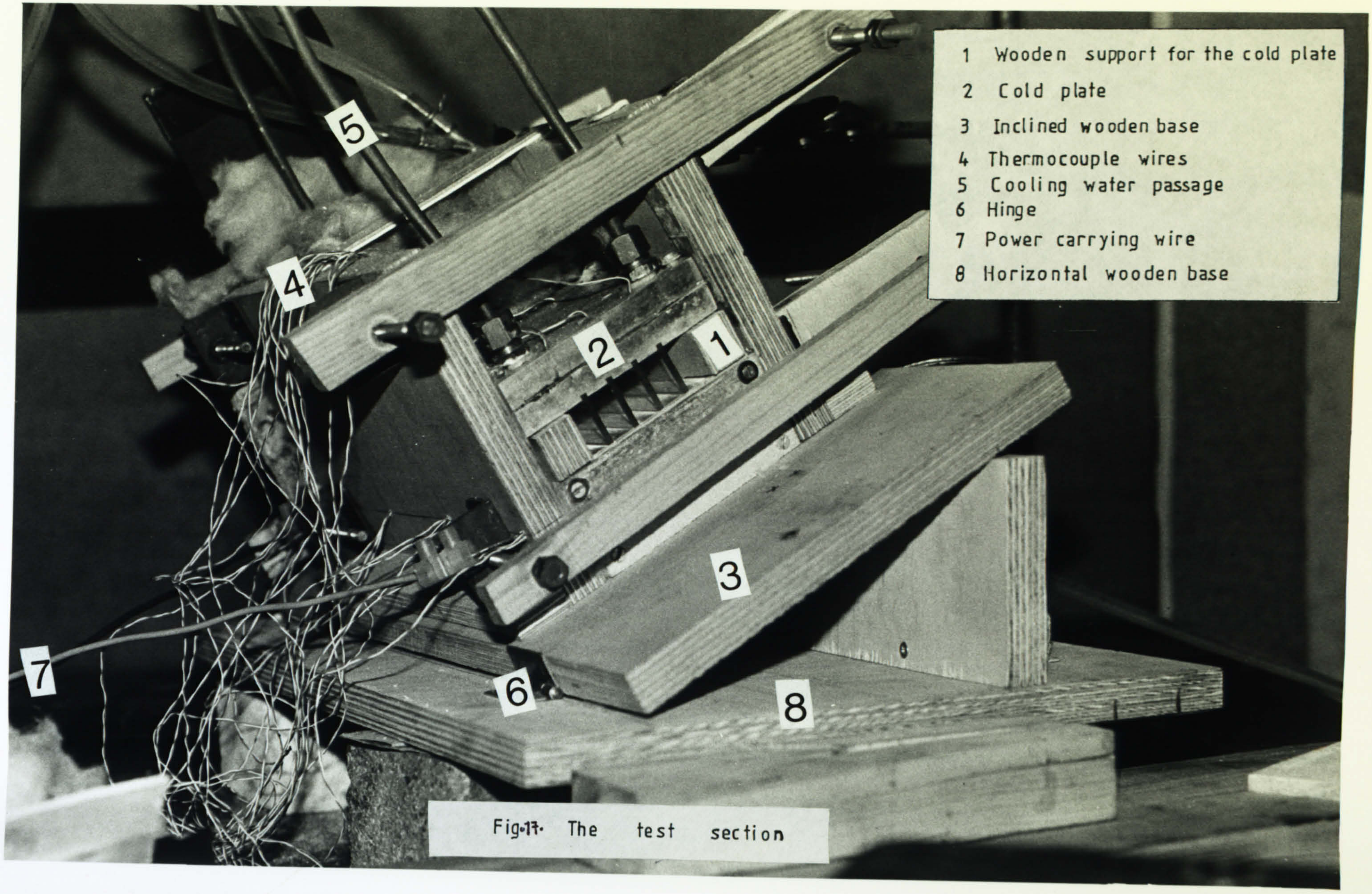

Fig.17. The test section

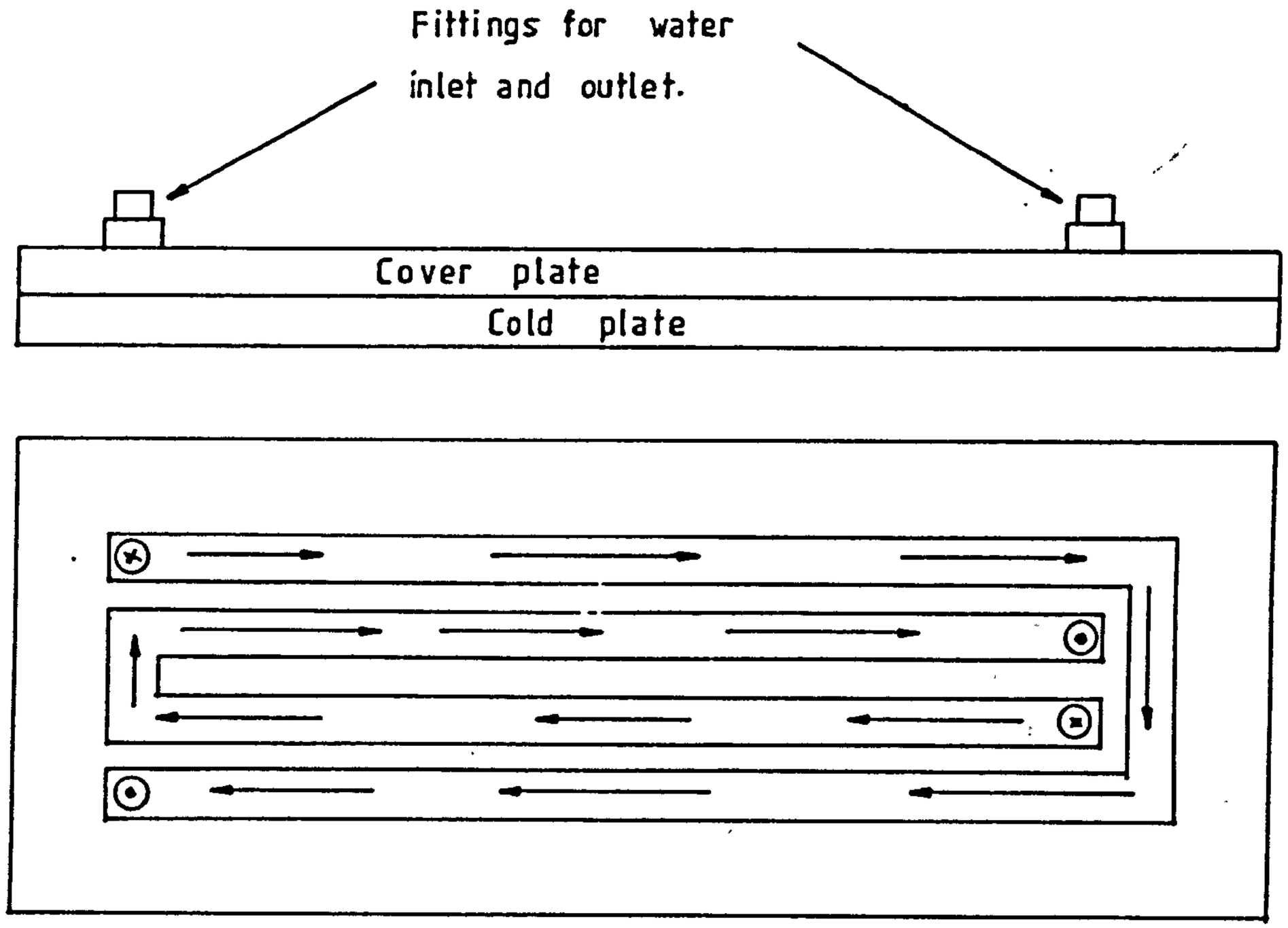

Note:
× Cooling water inlet
• Cooling water outlet

Fig.18 A schematic diagram of the cold plate, showing cooling water passages.

normal to the test beam were covered with glass sheets so as to prevent draught into the test section.

5.3.2 Thermometry.
The pertinent measured temperatures were those of the hot and cold plate surfaces which were in contact with the flow field. This was achieved using copper-constantan thermojunctions positioned as shown in fig.19. The thermocouples were inserted into 1.25mm ceramic tubes and held in 1.3mm blind holes drilled to within 2.5mm of the surfaces in contact with the flow field — see fig.2Ø. The wires in the hot plate were brought out from underneath and parallel to the plate through 3mm wide grooves, and held onto the plate using Araldite adhesive. Those from the cold plate were brought out through 1.4mm blind holes drilled into the cover plate and held tight also using Araldite.
A schematic arrangement of the thermocouple circuitry is shown in fig.21. The cold junction consisted of a glass tube containing kerosene and partially immersed in a mixture of shaved ice and water contained in a vacuum flask.

5.3.3 Power supply.
The power supplied to the heater was controlled by means of a variac operating off the 24Ø volts mains supply.

5.4. TEST PROCEDURE.

For a fixed angle above the horizontal and height of the air-cells, the test section was aligned such that a sharp image was obtained on the screen. The variac which was used to control the temperature of the hot plate was then turned on and the cooling water was allowed to circulate through the upper plate. It was then left for a steady-state to be attained. This took roughly ten hours. After reaching a steady-state, the photographic camera was focused. The interferometer was then arranged for the infinite fringe setting. One large fringe on the screen was an indication of such a setting. The test section was then introduced into the test beam region and the photograph of the fringes taken. The temperaures of the hot and cold plates were then recorded. The atmospheric pressure was read off the barometer. The temperature of the hot plate was then changed by either increasing or decreasing the power supply using the variac, and the process repeated.
The height of the air-cells was then changed by altering the height of the Perspex sheets and the wooden supports.

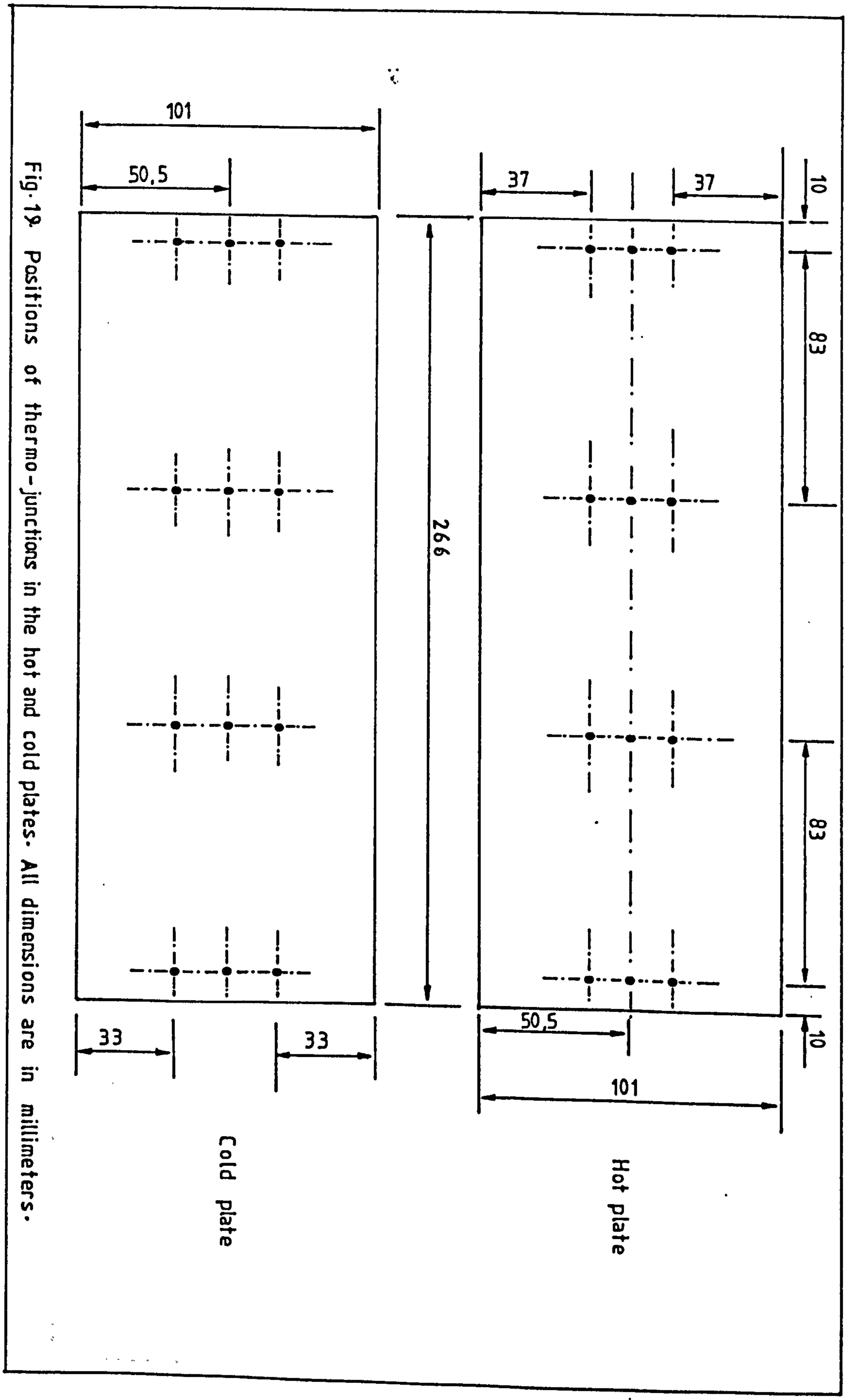

Fig. 19. Positions of thermo-junctions in the hot and cold plates. All dimensions are in millimeters.

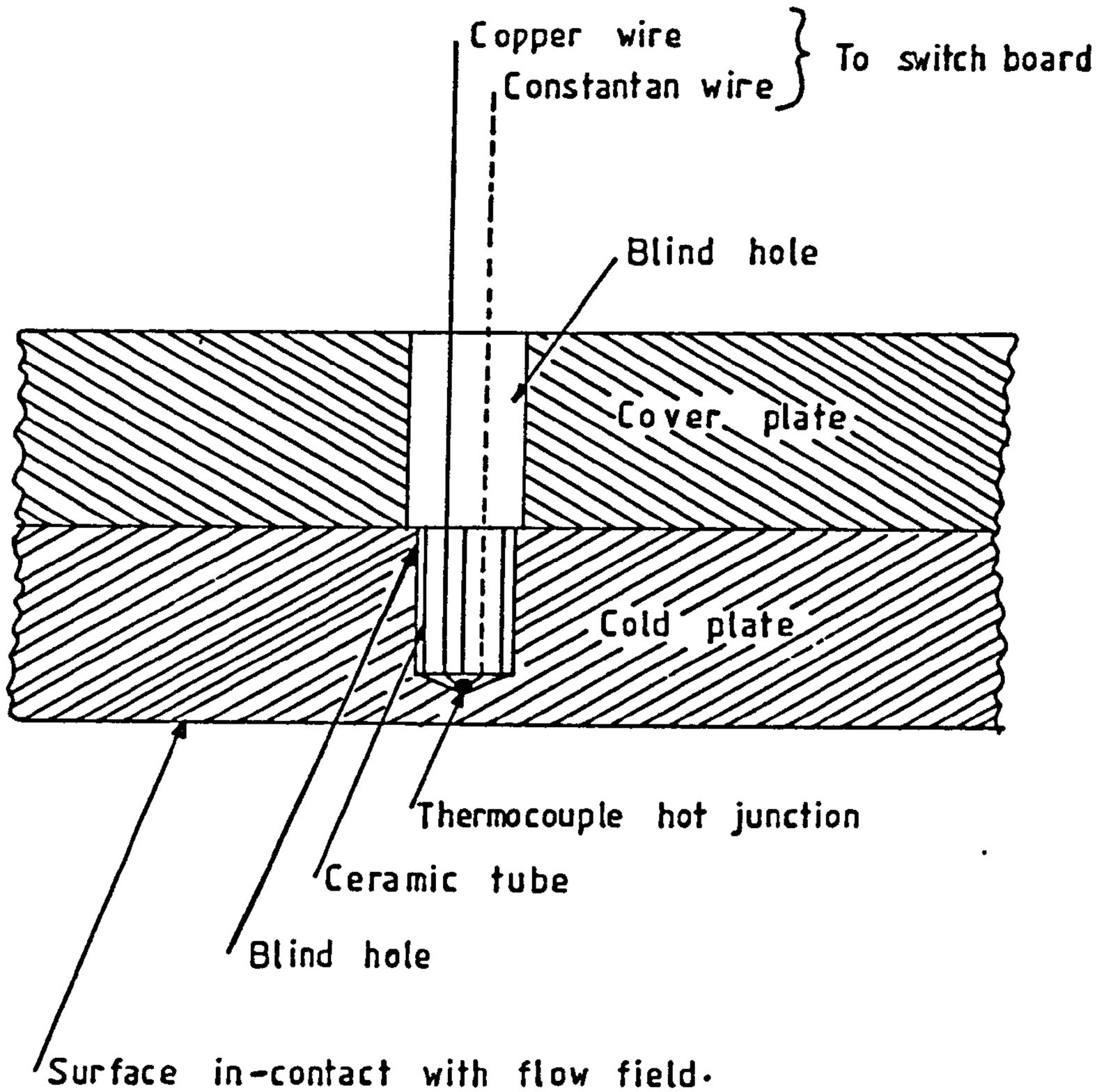

Fig. 20. A sketch indicating how thermo-junctions were fixed into the cold plate.

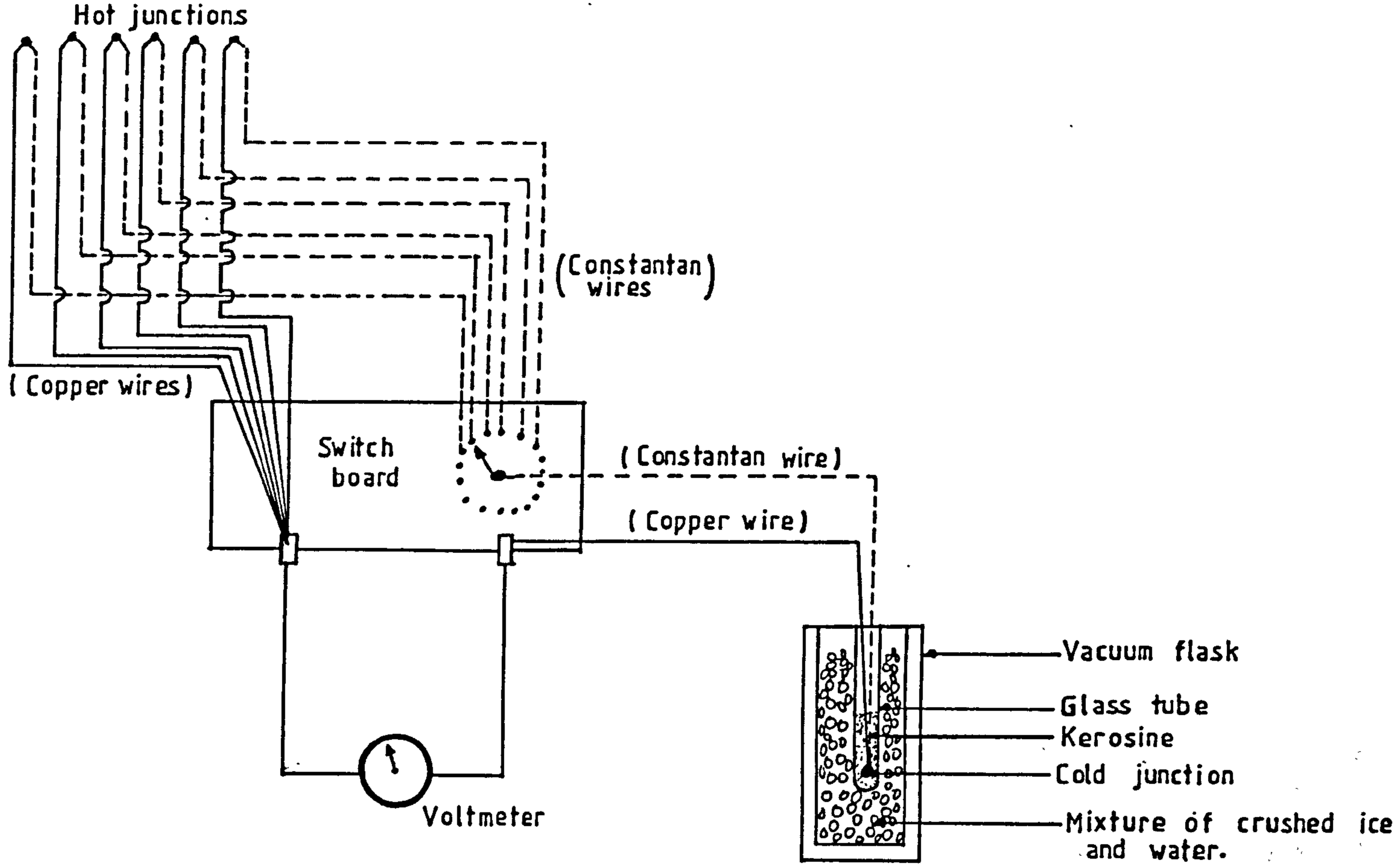

Fig·21 Thermocouple circuitry.

5.5 DATA REDUCTION.

The temperature of the hot surface was taken as the reference temperature. With the help of a travelling microscope, the distances of a maximum of four fringes from the hot surface were measured. If by observation, the first dark fringe from the hot surface was found not to lie within the reference boundary, then the temperature associated with the fringe was different from that of the reference hot surface. The relationship between them is expressed by equation (138), in-terms of the fringe shift. To determine this fringe shift from the interferogram, the distances from the hot surface, of the first and second fringes were measured. Because the fringe shift between the first and second fringes equals unity, direct proportionality between the distances and fringe shift was used to estimate the fringe shift between the first dark fringe and the reference hot surface. For example, if the distance between the reference hot surface and the first fringe was found to be y_1 and that of the second found to be y_2. Then the distance between the first and the second fringes was $(y_2 - y_1)$. This distance corresponds to unit fringe shift.
By using the direct proportionality therefore, we have:-

$$\frac{1}{(Y_2 - Y_1)} = \frac{FS}{Y_1} \qquad (141)$$

Therefore,

$$FS = Y_1 / (Y_2 - Y_1) \qquad (142)$$

where FS is the fringe shift between the first fringe and the reference hot surface.
The fringe shift between the second fringe and the hot surface would be:-

$$FS = 1 + FS \qquad (143)$$

whereas the fringe shift between the reference hot surface and the third and fourth fringes,would be respectively:-

$$FS = 2 + FS \qquad (144)$$

$$FS = 3 + FS \qquad (145)$$

If, however, the first fringe was observed to lie within the reference boundary, then:-

$$FS = 1,\ FS = 2,\ FS = 3 \text{ and } FS = 4 \qquad (146)$$

With the distances and fringe shifts determined, the temperature ratios T/T_o, were calculated from equations (138) and (140), and then converted to dimensionless temperature θ, as follows:-

$$\theta = \frac{[\ (T/T_o) - (T_c/T_o)\ ]}{[\ 1 - (T_c/T_o)\ ]} \qquad (147)$$

where the reference temperature T_o is equal to that of the hot plate and T_c being the temperature of the cold plate.
The measured distances were also non-dimensionlized by dividing the distances by the height of the interferogram, i.e. $Y_1 = y_1/L$, $Y_2 = y_2/L$, $Y_3 = y_3/L$ and $Y_4 = y_4/L$. The results would then look as follows:-

Fringe number.	Dimensionless temperature.	Dimensionless distance from the hot plate.
0	1.0	0
1	θ_1	Y_1
2	θ_2	Y_2
3	θ_3	Y_3
4	θ_4	Y_4

It should be noted that fringe number zero corresponds to the hot surface.
Recall, i.e. equation (52), that the Nusselt number on the hot surface is given by:-

$$Nu = - \left.\frac{\partial\theta}{\partial Y}\right|_{Y=0}$$

By using the straight line least-squares fit therefore, the temperature gradient at Y=0 was obtained which gave the Nusselt number values. This was done at various sections of the central air-cell to obtain the local Nusselt numbers from which the averages were obtained.

5.6 RESULTS AND DISCUSSIONS.

Fig.22 shows the graph of the average Nusselt number on the hot plate against temperature difference between the hot and cold plates, for the constant cell width of 10mm and cell-heights of 10mm, 20mm and 50mm considered, at $\Phi = 30°$.

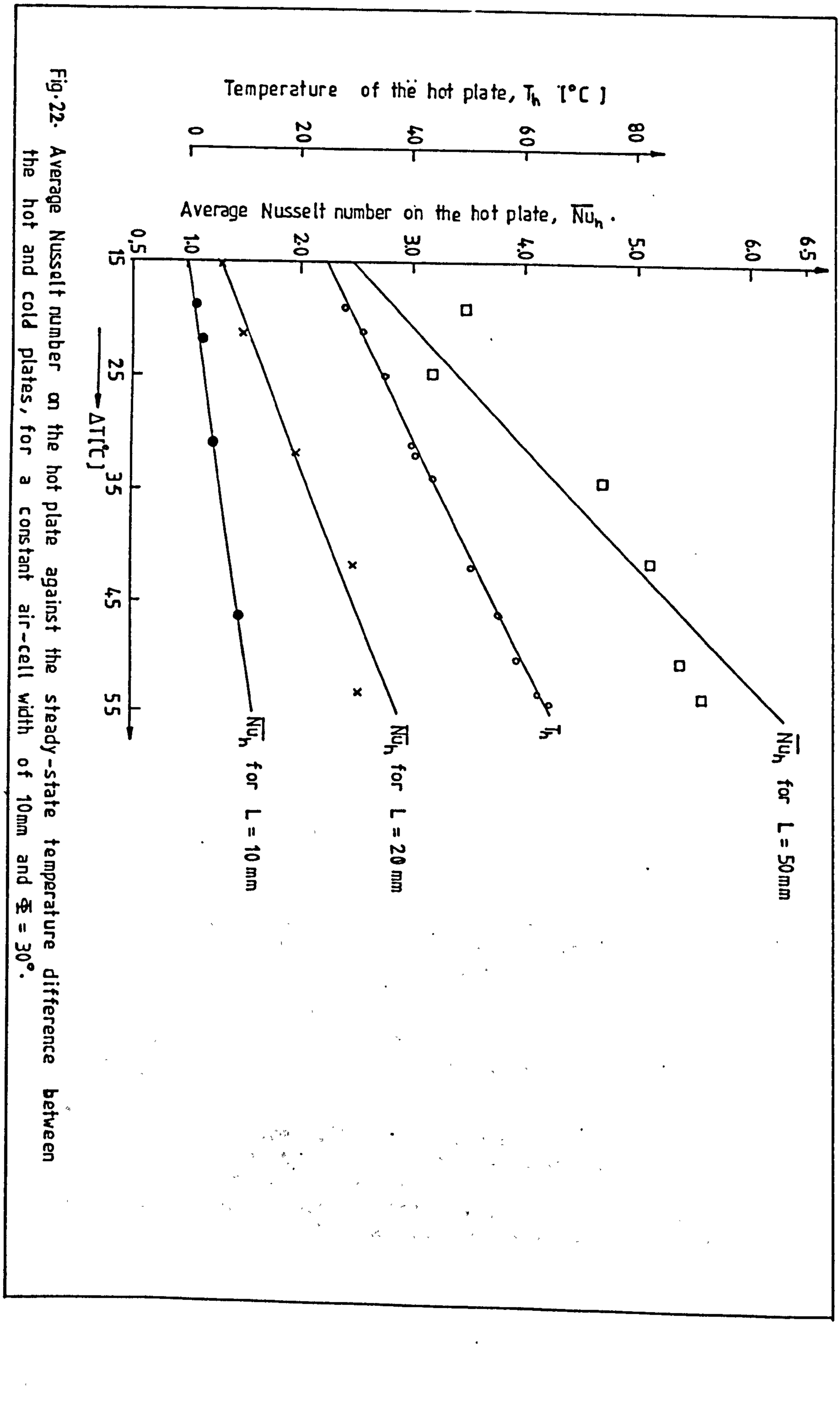

Fig.22. Average Nusselt number on the hot plate against the hot and cold plates, for a constant air-cell width of 10mm and $\phi = 30°$. steady-state temperature difference between

The temperatures attained on the hot surface are also indicated. These results were then converted to show the effect of the air-cell height on the overall convective heat transfer coefficient, for the constant cell-width of 10mm.This is shown in fig.23, where the overall convective heat transfer coefficient is plotted against the cell-height for fixed temperature differences between the hot and cold plates.

The results show that as the height of the air-cells was changed from 10mm through to 50mm, the overall convective heat transfer coefficient decreased. However, the decreases with height was only significant up to a height of about 30mm. Beyound this height, further increases did not result in any appreciable changes in the convective heat transfer coefficient. For example, at a temperature difference of 55°C, an increase in height from 10mm to 30mm accounted for about 82% of the total decrease in the overall heat transfer coefficient as the height was changed from 10mm to 50mm.

Figs.24 and 25 show some of the experimentally-measured local Nusselt number distributions for L=10mm and 20mm respectively, as compared with those predicted numerically. The measured and numerically- predicted distributions and values compare fairly favourably for L=10mm (i.e. A_x=1.0) as they do with the results of Meyer et al (Ref.20 and 25) previously shown. As the height increases from 10mm, the numerically- predicted and the experimentally measured Nusselt number distribution patterns remain similar. However, the numerically- predicted values become less than the experimentally- measured values. For example, the numerically- predicted average values are less by about 15%, 23% and 29% at ΔT=15.3°C, 21.3°C and 24.6°C respectively for L=20mm shown in fig.25.

The differences in magnitudes is basically thought to occur from the differences between the nature of flow predicted using the model and that obtained in practice within the test-cells. For example, Fig.26 shows the numerically-predicted flow pattern for L=20mm and ΔT=54°C (which was the highest temperature difference measured for this height), as that of a single-roll-cell rotating about an axis along the upslope direction. Whereas, a simple flow visualization tests for L=20mmm, revealed the formation of a vortex near the hot plate at ΔT=17.7°C. However, at ΔT=9.3°C, only a single-roll-cell (described earlier) was observed.

As the temperature difference increases, it is expected that a second vortex might be formed near the cold surface and rotating in the same direction to that formed near the hot plate, thus resulting into a stagnant layer of air at the central region of the air-cells.A similar effect is

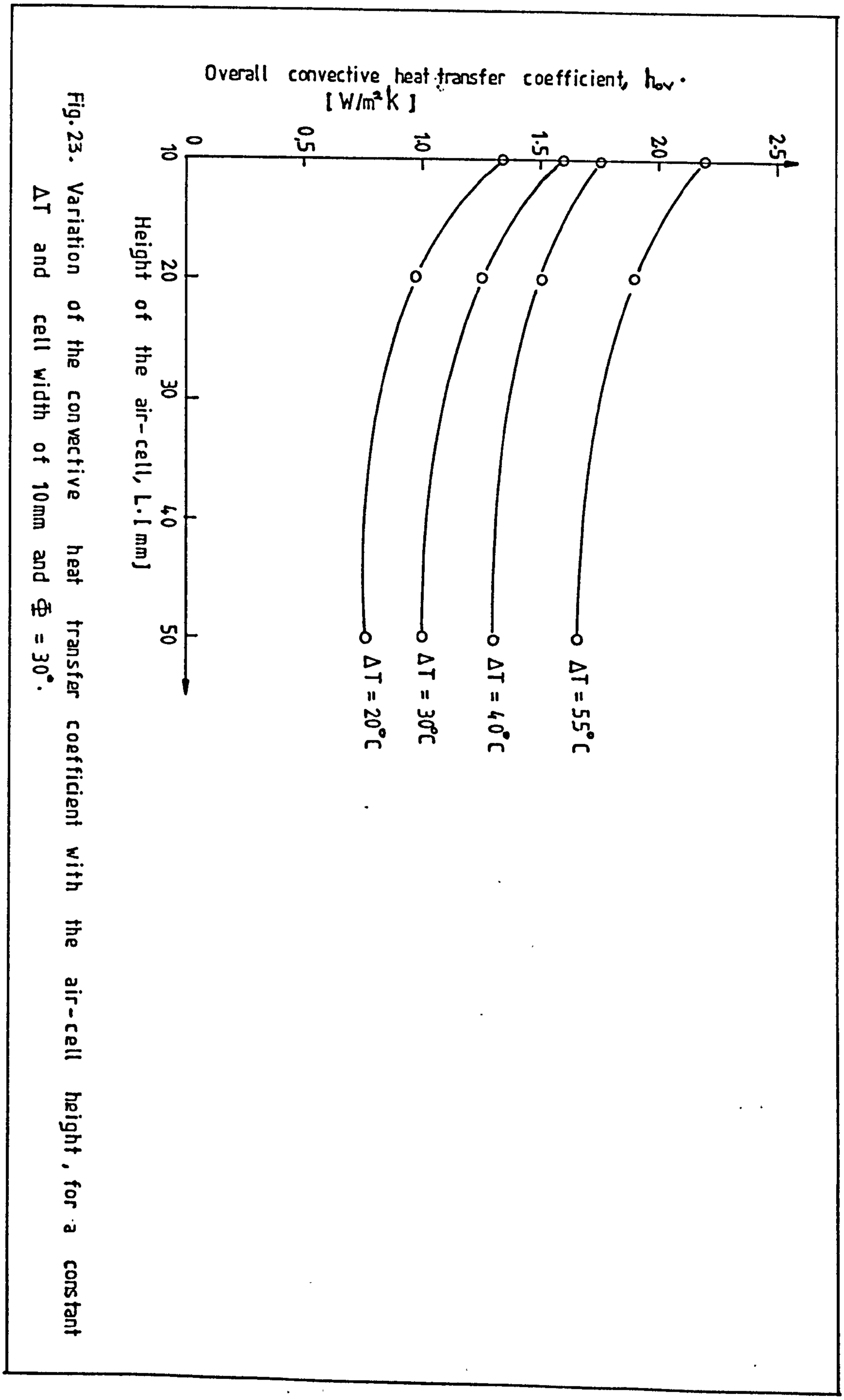

Fig. 23. Variation of the convective heat transfer coefficient with the air-cell height, for a constant ΔT and cell width of 10mm and $\phi = 30°$.

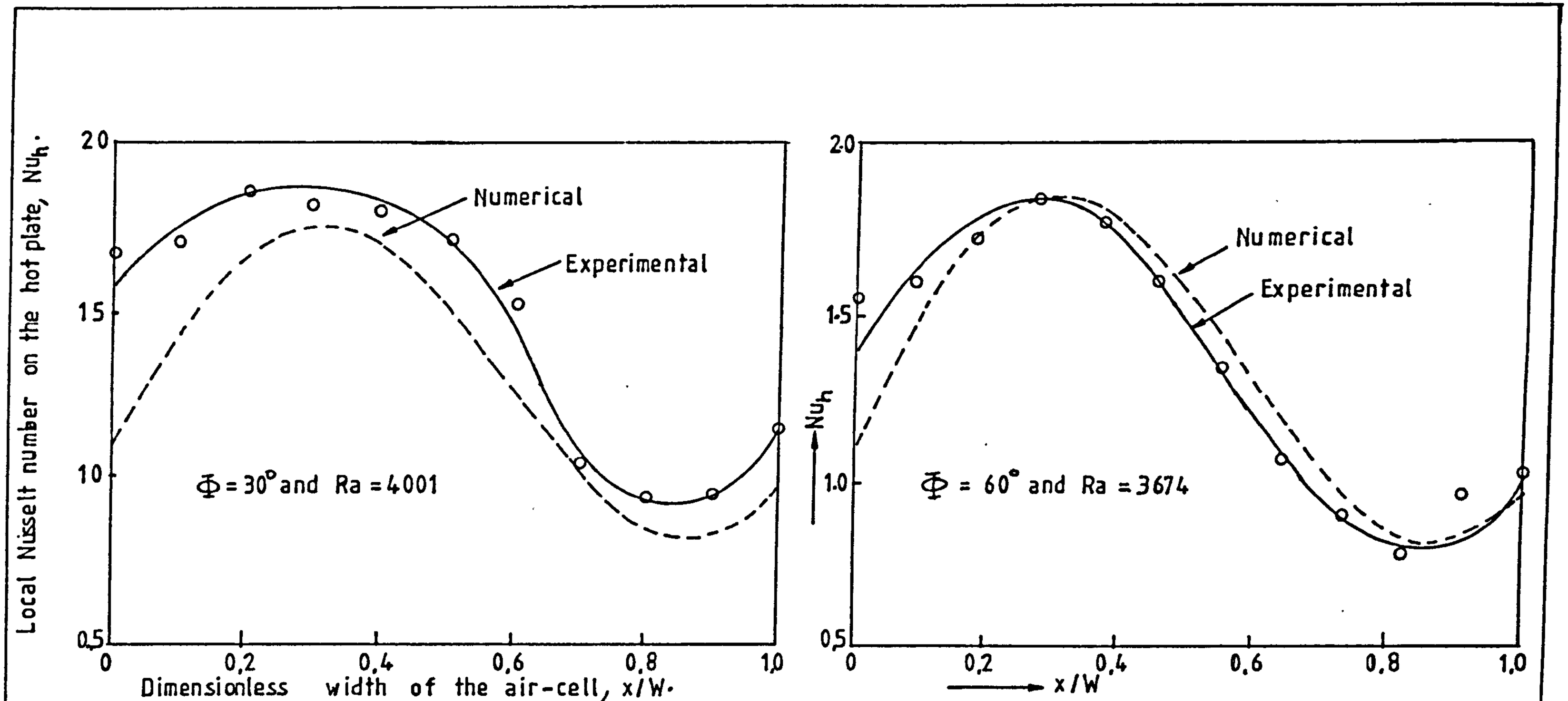

Fig.24. Comparison between this study's experimentally-measured and numerically-predicted local Nusselt numbers for A_r = 1.0.

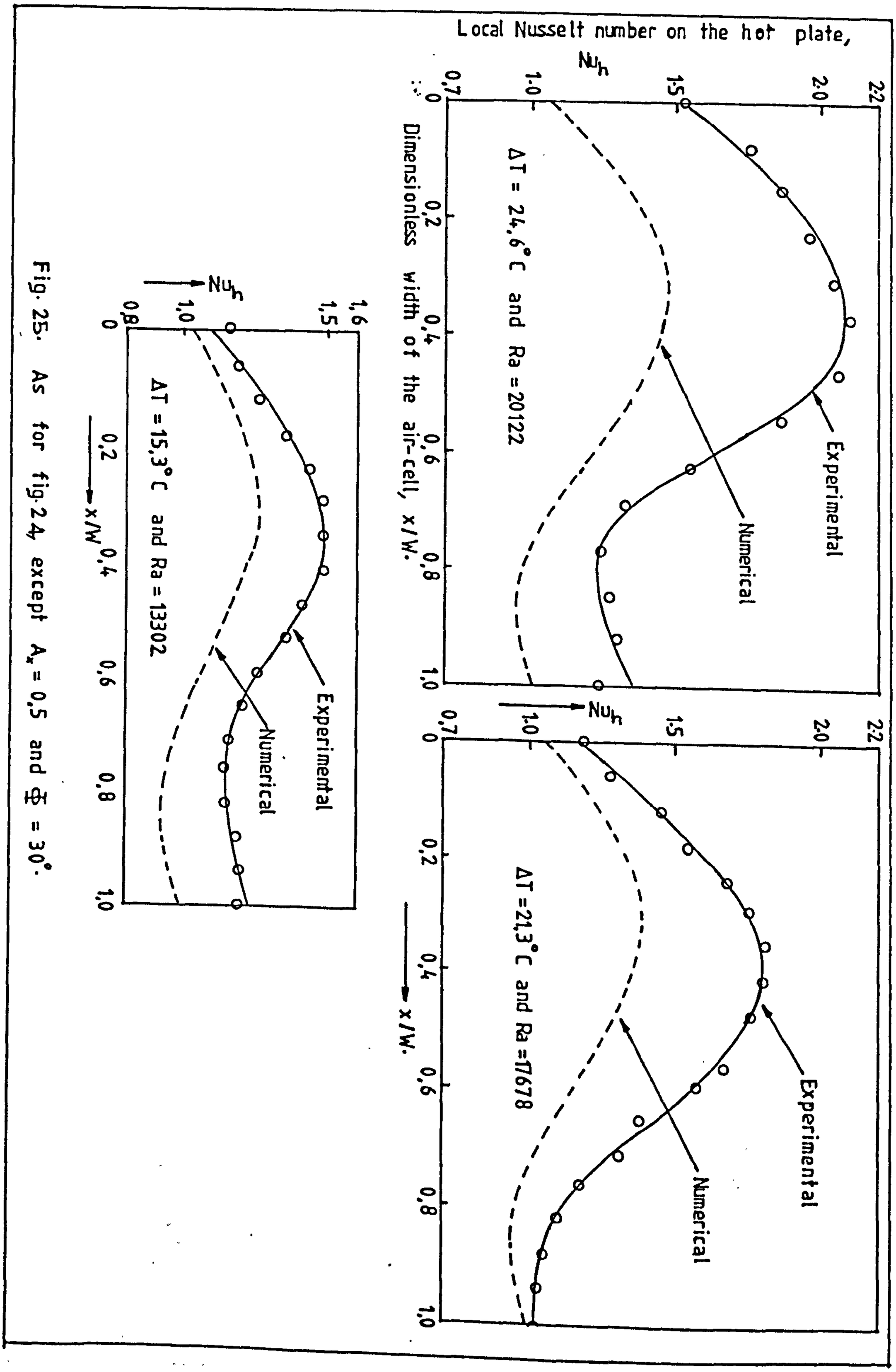

Fig. 25. As for fig. 24 except $A_x = 0,5$ and $\Phi = 30°$.

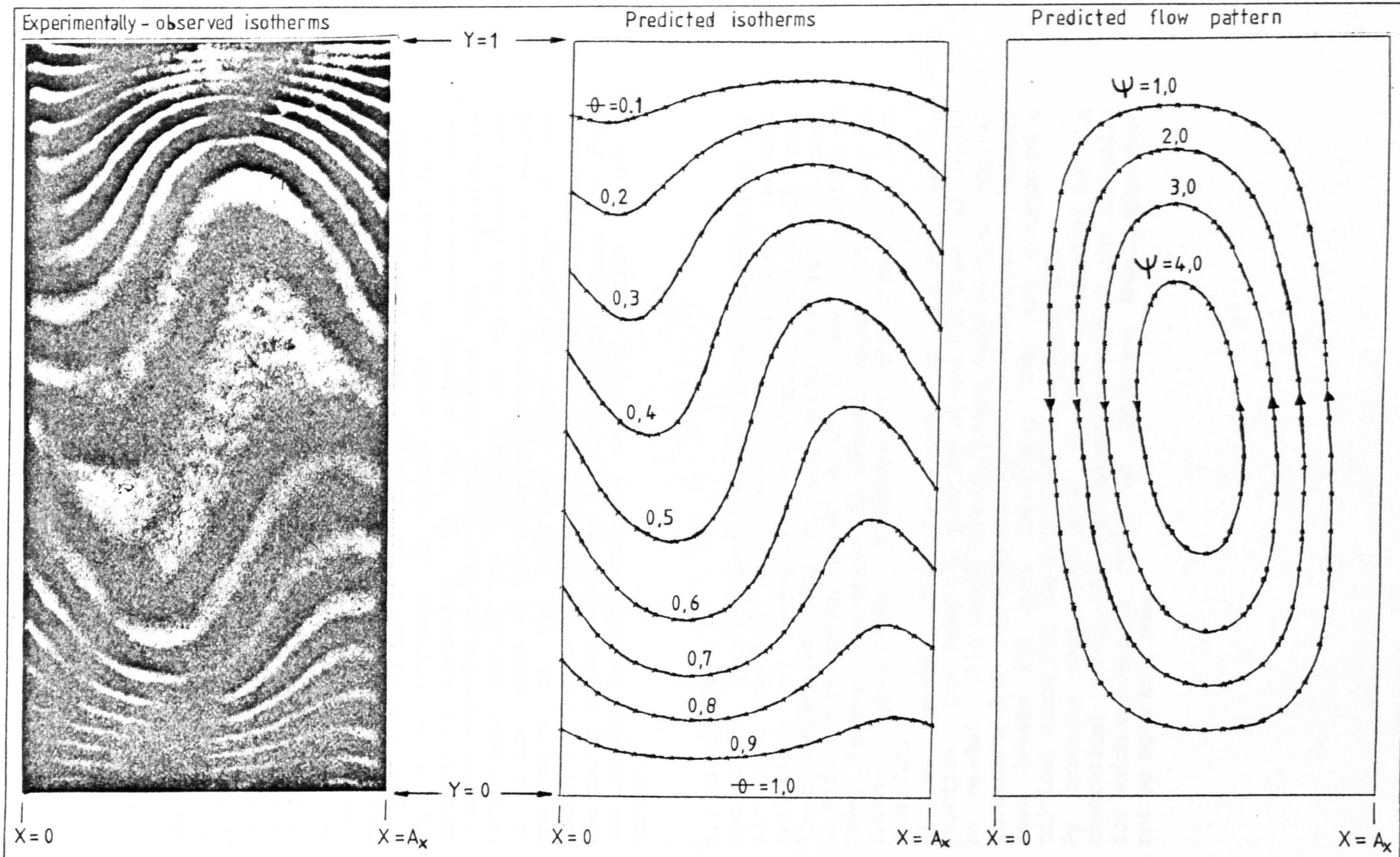

Fig·26· Experimentally-observed and numerically-predicted isotherms for $A_x = 0,5$, $\Delta T = 54°C$, $Ra = 34090$ and $\Phi = 30°$. Predicted flow pattern is also indicated.

expected to occur if the height, rather than ΔT, is increased. This point could be made clearer if we refer to the interferograms shown in figs.27 and 28. It is evident that as the height of the air-cells was increased from 10mm to 50mm for about the same ΔT, a wide stagnant central region of uniform temperature was formed. This argument was found to explain the results shown in fig.23, where the overall convective heat transfer coefficient was found to decrease with increases in the cell height, for the same ΔT.

However, as the height is further increased, the stagnant central region could become unstable and thus breaks up into a third vortex.It is thought that once this occurs, any further increases in height would not result in any appreciable reduction in the overall convective heat transfer coefficient.This latter argument was explained by Koutsoheras (Ref.19) as follows:- As the hot fluid rises around the region of the right hand spacer and falls around the region of the left hand spacer; and because of the relatively longer distance of travel upwards and downwards, the centre region which has low convective motion and thus low inertia becomes unstable and thus breaks up into a vortex.

5.7 CONCLUSIONS

The results obtained show that increasing the height of the air-cells, created by using a slatted CSD, for a constant cell-width and temperature difference, would result into lower convective heat transfer rates. However, the most significant reduction would occur at about a height of 30mm. Further increases in height would not result in further appreciable decreases in the convective heat transfer.

If we consider that the higher the air-cells are in practice, the more the quantity of the CSD material would be needed. This would certainly mean high initial capital investment for the CSD structures. As a compromise between heat losses and cost therefore, 30mm was considered a critical value for the height of the slatted CSD.

By relating this conclusion to that arrived at in the theoretical study, the corresponding width of the air-cells for which convection could be minimized should therefore not be more than 6mm.

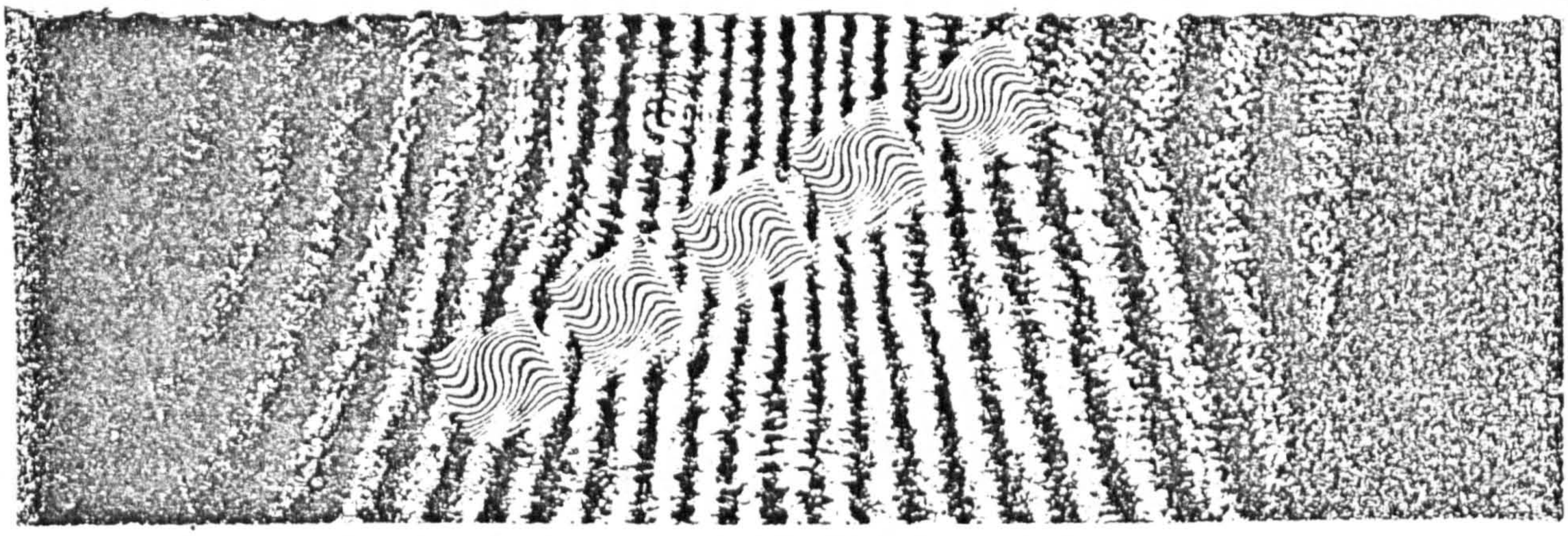

Fig.27a. Interferogram for L=10mm (A_x = 1,0), ΔT=46.2° C, Ra = 4001 and Φ = 30°.

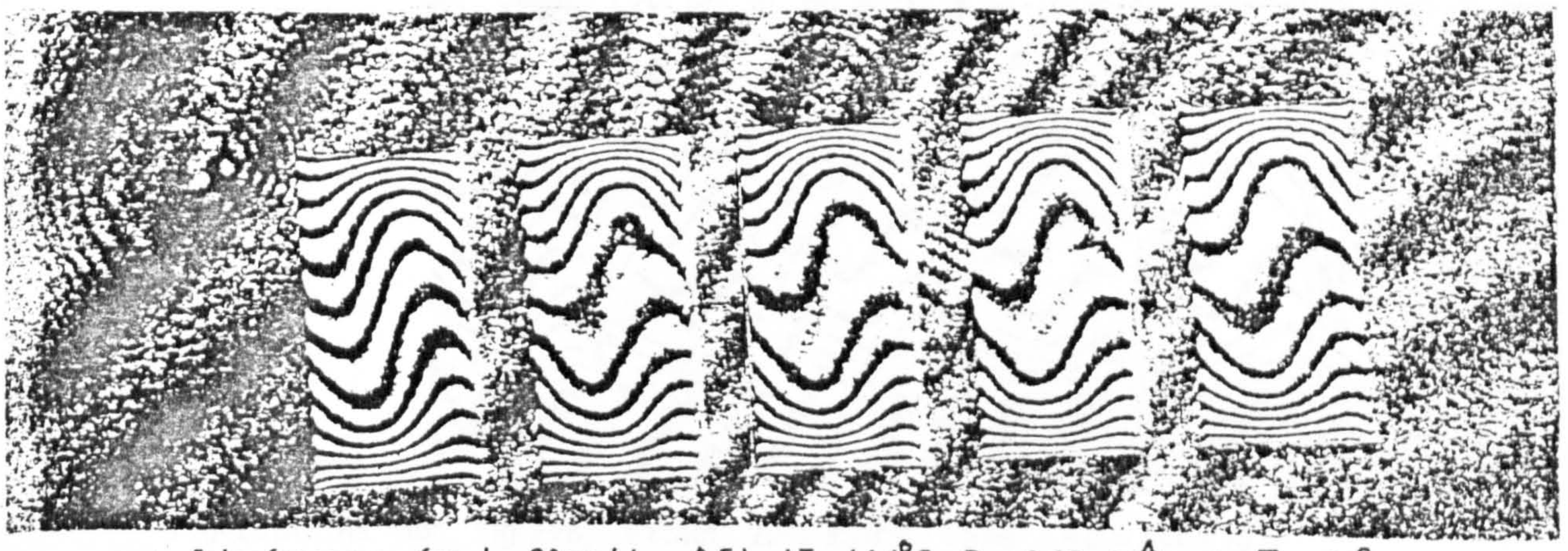

Fig.27 b. Interferogram for L = 20mm (A_x = 0,5), ΔT = 41.6° C, Ra = 2.93×10^4 and Φ = 30°.

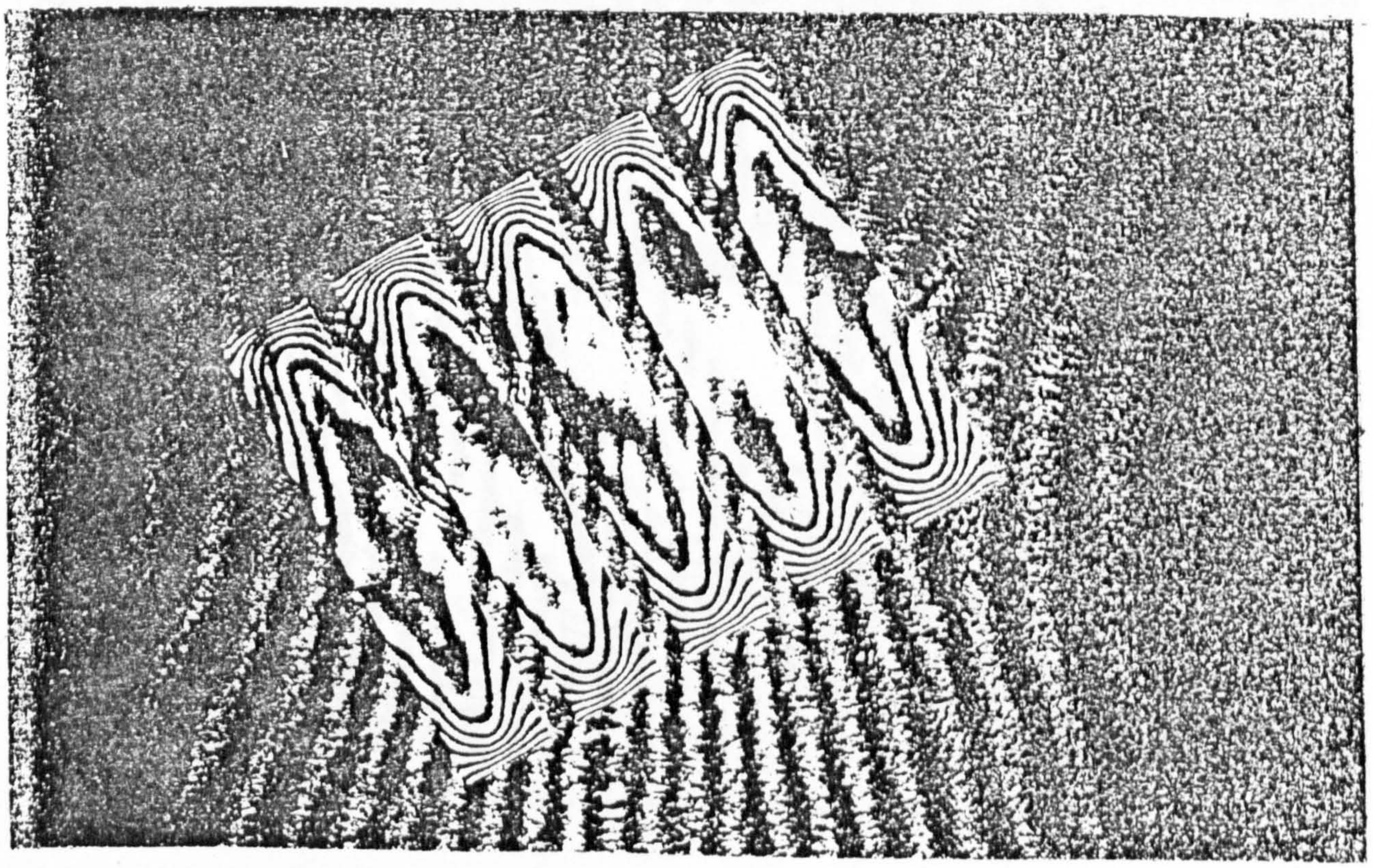

Fig.27c. Interferogram for L = 50mm (A_x = 0,2), ΔT = 41.4° C, Ra = 4.67×10^5 and Φ = 30

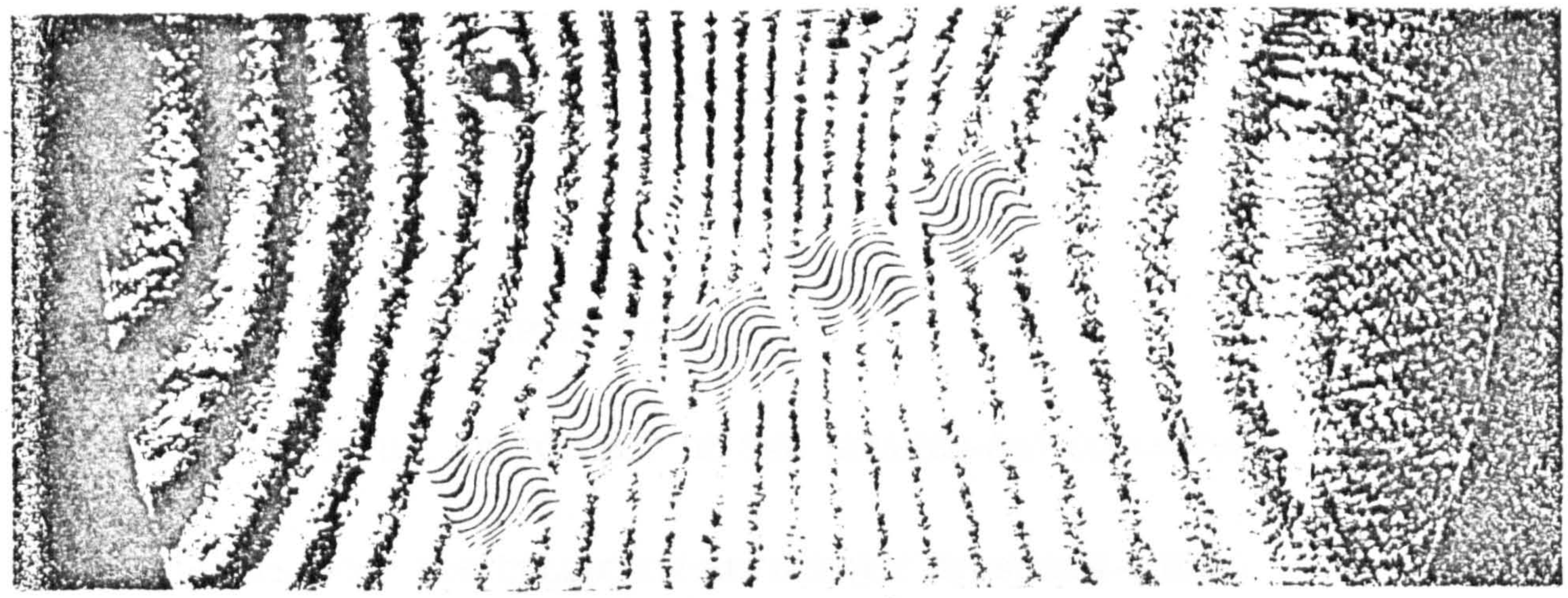

Fig-28a. As for fig-27a, except $\Delta T = 30,8^{\circ}C$ and $Ra = 3013$

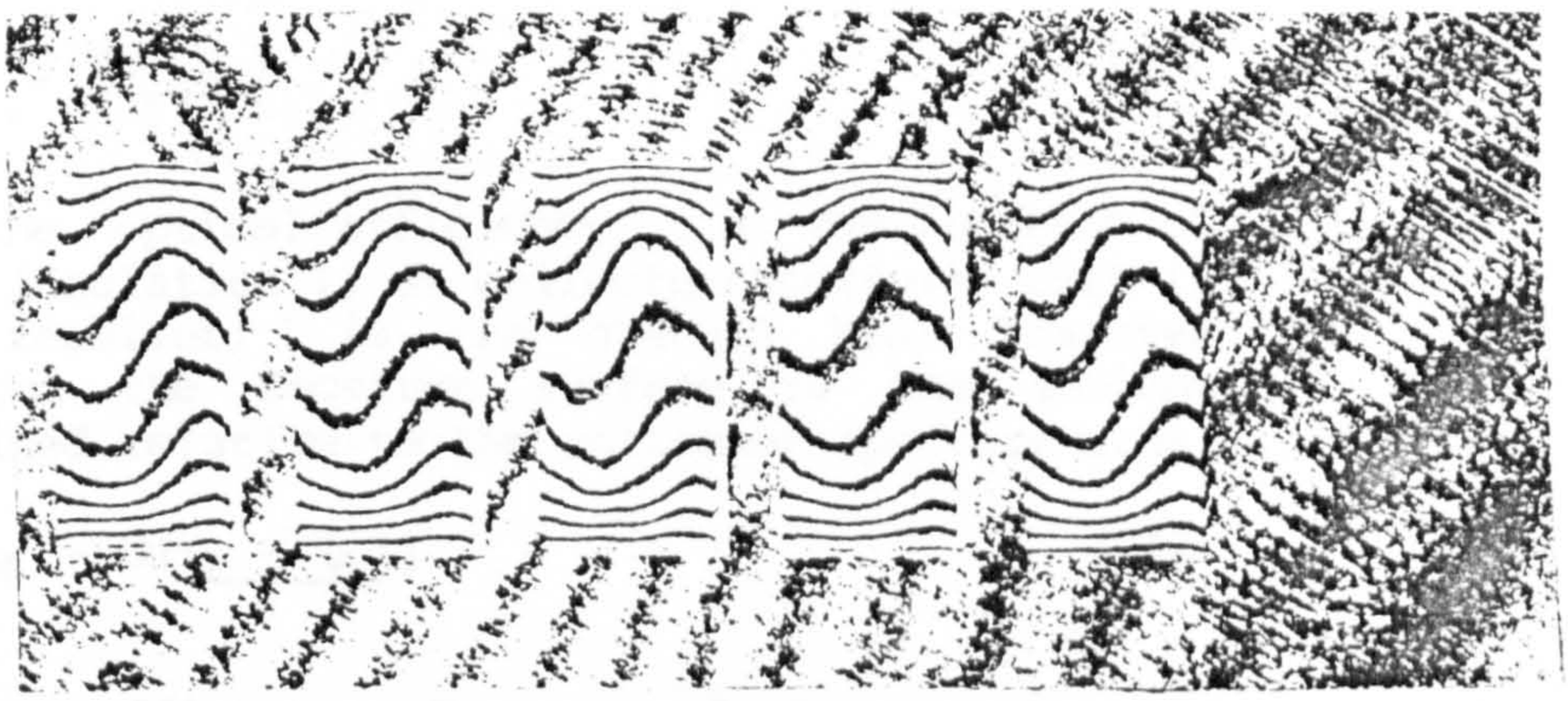

Fig. 28b. As for fig-27b, except $\Delta T = 31.8^{\circ}C$ and $Ra = 2.46 \times 10^{4}$.

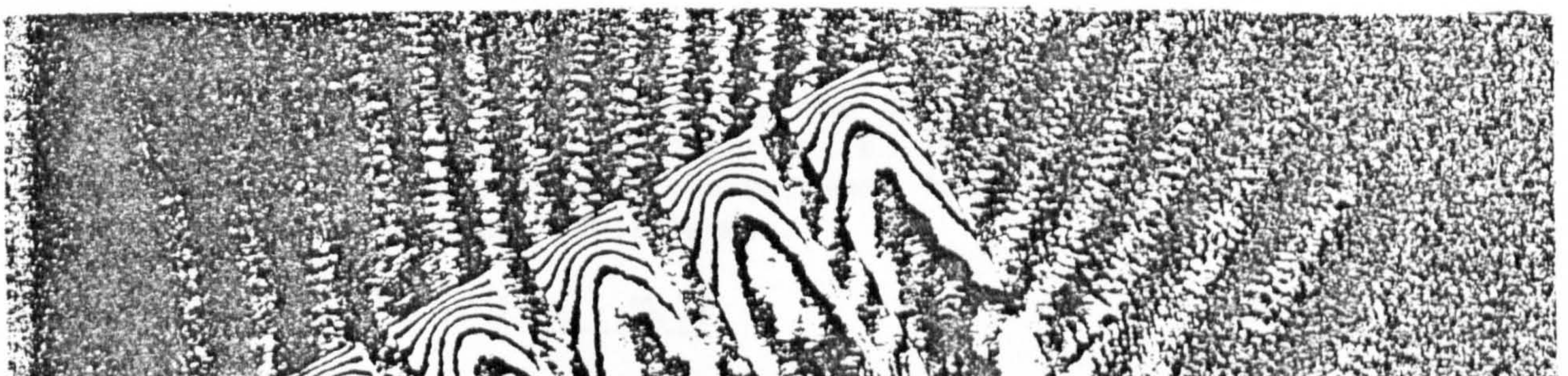

Fig-28c. As for fig-27c, except $\Delta T = 34.1^{\circ}C$ and $Ra = 4.03 \times 10^{5}$

CHAPTER SIX

PREDICTION OF THE EFFICIENCY OF THE SLATTED-CSD COLLECTOR.

6.1 EXPRESSIONS FOR COLLECTOR EFFICIENCY AT STEADY-STATE.

The following expressions may be used in defining the steady-state collector efficiency (Ref.35):-

$$(i)\ \eta_{col} = \eta_{op} - U\frac{(T_r - T_a)}{I} \qquad (148)$$

where η_{op} is the optical efficiency, i.e. the fraction of the total solar insolation I, at collector aperture that is absorbed by the receiver; U is the overall heat transfer coefficient from the receiver surface to the ambient environment defined relative to the collector aperture area.

$$(ii)\ \eta_{col} = F'\left[\eta_{op} - U\frac{(T_f - T_a)}{I}\right] \qquad (149)$$

where F' is the efficiency factor and T_f is the mean temperature of the heat removing fluid, i.e.,

$$T_f = (T_{in} + T_{out})/2 \qquad (150)$$

The efficiency factor is generally the ratio of the thermal conductance from the heat removing fluid to the ambient environment, to the thermal conductance from the receiver surface to the ambient environment.

$$(iii)\ \eta_{col} = F_R\left[\eta_{op} - U\frac{(T_{in} - T_a)}{I}\right] \qquad (151)$$

where F_R is the heat removal factor. It relates the actual useful gain of the collector to the useful gain if the whole collector surface were at the fluid inlet temperature.

$$(iv)\ \eta_{col} = \frac{F_R}{\left(1 - \frac{F_R U A'_p}{\dot{m} C_p}\right)}\left[\eta_{op} - U\frac{(T_{out} - T_a)}{I}\right] \qquad (152)$$

where A'_p is the collector aperture area and $\dot{m}$ and C_p are the mass flow rate and specific heat at constant pressure respectively, for the heat removing fluid.

The first expression is more convenient in expressing a theoretically- predicted efficiency, whereas the others

hold when experimental data are to be correlated.

6.2 THE OVERALL HEAT TRANSFER COEFFICIENT, U.

Because the ultimate objective in using the CSD will be to completely suppress convection, it was therefore assumed that for average receiver surface temperatures of up to 150°C, the convective flow will remain within the base flow regime (Ref.17). Heat losses from the receiver would therefore occur by conduction and radiation across the air-gap, conduction through the spacers and the insulation at the back of the receiver. It should be noted that m air-cells of width W each would be formed using (m+1) spacers of thickness t each; And that the aperture width of the collector unit so formed would be:-

$$W_{Col} = [m\,W + (m+1)t] \tag{153}$$

whereas, the collector aperture area A'_p would be:-

$$A'_p = Z\,W_{Col} = Z[m\,W + (m+1)t] \tag{154}$$

To facilitate visualization of the collector, refer to fig.2. To further facilitate perception, all quantities associated with the collector's receiver and glazing would henceforth be subscripted with the letters r and g respectively.

6.2.1 Heat transfer coefficient for radiation between the receiver and the glazing, h_1.

The net rate of heat losses $\dot{Q}_1$, by thermal radiation from the receiver area A'_r, may be expressed as follows (Ref.37):-

$$\dot{Q}_1 = \frac{A'_r \sigma (T_r^4 - T_g^4)}{\left(\frac{(1-\varepsilon_r)}{\varepsilon_r} + \frac{1}{(A'_r/A'_g)F_{rg}} + \frac{(1-\varepsilon_g)}{\varepsilon_g}\frac{A'_r}{A'_g}\right)} \tag{155}$$

where F_{rg} is the radiation view factor for the two areas. However, $A'_r = A'_g = mWZ$. Therefore, the radiative heat flux $\dot{q}_1$ with respect to the aperture area can be expressed as:-

$$\dot{q}_1 = \frac{m\,W\sigma(T_r^4 - T_g^4)}{\left(\frac{(1-\varepsilon_r)}{\varepsilon_r} + \frac{1}{F_{rg}} + \frac{(1-\varepsilon_g)}{\varepsilon_g}\right) W_{Col}} \tag{156}$$

The heat transfer coefficient for radiation h_1, from the receiver to the glazing with respect to the aperture area,

can therefore be expressed as:-

$$h_1 = \frac{\dot{q}_1}{(T_r - T_g)} \qquad (157)$$

6.2.2 The heat transfer coefficient for conduction via the air-gap, h_2.

The rate of heat losses via conduction across the air-gap may be expressed according to Fourier's law (Ref.36), i.e.:-

$$\dot{Q}_2 = A'_r \, K_a \frac{(T_r - T_g)}{L} \qquad (158)$$

The conductive heat flux rate $\dot{q}_2$, with respect to the aperture area may be expressed as:-

$$\dot{q}_2 = m \, W \, K_a \frac{(T_r - T_g)}{L \, W_{col}} \qquad (159)$$

It therefore follows that the conductive heat transfer coefficient h_2, would be:-

$$h_2 = \frac{\dot{q}_2}{(T_r - T_g)} \qquad (160)$$

6.2.3 The heat transfer coefficient for conduction via the CSD structures, h_3.

By using the Fourier's law as well, the rate of heat losses via conduction through the spacers can be expressed as follows:-

$$\dot{Q}_3 = (m + 1) \, t \, Z \, K_s \frac{(T_r - T_g)}{L} \qquad (161)$$

The conductive heat flux rate $\dot{q}_3$, with respect to the aperture area would therefore be:-

$$\dot{q}_3 = (m + 1) \, t \, K_s \frac{(T_r - T_g)}{L \, W_{col}} \qquad (162)$$

Therefore, the heat transfer coefficient for conduction via the spacers would be:-

$$h_3 = \frac{\dot{q}_3}{(T_r - T_g)} \qquad (163)$$

6.2.4 The heat transfer coefficient for conduction across the back insulation of thickness d.

The rate of heat losses via conduction across the back insulation of thermal conductivity K_b may be expressed according to Fourier's law as:-

$$\dot{Q}_6 = Z\, W_{col}\, K_b \frac{(T_r - T_a)}{d} \qquad (164)$$

The conductive heat flux rate $\dot{q}_6$, with respect to the aperture area would be:-

$$\dot{q}_6 = K_b \frac{(T_r - T_a)}{d} \qquad (165)$$

Therefore, the heat transfer coefficient h_6, can be expressed as:-

$$h_6 = \frac{\dot{q}_6}{(T_r - T_a)} \qquad (166)$$

6.2.5 The heat transfer coefficient for convection over the glazing.

Duffie and Beckman (Ref.37) intimated that the heat transfer coefficient for forced convection over the flat glazing, may be estimated from:-

$$h_4 = 5.7 + 3.8\, v \qquad (167)$$

where v is the estimated wind speed in m/s.

6.2.6. Heat transfer coefficient for radiation from the glazing to the surrounding environment.

The net rate of heat losses via radiation from the glazing to the surroundings may be expressed as (Ref.37):-

$$\dot{Q}_5 = Z\, W_{col}\, \varepsilon_g \sigma (T_g^4 - T_a^4) \qquad (168)$$

The radiative heat flux rate $\dot{q}_5$, with respect to the aperture area would be:-

$$\dot{q}_5 = \varepsilon_g \sigma (T_g^4 - T_a^4) \qquad (169)$$

Therefore, the heat transfer coefficient for radiation h_5, from the glazing to the surroundings, may be expressed as:-

$$h_5 = \frac{\dot{q}_5}{(T_g - T_a)} \qquad (170)$$

6.2.7 Expression for the overall heat transfer coefficient.

The equivalent thermal circuit for the steady-state heat losses from the receiver of the slatted CSD collector, to the surroundings is depicted in fig.29. It can be shown by electrical network analysis that the overall heat transfer coefficient is given by:-

$$U = [\, h_6 + U_t \,] \tag{171}$$

where U_t is the heat transfer coefficient from the receiver surface exposed to solar-radiation and the surroundings, i.e.,

$$U_t = \left[\frac{1}{(h_4 + h_5)} + \frac{1}{(h_1 + h_2 + h_3)} \right]^{-1} \tag{172}$$

In order to estimate the overall heat transfer coefficient at any chosen mean receiver temperature, the average temperature of the glazing must first be estimated. The process, however, is iterative because the temperature of the glazing is expressed in terms of heat transfer coefficients which depend on it. For example, by noting that the heat losses from the receiver surface (i.e. the surface exposed to solar-radiation) to the glazing, is the same as from the receiver surface to the surroundings, T_g can thus be expressed as:-

$$T_g = T_r - \frac{U_t}{(h_1 + h_2 + h_3)} (T_r - T_a) \tag{173}$$

For a chosen receiver temperature T_r, a guess was thus made for the value of T_g. The respective heat transfer coefficients that make up U_t were then evaluated. These were in turn used to evaluate a new value for T_g. This process was repeated until the values predicted for T_g converged. The overall heat transfer coefficient was then evaluated on the basis of the converged T_g value.

6.3 PREDICTED COLLECTOR EFFICIENCIES.

The collector considered is single glazed, i.e. using glass with $\tau_g = 0.90$ and $\varepsilon_g = 0.90$. Glass is considered for the glazing material because of its toughness and good weatherability. The receiver and the glazing are separated by a 30mm air-space. This being the critical height previously discussed. The air-space is subdivided into small air-cells each of width 4mm so that the air-cell aspect ratio is less than 0.2. The receiver is insulated

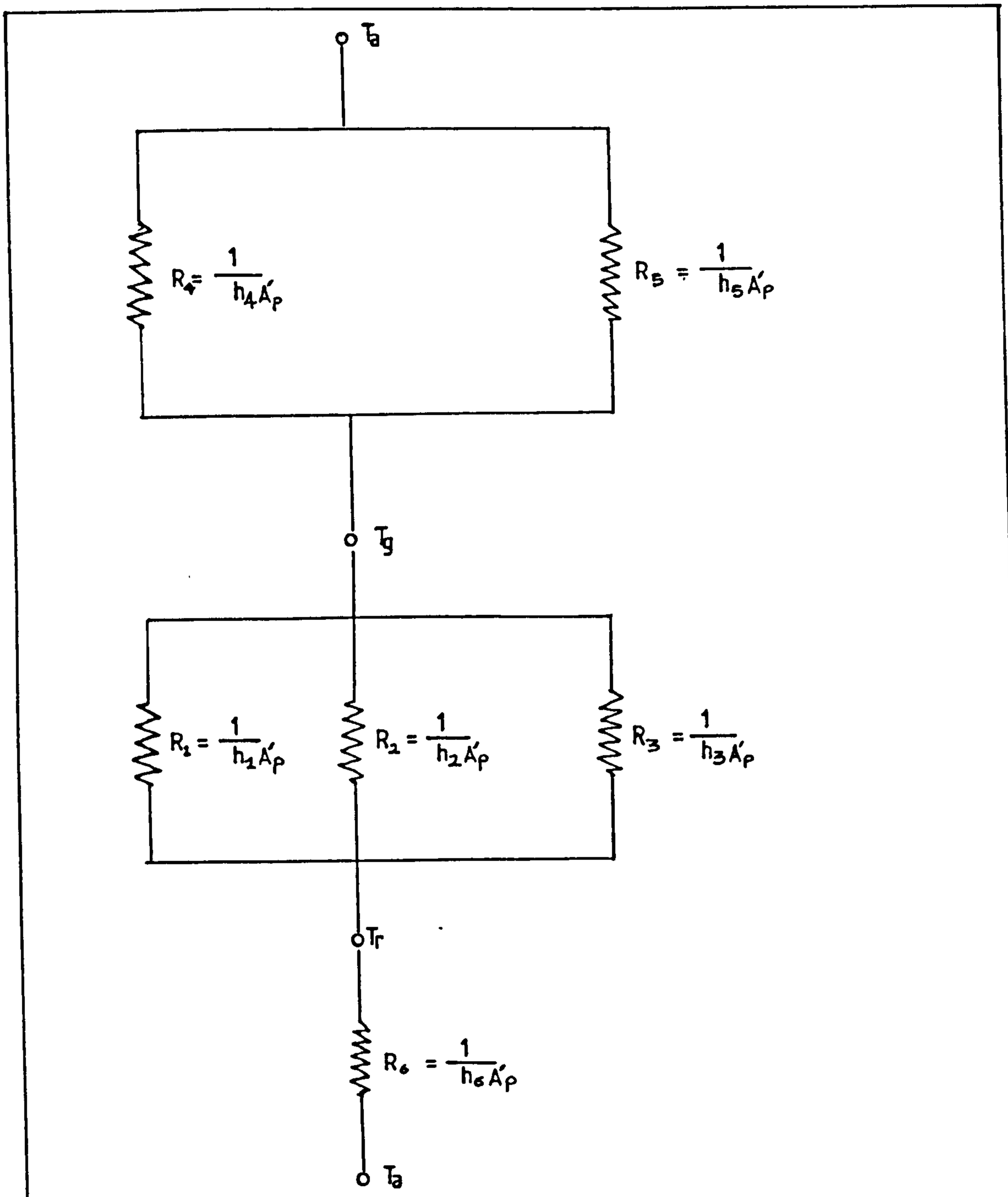

Fig. 29. The eqvivalent thermal circuit for the steady-state heat losses from the slatted-CSD collector.

from the back, using 5cm thick fibreglass of thermal conductivity of about Ø.Ø4 W/m K. A wind speed of about 3m/s is assumed, whereas the solar-radiation is taken at an average incidence angle of 3Ø°. At this incidence angle, solar radiation would cross about four spacers before reaching the receiver. This therefore allows the worst expected situation within about a five-hour daily collection of the Sun's energy to be studied.
Fig.3Ø shows the predicted efficiencies, as compared with that previously predicted for the GEC evacuated-tube collector, for the following specifications of the slatted-CSD collector design parameters.

(i) Graph B:-
Shows the slatted-CSD collector with a selective coating on the receiver plate and employing 1mm thick FEP Teflon spacers, i.e. ε_r=Ø.1Ø, α=Ø.9Ø, K_s=Ø.2Ø2 W/m K and t=1mm.

(ii) Graph C:-
As in B, except without selective coating, i.e. ε_r=Ø.9Ø, α=Ø.95, K_s=Ø.2Ø2 W/m K and t=1mm.

(iii) Graph D:-
Shows the slatted-CSD collector with a selective coating on the receiver plate and employing Ø.1mm thick glass spacers, i.e. ε_r=Ø.1Ø, α=Ø.9Ø, K_s=1.1 W/m K and t=Ø.1mm.

(iv) Graph E:-
As in D, except 1mm thick glass spacers employed, i.e. ε_r=Ø.1Ø, α=Ø.9Ø, K_s=1.1 W/m K and t=1mm.

Fig.31 shows the variation of the heat exergy rate per unit aperture area and the exergetic potential, with the mean receiver temperature for the collectors shown in fig.3Ø. The exergetic potential is a measure of the ability of the heat energy retained by the collector, to be translated to work, whereas the heat exergy is the maximum amount of the heat energy which is available to perform work (Ref.38).
It can be seen that the evacuated-tube collector shows better thermal performance than all the slatted-CSD collectors considered. However, the Slatted-CSD collector B which employs FEP Teflon as spacer material and with selective optical coating on the receiver surface shows the best thermal performance than that indicated for the standard collector without CSD. FEP Teflon would therefore be the best material for the spacer structures because of its low thermal conductivity of Ø.2Ø2 W/m K and high transmissivity of about Ø.96. Whereas glass has a thermal

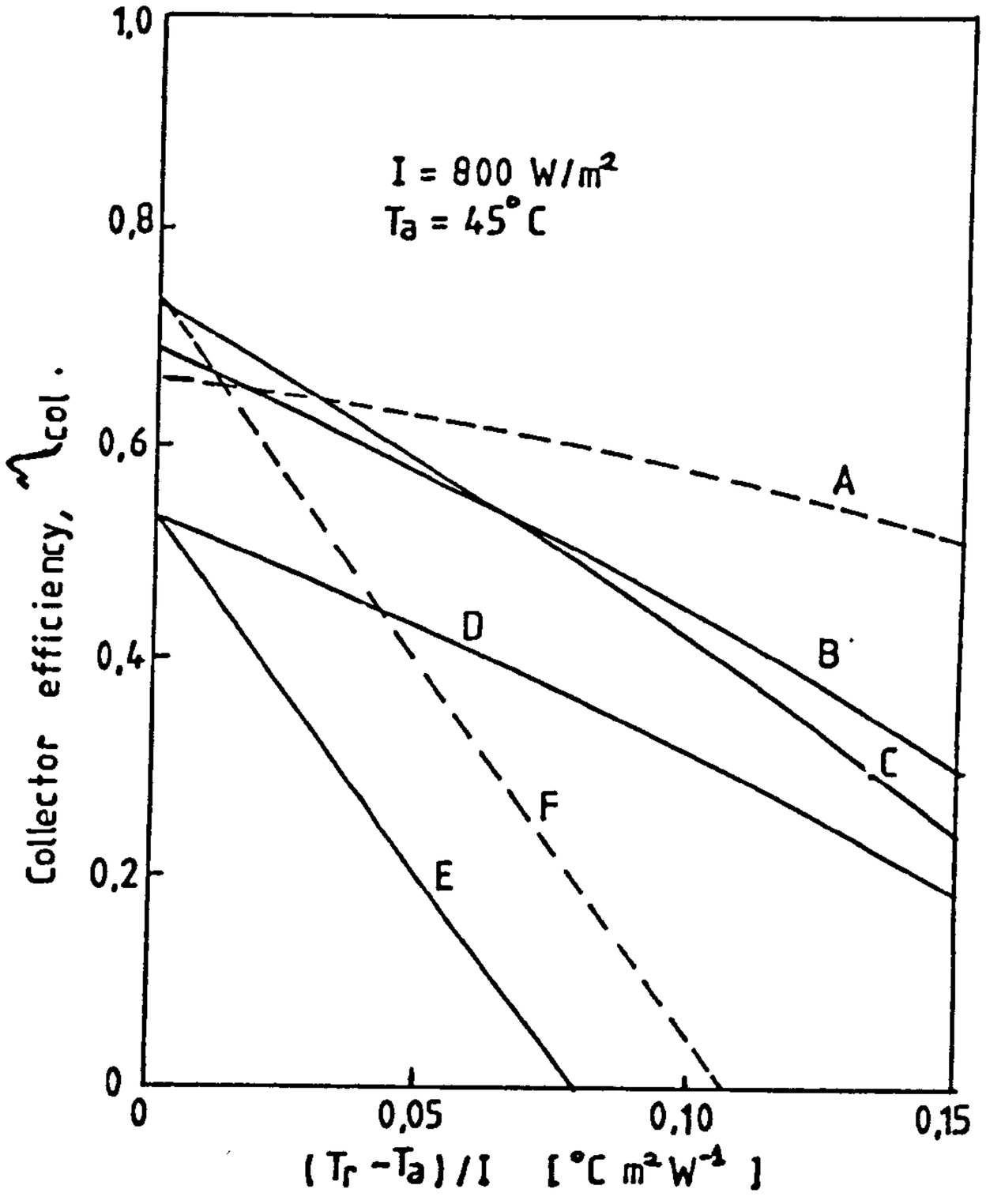

A Evacuated-tube collector.

B Slatted-CSD collector with selective optical coating and employing 1mm thick FEP Teflon as spacers, U ≃ 2.5 W/m²K.

C As in B, except without selective coating, U ≃ 3.0 W/m²K.

D As in B, except employing 0,1mm thick glass as spacers, U ≃ 2.2 W/m²K.

E As in B, except employing 1,0mm thick glass as spacers, U ≃ 6.7 W/m²K.

F Standard flat-plate collector (Ref. 17).

Fig. 30. Predicted efficiencies for the slatted-CSD collectors as compared with that predicted for the GEC evacuated-tube collector.

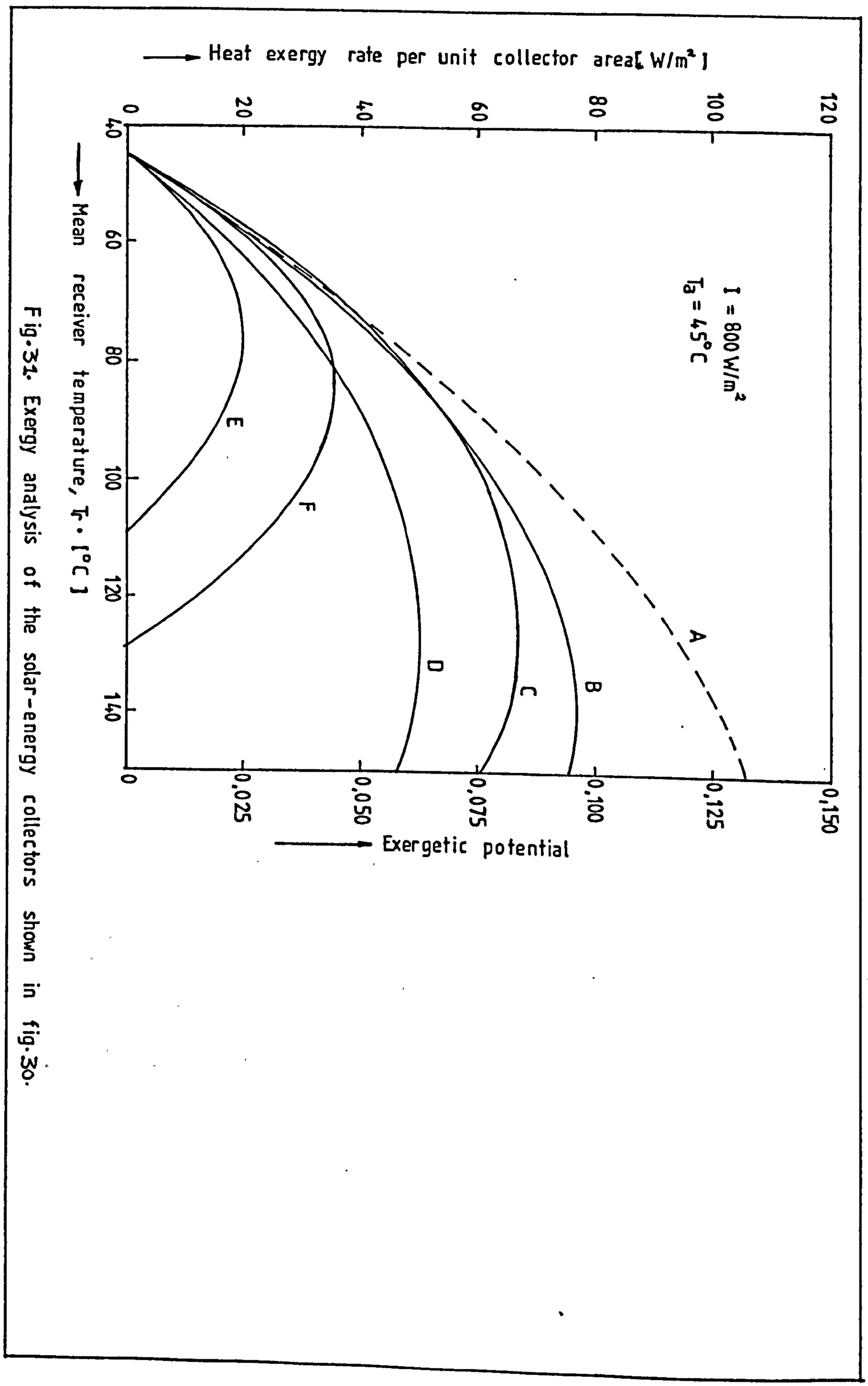

Fig.31. Exergy analysis of the solar-energy collectors shown in fig.30.

conductivity of 1.1Ø W/m K and transmissivity of about Ø.9Ø. Graphs E, D and F show that a Collector employing a CSD, where convection is suppressed, could still have a poorer thermal performance than a standard collector (i.e. without CSD), depending upon the thickness of the spacers. For example, the slatted-CSD collector employing 1mm thick glass spacers (i.e. Graph E) has a heat transfer coefficient comparable with that for the standard collector, i.e. U=7W/m^{2}K. However, its thermal performance is still poorer because of its lower optical efficiency as the result of attenuation of the solar-radiation by the glass spacers. If the thickness of the glass is reduced to Ø.1mm (i.e. Graph D), the reduction in overall heat transfer coefficient at higher temperatures compensates for the loss in optical efficiency and thus results in higher collector efficiencies than for the standard collector. However, glass thicknesses of the order of Ø.1mm are hard to come by, whereas FEP Teflon is available in thicknesses of even less than Ø.1mm.

6.4 CONCLUSIONS.

The predicted performance curves for the slatted-CSD collectors reveal that the use of a selective optical coating on the receiver plate and FEP Teflon as the spacer material, would give the best slatted-CSD collector thermal performance. For example, for values of $(T_r - T_a)/I$ between Ø.Ø7Ø and Ø.12 corresponding to average receiver surface temperture of about 1ØØ°C and 14Ø°C respectively, collector efficiencies of between 52% and 39% could be attained. If, for example, a maximum temperature difference of about 2Ø°C is allowed between the receiver surface temperature and the output temperature of the collector, this could therefore result in output temperatures of 8Ø°C and 12Ø°C respectively.

However, the maximum amount of thermal energy available to perform work is greater for the evacuated-tube collector. For example, at mean receiver surface temperature of 13Ø-14Ø°C, which corresponds to the maximum exergetic potential of about Ø.Ø96 for the slatted-CSD collector, a 3Ø% higher value is predicted for the evacuated-tube collector.

CHAPTER SEVEN

ECONOMIC APPRAISAL

In this chapter, the slatted-CSD and the evacuated-tube solar-energy collectors are appraised economically if each should supply the rate of heat energy requirement of the 'King Tut' pilot power plant, whose power ouput is required to be 5KW. The assessment is based on the pay-back periods and the cost per peak watt.

It was previously shown (i.e. in part A) that the idea of using the underground water in cooling the condenser of the Rankine-cycle is most desirable. The condenser temperature is therefore taken to be equal to that of the underground water estimated at 35°C. It is also assumed, from the performance tests conducted (Ref.39), that the expander has an average efficiency equal to 60% of that of an ideal Carnot engine operating between the same temperatures.

The average surface temperature of the collector is related to the output temperature by a temperature difference which is bound to occur because of thermal resistances between the receiver and the Rankine-cycle working fluid, i.e.,

Average receiver temperature	=	Collector output temperature	+	Temperature drop

Because of the difficulties in estimating the temperature difference, Robert (Ref.40) assumed a 5% difference between the average receiver and output temperatures of the collector. However, in this study a less optimistic value of 20°C maximum, is assumed. This should be regarded only as a crude estimate. In practice, it will depend on the conductance between the receiver surface and the working fluid as well as the mass flow rate of the working fluid.

For a chosen output temperature the mean receiver temperature is therefore estimated by adding 20°C. By using the insolation value of 800 W/m^2 and the ambient temperatue of 45°C used in predicting the collectors's efficiencies, the ratio $(T_r-T_a)/I$ is evaluated and the corresponding collector efficiency read off from fig.30. The slatted-CSD collector whose thermal performance is represented by graph B in fig.30 is used.

The overall efficiency of the pilot power plant is defined simply as the product of the solar-energy collector and the expander efficiency, i.e.,

Overall efficiency	=	Collector efficiency	X	Expander efficiency.

The rate of input solar-energy into the system would be the ratio of the output power (i.e. 5KW) to the overall system efficiency, i.e.,

$$\text{Input solar-power [KW]} = \frac{\text{Output power [KW]}}{\text{Overall efficiency}}$$

For an average five-hour daily collection of solar power, the annual input solar power would be:-

$$\text{Annual input solar-power (KW hr.)} \quad \text{Input solar-power} \times 5 \times 365$$

Electricity is taken as the reference source of power. The cost of electricity which were to be incurred annually in order to provide the required amount of input power is referred to as the annual cost of power saved. The cost of the annual power saved is therefore estimated from:-

$$\text{Annual cost of power saved} = \text{Annual input solar power (KW hr.)} \times \text{Cost of electricity (£/KW hr.)}$$

The initial capital investment on the collectors is obtained from:-

$$\text{Initial investment on collectors} = \text{Collector cost per unit area} \times \text{Collector area needed to meet the input solar-power.}$$

The cost of the GEC evacuated-tube collector is estimated at £196/m^2 (Ref.39). Robert (Ref.40) estimated the cost of a flat-plate collector at about £46/m^2. However, a less conservative figure of £100/m^2 is assumed for the slatted-CSD collector in this study.

THE SIMPLE PAY-BACK PERIOD (SPBD):

This is a simple way of looking at an investment. The initial cost of the investment (i.e. the cost of the solar-energy collectors in this study) is divided by the yield of the investment (in otherwords the cost of annual

Power saved) to give the number of years it would take to recoup the investment, i.e.,

$$SPBP = \frac{\text{Initial capital cost of the collectors}}{\text{Annual cost of Power saved.}}$$

However, this method assumes that the interest rate is zero, i.e. savings made in the first year will be worth the same as the savings made in the sixth year, say. Whereas, the savings made in the first year of an investment could be invested elsewhere and interest earned for five years and is therefore more valuable than the same savings in the sixth year (unless inflation is rampant and is therefore worthless). Similarly a sum of money in the future can be reduced according to the interest rate, to give it a present worth. This process is called discounting.

PRESENT WORTH (PW):-

If a sum of money G, is invested in the Bank with an annual interest rate i; then at the end of the first year the accumulated sum would become:-

$$S1 = G(1+i)$$

At the end of the second year:-

$$S2 = G(1+i) + G(1+i)i$$
$$= G(1+i)^2$$

Similarly at the end of the n^{th} year:-

$$Sn = G(1+i)^n$$

Therefore the present worth (PW) of a future sum of money can be expressed as:-

$$PW = \frac{\text{Future sum}}{(1+i)^n}$$

The present worth of a future sum of money is therefore, its value at the present time that with compounded interest over a period under consideration, will be equivalent to the future sum.

If, however, the payments of the sum G is regular and is made at the end of each year; then at the end of the first period, the accumulated sum of money S1 will only be the first payments made, i.e:-

$$S1 = G$$

At the end of the second year, the accumulated sum would, however, be:-

$$S2 = G(1+i)+G$$
$$= G[(1+i)+1]$$

At the end of the third year, S3 would be:-

$$S3 = G[(1+i)+1] + G[(1+i)+1]i + G$$
$$= G[(1+i)^2 + (1+i) + 1]$$

Similarly, at the end of the n^{th} year, Sn would be:-

$$Sn = G[(1+i)^{n-1} + (1+i)^{n-2} + (1+i)^{n-3} + \ldots\ldots + (1+i) + 1]$$

The sum of the bracketted series can be expressed as (Ref.42):-

$$\frac{[(1+i)^n - 1]}{i}$$

Therefore, the accumulated sum at the end of the n^{th} year would be:-

$$Sn = G\frac{[(1+i)^n - 1]}{i}$$

Applying the present worth formula , the present worth of the future sum Sn can be expressed as:-

$$PW = G\frac{[(1+i)^n - 1]}{[i(1+i)^n]}$$

DISCOUNTED PAY-BACK PERIOD (DPBP):

The discounted pay-back period may be expressed as follows (Ref.43):-

$$DPBP = n \times CB$$

where,

n = System's life-time

CB = Cost-to-benefit ratio defined as (Ref.43):-

$$CB = \frac{\text{Initial capital cost of the collectors}}{\text{Present worth}}$$

where,

$$\text{Present worth} = \text{Annual cost of energy saved} \times \frac{[(1+i)^n - 1]}{i(1+i)^n}$$

i = Discount rate.
A discount rate of 10% used by Jacques (Ref.41) and also suggested by Malcolm (Ref.44) was considered a reasonable value and is thus used here.
It should, however, be noted that if the cost-to-benefit ratio is greater than unity, the system will not be cost effective.
The discounted pay-back period may thus be rewritten as:-

$$DPBP = \frac{\text{System's life-time} \times \text{Capital cost of collectors}}{\text{Annual cost of Power saved} \times \frac{[(1+i)^{\wedge}-1]}{i(1+i)^{n}}}$$

COST PER PEAK WATT:

The cost per peak watt for the solar-energy collector system is estimated from:-

$$\text{Cost per peak watt} = \frac{\text{Collector cost + Cost of hardware}}{\text{Output power in watts.}}$$

where the hardware refers to the expander, feed-pump, condenser, pipework and other equipment that make up the pilot power plant. The cost of which is estimated at £30000 (Ref.39).

These methods of economic assesment have therefore been applied to the evacuated tube and the slatted-CSD collectors against electricity, if each should supply the input power requirement of the 'King Tut' Rankine cycle pilot power plant, whose power output is required to be 5KW.
Performance at moderate collector output temperatures of 80°C to 130°C are considered. The appraisal is presented in Table 2 for an electricity cost of £0.05/KW hr. Fig.32 shows the estimated overall efficiencies and cost per peak watt for the pilot power plant, whereas fig.33 shows the pay-back periods against the cost of electricity for the two collectors.

For the conditions considered in Table 2, the results indicate that over the life-time of about 20 years, the slatted-CSD collector would have a simple break-even time of about 2 years against electricity. Whereas that for the evacuated tube collector would be about 3 years. However, when savings are discounted over the life-time, the break-even times become about 4 and 7 years for the slatted-CSD and evacuated-tube collectors respectively. The predicted costs per peak watt over the range of operating temperatures considered are lower for the slatted-CSD collector system than for the evacuated-tube collector system. For example, at collector

Table 2. Economic appraisal of the solar-energy activated pilot power plant.

	Slatted-CSD collector system				Evacuated-tube collector system			
Collector output temperature [°C]	80	90	100	120	80	90	100	120
Collector efficiency	0,52	0,49	0,46	0,39	0,61	0,60	0,58	0,55
Expander efficiency	0,076	0,091	0,105	0,130	0,076	0,091	0,105	0,130
Overall efficiency	0,040	0,045	0,048	0,051	0,046	0,055	0,061	0,072
Input solar-power for 5 KW output [KW]	125.0	111.1	104.2	98.0	108.7	90.9	82.0	69.4
Annual input solar power for 5hrs daily collection. [KW hr.]	228125.0	202757.5	190165.0	178850.0	198377.5	165892.5	149650.0	126655.0
Annual cost of electricity saved at £0.05/KW hr. [£]	11406.25	10137.88	9508.25	8942.5	9918.88	8294.6	7482.5	6332.75
Collector area needed to collect the input solar-power [m^2].	156.3	138.9	130.3	122.5	135.9	113.6	102.5	86.8
Collector cost per unit area [£/m^2]	100	100	100	100	196	196	196	196
Capital cost of the collectors [£]	15630.0	13890.0	13030.0	12250.0	26636.4	22265.6	20090.0	17012.8
System's expected life-time [yrs]	20	20	20	20	20	20	20	20
Cost-to-benefit ratio	0,16	0,16	0,16	0.16	0,32	0,32	0,32	0,32
Simple pay-back period [yrs]	1.4	1.4	1.4	1.4	2.7	2.7	2.7	2.7
Discounted pay-back period [yrs]	3,2	3,2	3,2	3,2	6,3	6,3	6,3	6,3
Estimated cost of other hardware and instruments for the 5KW pilot power plant [£]	30000	30000	30000	30000	30000	30000	30000	30000
Estimated total cost of the pilot power plant [£]	45630	43890	43030	42250	56636.4	52265.6	50090.0	47012.8
Cost per peak watt [£/W]	9.13	8.78	8.61	8.45	11.33	10.45	10.02	9.40

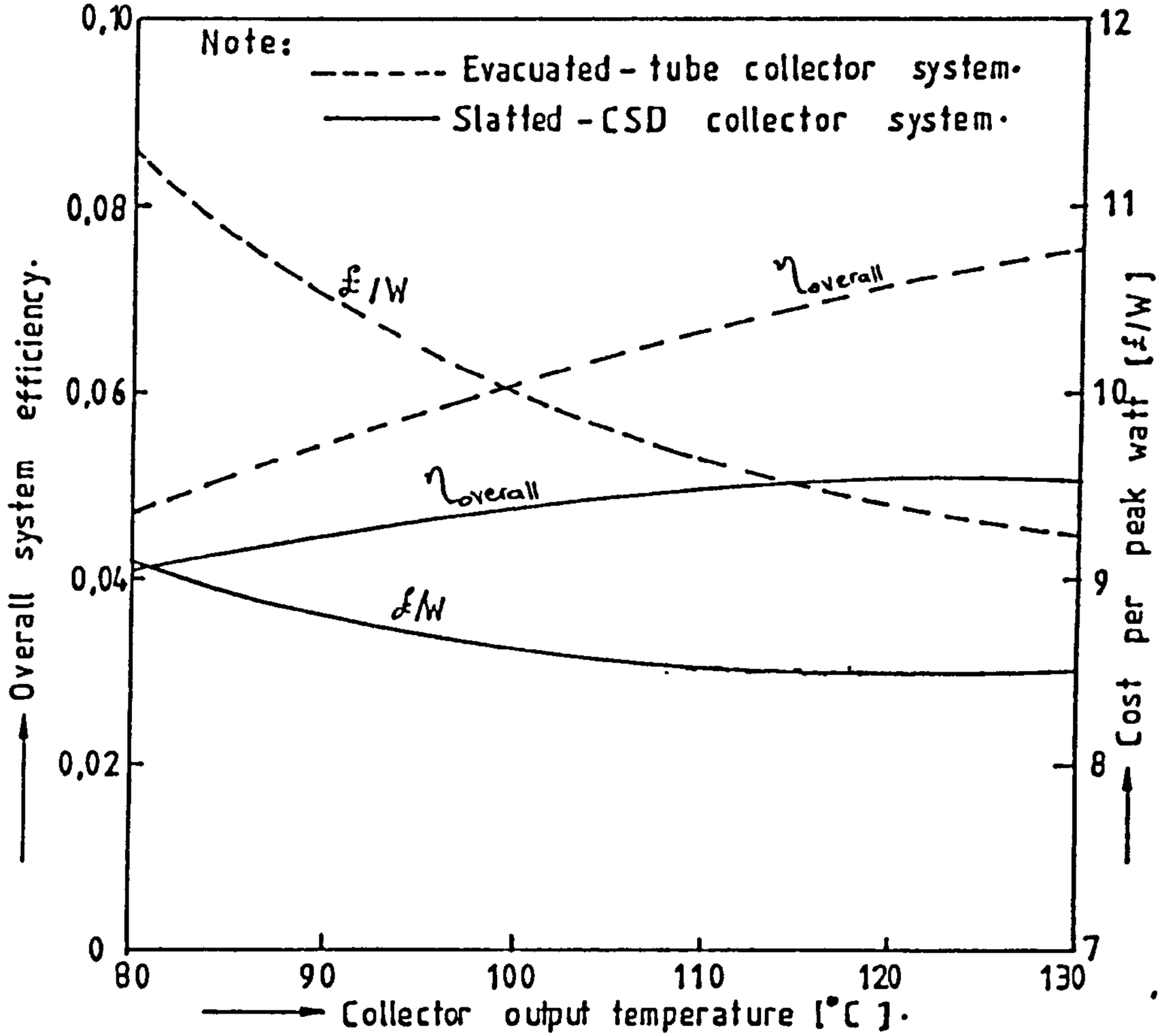

Fig.32. Estimated overall efficiency and cost per peak watt for the solar energy activated 5KW pilot power plant.

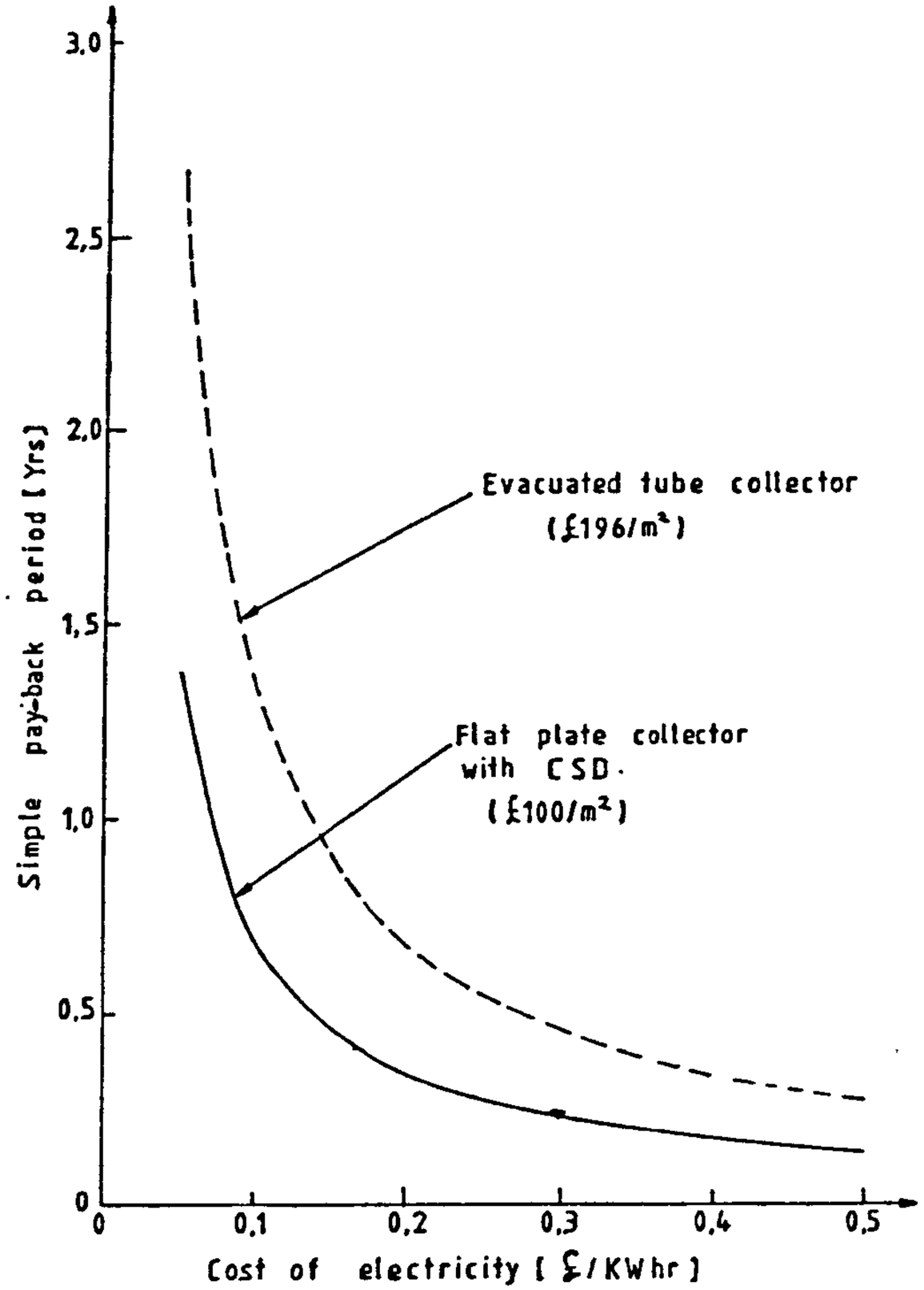

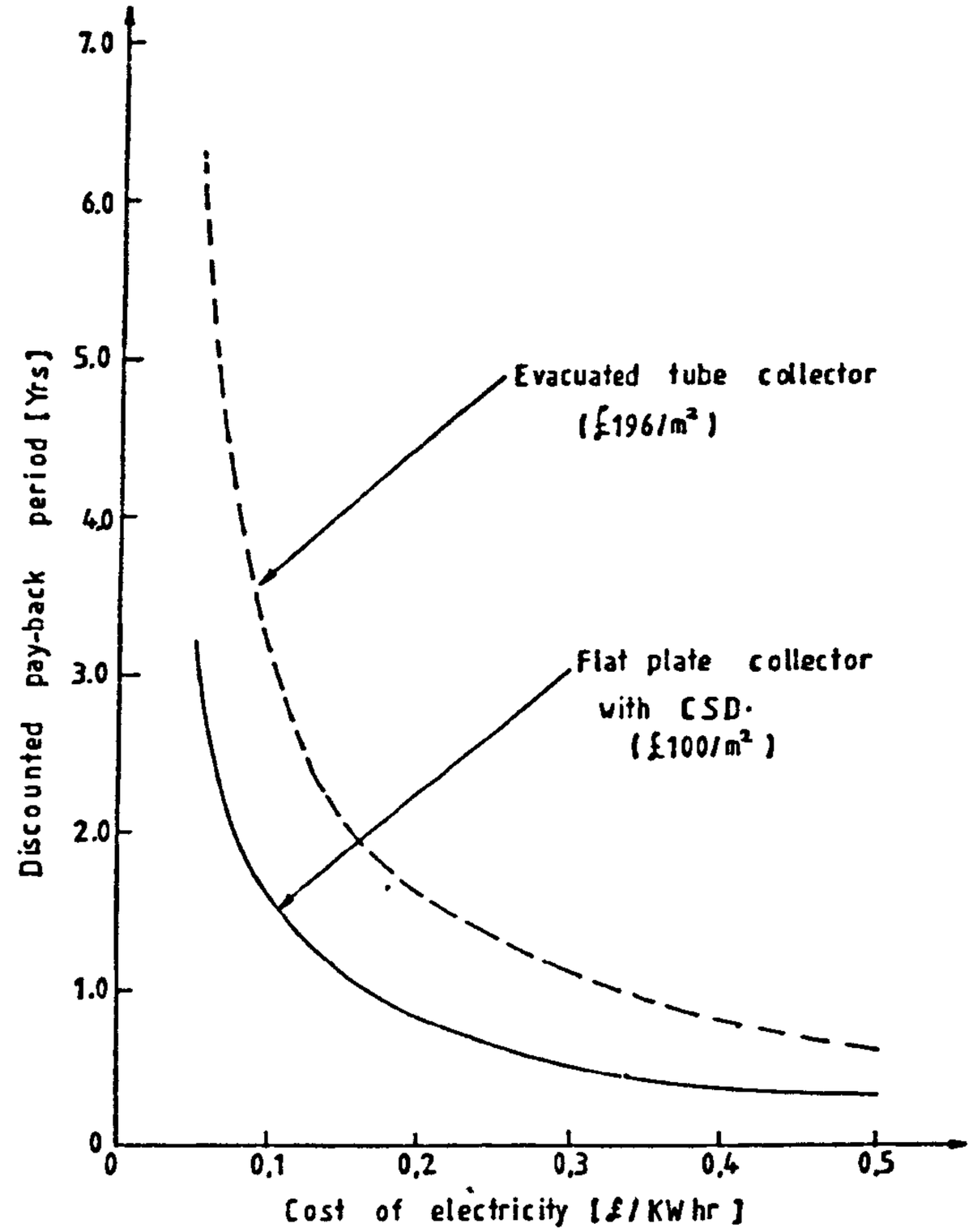

Fig-33· Pay-back period against cost of electricity for the solar collectors shown, if employed to activate the 5KW pilot power plant, for operating temperature of about 100°C·

output temperature of about 120° C, the slatted-CSD collector system would give one peak watt at a cost of about £8.45. Whereas the evacuated-tube collector system would give about £9.4 per peak watt, i.e. about 11.2% higher cost per peak watt.

However, it is pertinent to mention that for all the collector output temperatures considered, higher overall system efficiencies are predicted for the evacuated-tube collector system than for the slatted-CSD collector system. For example, at a collector output temperature of 120° C, which corresponds to the maximum overall efficiency of 5.1% for the slatted-CSD collector system, a 7.2% overall efficiency is predicted for the evacuated-tube collector system.

CONCLUSIONS

In using solar-power to activate the 5KW organic Rankine-cycle pilot power plant, it is considered that a flat-plate solar-energy collector with an effective convection suppression device and an initial capital cost of about £100 per square meter, would be more cost effective than the evacuated-tube collector for operating temperatures of 80° C to 120° C. This follows from the predicted discounted pay-back period of about 4 years for the slatted-CSD collector as against about 7 years for the evacuated-tube collector. Lower cost per peak watt of about £(8.45-9.13) is also predicted for the slatted-CSD collector system as compared with £(9.4-11.33) for the evacuated-tube system, depending upon the operating temperature.

However, these economic advantages for the slatted-CSD collector system over the evacuated-tube collector system would occur at the expense of the overall system efficiency. For example, at an operating temperature of about 120° C which corresponds with the maximum overall efficiency of 5.1% for the slatted-CSD collector system, the evacuated-tube collector system could give 7.2% overall efficiency. It is, however, considered that this draw-back is compensated for by the lower initial capital investment, lower break-even time and cost per peak watt.

CHAPTER EIGHT

CONCLUSIONS AND RECOMMENDATIONS

In practice, the slatted-CSD studied would consist simply of a set of high transmissivity spacers, oriented along the east-west direction and normal to the collector absorber and glazing. The spacers would subdivide the air-space between the receiver and the glazing into smaller air-cells. In this study, however, the collector was simulated using a rectangular box bounded at the top and bottom by aluminium alloy plates. The bottom plate was heated from below and the top plate cooled to simulate the receiver and glazing respectively. The air-space between the top and bottom plates was subdivided into smaller air-cells using perspex.

The theoretical study carried out showed that, for minimal convective heat transfer from the bottom plate, the air-cell aspect ratio should be about Ø.2. And that the spacer material should have a low thermal conductivity and also be as thin as is practicable.
However, because the air-cell aspect ratio is the ratio of width-to-height of each of the air-cells, a criterion for stating either the cell-width or the cell-height became essential. This was to enable define the size of the air-cells.

The experimental study was therefore set up to investigate the effect on convective heat transfer of decreasing the air-cell aspect ratio by varying the cell-height, for constant cell-width. The results obtained showed that, for a fixed temperature difference across the air-cells, the overall convective heat transfer coefficient decreased with increase in the cell-height. However, the most significant reduction occurred at about a height of 3Ømm. In view of this and the fact that further increases in cell-height would in practice mean higher capital investment on the spacer material; 3Ømm was therefore considered a critical height for a slatted-CSD.

The steady-state thermal performance of a flat-plate solar-energy collector, employing (i) glass and (ii) Teflon FEP as spacer material, was analysed theoretically for a cell-height of 3Ømm and cell-width of 4mm. The glazing was taken to be made of glass in all cases. It was, however, assumed that convection in the air-cells would remain within the base flow regime for receiver surface temperatures of up to 15Ø°C. The analysis showed that Tefon FEP would give better collector thermal performance than

glass, because of its lower thermal conductivity and higher transmissivity. It also has the advantage of being available in very thin thicknesses (e.g. less than 1mm).

With 1mm thick Teflon FEP as spacers and a selective optical coating on the receiver, collector efficiencies of between (52→39)% were predicted for collector output temperatures of between (35→75)°C above the ambient temperature. This thermal performance was, however, found lower than that predicted for the evacuated-tube collector.

However, the economic appraisal carried out showed that, for moderate collector output temperatures of (80→120)°C, the slatted-CSD collector with an initial capital cost of about £100/m² would be more cost effective than the evacuated-tube collector employed to activate the 'King Tut' pilot power plant. This followed from the predicted simple break-even time against electricity of about 2 years for the slatted-CSD collector system and 3 years for the evacuated-tube collector system. However, when savings were discounted over the system's life-time of 20 years, the break-even times became 4 years and 7 years for the slatted-CSD and evacuated-tube collector systems respectively. The economic advantage would, however, occur at the expense of the system's overall efficiency. The overall efficiency could fall by an average value of about 23% depending upon the operating temperature.

RECOMMENDATIONS

The followings are suggestions for further studies:-
(i) As intimated by Hollands et al (Ref.8), perhaps convective rolls may form both along the upslope and longitudinal directions of the air-cells. A comprehensive flow visualization tests should be carried out along the two directions, so as to establish the direction in which the convective rolls is strongest.

(ii) Perhaps slatts oriented at 45° to the two directions could reduce the extent of the convective phenomena in both directions at the same time.

(iii) Correlations for the average Nusselt number against the Rayleigh number for air-cell aspect ratios of less than unity. It is, however, envisaged that this may be practicable only when the cell-width rather than the cell-height is varied. The latter case would enable dynamically similar situations to be compared.

(iv) The use of finer grid-size in the numerical study. This may reveal secondary flow formation. It should, however, be noted that disproportionate increase in the running time for the computer program may occur.

(v) Extension of the theoretical study to include three-dimensional and radiation effects.

(vi) Construction and testing of the collector unit.

(vii) Study of a means of minimizing the thermal resistances across the ball-and-socket joint employed with the high-vacuum solar-energy collector.

REFERENCES

1. Harb, S.
'Characteristic features of radiation field in Egypt.'
Release by the Ministry of Electricity and Energy, Egyptain Solar Energy Commission, Feb.(1978).

2. Kaltum, M. M.
Selective Optical Surfaces for Solar-energy Converters, Allerton Press, New York(1981).

3. Wolf, R. E.
'Solar collector performance: Dependence upon coating.'
J. of Coating Tech., 56, 652,pp49-53(1979).

4. Benard, H.
'Les tourbillous cellulaires dams une nappe liquide transportant de la chaleur par convection en regime permanent.'
Ann. Chim. Phys., 7 , pp62-144(19Ø1).

5. Lord Rayleigh,
'On convective currents in a horizontal layer of fluid when the higher temperature is on the underside.'
Phil. Mag., 56, 32, pp529-546(1916).

6. De Graaf, J. G. A. and Van der Held, E. F. M.
'The relation between the heat transfer rate and the convective phenomena in enclosed plane air layers.'
Appl. Sci. Res., A, 3, pp393-4Ø9(1953).

7. Peterson, L. F.
'An examination of the stability criterion for fluid layers subject to adverse temperature gradients.'
M.Eng. Thesis, Melbourne University, Australia(1971).

8. K. G. T. Hollands, G. D. Raithby and T. E. Unny.
'Studies on methods of reducing heat losses from flat-plate solar collectors.'
Annual Progress Report, University of Waterloo, Ontario, Canada, Feb.(1977).

9. K. G. T. Hollands, T. E. Unny, R. D. Raithby and L. Konicek.
'Free-convection heat transfer across inclined air-layers.'
J. of Heat Transfer, 98, pp189-193(1976).

10. K. R. Randall, J. W. Mitchell and M. M. El-Wakil.
'Natural convection heat transfer characteristics of flat-plate enclosures.'
J. of Heat Transfer,101, pp120-125(1979).

11. E. M. Elsherbiny, G. D. Raithby and K.G. T. Hollands.
'Heat transfer by natural convection across vertical and inclined air-layers.'
J. of Heat Transfer, 104, 1, pp96-102(1982).

12. Buchberg, H., Catton, I. and Edwards, D. K.
'Natural convection in enclosed spaces: A review of applications to solar-energy collectors.'
J. of Heat Transfer, 98, pp182-186(1976).

13. J. C. McMurrin, N. A. Djordjevic and H. Buchberg.
'Performance measurements of a cylindrical glass honeycomb solar collector compared with predictions.'
J. of Heat Transfer, 99, pp169-173(1977).

14. R. L. D. Cane, K. G. T. Hollands, R. D. Raithby and T. E. Unny.
'Free convection heat transfer across inclined honeycomb panel.'
J. of Heat Transfer, 99, 1, pp86-91(1977).

15. J. N. Arnolds, D. K. Edwards and I. catton.
'Effect of tilt and horizontal aspect ratio on natural convection in a rectangular honeycomb.'
J. of Heat Transfer, 99, 1, pp120-122(1977).

16. W. W. S. Charters and K. I. Guthrie.
'Experimental evaluation of a slatted convection suppression device.'
Solar World Forum, 1, pp181-184(1982).

17. K. G. T. Hollands.
'Honeycomb devices in flat-plate solar-energy collectors.'
Solar Energy, 9, 3, pp159-164(1965).

18. J. G. Symons.
'The solar transmittance of some convection suppression devices for solar-energy applications: An experimental study.'
J. of Solar Engineering, 104, pp251-256(1982).

19. W. Koutsoheras.
'Natural convection phenomena in inclined cells with finite side walls: A numerical study.'
M.Eng. Thesis, University of Melbourne, Australia(1976).

20. B. A. Meyer, J. W. Mitchell and M. M. El-Wakil
'Natural convection heat transfer in moderate aspect ratio enclosures.'
J. of Heat Transfer, 101, 4, pp655-659(1979).

21. Herman Schlichting.
Boundary Layer Theory, 7 Edition, Mcgraw-Hill Publishers(1979).

22. B. A. Meyer.
'An experimental and numerical study of natural convection heat transfer in moderate aspect ratio and vee-groove enclosures.'
Ph.D Thesis, University of Wisconsin, U.S.A.(1980).

23. Kreith, F.
Principles of Heat Transfer, 3 Edition, Harper and Row Publishers, New York(1976).

24. Boas, M. L.
Mathematical Methods in the Physical Sciences, John Wiley and Sons, New York(1966).

25. B. A. Meyer, J. W. Mitchell and M. M. El-Wakil.
'The effect of thermal wall properties on natural convection in inclined ractangular cells.'
J. of Heat Transfer, 104, 1, pp103-110(1982).

26. David, H. S.
'Numerical solution for the flow of a fluid in a heated closed cavity.'
Quaterly J. of Mechanics and Applied Mathematics, 26, 2, pp173-191(1973).

27. Poots, G.
'Heat transfer by laminar free convection in enclosed plane gas layers.'
Quaterly J. of Mechanics and Applied Mathematics, 11, pp257-273(1958).

28. Wilkes, J. O. and Churchill, S. W.
'The finite-difference computation of natural convection in a ractangular enclosure.'
Am. Inst. of Chem. Engr., 12, pp161-166(1966).

29. Greenspan Donald.
Discrete Numerical Methods in Pysics and Engineering, Academic Press, New York(1974).

30. G. D. Smith.
Numerical Solution of Partial Differential Equations: Finite-Difference Methods, 2 Edition, Clarendon Press, Oxford(1978).

31. R. J. Hosking, D. C. Joyce and J. C. Turner.
First Steps in Numerical Analysis, Hodder and Stoughton Press(1981).

32. Brooks, R. G., Probert, S. D. and Maxwell, J.
'Mach-Zehnder interferometer for heat transfer studies.'
Measurement and Control, 1, pp9-15(1968).

33. E.R.G. Eckert and R. J. Goldstein.
Measurements in Heat Transfer, 2 Edition, Mcgraw-Hill Publishers(1976).

34. Jacob Max.
Heat Transfer, Vol.I, John Wiley, New York(1949).

35. Manuel, C.P. and Ari Rabl.
'Simple procedure for predicting long-term average performance of non-concentrating and concentrating solar collectors.'
Solar Energy, 23, pp235-253(1979).

36. W. H. McAdams.
Heat Transmission, 3 Edition, Mcgraw-Hill, Kogakusha, Japan(1954).

37. J. A. Duffie and W. A. Beckman.
Solar Energy Thermal Processes, Wiley-Interscience, New York(1974).

38. P. W. O'Callaghan and S. D. Probert.
'Exergy and Economics.'
Applied Energy, 8, pp227-243(1981).

39. P. W. O'Callaghan, M. Hussein, J. Whitehouse and D. Pollard.
King Tut Project - Solar Driven Power Generator Project Document(1981).

40. Robert, E. B.
'Current costs of solar powered organic Rankine cycle engines.'
Solar Energy, 20, 1, pp1-6(1978).

41. Jacques Percebois.
'Solar energy: True computations and deceiving hopes.'
Int. J. of Ambient Energy, 3, 2, pp81-88(1982).

42. W. E. Stoecker.
Design of Thermal Systems, Mcgraw-Hill, Kogakusha Ltd., Tokyo, Japan(1971).

43. R. A. Lebens and A. Myer(Ed.).
Passive Solar Handbook, Commission of European communities Publishers, pp337-389 (Draft Copy 1983).

44. Malcolm Slesser.
Energy in the Economy, The Macmillan Press, London(1978).

APPENDIX A

COMPUTER PROGRAM FOR THE FINITE-DIFFERENCE SOLUTION TO A LAMINAR FREE CONVECTION HEAT TRANSFER PROBLEM IN AN INCLINED RECTANGULAR AIR CAVITY HEATED FROM BELOW.

The computer program referred to in section 4.4 of chapter four is hereby presented. It should be noted that the computer does not recognise subscripts and Greek alphabet. Some of the quantities in the text which are denoted by subscripted and Greek symbols are therefore replaced with more convenient symbols in the program. These symbols and others are first defined for easy apprehension of the program. The rest of the symbols are as defined in the text.

AX	Air-cell aspect ratio.
AS	Spacer aspect ratio.
AD	Switch which indicates the 'ZHF' boundary condition.
DEG	Angle of tilt in degrees.
EPS	Allowable error between successive values.
MRUN	Number of iterations.
NDXS	Number of grid-divisions in the X-direction of the spacer.
RK	Ratio of air to spacer thermal conductivities. Also used as a switch to indicate the 'LTG' boundary condition.
MAXR	Maximum number of iterations allowed.
SF	Dimensionless streamfunction.
TC	Dimensionless air-cell temperatures.
TS	Dimensionless spacer temperatures.
VO	Dimensionless vorticity function.
NSF NTC	Counters.
NTS NVO	
YNU	Nusselt number.

The flow chart for the sequential execution of the proram is shown in fig.A1.

It should also be noted that:-

(i) If the 'ZHF' boundary condition is assumed, then the following variables should be assigned the quantities stated below:

AD = 1.Ø
RK = 2.Ø
AS = Ø.Ø

(ii) If the 'LTG' boundary condition is assumed, then the following variables should be assigned the quantities stated below:

AD = 2.Ø
RK = Ø.Ø
AS = Ø.Ø

(iii) If, however, the effect of the spacer thermal property is to be considered, then:

AD = 2.Ø

whereas 'RK' and 'AS' should take the values you intend them to have.

Points of equal temperatures and streamfunctions were located using a subroutine called 'SORT', which is presented after the main program called 'LFC'. The locations are obtained by linear interpolation of the computed values at the grid-points. The following variables are defined with respect to the subroutine:-

FUC	Function under consideration, e.g. SF, TC and VO.
SVOF	Specified value of the function whose locations are to be found and stored in the array (X,Y).
NN	Number of locations in the array (X,Y).
M, N, NDX	and MDY are as defined in the text.

The output from the subroutine are therefore the locations (X,Y) and the number of locations 'NN', whereas the input are 'FUC' and 'SVOF'.

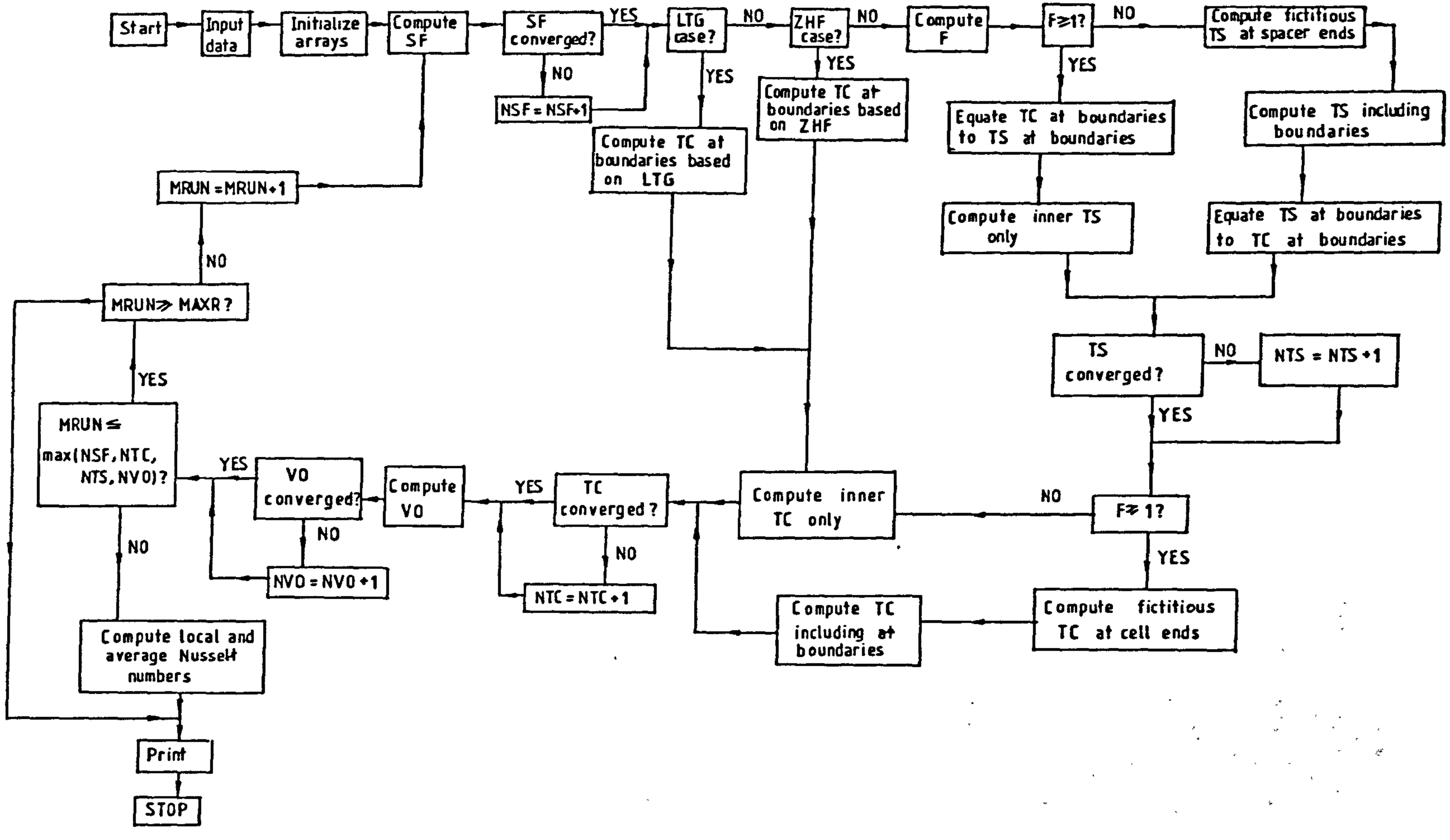

Fig A1. Flow diagram of the sequential execution of the computer program.

```
CC                PROGRAM LFC.FOR
CC*************************************************************
          PARAMETER(NDX=20,MDY=20,NDXS=20,B=1.2,
     1    PR=0.733,PI=3.14159)
          DIMENSION YNU(2:NDX+2),TC(NDX+3,MDY+1),VO(NDX+3,MDY+1),
     1    SF(NDX+3,MDY+1),SSF(NDX+3,MDY+1),TS(NDXS+3,MDY+1),
     2    STS(NDXS+3,MDY+1),STC(NDX+3,MDY+1),SVO(NDX+3,MDY+1)
     3    ,YNUC(2:NDX+2)
CC*************************************************************
          READ(5,*)AX,RA,DEG,AD,RK,AS,EPS,MAXR
CC*************************************************************
          TILT=DEG*PI/180.0
          DX=AX/FLOAT(NDX)
          DY=1.0/FLOAT(MDY)
          DXS=AS/FLOAT(NDXS)
          R=DX/DY
          RS=DXS/DY
          N=NDX+2
          M=MDY+1
          NS=NDXS+2
          RSQ=R**2
          RSSQ=RS**2
          DXSQ=DX**2
          DYSQ=DY**2
CC*************************************************************
CC                INITIALIZE ARRAY & BOUNDARY CONDITIONS
          DO 15 J=1,M
          DO 10 I=1,N+1
          SF(I,J)=0.0
          VO(I,J)=0.0
          SSF(I,J)=0.0
          SVO(I,J)=0.0
          STC(I,J)=0.0
          TC(I,J)=1.0-FLOAT(J-1)*DY
10        CONTINUE
          DO 15 K=1,NS+1
          STS(K,J)=0.0
          TS(K,J)=1.0-FLOAT(J-1)*DY
15        CONTINUE
CC*************************************************************
CC                COMPUTE STREAM FUNTIONS
2         CONTINUE
5         DO 35 J=2,M-1
          SF(3,J)=0.25*SF(4,J)
35        SF(N-1,J)=0.25*SF(N-2,J)
          DO 40 I=4,N-2
          SF(I,2)=0.25*SF(I,3)
40        SF(I,M-1)=0.25*SF(I,M-2)
37        DO 45 I=4,N-2
          DO 50 J=3,M-2
          F1=SF(I+1,J)+SF(I-1,J)
          F2=SF(I,J+1)+SF(I,J-1)
          SF3=(F1+F2*RSQ+VO(I,J)*DXSQ)/(2.0*(1.0+RSQ))
          SF(I,J)=SF(I,J)*(1.0-B)+B*SF3
50        CONTINUE
45        CONTINUE
CC*************************************************************
CC        TEST STREAMFUNCTIONS FOR CONVERGENCE
          DO 52 J=2,M-1
          DO 52 I=3,N-1
          DIFF=ABS(SF(I,J)-SSF(I,J))
          IF(DIFF.GT.EPS)GO TO 53
52        CONTINUE
```

```
          GO TO 54
53        NSF=NSF+1
54        CONTINUE
CC*****************************************************
          IF(ABS(AD-1.).LE.0.001) GO TO 25
          IF(ABS(RK).LE.0.00001)GO TO 21
CC*****************************************************
          F=RK*DXS/DX
          IF(F.GE.1.0)GO TO 400
CC*****************************************************
CC        COMPUTE FICTITIOUS TEMPERATURES AT THE SPACER ENDS
          DO 180 J=2,M-1
          TS(1,J)=TS(3,J)+F*(4.*TC(N-1,J)-3.*TC(N,J)-TC(N-2,J))
          TS(NS+1,J)=TS(NS-1,J)+F*(4.*TC(3,J)-3.*TC(2,J)-TC(4,J))
180       CONTINUE
          K1=2
          K2=NS
          GO TO 450
CC*****************************************************
400       TS(2,J)=TC(N,J)
          TS(NS,J)=TC(2,J)
          K1=3
          K2=NS-1
CC*****************************************************
CC        COMPUTE SPACER   TEMPERATURES
450       DO 102 K=K1,K2
          DO 102 J=2,M-1
          T1=TS(K+1,J)
          T3=TS(K-1,J)
          T2=TS(K,J+1)
          T4=TS(K,J-1)
          T5=(T1+T3+RSSQ*(T2+T4))/(2.0*(1.0+RSSQ))
          TS(K,J)=TS(K,J)*(1.0-B)+B*T5
102       CONTINUE
CC*****************************************************
CC        TEST SPACER TEMPERATURES FOR CONVERGENCE
          DO 55 J=1,M
          DO 55 K=1,NS+1
          DIFF=ABS(TS(I,J)-STS(I,J))
          IF(DIFF.GT.EPS)GO TO 56
55        CONTINUE
          GO TO 57
56        NTS=NTS+1
57        CONTINUE
          GO TO 23
CC*****************************************************
CC        COMPUTE AIR-CELL BOUNDARY TEMPERATURES FOR THE
CC        ADIABATIC BOUNDARY CONDITION.
25        DO 183 J=2,M-1
          TC(2,J)=(4.*TC(3,J)-TC(4,J))/3.
          TC(N,J)=(4.*TC(N-1,J)-TC(N-2,J))/3.
183       CONTINUE
21        I1=3
          I2=N-1
          GO TO 24
CC*****************************************************
23        CONTINUE
          IF(F.LT.1.0)THEN
          DO 51 J=2,M-1
          TC(2,J)=TS(NS,J)
51        TC(N,J)=TS(2,J)
          I1=3
          I2=N-1
```

```
      ELSE
CC*****************************************************
CC      COMPUTE FICTITIOUS TEMPERATURES AT THE AIR-CELL
CC      ENDS.
      DO 410 J=2,M-1
      TC(1,J)=TC(3,J)+(-3*TS(NS,J)+4.*TS(NS-1,J)-TS(NS-2,J))
     1  /F
410   TC(N+1,J)=TC(N-1,J)+(-3.*TS(2,J)+4.*TS(3,J)-TS(4,J))
     1  /F
      I1=2
      I2=N
      ENDIF
CC*****************************************************
CC      COMPUTE INTERIOR AIR-CELL TEMPERATURES
24    DO 65 I=I1,I2
      DO 65 J=2,M-1
      GAM=SF(I+1,J)-SF(I-1,J)
      DEL=SF(I,J+1)-SF(I,J-1)
      T1=TC(I+1,J)
      T3=TC(I-1,J)
      T2=TC(I,J+1)
      T4=TC(I,J-1)
      T5=2.0*(T1+T3)+2.0*RSQ*(T2+T4)
      IF(DEL.GE.0.0)GO TO 70
      C1=-R*DEL
      C2=C1*T1
      GO TO 75
70    C1=R*DEL
      C2=C1*T3
75    IF(GAM.GE.0.0)GO TO 85
      C3=-R*GAM
      C4=C3*T4
      GO TO 90
85    C3=R*GAM
      C4=C3*T2
90    T8=(T5+C2+C4)/(4.0*(1.0+RSQ)+C1+C3)
91    TC(I,J)=TC(I,J)*(1.0-B)+B*T8
65    CONTINUE
CC*****************************************************
CC      TEST AIR-CELL TEMPERATURES FOR CON VERGENCE
      DO 58 J=2,M-1
      DO 58 I=2,N
      DIFF=ABS(TC(I,J)-STC(I,J))
      IF(DIFF.GT.EPS)GO TO 59
58    CONTINUE
      GO TO 22
59    NTC=NTC+1
22    CONTINUE
CC*****************************************************
CC      COMPUTE AIR-CELL BOUNDARY VORTICITIES
145   DO 95 J=1,M
      VO(2,J)=(SF(4,J)-3.0*SF(3,J))/(2.0*DXSQ)
      VO(N,J)=(SF(N-2,J)-3.0*SF(N-1,J))/(2.0*DXSQ)
95    CONTINUE
      DO 100 I=3,N-1
      VO(I,1)=(SF(I,3)-3.0*SF(I,2))/(2.0*DYSQ)
      VO(I,M)=(SF(I,M-2)-8.0*SF(I,M-1))/(2.0*DYSQ)
100   CONTINUE
CC*****************************************************
CC      COMPUTE INTERIOR AIR-CELL VORTICITIES
      DO 125 I=3,N-1
      DO 125 J=2,M-1
      V1=VO(I+1,J)
```

```
      V3=VO(I-1,J)
      V2=VO(I,J+1)
      V4=VO(I,J-1)
      T1=TC(I+1,J)-TC(I-1,J)
      T2=TC(I,J+1)-TC(I,J-1)
      V5=2.0*(V1+V3)+2.0*RSQ*(V2+V4)+RA*COS(TILT)*T1*DX
     1  -RA*SIN(TILT)*T2*R*DX
        GAM=SF(I+1,J)-SF(I-1,J)
        DEL=SF(I,J+1)-SF(I,J-1)
        IF(DEL.GE.0.0)GO TO 130
        C2=-DEL*R/PR
        C3=C2*V1
        GO TO 135
  130   C2=DEL*R/PR
        C3=C2*V3
  135   IF(GAM.GE.0.0)GO TO 140
        C4=-GAM*R/PR
        C5=C4*V4
        GO TO 150
  140   C4=GAM*R/PR
        C5=C4*V2
  150   V8=(V5+C3+C5)/(4.0*(1.0+RSQ)+C2+C4)
  151   VO(I,J)=VO(I,J)*(1.0-B)+B*V8
  125   CONTINUE
CC**********************************************************
CC      TEST VORTICITY FOR CONVERGENCE
        DO 141 J=1,M
        DO 141 I=2,N
        DIFF=ABS(VO(I,J)-SVO(I,J))
        IF(DIFF.GT.EPS*10.)GO TO 142
  141   CONTINUE
        GO TO 143
  142   NVO=NVO+1
  143   CONTINUE
CC**********************************************************
  121   CONTINUE
        IF(MRUN.LE.MAX(NTC,NTS,NSF,NVO))GO TO 128
        GO TO 157
  128   CONTINUE
        IF(MRUN.GT.MAXR)GO TO 175
        MRUN=MRUN+1
        DO 501 J=1,M
        DO 501 I=2,N
        SSF(I,J)=SF(I,J)
        SVO(I,J)=VO(I,J)
        STC(I,J)=TC(I,J)
  501   CONTINUE
        DO 502 J=1,M
        DO 502 K=1,NS+1
        STS(K,J)=TS(K,J)
  502   CONTINUE
        GO TO 2
  157   CONTINUE
CC**********************************************************
CC          COMPUTE LOCAL NUSSET NUMBERS ON HOT SURFACE
        SUMM=0.
        DO 155 I=2,N
        YNU(I)=(3.*TC(I,1)-4.*TC(I,2)+TC(I,3))/(2.*DY)
  155   CONTINUE
CC**********************************************************
CC      COMPUTE AVERAGE NUSSELT NUMBER ON THE HOT SURFACE
CC      BASED ON SIMPSON'S NUMERICAL INTERGRATION RULE.
        SUMM1=0
```

```
            SUMM1=SUMM1+YNU(2)+YNU(N)
            SUMM2=0
            DO 700 I=3,N-1,2
  700       SUMM2=SUMM2+4.*YNU(I)
            SUMM3=0
            DO 800 I=4,N-2,2
  800       SUMM3=SUMM3+2.*YNU(I)
            SUMM=(SUMM1+SUMM2+SUMM3)*DX/3.
            ANU=SUMM/AX
CC**********************************************************
            CONTINUE
CC**********************************************************
            IF(AD.EQ.1.0)THEN
            WRITE(9,8)
  8         FORMAT(1HO,'ADIABATIC BOUNDARY CONDITION ASSUMED')
            ELSEIF(RK.EQ.0.0)THEN
            WRITE(9,7)
  7         FORMAT(1HO,'LINEAR BONDARY TEMP.DISTRIBUTION ASSUMED')
            ELSE
            WRITE(9,4)
  4         FORMAT:(1HO,'REAL SPACER CONSIDERED')
            ENDIF
CC**********************************************************
            WRITE(9,*)
            WRITE(9,500)DEG,RA,AS
  500       FORMAT:(1HO,'TILT ANGLE=',F4.1,5X,'RALEIGH NUMBER=',F9.1,
           1  5X,'SPACER ASPECT RATIO=',F10.3)
            WRITE(9,550)AX,RK
  550       FORMAT(1H ,'CELL ASPECT RATIO=',F7.5,5X,'AIR TO SPACER'
           1  '  CONDUCTIVITIES=',F10.3)
            WRITE(9,560)AS*RK,NDX+1,MDY+1
  560       FORMAT:(1H ,'CELL COUPLING FACTOR=',F9.3,2X,'GRID SIZE=',I2,
           1  '*',I2)
CC**********************************************************
  508       WRITE(9,900)
  900       FORMAT(1HO,'HOT PLATE LOCAL NUSSELT NUMBERS')
            WRITE(9,*),(YNU(I),I=2,N)
CC**********************************************************
            WRITE(9,940)SUMM/AX
  940       FORMAT:(1HC,'AVERAGE NUSSELT NUMBER=',F5.3)
CC**********************************************************
CC**********************************************************
  175       CONTINUE
  509       IF(MRUN.LE.MAXR)GO TO 176
            WRITE(9,177)AX,RA,DEG,RK
  177       FORMAT:(1HO,'ASPECT RATIO=',F7.5,5X,'RALEIGH'
           1  'NO.=',F9.1,5X,'TILT=',F4.1,5X,'AIR/SPACER'
           2  'CONDUCTIVITY=',F5.3)
  176       WRITE(9,12)MRUN,NSF,NTS,NTC,NVO

  12        FORMAT:(1HO,'MRUN=',I5,2X,'NSF=',I5,2X,'NTS=',I5,2X,
           1  'NTC=',I5,2X,'NVO=',I5)
  11        CONTINUE
            STOP
            END
```

```
CC      PROGRAM SUBROUTINE SORT.
CC*************************************************************
        SUBROUTINE SORT(SVOF,FUC,M,N,NDX,MDY,X,Y,NN)
        DIMENSION FUC(NDX+3,MDY+1),X(100),Y(100)
        NN=0
        DO 7000 J=1,M
        DO 7000 I=2,N-1
        IF(FUC(I,J).LE.SVOF.AND.FUC(I+1,J).GE.SVOF)GO TO 8000
        IF(FUC(I,J).GE.SVOF.AND.FUC(I+1,J).LE.SVOF)GO TO 9000
        GO TO 7000
8000    NN=NN+1
        IF(FUC(I,J).EQ.FUC(I+1,J))THEN
        FS=0.
        ELSE
        FS=(SVOF-FUC(I,J))/(FUC(I+1,J)-FUC(I,J))
        ENDIF
        GO TO 6000
9000    NN=NN+1
        IF(FUC(I,J).EQ.FUC(I+1,J))THEN
        FS=0.
        ELSE
        FS=(FUC(I,J)-SVOF)/(FUC(I,J)-FUC(I+1,J))
        ENDIF
6000    X(NN)=(FLOAT(I-2)+FS)
        Y(NN)=FLOAT(J-1)
7000    CONTINUE
        DO 1100 I=2,N
        DO 1100 J=1,M-1
        IF(FUC(I,J).LE.SVOF.AND.FUC(I,J+1).GE.SVOF)GO TO 1200
        IF(FUC(I,J).GE.SVOF.AND.FUC(I,J+1).LE.SVOF)GO TO 1300
        GO TO 1100
1200    NN=NN+1
        IF(FUC(I,J).EQ.FUC(I,J+1))THEN
        FS=0.
        ELSE
        FS=(SVOF-FUC(I,J))/(FUC(I,J+1)-FUC(I,J))
        ENDIF
        GO TO 1400
1300    NN=NN+1
        IF(FUC(I,J).EQ.FUC(I,J+1))THEN
        FS=0.
        ELSE
        FS=(FUC(I,J)-SVOF)/(FUC(I,J)-FUC(I,J+1))
        ENDIF
1400    X(NN)=FLOAT(I-2)
        Y(NN)=(FLOAT(J-1)+FS)
1100    CONTINUE
        RETURN
        END
```